A Multi-Modal Approach to Functional Neuroimaging

By Matthew Jon Brookes, M.Sci.

Thesis submitted to the University of Nottingham for the degree of Doctor of Philosophy, July 2005

This thesis is dedicated to my late grandfather

Capt. Ernest Brookes

ACKNOWLEDGEMENTS

I would like to begin by expressing my sincere thanks to my supervisor, Prof Peter Morris, for his help, advice and encouragement over the past three years. I would also like to thank Dr. Sue Francis for all of her help, particularly with the ASL work, Dr. Andy Gibson for his help with fMRI, Prof Penny Gowland and Prof Richard Bowtell for their helpful advice, and Dr. Caroline Hoad for introducing me to perfusion imaging. Thanks also to all those who helped me with my experiments: Dr Andy Peters, Ms. Kay Head, Dr Ron Coxon and all of the volunteers who have taken part in my studies. I would also like to express thanks to my collaborators at the MEG Lab in Aston, both for teaching me how to use their scanner, and for all of their help in analysing results. Particular thanks must go to Dr. Gareth Bares and Dr. Arjan Hillebrand for their advice on the use of beamformers for MEG analysis.

Next I'd like to thank all of my friends and colleagues (past and present) from the MR centre who have not only made the past three years extremely enjoyable, but also for their help and advice with many aspects of this work Names that spring to mind are Anthony, Bhavana, Wietske, Karen, Sarah, Alex, Sean, Arthur, Nic, Elliot, Ian, Emily, Alexa, Gianlo and anyone else whose name I've left out! Thanks also to my friends back in Leicester, especially everyone at Whetstone badminton club, Wyggeston badminton club, Leicester Vipers rugby club and the Martin Taylor cricket club for providing me with a constant distraction from work! Extra special thanks however must go to Mark Rick Vanessa, Becky, Gary, Luke, Bryony, Helen, Louise, Johnny, Gwen and Mark, not just for putting up with my constant ramblings on physics, but for always coming back for more!

Last, but by no means least, I'd like to thank my family, for their constant, unwavering, support throughout 7 years of university. Special thanks must go to Mum and Dad, for their financial support and encouragement throughout my time in Nottingham. Thanks also to my brother Chris, my grandparents, but most of all Emily and Lucy, for keeping me smiling!

As one, final note, I would like to say one last thank you to Mr. James Hobbs, whose help throughout my A-levels and degree was invaluable, but whose knowledge and enthusiasm for the subject had way more influence than he'll ever know, Cheers Jim!

M.J.B. Nov. 2005

CONTENTS

CHAPTER 1: INTRODUCTION

1.1 THE HUMAN BRAIN 1

1.2 TECHNIQUES FOR FUNCTIONAL BRAIN IMAGING **3**

1.2.1 Functional MRI **3**

1.2.2 Positron Emission Tomography **4**

1.2.3 Electroencephalography **4**

1.2.4 Magnetoencephalography **5**

1.3 SCOPE OF THIS THESIS **6**

1.3.1 Fundamental question **6**

1.3.2 Thesis Overview **6**

1.4 REFERENCES **9**

CHAPTER 2: NUCLEAR MAGNETIC RESONANCE THEORY

2.1 BASIC RESONANCE PROPERTIES OF THE NUCLEUS **10**

2.1.1 An introduction to spin angular momentum **10**

2.1.2 The application of a magnetic field **12**

2.2 THE CLASSICAL DESCRIPTION OF NMR **15**

2.2.1 Larmor precession **15**

2.2.2 Interactions with RF radiation **16**

2.2.3 From single spins to bulk magnetisation **20**

2.3 INTERACTION BETWEEN NUCLEI **23**

2.3.1 A simple molecular description of nuclear spin relaxation **23**

2.3.2 Spin-lattice relaxation **24**

2.3.3 Spin-spin relaxation **26**

2.3.4 The Bloch equations **27**

2.3.5 The spin Hamiltonian **27**

2.4 NUCLEAR MAGNETIC RESONANCE EXPERIMENTS **28**

2.4.1 Free induction decay and phase sensitive detection **28**

2.4.2 Inversion recovery: Measurement of Ti **30**

2.4.3 The spin echo **32**

2.5 REFERENCES **36**

CHAPTER 3: NMR IMAGING: PRINCIPLES AND INSTRUMENTATION

3.1 MAGNETIC RESONANCE IMAGING **37**

3.1.1 Spatial encoding by gradient field **37**

3.1.2 Slice selection **39**

3.1.3 The gradient echo and spin warp imaging **42**

3.1.4 Image contrast **46**

3.1.5 Echo planar imaging **47**

3.1.6 Limitations of EPI: K-space sampling and voxel bandwidth **50**

3.1.7 Limitations of EPI: Image artefacts **51**

3.2 THE IMAGING SYSTEM **54**

3.2.1 System overview **54**

3.2.2 Safety in MR systems **59**

3.3 REFERENCES **61**

CHAPTER 4: MAGNETOENCEPHALOGRAPHY: THEORY AND INSTRUMENTATION

4.1 THE GENERATION OF NEUROMAGNETIC FIELDS **63**

4.1.1 Brain structure and function **63**

4.1.2 Neurons **65**

4.1.3 Glial cells **68**

4.1.4 Post-synaptic potentials and the generation of neuromagnetic fields 70
4.1.5 Action potentials and the generation of neuromagnetic fields 72

4.2 DETECTION OF NEUROMAGNETIC FIELDS 74
4.2.1 Superconductivity 74
4.2.2 The order parameter and flux quantisation 76
4.2.3 Josephson junctions 77
4.2.4 Quantum interference 79
4.2.5 The DC SQUID operating principle and the MEG system 80
4.2.6 Noise reduction strategies 82

4.3 DETECTABLE NEUROMAGNETIC EFFECTS 87
4.3.1 The evoked response and sustained field effects 87
4.3.2 Oscillatory effects 88

4.4 REFERENCES 90

CHAPTER 5: A NOVEL DETECTION METHOD FOR NEUROMAGNETIC SIGNALS

5.1 THE FORWARD PROBLEM 92
5.1.1 Maxwell's equations and the quasi-static approximation 93
5.1.2 The solution to the MEG forward problem 95

5.2 THE INVERSE PROBLEM 99
5.2.1 Lead fields 100
5.2.2 The Linearly Constrained Minimum Variance Beamformer Problem 101
5.2.3 Solution to the L.C.M.V. Beamformer Problem 102
5.2.4 The Hilbert transform 106
5.2.5 The general linear model 108
5.2.6 Summary 111

5.3 THE GLM-BEAMFORMER APPLIED TO SIMULATIONS **111**
5.3.1 Simulation of data **111**

5.3.2 The covariance window and band pass filtering 112

5.3.3 Source detection 113

5.3.4 Statistical testing of the GLM-beamformer method 116

5.3.5 Results of the simulations — source localisation 116

5.3 EXPERIMENTAL EXAMPLE — THE SCINTILLATING SCOTOMA 120

5.4.1 Collection and analysis of experimental data 120

5.4.2 Results — The scintillating scotoma 122

5.5 DISCUSSION — THE GLM-BEAMFORMER METHOD 124

5.6 CONCLUSION 126

5.7 REFERENCES 128

CHAPTER 6: THE COMBINATION OF FMRI AND MEG

6.1 INTRODUCTION 134

6.1.1 Introduction to the BOLD response 134

6.1.2 BOLD contrast mechanisms 135

6.1.3 The haemodynamic response 139

6.1.4 BOLD fMRI and MEG 140

6.2 EXPERIMENTAL METHOD 142

6.2.1 The visual paradigm 142

6.2.2 Functional MRI data collection 142

6.2.3 Functional MRI data analysis 144

6.2.4 MEG data collection 146

6.2.5 MEG data analysis 147

6.2.6 Quantitative assessment of spatial localisation and temporal analysis 149

6.3 RESULTS 150

6.4 DISCUSSION: NEUROMAGNETIC EFFECTS AND BOLD FMRI 156

6.4.1 The neuromagnetic effects 156

6.4.2 Spatial localisation and brain metabolism **157**

6.4.3 Limitations to the present study **158**

6.5 CONCLUSION **159**

6.6 REFERENCES **160**

CHAPTER 7: QUANTITATIVE MEASUREMENTS USING FMRI

7.1 INTRODUCTION **164**

7.2 THEORY **169**

7.2.1 The LL-EPI pulse sequence **169**

7.2.2 LL-EPI sequence to measure Ti relaxation **170**

7.2.3 LL-EPI and arterial spin labelling **171**

7.2.4 Mathematical modelling of the aCBV signal **174**

7.3 EXPERIMENTAL METHOD **181**

7.3.1 Sequence optimisation **181**

7.3.2 Spoiler gradients **182**

7.4 PHANTOM T1 MEASUREMENTS **183**

7.4.1 Experimental method and data processing **184**

7.4.2 Results **186**

7.4.3 Discussion **187**

7.5 ACBV MEASUREMENTS — EXPERIMENTAL SET UP **188**

7.5.1 ASL sequence geometry **188**

7.5.2 Diffusion weighting and b-values **189**

7.5.3 The difference signal **191**

7.5.4 Experimental details **193**

7.6 RESULTS **194**

7.6.1 Quantitative aCBV measurements **194**

7.6.2 LL-EPI-FAIR with diffusion weighting **197**

7.6.3 LL-EPI-FAIR vs. LL-EPI-STAR **200**

7.7 ACTIVATION INDUCED CHANGE IN ACBV - A PILOT STUDY 202

7.8 DISCUSSION - THE LL-EPI-ASL SEQUENCES 204

7.9 CONCLUSION 206

7.10 REFERENCES 207

CHAPTER 8: CONCLUSIONS AND FUTURE DIRECTIONS

8.1 THE MEG BEAMFORMER - LIMITATIONS AND EXTENSIONS 210

8.2 NEUROMAGNETIC EFFECTS AND THE BOLD RESPONSE 214

8.3 QUANTITATIVE IMAGING AND ACBV 216

8.4 CONCLUSING REMARKS 217

8.5 REFERENCES 218

APPENDIX: JOURNAL PUBLICATIONS

ABSTRACT

The work undertaken involves the use of functional magnetic resonance imaging (fMRI) and magnetoencephalography (MEG) as separate but complementary non-invasive functional brain imaging modalities. The aim in combining fMRI and MEG is centred around exploitation of the high temporal resolution available in MEG, and the high spatial resolution available in fMRI. However, whilst MEG represents a direct measure of neuronal activity, BOLD fMRI is an indirect measure and this makes the two modalities truly complementary. In both cases, the imaging signals measured are relatively poorly understood and so the fundamental question asked here is: How are the neuromagnetic effects detectable using MEG related to the metabolic effects reflected in the fMRI BOLD response?

Initially, a novel technique is introduced for the detection and spatial localisation of neuromagnetic effects in MEG. This technique, based on a beamforming approach to the MEG inverse problem, is shown to yield accurate results both in simulation and using experimental data. The technique introduced is applied to MEG data from a simple experiment involving stimulation of the visual cortex. A number of heterogeneous neuromagnetic effects are shown to be detectable, and furthermore, these effects are shown to be spatially and temporally correlated with the fMRI BOLD response. The limitations to comparing only two measures of brain activity are discussed, and the use of arterial spin labelling (ASL) to make quantitative measurements of physiological parameters supplementing these two initial metrics is introduced. Finally, a novel technique for accurate quantification of arterial cerebral blood volume using ASL is described and shown to produce accurate results. A concluding chapter then speculates on how these aCBV measurements might be combined with those from MEG in order to better understand the fMRI BOLD response.

CHAPTER ONE

INTRODUCTION

1.1 THE HUMAN BRAIN

The human brain is perhaps the single most complex and remarkable structure known to man. It contains in excess of 10^{10} neurons in the outermost layer (the cerebral cortex) alone [1], and these cells transmit electrical signals between one another via approximately $10^{"}$ axonal connections [2]. It is these signals that allow us to function as human beings. Not only do they mediate fundamental functions such as breathing or vision, but they also control who we are — in effect they represent the fabric of our personality.

For centuries humankind has been driven to understand the internal workings of the brain. This has been born both of curiosity, and the will to cure those who suffer from mental disorders. Evidence suggests that even as far back as 7000 years ago, our ancestors were boring holes in each other's skulls with the aim not to kill, but to cure. Humanoid skulls found during archaeological digs and dating back several millennia show signs of healing after operation, indicating that procedures were carried out on live subjects with a view to cure them of brain disorder. Quite what our ancestors hoped to achieve by their early forays into the world of neuroscience is unclear, however, their curiosity and desire to cure remains. In the 21^{St} century, scientific discovery has led to a great many afflictions, from broken limbs to heart disease, becoming treatable and curable by modern medicine. However, despite the advances, the brain remains something of a mystery to us, partly due to its complex nature, and partly because until recently tools have not been available to examine its functionality in vivo.

The first real attempts at application of scientific techniques to the understanding of human brain function were made by F.J. Gall in the 19^{th} century. He hypothesized that the brain was made from a complex mosaic of 'mental organs' each of which represented a particular function, and was anatomically localised within the cortex. Inspired by his

findings, many scientists began investigation into human brain functionality, however the lack of non-invasive investigative techniques meant that they were limited to ex-vivo study. In 1862, Paul Broca, a French neuroscientist demonstrated a brain lesion well localised to the lower left frontal lobe in a patient who had suffered from aphasia. Broca concluded that this particular cortical region (now known as Broca's area) must be responsible for aspects of speech, thus explaining his patient's condition. Many people now believe this to be the first experimental evidence of the functional divisions in the human cortex previously suggested by Gall.

Work in this area progressed and in the late 19th century, electrical stimulation of the cortex lead to the mapping of motor function in animals and later in humans, however, results showed a great deal of inconsistency. This work continued into the 20th century when more reliable measurements were made by Penfield, who managed to map the motor and somatosensory cortices of patients undergoing neurosurgery.

As the 20th century progressed, advances in physics lead to the introduction of new methods to investigate brain structure and function. In 1929, Hans Berger, a German physician, showed that it was possible to measure spontaneous fluctuations in electrical potentials on the scalp brought about by neuronal currents within the cerebral cortex. This represented the birth of the technique now known as electroencephalography [3] and was the first, true, non-invasive method for functional brain investigation. In the latter half of the 20th century, neuroscience was revolutionised by the introduction of medical imaging [4]. In the 1970's the advent of x-ray computed tomography (CT) allowed clinicians to see anatomical features inside the heads of patients without the need for surgery. X-ray CT was later developed into radioisotope imaging, a generic name given to several techniques in which a small radioactive source is implanted inside the patient and the resulting distribution of emitted radiation recorded. Also in the 1970's, a new technique was being developed by physicists based on nuclear magnetic resonance. This promised even better anatomical images than those produced by x-ray CT. In the late 1970's Magnetic Resonance Imaging (MRI) [5, 6] was introduced and has since been developed to produce images of the human body with unparalleled resolution and soft tissue

contrast. Furthermore, since MRI does not involve the use of ionising radiation, the risk to patients is minimal. Throughout the late 1970's and 1980's, a technique was developed that allowed the acquisition of single MR images in just a few hundred milliseconds [7]. This technique has subsequently been used in functional imaging of the heart, and the rapid determination of physiological parameters. In 1993, Ogawa et al [8] demonstrated that blood oxygenation could be used as an endogenous contrast agent in rapidly acquired MR images, allowing one to track the spatial distribution of dynamic changes in blood flow, blood volume and blood oxygenation in response to brain activation. This effect, now known as blood oxygenation level dependent (BOLD) functional MRI, provides a means to image human brain function non-invasively.

1.2 TECHNIQUES FOR FUNCTIONAL BRAIN IMAGING

The pioneering work described above has lead to the introduction and in some cases clinical use of a number of different functional brain imaging modalities. In general these techniques rely on the detection of either electrophysiological changes in the brain brought about by signalling currents in active cells, or the metabolic and haemodynamic changes that support this cellular activity. Imaging modalities relying on detection of electrophysiological changes are known as direct neuroimaging techniques since they measure quantities related directly to neuronal activity. Conversely, those modalities relying on detection of metabolic and/or haemodynamic processes are known as indirect measures since they are reliant on a secondary response to heightened cell activity. Four independent techniques for measurement of such parameters are described briefly below.

1.2.1 Functional MRI

Functional Magnetic Resonance Imaging (fMRI) [8] is now a relatively well-established technique for investigating the function of the human brain in vivo. Increases in neuronal activity are tightly coupled to localised reduction in paramagnetic deoxyhaemoglobin concentration, which results from an increase in cerebral blood flow (CBF) without a commensurate increase in the cerebral metabolic rate of oxygen (CMRO2). The increased signal in appropriately weighted MR images caused by this blood oxygenation level dependent **(BOLD)** effect is the basis for the majority of fMRI studies. BOLD based

fMRI allows acquisition of functional images showing active areas of cerebral cortex with excellent spatial resolution. However, the temporal resolution of BOLD imaging is limited by the blood flow response to neuronal activity. This haemodynamic lag represents a limitation to all indirect measures of brain activity. A further problem in' fMRI is that the underlying physiology of the BOLD response itself is poorly understood. This has lead to fMRI being limited to qualitative measurements of brain activity.

1.2.2 PET

Positron Emission Tomography (PET) [9] represents a means of imaging dynamic changes in the spatial distribution of radioactively labelled molecules that are selectively taken up by different regions of brain. In short, a positron emitter is attached to a carrier molecule and injected into the blood stream of a subject. The carrier molecule is chosen such that it will cross the blood / brain barrier and be distributed, selectively, throughout the brain. Positrons emitted from this small source annihilate with local electrons causing the emission of two photons of characteristic energy (y rays) that pass out of the head and are detected. Measurement of the extra-cranial count rate and appropriate reconstruction algorithms allow production of functional images showing the spatial distribution of carrier molecule uptake. Using PET, it is possible to measure physiological parameters such as blood flow, however such indirect measurements of brain activity are limited by our lack of understanding of the relationship between neuronal activity and metabolism.

1.2.3 EEG

Electroencephalography (EEG) [3] measures electrical potential at the scalp surface caused by electric fields associated with neuronal current flow in the brain. A number of electrodes are attached to the subjects' scalp (usually conductivity being maintained using a conductive gel) and electric potential recorded as a function of both time and electrode position. In the resting state a number of oscillatory effects have been observed, the largest of which is an 8 — 13 Hz waveform termed the 'alpha' wave. In response to external stimulation, both transient effects and changes in oscillatory power within specific frequency bands have been reported. EEG offers a direct measurement of neuronal activity and extremely high temporal resolution (i.e. it is not limited by blood

flow response as is the case with most fMRI and PET studies). However, its spatial resolution is severely limited for two reasons. Firstly, in order to obtain accurately the position of current sources responsible for the measured potentials, one has to reconstruct the electrical potential distribution measured outside the head into a map of current strength inside the head. This is known as the inverse problem and is ill-defined (i.e. it has no unique solution) meaning that source estimation in EEG is difficult. Inverse problem solutions do however exist, most of which base their results on some a-priori information on the current distribution sought. For example, assumptions about the number of active neuronal sources, and the form of those neuronal currents facilitate a least squares dipole fitting approach. In general, for any given experiment, an inverse problem solution should be chosen that is best tailored to the requirements of that particular paradigm. Further difficulties arise because changes in the conductivity profile between the brain, skull and scalp can distort spatially the measured electrical potentials. The conductance of both brain tissue and skin is much higher than that of the skull, across which most of the potential is dropped. If the skull maintained a uniform thickness throughout head this would not be a problem, however in practice spatial variations in skull thickness can bias the passage of currents. Currents will take a path of least resistance to the scalp surface and spatial variation of conductivity profile brought about by spatial variation of skull thickness will induce distortions in the measured potential distribution. For these reasons, whilst the temporal resolution of EEG is unparalleled, its spatial resolution is poor.

1.2.4 MEG

Magnetoencephalography (MEG) M is the magnetic counterpart of EEG, and detects magnetic fields outside the head induced by neuronal currents in the brain. The magnetic fields induced are extremely small (50 — 500 ff), however they are detectable using superconducting quantum interference devices (SQUIDs). The type of effect detectable in EEG is also detectable in MEG with equivalent temporal resolution. In addition, because the magnetic permeability of brain, skull and scalp does not differ significantly from that of free space, MEG does not suffer from the same spatial distortions that we observe in EEG. However, the problem of source reconstruction remains because due to field

cancellation effects, a single magnetic field distribution measured outside the head could result from an infinite number of current distributions inside the head. Despite the difficulties, a number of source reconstruction algorithms exist, and in general, MEG is thought to have a better spatial resolution than EEG.

1.3 SCOPE OF THIS THESIS

1.3.1 Fundamental question

Described above are four separate techniques for functional brain imaging. Each has its own specific advantages and disadvantages and is unique in the information that it provides. For this reason, the imaging modalities available should not be thought of as competitive but rather complementary techniques whose combination will allow exploitation of the relative advantages available in each. To this end, the work presented here is directed towards the combination of functional magnetic resonance imaging and magnetoencephalography.

This represents an ongoing scheme of work and the initial aim in combining fMRI and MEG was centred around exploitation of the high temporal resolution available in MEG, and the high spatial resolution available in fMRI. However, we also know that whilst MEG is a direct measure of neuronal activity, BOLD fMRI is an indirect measure and is thought to be loosely related to neuronal metabolism. This fact makes fMRI and MEG truly complementary techniques, however in both cases, the imaging signals measured are relatively poorly understood. The fundamental question asked here is therefore: How are the neuromagnetic effects detectable using MEG related to the metabolic effects reflected in the fMRI BOLD response?

1.3.2 Thesis Overview

This thesis will explore in detail the way in which fMRI and MEG might be combined in order to gain insight into the functional imaging signals recorded using the two modalities.

The thesis is split into two parts: Chapters two, three and four introduce the theory behind functional MRI and MEG. Chapter two will introduce the topic of Nuclear Magnetic Resonance (NMR). The fundamental quantum mechanical ideas underlying the resonant behaviour of nuclei in magnetic fields will be introduced along with a classical description of NMR, Laimor precession and the application of radio frequency (RF) pulses. The theory behind nuclear spin relaxation will be reviewed and the 'Bloch equations' derived. Some simple pulse sequences will also be introduced to measure both spin-spin and spin-lattice relaxation. Chapter three comprises a second MR theory chapter and provides an introduction to both MR imaging and instrumentation. The application of magnetic field gradients in order to encode spatially the precessional frequency of spins is reviewed, along with the combined use of gradient waveforms and RF pulse excitations to obtain MR images. The instrumentation used in subsequent experiments is also introduced including details of coils used to produce static, gradient, and RF magnetic fields and MR safety issues are discussed. The final theory chapter provides an overview of magnetoencephalography. Initially the neural basis of MEG is put forward with a particular emphasis on the types of cell found within the human brain, and their electromagnetic properties. Following this, the instrumentation used in MEG is discussed and fundamental concepts underlying the Superconducting Quantum Interference Device are explained along with the noise reduction strategies to be used in later experiments.

Chapters five six and seven contain the experimental work undertaken. Chapter five presents a technique for solution of the inverse problem and detection of neuromagnetic signals in MEG. The neuromagnetic inverse problem is introduced and a recently developed solution (the non-linear beamformer) is derived from first principles. This solution is then combined mathematically with the Hilbert transform and the General Linear Model to provide a novel method of source localisation that is statistically equivalent to that used in fMRI. The method is tested in simulation and on real MEG data, and is shown to locate accurately current sources in both cases. The technique described provides a useful mathematical framework for comparison of MEG and fMRI detectable effects to be investigated in subsequent chapters.

Chapter six describes the application of BOLD fMRI and MEG to a simple brain activation experiment. Initially, the fundamental physical principles behind the BOLD response are explained and possible connections between the haemodynamic changes measured in the BOLD response and the measurable neuromagnetic fields detected in MEG are discussed. The experiments, and data analysis techniques employed, are then described making use of the novel technique described in chapter five. Experimental results are described quantitatively and the spatial location of various heterogeneous neuromagnetic effects and the BOLD response are shown to coincide. A discussion of results is put forward including speculation as to possible links between the BOLD response and detectable neuromagnetic effects.

The final experimental chapter begins by discussing the limitations of BOLD imaging and how different MR methodology might help in answering fundamental questions about the relationship between MEG and the BOLD response. To this end, chapter seven presents a novel technique involving the use of arterial spin labelling (ASL) in order to measure cerebral blood volume (CBV). A substantial theory section reviews ASL techniques and the sequence that is to be developed. The experimental set up is described and results are given showing how the sequence can be used for the non-invasive measurement of aCBV. The discussion looks at the limitations of the technique described and its possible future application in activation studies.

Chapter eight takes results from all three experimental chapters and draws conclusions about both the advantages and limitations of the combination of BOLD fMRI and MEG. Finally, areas for future work are discussed with a particular emphasis on the inclusion of quantitative measurements of brain activation in the derivation of a relationship between neuromagnetic effects and the BOLD response.

1.4 REFERENCES:

1. Hamalainen, M., Hari, R., Ilmoniemi, R.J., Knuutila, J., Lounasmaa, 0.V., Magnetoencephalography - Theory, Instrumentation and applications to non-invasive studies of the working human brain. Reviews of Modern Physics, 1993. **21(2): p.** 413 - 460.

2. Bear, M.F., Connors, B.W., Paridiso, M.A., Neuroscience: Exploring the brain - Second Edition. 2001, Philadelphia: Lippincott, Williams and Wilkins.

3. Neidermeyer, E., Lopez da Silva, F., Electroencephalography: Basic principles, clinical applications and related fields. 1993, Baltimore: Williams and Williams.

4. Webb, S., The Physics of Medical Imaging. 2001, Bristol: Institute of Physics.

5. Lauterber, P.C., Image Formation by Induced Local Interactions: Examples employing nuclear magnetic resonance. Nature, 1973. **242: p.** 190.

6. Mansfield, P., Grannell, P.K., NMR 'Diffraction' in Solids. Journal of Physics C, 1973. **6: p.** L422.

7. Mansfield, P., Multi Planar Image Formation using NMR Spin Echoes. Journal of Physics C, 1977. **10: p. p** L55-L58.

8. Ogawa, S., Menon, R.S., Tank, **D.W.,** Kim, S-G., Merkle, H., Ellermann, J.M., Ugurbil, K., Functional brain mapping by blood oxygenation level dependent contrast magnetic resonance imaging. Journal of Biophysics, 1993. 64: p. 803-812.

9. Fox, P.T., Mintun, M.A., Raichle, M.E., Herscovitch, P., A non-invasive approach to quantitative functional brain mapping with $H2^{13}$ 0 and positron emission tomography. Journal of Cerebral Blood flow and Metabolism, 1984. **4: p.** 329-333.

CHAPTER TWO

NUCLEAR MAGNETIC RESONANCE THEORY

OVERVIEW

This chapter is intended to provide a basic overview of the theory behind Nuclear Magnetic Resonance (NMR). The discussion begins by introducing the fundamental quantum mechanical ideas underlying the resonant behaviour of nuclei in magnetic fields. Following this, a classical description of NMR will be given in order to describe Larmor precession and the application of a radio frequency (RF) pulse. The classical approach to NMR allows the formulation of a physical picture of nuclei that is both practical and intuitive, however to understand completely the physical interactions that manifest themselves in NMR experiments, a full quantum mechanical derivation must be used. In order to understand work presented here, this quantum mechanical description is not required. Therefore, for a complete description of NMR, the reader is referred elsewhere [1-5]. Finally, the theory behind nuclear spin relaxation is reviewed, the `Bloch equations' are derived using simple statistical ideas and some simple pulse sequences are introduced to measure both spin-spin and spin-lattice relaxation.

2.1 BASIC RESONANCE PROPERTIES OF THE NUCLEUS

2.1.1 An introduction to spin angular momentum

Spin angular momentum is an intrinsic property of both electrons and some atomic nuclei [6]. It is not connected with the movement of the centre of gravity of a particle in space and therefore classically we might describe it as the rotation of a particle about its own central axis. However, using this simple mechanical model we find that the theory can only account for the experimentally observed atomic properties if, in the case of the electron, it had a structure, and parts of that structure were travelling faster than light! This, of course, contradicts the theory of relatively and it turns out that there is no direct classical equivalent to spin angular momentum, meaning that spin angular momentum cannot be treated quantum mechanically using the method prescribed by Schr6dinger, in which classical dynamical values are replaced by mathematical operators. This problem

was solved, in part, by Pauli who by derivation of a set of quantum mechanical spin operators found that the value of spin angular momentum for the proton was ±-$^{1}_{2}$-h . However, it wasn't until the seminal work The principles of Quantum Mechanics' by P.A.M.Dirac [7] that Pauli's theory was combined with the quantum mechanics of dynamical quantities with classical equivalents to form a logical whole. Dirac showed that the precise value of measurable quantities depends not on a detailed definition of the operators associated with those quantities, but on the commutational rules obeyed by those operators. Dirac's theory is beyond the scope of this chapter, thus for the purposes of this initial discussion, we shall assume that a set of spin operators exist, and that unlike the orbital angular momentum operators, the precise definition of these spin operators is unimportant.

Spin angular momentum, **P ,** is a vector quantity, therefore one can postulate that in a Cartesian co-ordinate system, three components of spin angular momentum exist, P_x, $\mathbf{P_y}$ and $_{P.}$. Associated with each of these physical observables is a quantum mechanical operator thus:

$$P_x \text{ --> } \mathbf{hi_x} \text{ ; } \mathbf{P_y} \text{ —> } \mathbf{hi_{t'}} \text{ ; } \mathbf{P_Z} \text{ --> } \mathbf{hi_t} \qquad [2.1]$$

The operators themselves are, by convention, defined as dimensionless quantities, hence the appearance of the **h** in the above identities. The magnitude of **P** is defined as:

[2.2]

Where **I** is the spin quantum number. Since spin is a vector quantity, its direction is also quantised and it can be shown that for a single state **I,** there exists 2/ +1 possible values of the z-component of spin angular momentum, represented by quantum number m_i . These 21 +1 possible states are degenerate and it follows that m, is an eigenvalue of the operator $\mathbf{I_t}$. Taking the simplest possible example of the hydrogen atom, and considering the intrinsic spin angular momentum of its nucleus (a single proton), we find that, since for the proton **I =1, m, =±-$^{1}_{2}$- ,** and so there are two possible values of the z-component of spin angular momentum, and hence two degenerate states. A semi-classical interpretation of this is depicted in Figure 2.1.

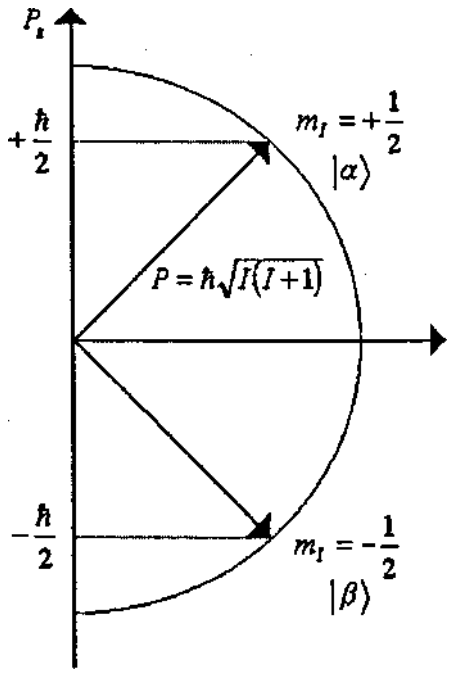

Figure 2.1: Semi-classical interpretation of the spin angular momentum states. Correct values fort PI and P_L are given, but nothing can be said about P_i" $_y$ since II $_e$I $_{vy}$l# 0

For a single, isolated nucleus it is sufficient to use the value of m_i to describe completely the spin state. Further, for a hydrogen atom, using Dirac notation, the m_l = +-İ state is termed the la) state whilst m_l =--+ is termed the $_{18)}$ state.

2.1.2 The application of a magnetic field

If it were possible to model proton spin in a classical sense then one could argue that since a single proton is essentially a spinning sphere of charge, it would behave in exactly the same way as a current travelling through a loop of wire, and would possess an associated magnetic moment. Whilst such a classical analogy yields incorrect quantitative results, this physical picture remains (to some extent) correct and protons do indeed possess an intrinsic magnetic moment, p , which is given by:

p = [2.3]

I.e. **p** is a vector quantity, parallel with, and directly proportional to, spin angular momentum. The constant of proportionality, y, is a scalar quantity known as the gyromagnetic ratio, and its value is dependent on the type of nucleus studied (for example the proton has a gyromagnetic ratio y = 2.67 x10^8 radiansr^{l}s^{-1}).

According to classical electromagnetism, a magnetic moment **p** placed in an external magnetic field **B** has energy given by:

E=-0.B [2.4]

It is the minimisation of energy associated with this interaction that causes a compass needle to rotate parallel to the Earth's magnetic field. The proton, when placed in a large external magnetic field, will act in an analogous way. In this case, we can use the rules set down by Schrodinger and replace the classical value for energy, E, with the Hamiltonian operator H . Combining Equations 2.1, 2.3 and 2.4 we find that:

H = —NB./ [2.5]

By convention, a static field is always applied parallel to the z-axis in the laboratory reference frame (i.e. **B**= B_zi where i is the unit vector in the z-direction), therefore:

z [2.6]

This particular Hamiltonian is known as the Zeeman Hamiltonian and describes the interaction of a nuclear spin with a magnetic field. In order to solve for the energy of the system we simply need to solve the eigenvalue equation:

m,) = Elm$_i$) [2.7]

Substituting for the Hamiltonian operator, this becomes

^{fi}lm') —hAzizimi) [2.8]

and since we already know that the eigenvalue of I_L is m,, it follows that:

[2.9]

Since for a spin-^{1} nucleus, the values that m_l can take are ±1/2, the energy of a spin in the la) state is — pie, and the energy of a spin in the Ifl) state is + -1-hyB_z. Thus, when a

proton is placed in a magnetic field, it looses its two fold degeneracy and an energy splitting is induced in which the energy difference between the la) and 1/3) states is:

$$AE = hA_z \qquad [2.10]$$

This energy splitting is known as Zeeman splitting and is depicted in Figure 2.2.

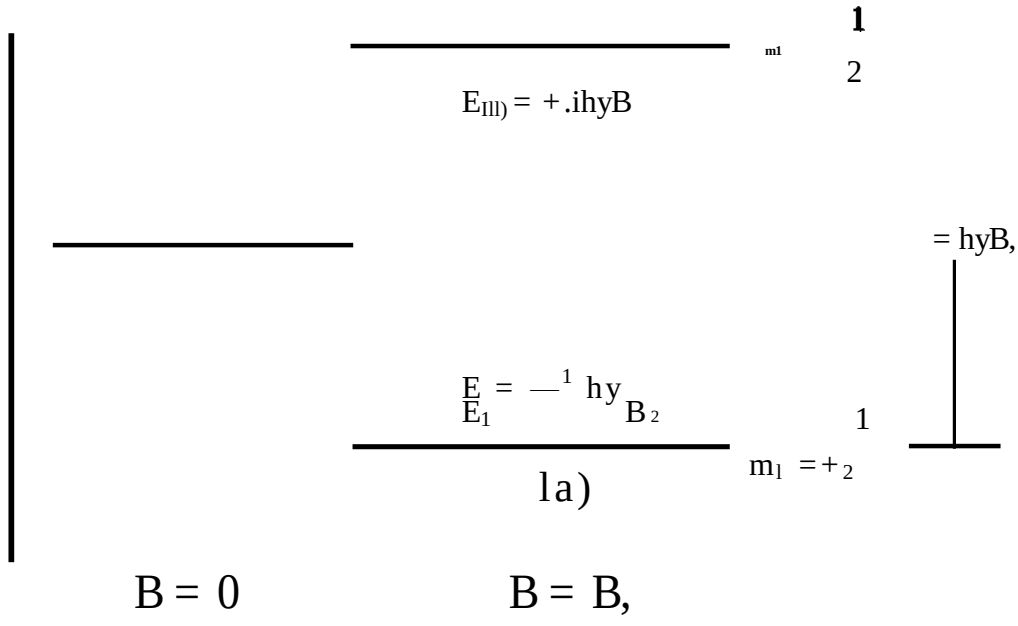

Figure 2.2: Zeeman Splitting

The existence of this energy difference allows a mechanism by which to induce transitions between spin states. This is achieved by application of electromagnetic radiation [8, 9]. A change in the nuclear spin state may be induced if an electromagnetic photon with energy equal to the Zeeman splitting energy AE is absorbed. The frequency of radiation required is given by:

$$v = \frac{}{2tr} \qquad [2.11]$$

For a 1T field this frequency, known as the resonant frequency of the spin system, is 42.58 MHz, which falls in the radiofrequency (RF) range of the electromagnetic spectrum. The application of 'on resonance' electromagnetic radiation to a sample containing a system of nuclear spins is the basis for all nuclear magnetic resonance, and magnetic resonance imaging experiments.

2.2 THE CLASSICAL DESCRIPTION OF NMR

2.2.1 Larmor precession

Having introduced the basic resonance properties of the nucleus we must now go on to look in more detail at the equation of motion of a nuclear magnetic moment both in static and dynamic electromagnetic fields. Consider first the simple case of a nuclear magnetic moment **p ,** placed in a magnetic field **B .** The nuclear magnetic moment will experience a torque that will tend to align the vector **p** along the field direction, however the proton already possesses angular momentum **P** due it its intrinsic spin. This is changed by the torque which acts in a direction perpendicular to **p ,** and therefore the resulting motion is a precession about the field axis. It is possible to derive an equation of motion for the nuclear magnetic moment by equating the torque experienced due to the external magnetic field with the change in angular momentum of the proton thus:

$$\frac{d\mathbf{P}}{dt} = \mathbf{p} \times \mathbf{B} \qquad [2.12]$$

Using Equation 2.3, this may be rewritten:

$$\mathbf{dt} = A\mathbf{p} \times \mathbf{B}) \qquad [2.13]$$

Equation 2.13 represents the classical equation of motion for a magnetic moment in the presence of an external magnetic field, and since the form of **B** is thus far undefined, it may represent either a static, or time dependent field. In the simple case of a static field placed along the z direction (i.e. $\mathbf{B} = \mathbf{B}_i\mathbf{t}')$ then:

$$\mathbf{dt} = \quad \times B_x f) \qquad [2.14]$$

and assuming that the starting values of p_x , $\mathbf{p_y}$ and $/i_x$ are /2,(0), $p_y(0)$ and p_i (0) respectively, then the general solution to this equation is, $p_x($ t

$$)= p_x (0)\cos(243{,}01- p_y(0)\sin(211_z t)$$

$$p_y(t)= —/i_x(0)\sin(g3A+ p_y(0)\cos()e_x t) \qquad [2.15]$$

$$,u_x(t)= p_x(0)$$

Equations 2.15 describe the precessional motion of the magnetic moment about the axis of the applied field. This motion is depicted in Figure 3.3 and is known as Larmor precession.

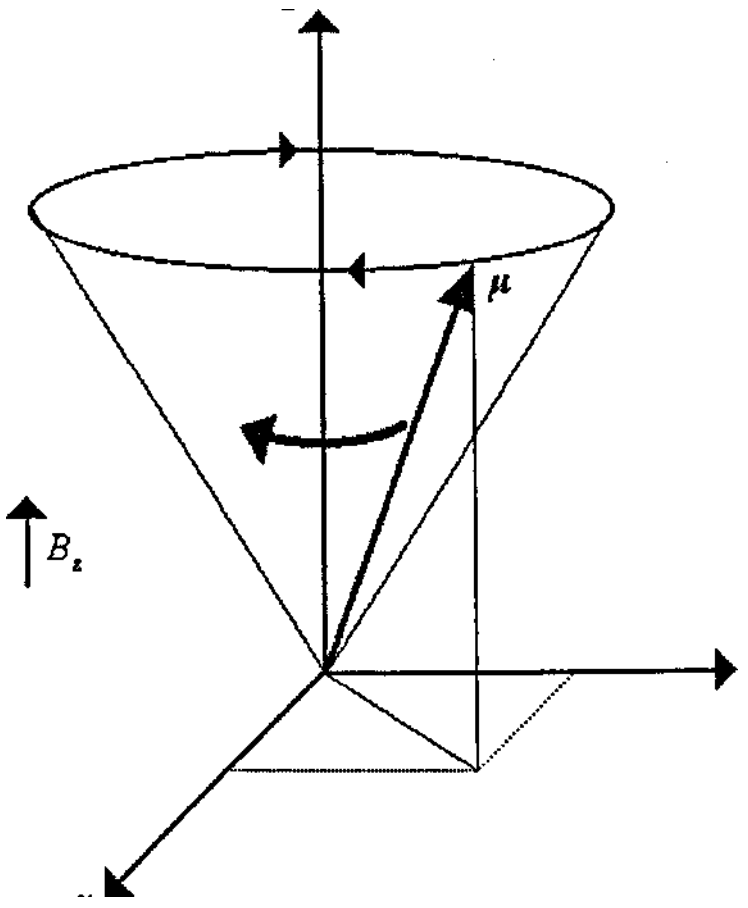

Figure 2.3: Larmor precession

The angular frequency of this precession is $\omega_L = \gamma B_z$, and is known as the Larmor frequency. Note the correspondence between this and Equation 2.11, implying that the resonant frequency of RF radiation required to drive transitions between the I a) and I /3) states is equivalent to the classically derived Larmor frequency of precession for a single proton.

2.2.2 Interactions with RF radiation

The changes in proton spin state induced by application of RF radiation are due to a magnetic dipole interaction between the RF field and the proton. (Not, as is the case with spectroscopy using visible light, an interaction between electric field components.) In

order to gain some insight into these magnetic dipole interactions, consider first the time dependent magnetic field component of the rf radiation $B_1(t)$ that is applied perpendicular to the applied static field **13,** such that:

$$\mathbf{B_i(t) = i2B_1 cos(cot)} \qquad [2.16]$$

This field can be resolved into two rotating components, $\mathbf{B_c(t)}$ which rotates clockwise with angular frequency — *co,* and $B_A(t)$ which rotates anticlockwise with angular frequency + w . Mathematically these fields are given by:

$$\mathbf{B_A(i) = B_i(i\ cos(aa\cdot) +}\ sinfraD$$
$$\mathbf{B_c(t) =}\quad cos(oa) - y\ sin(ax)) \qquad [2.17]$$

Consider for the moment only $\mathbf{B_c(t),}$ we ignore $\mathbf{B_A(t)}$ since it is off resonance and thus will have no effect on spin state. Returning to the general equation of motion and including the effects of the rotating $\mathbf{B_c(t)}$ field we see that:

$$\mathbf{dt} \qquad \text{x} \qquad + \mathbf{B; (I\ cos(cu)\ ol) - St}\ sin(cot))] \qquad [2.18]$$

It now proves instructive to move from our laboratory frame of reference (1, y, z) into a rotating frame of reference This *'Rotating Frame'* rotates clockwise with angular frequency — **co,** and its effect is to remove the time dependence of $\mathbf{B_c(t)}$ from Equation 2.18. Classical mechanics states that, if the time derivative of a vector r in the laboratory frame is given by $\left(\frac{dr}{dt}\right)_{14\cdot1}$, then the time derivative of the vector viewed in the rotating frame is given by:

$$\left(\frac{dr}{dt}\right) = coxr + \left(\frac{dr}{dt}\right) \qquad [2.19]$$

Where $\omega = a$ is the angular velocity. Applying this transformation to Equation 2.18 we obtain:

$$(cox\ II) + \left(\frac{414}{\mathbf{dt}}\right) = \mathbf{px[B,e+B_r il} \qquad [2.20]$$

A simple rearrangement gives:

$$\mathbf{E}_{d}^{IId}) \quad = y_i \, x \, [\{B_z — \underset{Y}{Ele} + B_i \; il = 214X \; B_{ell} \; [121/$$

Where B_{uff} is the effective magnetic field in the rotating frame and is given by:

$$B_o. = B_p i + (B_z \; \underset{Y}{-21e} \qquad [2.22]$$

Physically, Equation 2.21 implies that in the rotating frame of reference, the magnetic moment of a single proton will precess about the axis of the effective field k_{ir} in exactly the same way as it precesses about the axis of the static field in the laboratory frame in the absence of the rf-radiation (see Figure 2.4A). Of particular interest is the special case in which $B_z = r$ (or *to* $ro_{t.}$, the Larmor frequency). Here, the z'-component of the effective magnetic field will reduce to zero, and the magnetic moment will rotate about the x' axis (i.e. in the z' - y' plane) (see Figure 2.4B).

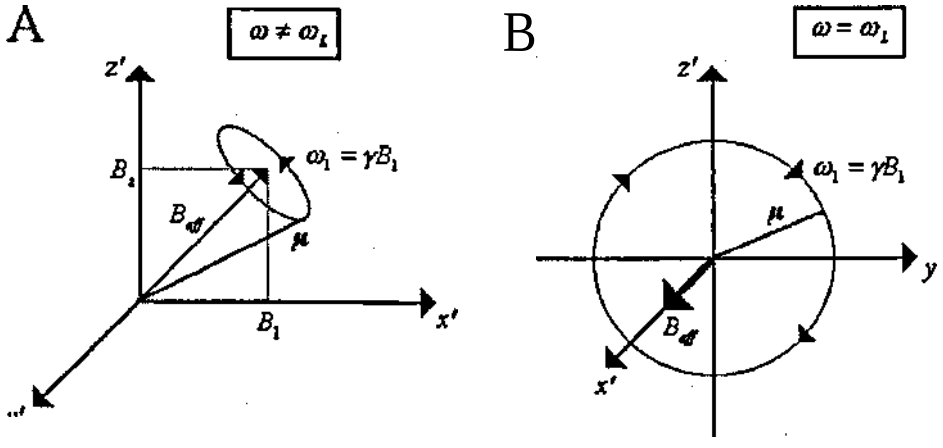

Figure 2.4: The effect of applying a rotating magnetic field to the magnetic moment of a proton. A) The general case in which to * ev_e . B) The special case in which co = $co_{l,}$.

The angular frequency of this induced rotation is given by (0_1 = $\underset{}{2B,}$ and therefore, if the rf-radiation is applied for duration t,,, then the magnetic moment will rotate through an angle ₀where:

$$0,, = A \; t_p \qquad [2.23]$$

This classical result suggests that the magnetic moment of the proton might assume any orientation with respect to the z-axis, which in turn allows a continuous range of possible values for the z-component of magnetic moment. It is here that the classical picture of NMR breaks down, since for a single proton, measurement of spin angular momentum results in the proton being in one of two possible states, I a) or I /3) . This means that there are just two possible values of m_I, and therefore two possible angles that **p** may subtend with respect to the field axis. (Note that it is possible to have a superposition state

A + fi)) however measurement forces the system into one of the two eigenstates.)

Despite the breakdown of the classical model it remains a useful and intuitive result. In the m, = +-1- state one might picture the magnetic moment as being aligned 'parallel' to and precessing about the applied static field whereas in the m, = state, the magnetic moment is aligned 'anti-parallel' to and precesses about the applied field. This semi-classical picture in the absence of RF radiation is shown in Figure 2.5. The application of rf radiation can be thought to induce 'transitions between these two eigenstates and therefore flip the polarity of the nuclear magnetic moment.

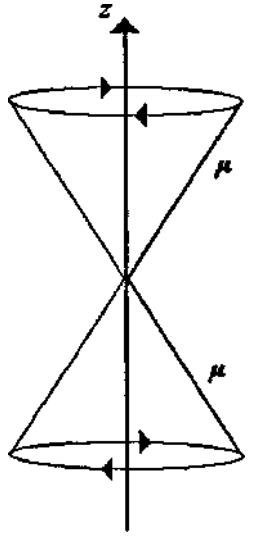

Ia)

I/3)

Figure 2.5: The semi-classical picture of the nuclear magnetic moment in the absence of rf radiation.

2.2.3 From single spins to bulk magnetisation

Thus far, the arguments put forward have involved only a single, isolated nuclear spin. In a real system, one **would** expect around 10^{22} individual spins and in any NMR experiment, one would expect to observe the macroscopic magnetic properties of the sample caused by the superposition of individual magnetic moments from all of these nuclear spins. This macroscopic magnetisation is known as the bulk magnetisation of a sample and it turns out that bulk magnetisation possesses very similar properties to those of the classical individual nuclear spin. Let us consider an ensemble of spin-1/2 nuclei each of which obeys the semi-classical model. We will also assume that any interactions between these nuclei are negligible.

Recall that for spin-1/2 nuclei there are two accessible **eigenstates of I. la)** and I fi). On application of a magnetic field, these two degenerate states undergo Zeeman splitting such that the energy difference between them is given by AE = hyB_z as per Equation 2.10. Assuming a state of thermal equilibrium, the relative populations of the two states are given by Boltzmann statistics, i.e.

$$\frac{N_{f\,t}}{N_a} = \exp\left(\frac{A\,E\,)}{k_B T}\right) \qquad [2.24]$$

Where $\mathbf{N_a}$ is the number of spins in the la) state, N_I, is the number of spins in the 1,3) state, **T is** the temperature and k is the Boltzmann constant. Equation 2.24 clearly shows that an excess number of nuclear spins lie in the la) state i.e. precessing about the z-axis and aligned parallel to it. In the limit where $k_BT >> AE$, we can expand the exponential keeping only the first term such that:

$$\mathbf{N_a - N_{fl} = N_{cr}\frac{yB,}{k_BT} \frac{N\ hg3,}{- 2\ k_BT}} \qquad [2.25]$$

Where **N** represents the total number of spins in the spin system. This is known as the high temperature approximation and holds for most typical laboratory magnetic fields. The total bulk magnetisation M is given by the vector sum of magnetic moments of all the individual spins in the system. Therefore the magnitude of the magnetisation parallel

to the static field (known as longitudinal magnetisation) is given by /14, $= N_a p,"$ $+ N_f pf$, and since $p," = -4 = IA$, we can write:

$$M, = \frac{N\ (hy)^2 13,}{4\ k_B T} \qquad [2.26]$$

This shows that the longitudinal magnetisation induced by placing nuclear spins in a magnetic field is directly proportional to the field strength. Magnetisation perpendicular to the applied field (known as transverse magnetisation) is dependent on phase coherence between precessing spins. Whilst each individual precessing nuclear magnetic moment encompasses a rotating transverse component of magnetisation, unless a significant fraction of these transverse components rotate in phase, then their vector sum will equal zero, and hence no observable transverse component of bulk magnetisation will exist. This is the case in the equilibrium state, and so if a sample is placed in a magnetic field and it remains unperturbed by rf radiation, no transverse component of magnetisation exists and the induced bulk magnetisation is given by $M = M_Z i$.

In applying the oscillating rf field, a change in the relative population of the $la)$ and I fi) states, and thus a change in the longitudinal magnetisation $Af,$ is induced. A secondary effect of the rf field is to introduce phase coherence between precessing spins. Whereas in the equilibrium state, no transverse magnetisation exists because all of the individual nuclear magnetic moments will have a random phase, following the application of an rf pulse, the induced phase coherence produces a finite component of transverse magnetisation that will rotate in the transverse plane at the Larrnor frequency (in the laboratory frame).

Mathematically, it can be shown that the expectation value of the bulk magnetisation M obeys the same classical equation as that used in section 2.3.1 to describe a single spin, i.e.

$$= \frac{dM,}{dt} \quad xB) \qquad [2.27]$$

Given an initial state of thermal equilibrium such that M(0)= M_zi, we can use the equation of motion to derive the subsequent time evolution of bulk magnetisation. From the above calculations, we deduce that if an rf-field is applied at the Larmor frequency then M will be tipped away from the z-axis and a transverse component of magnetisation exists. Again the angle through which M is tipped is given by 0= At_p

where t_p is the duration of the rf pulse. (Notice that this is equivalent to Equation 2.23, except in this case, no restrictions on the angle are introduced by quantum mechanics since M is a macroscopic property and so does not obey the same quantum mechanical rules.) By the use of if-pulses of appropriate lengths, the angle through which M rotates can be controlled, and of particular interest are the special cases in which 0= 90°, and 0=180°. In the case of the 90-degree pulse, the relative populations of the la) and 1/3) states are equalised such that no longitudinal magnetisation exists and the transverse component of M is a maximum. In the case of the 180-degree pulse, the equilibrium magnetisation is inverted such that M = —M_zi and the transverse component is reduced to zero. The effect of an rf pulse is depicted in Figure 2.6 for the special case where 0= 90°.

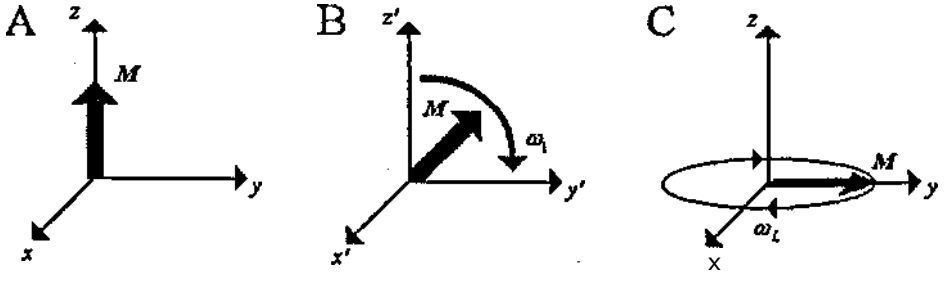

Figure 2.6: Motion of bulk magnetisation before, during and immediately after the application of a 0=90° RF pulse. A) The equilibrium magnetisation aligned parallel to the z-direction and hence the applied static field. B) Motion of bulk magnetisation during application of the RF pulse. Magnetisation is shown in the rotating frame and the pulse causes a rotation about the x'-axis into the transverse plane. C) Bulk magnetisation immediately after application of an RF pulse shown in the laboratory frame.

2.3 INTERACTION BETWEEN NUCLEI

In the classical description of NMR, no reference has been made to the interaction between nuclei in a spin system, such interactions are however key to all MRI experiments. This section therefore presents a brief introduction to spin relaxation, and some of the more subtle interactions between spins in a simple spin system.

2.3.1 A simple molecular description of nuclear spin relaxation

If left undisturbed for a long time in the presence of a magnetic field, a spin system reaches a state of thermal equilibrium implying that i) No phase coherence exists between individual spins, and the relative populations of the la) and l/) states are given by the Boltzmann distribution. The application of an RF pulse sends such a system into a state of non-equilibrium, and following this, some mechanism by which to return it to its initial equilibrium state must be available. This is known as nuclear spin relaxation, and involves transitions in spin state (i.e. I a) H */ fi)).*

A simple molecular description of nuclear spin relaxation can be given in terms of the Brownian motion experienced by molecules as they tumble around a sample. As molecules move their constituent nuclei move with them. Since each nucleus carries a magnetic moment, this causes a randomly fluctuating magnetic field, k^m), that is experienced by neighbouring nuclei. Let us suppose that we could resolve this field into its frequency components by Fourier analysis, and then decompose it into components acting parallel and perpendicular to the applied field **B.**

Components of $\mathbf{k^m}$ that are both perpendicular to $\mathbf{B_L}$ and at the Larmor frequency can cause changes in state in exactly the same way as the RF field does. These changes in state cause changes in relative populations of the two basis states, which, in turn, cause the longitudinal magnetisation to change, relaxing back to its initial baseline state. This is commonly known as spin-lattice relaxation and is characterised by a time constant T, .

Components acting parallel to **B,** will cause small changes in the resonant frequency of the nuclear spins in the system. Quantum mechanically this may be thought of as a broadening of the linewidth in the energy spectra. Such effects can cause a loss of phase coherence between nuclear spins in the system and hence the relaxation of the transverse magnetisation. This is known as spin-spin relaxation and is characterised by time constant $\mathbf{T_2}$**.** Spin-spin relaxation is not solely due to molecular motion. Due to spin

lattice relaxation, the lifetime & of a spin in a particular state is finite. The Heisenberg uncertainty principle states that (Z.& > h, and since & is finite, this implies that SE must also be finite, again implying a broadening of the spectral lines, and hence a loss of phase coherence.

2.3.2 Spin-lattice relaxation

In order to look closer at the mechanism of spin-lattice relaxation, we must consider how the spin state populations change in the presence of a randomly fluctuating magnetic field. The kinetic equation for the **la)** state population is:

$$\frac{dP_a}{dt} = -W_{co}p_a + W_{fia}p_{fl} \qquad [2.28]$$

Where W_{aft} is the probability of a spin transferring from the la) state to the 1a) state, W_{fla} is the probability of a spin transferring from the 113) state to the l a) state, p_c, is the fraction of spins already in the **la)** state and p_a is the fraction of spins already in the $l_i g)$ state. (Note that $p_a + {}_{/0,6} = 1.$) In a similar fashion, the kinetic equation for the I /3) state population is given by:

$$\frac{dp_{al}}{} \qquad [2.29]$$

The transition probabilities are defined by the equations:

$$\begin{aligned} W_{aft} &= W(1--1K) \\ W,_q &= W\ (1+\ K \end{aligned}, \qquad [2.30]$$

Where $K = T_B^{7/w}$ is the Boltzmann factor and W is the mean probability of a transition, i.e. W = i **(W_{aft} + w_{fl_a}** . Notice that the two probabilities differ by the Boltzmann factor, it is this difference, caused by Zeeman splitting, which ensures that in the resting state, the number of spins in the la) state is slightly larger than the number of spins in the IP) state. The probability of transitions between the two basis states is proportional to both (B_x''''), the root mean square value of the x-component of k^m), and 3( ), the normalised spectral density function of k^m), evaluated at the Larmor frequency. In fact, the mean transition probability W can be written as:

$$W = 2Y2(BlM))9(wL) \qquad [2.31]$$

We know that the z-component of magnetisation is dependent on the population difference between the l a) and IM states, i.e.:

$$M \ll p_a — p_{fl} \qquad [2.32]$$

By differentiating Equation 2.32 and substituting in Equations 2.28 and 2.29 it follows that:

$$\frac{dM}{dt} \quad \frac{dPa}{dt} \quad \frac{dpi}{dt} = \_w_{aft\,pa} + W_{fla}p \qquad [2.33]$$

Finally by combining Equations 2.33, 2.32 and 2.30 and recalling that $p_{er} + 1_{,1)} = 1$ we find that:

$$\frac{dM}{dt} = —2W(M — M_0) \qquad [2.34]$$

Which may be rewritten:

$$\frac{dMz}{\qquad\qquad} \qquad dt$$

Where T_1 is the spin-lattice time constant for longitudinal relaxation and is inversely proportional to the mean transition probability ($T_, = y_{2w}$). The value of T, is a property of any given material and, as we shall see later in this chapter, can be measured using simple NMR techniques. For pure samples, the solution of Equation 2.35 is:

$$M_z(t) = M_0(1 + (\cos(0) - 1)\exp(-t/T_1)) \qquad [2.36]$$

Where 0 is the angle through which the bulk magnetisation has been flipped by interaction with an RF field.

2.3.3 Spin-spin relaxation

Spin-spin relaxation theory describes the recovery of transverse magnetisation, characterised by the dephasing of precessing spins. This process may also be viewed as the result of quantum transitions. In order to demonstrate this, consider again the rotating fame of reference in which the transverse magnetisation is static and aligned along the x' axis. The spin operator I_x has two eigenfunctions with eigenvalues $\pm i$, however, unlike the case with i_x, these two states are degenerate, and hence the two states should be equally populated. Knowing that for the spin-spin case $K = 0$, and proceeding through a similar derivation to that used to describe spin lattice relaxation, we find that:

$$\frac{dM_{x'}}{dt}$$

and similarly for the y' axis:

$$\frac{dM_{y'}}{dt} = -2W_1 \langle 1 \rangle \qquad [2.38]$$

Symmetry arguments suggest that $W_{x'} = W_{y'} = W_1$ and letting $\langle 1 \rangle = (M_x^2 m)_0 +$ and $\frac{1}{T_2} = 2W_1$ we find that:

$$\frac{dM}{dt} = \frac{M_1}{T_2} \qquad [2.39]$$

Again, for a pure sample the solution to Equation 2.39 is:

$$M_1 = M_0 \sin\theta \exp(-\qquad [2.40]$$

This shows that following the induction of some finite component of transverse magnetisation by an **RF** pulse. Immediately following the offset of RF stimulation, the induced magnetisation relaxes exponentially back to zero.

2.3.4 The Bloch Equations

Equations 2.35 and 2.39 can be combined with Equation 2.27 to obtain the Bloch equations [8], which provide a general framework for derivation of the evolution of magnetisation. The equations describe the motion of the three orthogonal components (x, y and z) in the rotating frame thus:

$$\frac{dM_{2.41}}{dt} = (_{B}w\,M_{Y}\,o\,y\,T_{2} \qquad \textbf{[2.41]}$$

$$\frac{di\ 1}{dt} = 2^{,31}zBI^{-}2^{111},,(B0^{-6}4)^{-}{}_{1}{}^{M}{}_{T}: \qquad \textbf{[2.42]}$$

$$\frac{dM}{dt} = \frac{dMM - M_{\circ}}{B,\ y\ z} \qquad \textbf{[2.43]}$$

23.5 The Spin Hamiltonian

In addition to those caused by the externally applied static and dynamic magnetic fields, other terms exist in the spin Hamiltonian caused by interaction between nuclei and their surroundings. Such terms are not important for work presented in this thesis but, for completeness, should be mentioned briefly. For spin 1/2 nuclei these interactions can be summarised by three terms in the spin Hamiltonian, namely the chemical shift, the dipolar interaction, and J-coupling.

Because electrons possess magnetic properties, the local magnetic field at any given nucleus will depend on its local electronic environment. The small magnetic fields generated by electrons either add to, or subtract from, the externally applied static magnetic field, causing slight shifts in the Larmor frequency. This effect is known as chemical shift, and if a number of different molecular species are present in the sample, then a Fourier transform of the received NMR signal reveals a number of chemically specific resonant frequencies, each corresponding to a different molecular environment.

The chemical shift is exploited in magnetic resonance spectroscopy, where the dependence of the received signal on the local chemical environment means that one can ascertain the chemical structure of molecules within the sample.

Dipole — dipole coupling is a direct magnetic coupling between nuclear magnetic moments and is largely responsible for spin relaxation. Since each nuclear spin behaves essentially as a magnetic dipole, it generates a magnetic field that loops around the surrounding space. If a second nuclear spin exists within this field it will interact, causing slight shifts in resonant frequency. The dipole interaction is most prominent in solid-state NMR experiments, however its effects can also be observed in the liquid state.

.1-coupling is a somewhat more subtle interaction and is brought about due to electron spin state and the Pauli exclusion principle. It is based on the fact that energy differences are observed depending on whether protons are aligned parallel or anti-parallel with respect to electron spins. Such interactions can be manipulated by `J-editing' MR sequences and are important for spectroscopic techniques.

2.4 NUCLEAR MAGNETIC RESONANCE EXPERIMENTS

2.4.1 Free induction decay and phase sensitive detection

Following the application of an **RF** pulse, the induced precessing transverse magnetisation can be used to induce a radio frequency oscillating current in a coil placed close to the sample and by convention, oriented along the x-axis of the laboratory frame, (this experimental set up is shown in Figure 2.7A). The induced oscillating electrical current is small, but detectable due to its well-defined frequency of oscillation. It decays as per the Bloch equations, and is known as a Free Induction Decay (HD).

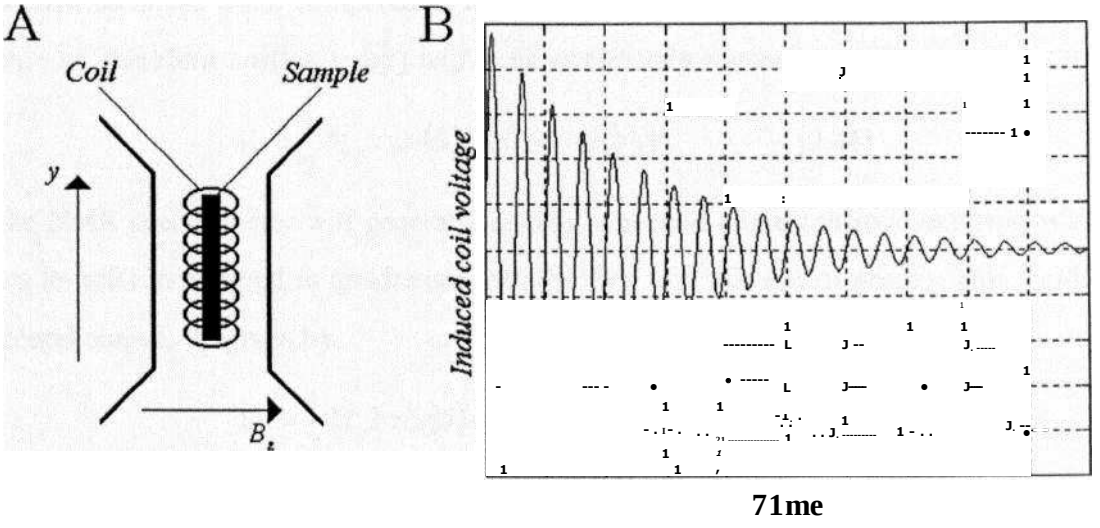

Figure 2.7: A) An example of a simple experimental set up for an **NMR** *experiment. B) The free induction decay detected by the pickup coil.*

Detection of the NMR signal usually involves the use of a phase sensitive detector. This works by multiplication of the signal from the coil, v_{NmR}, by a reference signal v_{REF} and integration of the resulting product over period *gt* . For the moment we ignore the effects of relaxation and let $v_{NMR} = M\ sin(9)cos(co_L t)$, and we assume that that the reference signal is oscillating such that $v_{REF} = bCOS(OX)$, then the product signal is given by $v_{PRODUCT} = M\ sin(19)cos(ta_L t)b\ cosfrot)$. Therefore taking the integral we find that the detected signal is given by:

$$V, = SM_0\ sin(0)cos((o_L tkcos(ax0 \qquad [2.44]$$

This may also be written:

$$= 2\ M_o b\ sin(19 \left| \quad SCOS(\{0)\ COitkit\ SCOAW - (0141t\} \right. \qquad [2.45]$$

The time interval ot will span many cycles of the $0)_L + to$ frequency component, therefore the first integral will effectively average to zero. Conversely, the time interval

& will be small when compared to a single cycle of the second frequency component $to_{/.}$ — w, therefore $cos(k_{\cdot} — 04)$ will be approximately constant therefore:

$$V, = M_o b\ sin(0)cos([\omega_L — \omega]t)ri \qquad [2.46]$$

The NMR spectrometer will generally contain a second phase sensitive detector, which has its reference signal in quadrature with the first (i.e. 90° out of phase). This yields a second output, $\mathbf{V_2}$ given by:

$$\mathbf{V_2} = M_o b\ sin(0)sin([\omega_L — to]t)St \qquad [2.47]$$

This means that if the frequency of the reference signal is equal to the Larmor frequency then the two signals, V, and $\mathbf{V_2}$ can be thought of as the x and y components of the transverse magnetisation in the rotating frame. The full FID signal is generally written as the complex quantity $F(t)$= V, (t)+ $iV_2(t)$, and adding in the effects of dephasing as discussed above, then the final detected signal is given by:

$$F(t)= M_0\ sin(0)expW)exp(i[co_L —\omega]t) \qquad [2.48]$$

2.4.2 Inversion recovery: measurement of T_1

The value of T, provides valuable information about the properties of a given sample, be it a molecular species, a liquid, solid, or even human tissue. Its accurate measurement is therefore a very important quantity. The most common technique for measurement of T_1 is known as the inversion recovery sequence. The pulse sequence is very simple and consists of just two rf pulses, a 180 degree inversion pulse and a 90 degree pulse separated by a time $\mathbf{t_i}$ (Shown in Figure 2.8).

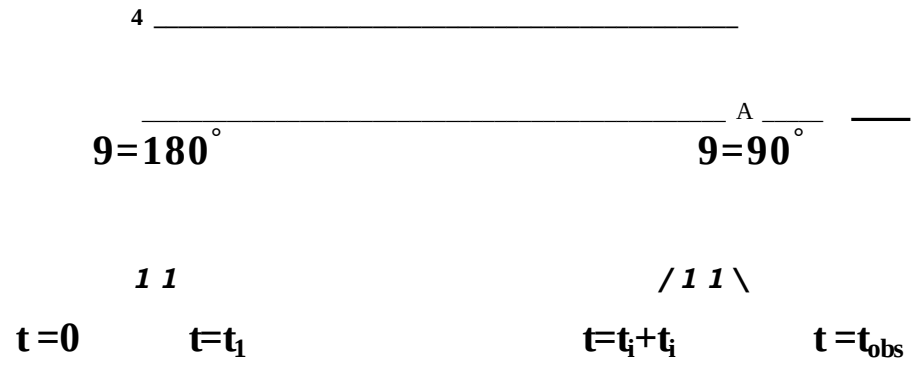

Figure 2.8: The Inversion Recovery pulse sequence.

At time t = 0, (prior to the 180 degree inversion pulse) we assume that the spin system has been left unperturbed for an adequate length of time such that the spin populations are given by the Boltzmann distribution and no phase coherence exists between precessing spins. This being the case, the initial magnetisation is simply the equilibrium magnetisation given by:

$$M(0) = M_o i \qquad [2.49]$$

The inversion pulse ($9 = 180^\circ$) is then applied and the magnetisation is inverted such that:

$$M(t_i) = -M_o ts \qquad [2.50]$$

The longitudinal magnetisation is then allowed to evolve for a time t_i , and in doing so, relaxes back towards its equilibrium value according to the Bloch equations so that at time $t = t, + t_i$, the magnetisation is given by:

$$M(t, +t_i)=M_0(1-2\exp(-t\ t_{7,1})) \qquad [2.51]$$

At this point, a second RF pulse ($9 = 90^\circ$) tips the remaining longitudinal magnetisation into the transverse plane, giving an observable component of amplitude:

$$S = M_0(1- 2\ \exp(-t_i\ T_i)) \qquad [2.52]$$

By varying the delay time t_o one can perform a sequence of inversion recovery experiments, and by plotting the magnitude of the measurable response against $t_;$, and fitting Equation 2.43 to this data, it becomes possible to fit the data for the parameter T_i (an example of this is shown in Figure 2.9).

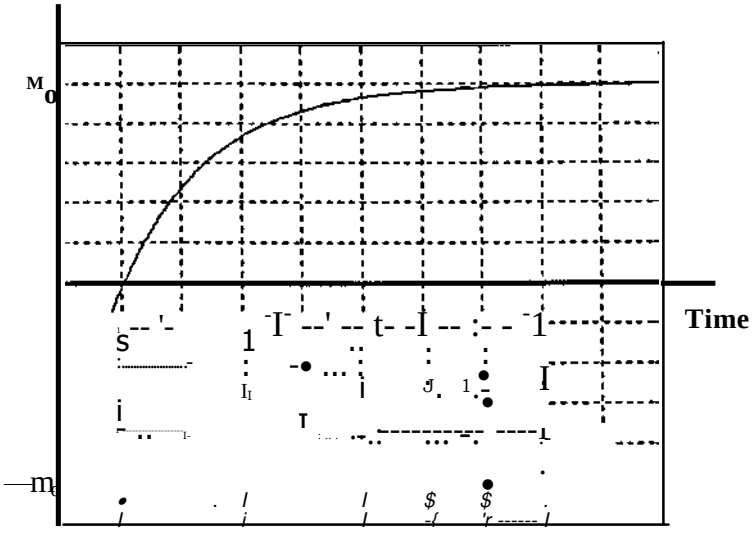

Figure 2.9: The inversion recovery curve

2.4.3 The spin echo

The decay of transverse magnetisation can occur via two mechanisms. The fluctuating microscopic fields oriented parallel to the applied static magnetic field cause slight fluctuations in the resonant frequency of nuclei, this causes precessing nuclei to dephase, which in turn causes the decay of transverse magnetisation. This process is characterised by time constant $\mathbf{T_2}$**.** In addition to this however, deviations in the applied magnetic field caused either by susceptibility effects, or instrumental imperfections may also cause dephasing of nuclear spins again resulting in further decay of transverse magnetisation. These secondary effects are characterised by time constant T_2', and they differ from $\mathbf{T_2}$ effects since they are caused by a shift in the static magnetic field that does not vary in time. This means that in principle, dephasing due to $\mathbf{T_2}'$ effects can be refocused.

In practice $7'_2$ and $\mathbf{T_2'}$ effects add together such that the total transverse relaxation (due to both $\mathbf{T_2}$ and $\mathbf{T_2'}$) can be characterised by a third time constant $\mathbf{T_2^*}$, where:

$$\frac{1}{T_2^*} = \frac{1}{T_2} + \frac{1}{T_2'} \qquad [2.53]$$

By simply fitting the envelope of a free induction decay to the solution to the appropriate Bloch equation, $\mathbf{T_2^*}$ can be measured, however in order to obtain an accurate measure of $\mathbf{T_2}$, the spins must be manipulated in some way in order to ensure that $\mathbf{T_2'}$ effects are reversed. This is achieved by use of the spin echo sequence [10] shown in Figure 2.10.

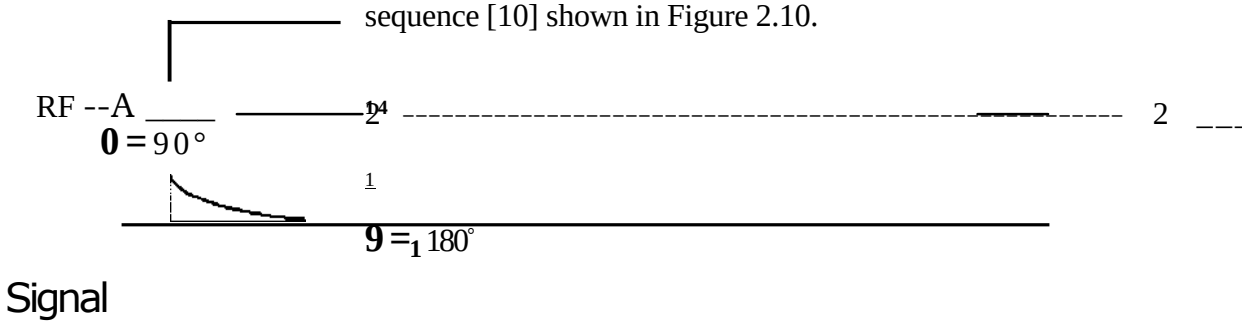

Figure 2.10: The spin echo sequence

The pulse sequence consists of two pulses, a 90-degree pulse about the x-axis, followed by a 180-degree pulse about the y-axis. The pulses are separated by a time interval %, and this same interval is left after the second pulse before sampling is initiated. The evolution of spins according to the classical model is depicted in Figure 2.11.

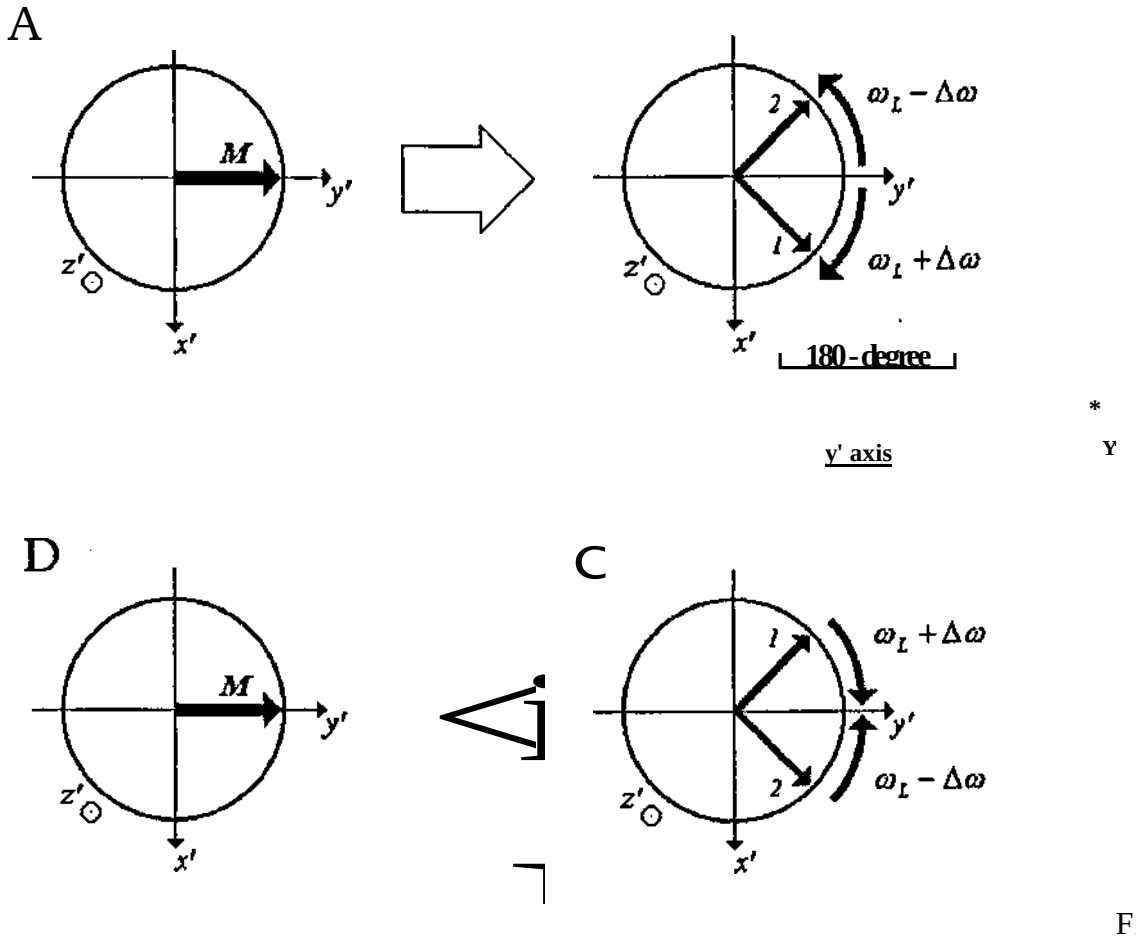

Figure 2.11: The evolution of classically modelled spins during a spin echo experiment.

Following the first (90-degree) pulse, inhomogeneities in the static magnetic field will cause different spins to precess at slightly different frequencies, some slightly faster than the Larmor frequency, some slightly slower. If we view this in the rotating frame, we find that those spins precessing at frequency co_L + &o will rotate clockwise in the transverse plane of the rotating frame, whereas those precessing at to/. —Jo) will rotate anticlockwise. Hence magnetic moments will slowly fan out and dephase. The application of a 180-degree pulse causes a rotation of the magnetisation, through 180 degrees about the y'-axis in the rotating plane. The 180-degree pulse does not alter the fact that spins are still precessing at different frequencies; it does however set up a state in which the slowly precessing spins are 'ahead' of the Larmor frequency, whereas the faster precessing spins are 'behind' it. After an appropriate interval the spins then rephase, causing an observable `spin echo'.

In order that a perfect echo is formed, the magnetic field must not change throughout the duration of the pulse sequence. (This will ensure that for any given spin, the precession angle during the first zA interval will be exactly the same as that for the second.) This will generally be the case for magnetic field imperfections or field shifts caused by susceptibility effects; the field fluctuations caused by molecular motion will of course change in time. It is this fact that allows us to measure T_2 and eliminate T_2' effects using the spin echo. By performing a succession of spin echo experiments, each with a different time constant **r,** and plotting the amplitude of the spin echo for each experiment, the decay of longitudinal magnetisation due to T_2 effects can be plotted as a function of time, and hence an accurate value of T_2 can be measured. Tthe difference between

2.5 REFERENCES

1. Mansfield, P., Morris, P.G., Nuclear Magnetic Resonance in Biomedicine. 1982, New York: Academic Press.

2. Morris, P.G., Nuclear magnetic resonance imaging in medicine and biology. 1986, New York: Acedemic Press.

3. Callaghan, P.T., Principles of Nuclear Magnetic Resonance Spectroscopy. Oxford Science Publications. 1993, Oxford: Clarendon Press.

4. Hennel, J.W., Klinowski, J., Fundamentals of Nuclear Magnetic Resonance. 1993: Longman Scientific and Technical.

5. Levitt, M.H., Spin Dynamics. 2003, New York: John Wiley and Sons.

6. Rae, A.M., Quantum Mechanics, 3rd Edition. 1992, Bristol: Institute of Physics Publishing.

7. Dirac, P.A.M., Principles of quantum mechanics, 1st ed. 1930.

8. Bloch, F., Hansen, W.W., Packard, M.E., Nuclear Induction. Physics Review, 1946. 69: p. 127.

9. Purcell, E.M., Torrey, H.C., Pound, R.V., Resonant absorption by nuclear magnetic moments in solids. Physics Review, 1946. 69: p. 37.

10. Hahn, E.L., Spin Echoes. Physics Review, 1950. **80:** p. 580-594.

CHAPTER THREE

NMR IMAGING: PRINCIPLES AND INSTRUMENTATION

OVERVIEW

This second MR theory chapter provides an introduction to both the principles behind MR imaging and the types of instrumentation commonly used. Initially the application of magnetic field gradients in order to encode spatially the precessional frequency of spins in a sample is reviewed. Following this, the combination of gradient waveforms and RF pulse excitations to obtain MR images is considered. Various types of spatial encoding are reviewed, and the k-space description of imaging is used to introduce echo planar imaging, which is of most practical benefit in functional MRI studies. Finally, the instrumentation used in MRI is discussed including both details of coils used to produce static, gradient, and RF fields. MR safety issues are also considered. Particular emphasis is placed on the 3T system at the Sir Peter Mansfield Magnetic Resonance Centre, University of Nottingham where all of the experiments to be described in later chapters were carried out.

3.1 MAGNETIC RESONANCE IMAGING

3.1.1 Spatial encoding by gradient field

In chapter 2, it was shown that the Larmor frequency of precession for nuclear spins in a magnetic field is given by $co = gl_o$, where y is the gyromagnetic ratio and B_o is the static magnetic field applied parallel to the z-axis. This means that since the precessional frequency of nuclear spins varies linearly with field strength, if the magnetic field is made to vary spatially across the sample, then so does the Larmor frequency. Further, if the induced NMR signal were to be detected from a sample placed in a spatially varying magnetic field and then Fourier transformed, the result would be a set of frequency components representing all of the Larmor frequencies induced. It is this spatial encoding of precessional frequency using magnetic field gradients that underpins magnetic resonance imaging [1-31

In MRI, three orthogonal magnetic gradient fields are used in order to spatially encode nuclear spins within a sample. The strength of the gradient field is given by

$G = \frac{dB}{dx} + \frac{dB}{dy} j + \frac{dB}{dz} k$, and for some position r within the sample the corresponding Larmor frequency is given by:

$$o)(r) = 7(B_o + G.r) \qquad [3.1]$$

This means that, using a quadrature phase sensitive detection system (see chapter 2), the received signal oscillates at frequency IG $.r$ and can be described mathematically as:

$$S(t) = filip(r)exAG.rt)dr \qquad [3.2]$$

Where $p(r)$ represents the density of nuclear spins as a function of position within the sample, and V represents the sample volume. We now introduce a transformation by definition of a vector k such that:

$$k =)Gt \qquad [3.3]$$

Inserting this into Equation 3.2 gives:

$$S(k) = iffp(r)exp(ik\ 4dr \qquad [3.4]$$

This means that the spatially encoded signal is a function of the vector k and the spatial encoding strategy is said to be a function of k-space [4]. Equation 3.4 has the form of a Fourier transform and it follows simply that the three-dimensional inverse Fourier transform of the spatially encoded signal $S(k)$ yields a spatial map of proton density:

$$p(r) = (2^{1}\ RIS(k)exp(— ik.r)dk \qquad [3.5]$$

Equations 3.2 to 3.5 represent the fundamental principle behind magnetic resonance imaging with field gradients. K-space can be sampled over time with the direction and spatial frequency of sampling defined by the direction and duration of field gradient pulses. Having sampled an appropriate amount of k-space, the signal can be inverse Fourier transformed to give a spin density map in real space. A number of mechanisms by which to sample k-space have now been invented. Furthermore, relaxation mechanisms (or in some cases variations in other nuclear interactions) can be exploited in order to add additional contrast to MR images beyond simple proton spin density.

3.1.2 Slice Selection

The above theory implies that gradient fields can be used to perform spatial encoding in three orthogonal dimensions. However, in practice, many (but not all) imaging experiments are performed in two dimensions for simplicity. Converting the imaging problem from three dimensions into two dimensions is achieved by a process known as ***selective excitation*** or ***slice selection,*** in which a field gradient is applied and a temporally modulated RF pulse is used to selectively excite a thin slice within the sample [5]. In order to explain the process of slice selection, consider again the Bloch equations in the rotating frame in the presence of the static field, the rf field, and a gradient field applied in the z-direction such that $\mathbf{B_z = B_0 + G_z z}$. Neglecting the effects of relaxation, the

evolution of magnetisation can be described by:

$$\frac{dM_x}{dt} = \gamma M_y G_z z \qquad [3.6]$$

$$\frac{dM_y}{dt} = \gamma M_x G_z z - \gamma B_1(t) M_z \qquad [3.7]$$

$$\frac{dM_z}{dt} = \gamma B_1(t) M_y \qquad [3.8]$$

In order to show exactly how slice selection works it now proves useful to move into a new rotating frame of reference [3, 6] that rotates at angular frequency 7G, z about the z-

axis with respect to the normal rotating frame. This of course means that the rotational frequency is different for each value of z. If the new rotating frame is denoted by x'', y", z" then geometrical arguments suggest that:

$$\frac{dM_{x''}}{dt} = \gamma M_{y''} B_1(t) \sin[G_z z''(t+T)] \qquad [3.9]$$

$$\frac{dM_{y''}}{dt} = \gamma M_{z''} B_1(t) \cos[G_z z''(t \qquad [3.10]$$

$$dt \quad \gamma[M_s B_{z''} - M_{z''} B_1] \qquad [3.11]$$

Where t represents time and the RF pulse extends between $-T$ and T. To simplify the problem further, we make three assumptions; i) the response of the spin system to the RF pulse is linear, ***ii)*** the z-component of magnetisation does not vary greatly over time (i.e.

$\frac{dM_{z..}}{dt}$ = 0) and *iii)* $M_{z..} = M_{0}$. Using these assumptions, substituting for M_{z} and combining $M_{x..}$ and $M_{g..}$ as the real and imaginary components of M respectively we find that:

$$\frac{dM_{xy}}{dt} = {}_{0}B_{1}(t)\exp(i;G_{z}..z''(t+T)) \qquad [3.12]$$

Integrating and converting back to the original rotating frame we find that the measurable component of magnetisation in the transverse plane is given by:

$$M_{+} = {}_{0}\exp(— i7GzT)\ SB_{1}(t)\exp(i7G_{z}zt) \qquad [3.13]$$
$$-T$$

Equation 3.13 shows that under the approximations listed, the measurable component of transverse magnetisation is a function of z and (perhaps unsurprisingly) is directly proportional to the Fourier transform of the RF pulse profile $B_1(t)$. So, for example, a rectangular slice profile in the z-axis would be obtained if the oscillating RF field were modulated by *a sine* function. Equation 3.12 also contains a phase term *exp(— iiG$_z$zT)* meaning that transverse magnetisation at position z will be dephased through angle)G$_1$zT with respect to z = O. This magnetisation can be re-phased following offset of the RF pulse by application of a field gradient of amplitude — *G,* and time *T* .

In reality it is not possible to obtain a full sinc modulated pulse since this extends infinitely in time. In practice therefore the sinc function is usually truncated at the third zero crossing on each side of the primary peak. This has been shown to yield reasonable pulse profiles for reasonably short pulse durations.

The bandwidth of a sinc pulse is given by $Ay = \frac{1}{t_0}$, where t_0 is the time from the sinc maximum to the first zero crossing. The thickness of the selected slice, Az is then given by:

$$= 2/rA\ v \qquad [3.14]$$
$$G_{z}y$$

Thus both pulse bandwidth and gradient strength can be used to manipulate the slice width. In practice however it is advantageous to use both a high bandwidth and high gradient strength as this maximises the frequency difference between adjacent slices and so minimises slice selection errors due to other effects such as magnetic field inhomogeneity caused by susceptibility artefacts. In order to shift between adjacent slices within the sample, the carrier frequency of the RF pulse is adjusted with respect to the static magnetic field.

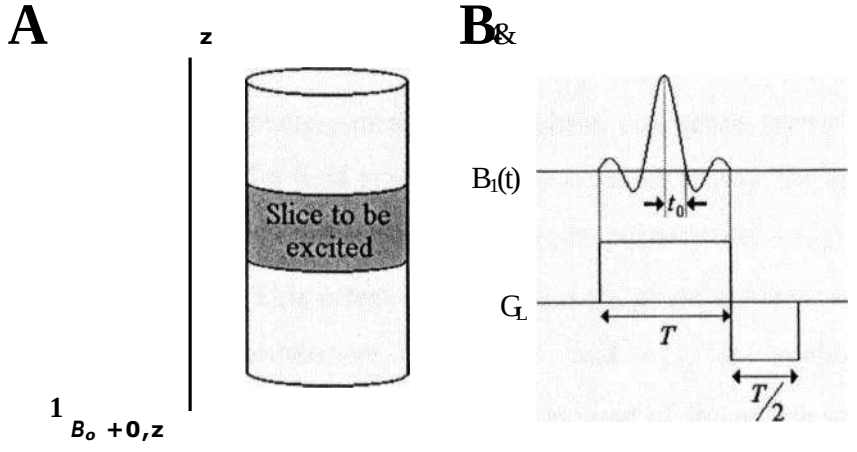

Figure 3.1: The principle of slice selection. A) The slice to be excited. **B)** The sinc RF pulse, gradient waveform and slice refocusing lobe.

The assumption set used to derive this model is unquestionably wrong, the approximation

$$\frac{dM}{dt}$$

that _____ z — 0 means that an extremely low flip angle must be employed, which is clearly of limited use since high flip angles (i.e. —90°) are generally used to obtain

measurable **MR** signals. Having said this, the above simple derivation works surprisingly well in most cases and whilst the sinc modulated RF pulse does not provide a perfect rectangular pulse profile, it remains a useful pulse shape and finds extensive use in later experiments.

3.1.3 The gradient echo and spin warp imaging

The presence of field gradients across a sample causes precessing spins to dephase leading to a loss of transverse magnetisation. In order to illustrate this principle, consider a selective excitation, centred at $z = z_o$ with slice width A . In the presence of a field gradient G_z, spins at position $z_o + \frac{A}{2}$ will precess at frequency $B_o + G_z\left(z_o + \frac{A}{2}\right)$, whilst spins at position $z_o - \frac{A}{2}$ will precess at ... frequency $B_o + G_z\left(z_o - \frac{A}{2}\right)$. Spins between these slice extremities will precess at intermediate frequencies, meaning that phase coherence across the slice is destroyed by the application of a field gradient. In much the same way, the application of a second field gradient with equal magnitude but opposite polarity (i.e. $-G_z$) will refocus the dephased magnetisation. (This effect is used to ensure phase coherence following a slice selective RF pulse.) Furthermore, if both G_z and are applied for equal durations, **T,** then at time t = 2T an observable component of transverse magnetisation will be induced. This effect is known as a gradient echo and is illustrated in Figure 3.2. It can be thought of as a means of controlling the dephasing and rephasing of spins and represents an alternative to the spin echo. However, whereas the spin echo will refocus T_2' effects (i.e. dephasing due to susceptibility or field inhomogeneity effects) the gradient echo will only refocus gradient field effects. This means that whilst the spin echo can be used to measure T_2 (as described in the previous chapter), an equivalent experiment using gradient refocused echoes would only yield accurate measurement of T_2^* . Despite this, we shall see that the gradient echo does find extensive use in magnetic resonance imaging.

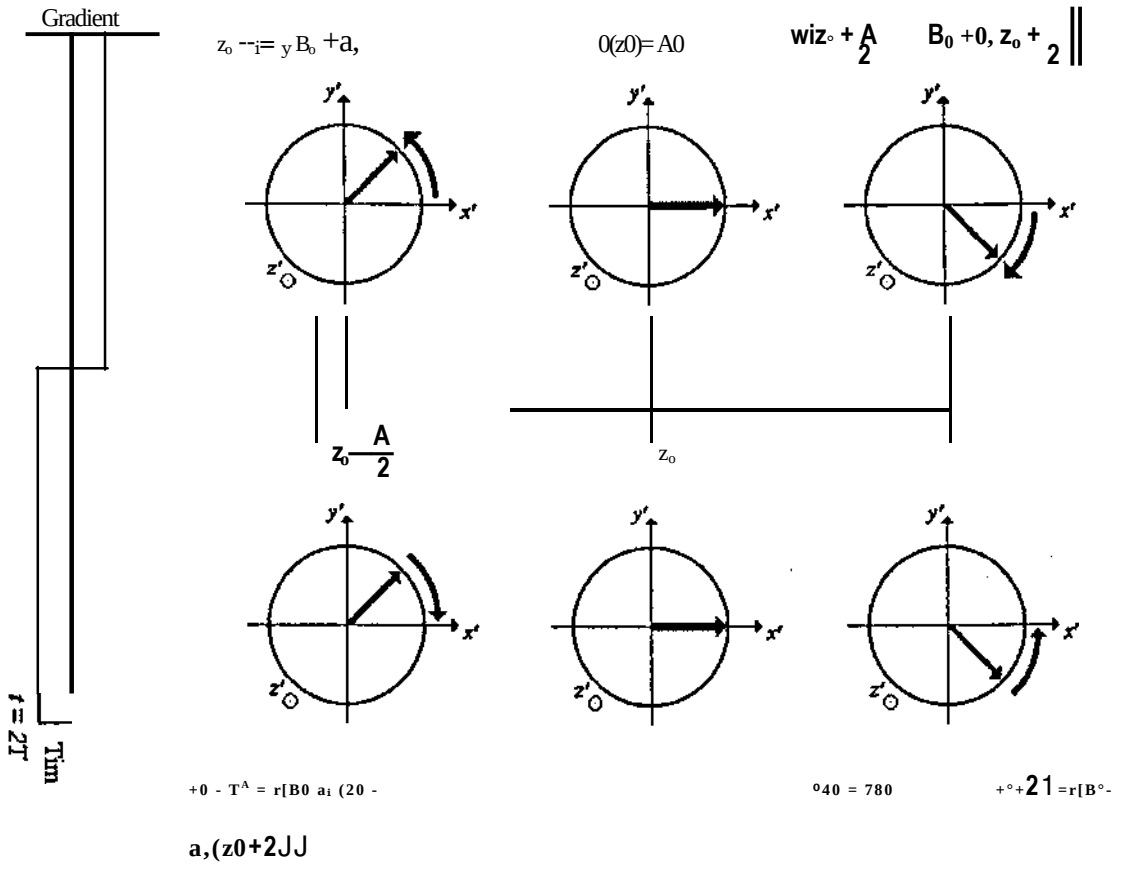

Figure 3.2: Principle of the gradient echo. Spins are allowed to dephase for time Tin the presence of a field gradient G. The polarity of the gradient is then reversed and spins evolve for a further duration T after which the gradient echo is formed.

As described above, the application of selective excitation reduces the MR imaging problem from 3-dimensions to 2-dimensions. This means that only a two dimensional area of k-space now requires sampling. Consider again Equation 3.5 but now reduced to two dimensions such that:

$$p(x,y)= \frac{1}{(2\pi)^2} \iint_A jAk_x, k_y)\exp(-i[k_x x + k_y y Ddk_x, dk_y \qquad [3.15]$$

This equation now shows that the nuclear spin density is the inverse Fourier transform of a now two dimensional k-space signal. We also recall that $k_x = \gamma G_x t_x$ and $k_y = \gamma G_y t_y$

where t_x and t_y are the durations of the x and y gradient pulses respectively, which

shows that the k-space position vector, is manipulated by sequential application of field gradients.

Imaging sequences differ primarily in the way they sample k-space. Many such sequences exist and have been specifically designed to optimise, for example, sampling speed, resolution, or contrast (which in turn involves manipulation of relaxation delays). It is beyond the scope of this thesis to describe in detail all of the MR imaging sequences currently in use; instead we concentrate on the illustration of physical principles. One of the first imaging sequences to be developed, and one of the most widespread is known as the 'Spin Warp' technique [7]. The sequence can be performed using either gradient or spin echos. For simplicity, consider first the gradient echo experiment pictured in Figure 3.3.

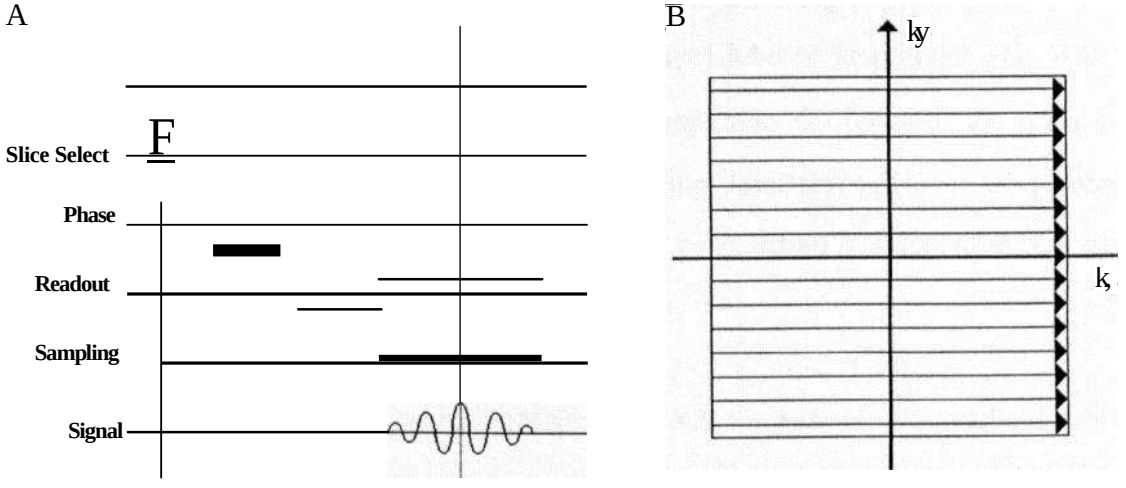

Figure 3.3: Spin Warp Pulse Sequence and k-space trajectory.

The spin warp sequence employs a slice selective gradient G_y, a readout gradient Gy and a phase encode gradient G_y in order to spatially encode the NMR signal. The readout gradient is used in order to form the gradient echo, and traverses k-space in the k, direction. The phase encode gradient is used to offset the gradient echo in the k,, direction. Using spin warp imaging, a single line of k-space is sampled for each individual RF pulse. A 90-degree pulse is applied in the presence of a slice selective

gradient pulse in order to selectively excite a thin slab of material within the sample. Following this, a phase encoding gradient pulse G_y is applied, which shifts the phase of the magnetisation by amount:

$$= k_y y =)G_y AT_y y \qquad [3.16]$$

Where AT_y is the duration of the gradient pulse. In other words, the magnetisation phase becomes dependent on its position along the y-axis within the sample. The magnitude of the phase encode pulse differs for each repeat of the sequence ensuring that each gradient echo acquired has been offset by a different amount in the k_y direction. However, AT, is maintained constant and this has the effect of eliminating distortion due to B_o field inhomogeneity in the phase encode direction. (This was crucial for early MR scanners in which low homogeneity magnets were used.) Phase encoding using this technique is employed in many MR sequences. Following the phase encoding step, a bipolar gradient pulse is applied along the x-axis. The first (negative) lobe of amplitude —G, acts to dephase the spins; the second (positive) lobe of amplitude G., rephases the spins and induces the measurable echo. Sampling of the resulting signal takes place in the presence of this readout gradient. Thus, a single line in the k., direction is sampled during each readout gradient pulse.

In order to acquire an image with dimensions N_x x N_y a total of N_y gradient echoes must be acquired following N_y different phase encode gradient strengths. The phase encode gradient is incremented in steps of AG_y between — G_y and G_y. For each of these steps, N_x samples of the induced magnetisation are recorded. The choice of k-space sampling strategy will define completely the final image parameters. The field of view (FONT) is inversely proportional to both gradient strength and sampling interval and the imaging resolution (fir ,) is inversely proportional to gradient strength, sampling interval and number of samples. These relationships are summarised in Equations 3.17 and 3.18:

$$FOV_y = \frac{2z}{\gamma G_y t_y} \qquad [3.17]$$

$$8x = \frac{2z}{N_{ic}\gamma G_x t_1 N_x} = \frac{2z}{N_y \gamma G_y t_y N_y} \qquad [3.18]$$

Where t_y is the duration of the phase encode gradient pulse, and $N_{ic}t_x$ is the duration of the sampling window (which is not necessarily equal to the duration of the positive lobe of the readout gradient).

In order to avoid signal decay due to $\mathbf{T_2}$ * effects and hence image distortion in the readout direction, the spin warp sequence can be run using spin echoes rather than gradient echoes. This is achieved by inserting an additional 180° pulse between the initial excitation pulse and the imaging gradients. The effect of this inversion pulse is a reflection through the diagonal in k-space.

3.1.4 Image contrast

In the description of spin warp imaging given, we assume that: i) the acquisition time for a single line of k-space is negligible when compared to $\mathbf{T_2}$ * **,** and ii) the spin system is in thermal equilibrium prior to the excitation pulse. Using a short acquisition and long repetition time these conditions can be met, however, different contrasts can be achieved in MR images if timings are chosen such that the relaxation parameters of the constituent parts of the sample are allowed to influence the final measured signal. The final result can be thought of as a contrasted spin density map, i.e. C(r)p(r) where C(r) represents the contrast parameter for each individual voxel. Contrast mechanisms in MR images are usually dominated by either T_1 , T_2 or $\mathbf{T_2}$ * relaxation effects. For example, suppose an image was required with $\mathbf{T_2}$ * weighted contrast, this could be achieved simply by lengthening the echo time, TE, in a gradient echo type experiment. In **doing** this we allow some $\mathbf{T_2}$ * relaxation prior to acquiring an image. Therefore, in the final image, some contrast will be observed between those sample components with a short $\mathbf{T_2}$ * **,** and those with a long $\mathbf{T_2}$ * **.** $\mathbf{T_2}$ contrast can also be easily produced by lengthening the echo time, however, rather than using a gradient echo, a spin echo type experiment is required

in order to refocus static field inhomogeneity effects. 7; contrast is usually achieved either by the use of a short TR, or by means of an inversion recovery experiment. In the latter case, an inversion pulse is used in order to invert the longitudinal magnetisation within a region of interest across the sample. The longitudinal magnetisation is then allowed to decay back towards baseline for a time **TI** prior to sampling, meaning that in the final image, contrast is observed between sample regions with large T, and those with smaller T. In MRI of human subjects, different tissues are found to have different relaxation times, which allows for separation of different anatomical regions in MR images. For example at 3 T, the 21 of grey matter in the human brain is approximately 1300 ms whilst the T_1 for white matter is approximately 800 ms. Therefore by use of an inversion pulse coupled with appropriately selected **TI ,** final image contrast between grey and white matter can be achieved. 7, $\mathbf{T_2}$ and $\mathbf{T_2}$ ***** are however dependent on field strength, T_1 increases with field, whilst $\mathbf{T_2}$ and $\mathbf{T_2}$ ***** decrease. This means that if the same sequence is run at two different field strengths, final image contrasts will differ.

In addition to T, $\mathbf{T_2}$ and $\mathbf{T_2}$ ***** contrast, other contrast mechanisms have been used in MR images and it is beyond the scope of this thesis to mention specifically them all. One large area of research which should be mentioned involves the use of artificial contrast agents. If more contrast is required than is naturally available then it is possible to inject some substance into the body that is easily identifiable by MR imaging. Perhaps the most widely used MR contrast agent is the gadolinium chelate Gd-DTPA, a strongly paramagnetic substance that decreases relaxation times of surrounding protons. Amongst other things, this has been used in both animal and human studies to obtain quantitative measures of cerebral blood volume [8].

3.1.5 Echo Planar Imaging

The spin warp pulse sequence provides a useful illustration of the way in which k-space can be used to describe MR imaging sequences, and it has been used in a wide variety of applications [7]. However, a great deal of recent MR literature has focused on the use of imaging to track dynamic processes in the human body, for example, real time imaging of

the heart, and functional imaging of blood flow and blood oxygenation in the brain. The use of the spin warp sequence in these applications is severely limited for two reasons: Firstly, multiple RF excitations are required to obtain a single image, which limits temporal resolution. Secondly, to obtain maximal signal to noise, the excitation pulse should flip the bulk magnetisation through 90°. Following excitation the magnetisation should be left to relax back to its baseline state, which again limits temporal resolution. In practice low flip angle pulses can be employed in order to optimise imaging speed but the use of the spin warp technique in functional imaging still remains limited. These difficulties were solved by Mansfield et al in 1977 by the introduction of the Echo Planar Imaging (EPI) technique [1, 2, 9-11]. Using EPI, two-dimensional k-space is sampled completely following a single excitation pulse, meaning that single images can be acquired in just a few milliseconds and an entire head volume can be covered in a few seconds. There have been a number of different k-space trajectories used in echo planar imaging, two are introduced here, single shot and multi-shot.

In single shot EPI (SS-EPI), all of the lines in k-space are sampled in a single acquisition using a rapidly switched readout gradient and either a constant (SEPI) or blipped (MBEST EPI) phase encode gradient. The sequence is shown along with the k-space trajectory in Figure 3.4:

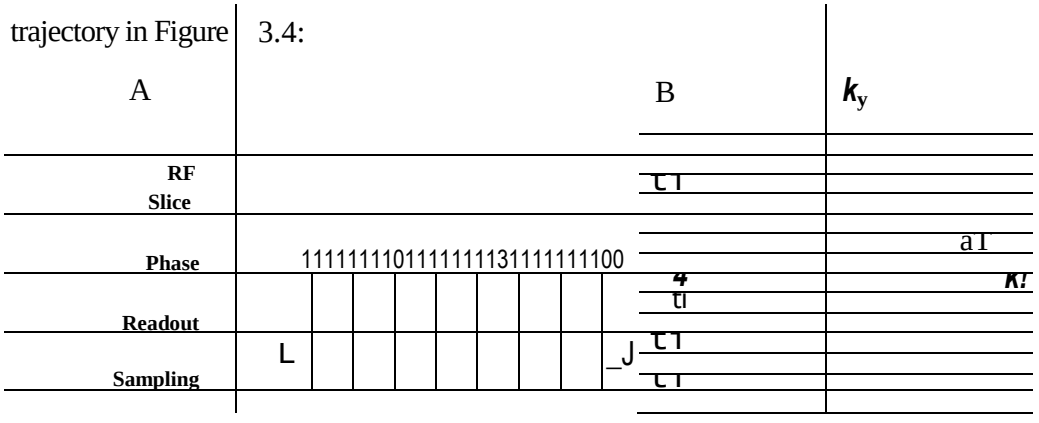

Figure 3.4: The EPI pulse sequence (A) and associated k-space trajectory (B). The slice select gradient is used in the usual manner to selectively excite a thin slab of the sample. The readout gradient is then used in order to allow for gradient echo formation and to traverse k-space in the k_r direction. The phase gradient is used to traverse k-space in the k_y direction.

The EPI sequence begins with a standard slice selective excitation pulse flipping some component of the bulk magnetisation into the transverse plane. A rephasing gradient is also applied in order to ensure phase coherence. Following slice selection, we begin at the centre of k-space and initially pre-excursion gradient pulses are applied in both the k_x and k_y directions in order to move to the bottom left corner of k-space where sampling will begin. Having moved to an appropriate starting position, a sequence of gradient echoes is formed using a rapidly switched readout gradient waveform as shown in Figure 3.4. The readout gradient sequentially de-phases and rephases the spins causing a succession of gradient echoes. This readout gradient also provides frequency encoding in the k_x direction in much the same way as for the spin warp technique. The phase encode gradient provides spatial encoding in the k_y direction by use of a single gradient pulse following each echo that increments k_y on each iteration. (This is called MBEST EPI. In the original implementation of EPI a constant low amplitude phase gradient was applied throughout the duration of the readout gradient forming diagonal lines in k-space).

Using EPI it is important to note that successive gradient echoes are acquired in the presence of readout gradients with opposite polarity. This means that each echo traverses k-space in the opposite direction to the previous echo. Thus, before the image is formed by Fourier transformation, the sampled data must be reordered to account for this reversed direction of sampling.

In multi-shot EPI (often known as segmented EPI) the sampling of k-space is divided into a number of segments, such that not all of the lines of k-space are sampled in a single FID. In order to reduce ghosting artefacts using MS-EPI, the lines of k-space are generally interleaved. The advantage of MS-EPI over SS-EPI is that it places less strain on the gradient coils and can increase the frequency separation between points in the phase encode direction, leading to a reduction in susceptibility artefacts. However, the obvious disadvantage is that it takes longer to acquire a single image and therefore brings a loss of temporal resolution for functional studies as well as increased risk of motion artefact.

3.1.6 Limitations of EPI: K-space sampling and voxel bandwidth

The frequency of k-space sampling defines completely what is known as the voxel bandwidth, which in turn has an effect on the scale and type of image artefact observed in EPI images. Voxel bandwidth depends on direction such that the bandwidth in the x-direction (measured in Hz) is given by:

$$Av = \frac{1}{NA,} \qquad [3.19]$$

and the bandwidth in the y-direction is given by:

$$\mathbf{A\,v} — \frac{1}{N_y N_x t_x} \qquad \mathbf{[3.20]}$$

where N, is the number of samples per echo, t_x is the interval between sampling or dwell time, and N_y is the number of echoes (number of broadening 'blips,' or number of lines in k-space). The pixel bandwidth represents the maximum frequency separation between voxels in both the x- and y-directions that can be adequately sampled. So, for example with a 128 x128 image matrix size and a 1 kHz switching frequency, the pixel bandwidth in the x-direction is 1000Hz. However, the pixel bandwidth in the y-direction is only / 28x1x10- ^{3}) = 7.8 Hz. This low pixel bandwidth can cause image artefacts in EPI since spatial distortions in the final image are observed if the quantum mechanical linewidth is greater than the bandwidth per pixel in the y-direction.

Line broadening can be caused by field inhomogeneities and, in general, the linewidth in the absorption spectrum is given by $\text{tico,} = —^{2}$. This, coupled with the finite bandwidth in the y-direction therefore limits the ultimate resolution of the sequence such that adjacent pixels will be indistinguishable if $\mathbf{T_2^*} > \frac{2}{2rA\,v_Y}$. In the case of the example given above then we must have $\mathbf{T_2^*} > \frac{1}{x\ 7.8}$ 40 ms to avoid blurring. However, this problem becomes greater at larger field strengths since $\mathbf{T_2^*}$ decreases as the static magnetic field increases.

The field inhomogeneity problem can be dealt with by the use of spin echo (rather than gradient echo) EPI. However, even in the absence of field inhomogeneity, resonance lines exhibit a finite linewidth due to inherent **T2** effects. This line broadening is large for biological samples and can itself lead to blurring in the phase encode direction.

In practice the effects of field homogeneity across the sample can be minimised by effective shimming. In addition, an increase in sampling rate (i.e. a decrease in dwell time) will also cause an increase in the bandwidth per voxel in both the x- and y-directions leading to a decrease in sensitivity to field inhomogeneities. However, it should be noted that an increase in bandwidth causes a decrease in signal to noise ratio in the final data, thus introducing a trade off between bandwidth and signal to noise.

Finally, a technological challenge of EPI is the rapidly switched read gradient waveform and the most efficient method to do this is by the use of a sinusoidal gradient waveform and resonant circuit. (Note that this must be coupled with a non-linear sampling strategy in order to ensure that k_s is sampled in equal increments.) The use of a resonant circuit allows for higher currents, and hence higher field gradients in EPI. This, in turn, means that for some given spatial resolution, less time is required to traverse k-space, therefore making a higher bandwidth per pixel in both the x- and y-directions achievable.

3.1.7 Limitations of EPI: Image artefacts

As with all imaging techniques, image artefacts (features of the image that are not an accurate representation of the sample) are a problem in EPI and the most common cause of these problems (in EPI) is field inhomogeneity effects. We have already seen that spatial information about the sample is encoded by the superposition of the static field B_0, and field gradients in the three orthogonal directions. This means that any local perturbations in the magnetic field will cause a shift or distortion of that part of the sample in the final MR image. Sampling errors can also cause artefacts in EPI and in general, the effects responsible for image artefacts can be divided by into five categories: magnetic field homogeneity, magnetic susceptibility, gradient induced eddy currents, chemical shift and sampling errors.

Magnet homogeneity

Following spin excitation, the transverse magnetisation will decay with relaxation constant $\mathbf{T_2}$ ***.** In EPI, this time must be sufficient to encode the entire image and this therefore requires the magnetic field to be sufficiently homogeneous. In old resistive style magnets, field homogeneity was a problem, however MR experiments to be described in this thesis were carried out using a 3 **T,** Oxford Instruments superconducting magnet, with shim coils in place. With effective shimming and the superconducting magnet, field inhomogeneity is minimised.

Magnetic Susceptibility

Magnetic susceptibility, $\%_{m'}$ is defined as the contribution made by a substance, when subjected to an external magnetic field, to the total magnetic flux density present within the material. Mathematically it is defined by:

irs" [3.21]

Where **M** is the induced magnetisation and **H** is the external magnetic field. Diamagnetic materials tend to have a low, negative magnetic susceptibility. This is brought about by the orbital motion of electrons acting as current loops, which induce magnetic fields opposing the applied external magnetic field (a result of Lenz's law). All materials are essentially diamagnetic; it is however a weak form of magnetism and is often masked by other types. Paramagnetic materials have a low positive magnetic susceptibility, and this is brought about by their constituent atoms or molecules ability to align with the externally applied field. Paramagnetism occurs in all atoms and molecules with unpaired electrons and this difference between diamagnetism and paramagnetism will become increasingly important in later discussions on BOLD imaging. Ferromagnetic materials will have a high positive magnetic susceptibility; this is brought about by the alignment of atomic magnetic moments, which ensures that magnetisation persists after removal of the external magnetic field. Within the body, certain regions give rise to large susceptibility changes, for example the air/tissue boundaries that surround the sinuses. Such large changes in susceptibility cause localised changes in magnetic field, meaning that field gradients are set up which can rapidly dephase local spins. This $\mathbf{T_2}$ * dephasing

causes a loss of signal in T_2^* weighted images. Careful shimming can serve to minimise these effects, however signal loss remains a problem particularly around the sinuses.

Gradient induced eddy currents

Eddy currents are produced when a current is induced in conducting materials by the rapidly switching gradient field. These eddy currents will induce their own magnetic field in the sample that will decay with time depending on the form of the conductor. Eddy current fields can affect field homogeneity and influence image artefacts such as ghosting and signal stability with respect to time. This effect is reduced either by gradient coil shielding, or by pre-emphasis correction (see later).

Chemical Shift

As noted in the previous chapter, chemical shift is a local shift in the magnetic field caused by the electronic environment. This becomes a problem in imaging because protons within water molecules in fat have a different electronic surrounding to those in tissue. This means that the resonant frequency of fat is shifted slightly with respect to the resonant frequency of tissue water. In practice this causes an image artefact commonly known as a fat ring, which appears as a ghost image of fat, shifted spatially with respect to the tissue image in the y-direction.

Sampling errors and the N/2 Ghost

Finally, image artefacts can arise in MRI due to sampling errors, and in EPI the most common artefact is the Nyquist or N/2 ghost. It is not uncommon for the raw data in each line of k-space to be offset relative to the centre of k-space. This can be caused by timing errors between the start of the read gradient and start of sampling, imperfect gradient profiles or eddy currents. Using standard imaging techniques such as spin warp this is not a problem because each line of k-space is traversed in the same direction, therefore all of the k-space lines have the same offset, and the error does not appear in the final magnitude image. However, in EPI, we have seen that the polarity of the read gradient changes in alternate echo readouts and therefore in reconstructing the image it is necessary to reverse the directions of alternate lines in k-space. This reversal means that

any offset from k-space centre alternates from line to line. Following Fourier transformation, an extra periodicity will be introduced into the image with frequency $2Ak_y$ and a ghost image is observed, shifted in the read direction by half the field of view. Other ghosting artefacts (the 'quad ghost') can be caused by a mismatch in amplification of the real and imaginary components of the data. However careful adjustment of raw k-space data can eliminate these problems and both the `Nyquist' or `N/2' ghost and the 'quad' ghost can be corrected either manually or automatically immediately following k-space signal acquisition [12].

3.2 THE IMAGING SYSTEM

3.2.1 System overview

All of the MR experiments presented in this thesis (unless otherwise stated) were carried out on the 3 T imaging system [13] at the Sir Peter Mansfield Magnetic Resonance Centre (SPMMRC), University of Nottingham, UK. The system comprises a 3T superconducting magnet (bore diameter of 90 cm), a shim coil (incorporated within the magnet itself), an insert head gradient coil of internal diameter 38 cm and a transverse electromagnetic (TEM) RF coil (internal diameter 27cm). This hardware is supported by gradient and RF amplifier systems, a waveform controller, RF electronics and a computer running purpose written software. A diagrammatic overview of the imaging system is shown in Figure 3.5.

The required pulse sequences (gradients and RF) are stored by the main system computer. On running a particular sequence, the computer must communicate with the appropriate hardware in order to output the correct series of gradient and RF pulses, and record the resulting signals. Gradient waveforms are passed from the computer to the waveform generator where they are converted from digital to analogue, amplified, and sent to the three orthogonal gradient coils. In some cases, prior to amplification, pre-emphasis correction is applied in order to offset eddy current problems. RF pulses are passed from the computer to the spectrometer where they are converted from digital to analogue and amplified by the RF amplifier. The T_x/R_x control acts as a simple 2-way switch allowing the RF pulse to be sent to the coil during transmission, and allowing the induced FID to

be passed back to the spectrometer when in receive mode. Received signals are converted from analogue to digital by the spectrometer, and then passed to the computer where they are stored and displayed. Shim coils are used to correct for field inhomogeneity, and can either be set manually at the shim PSU, or automatically by the computer.

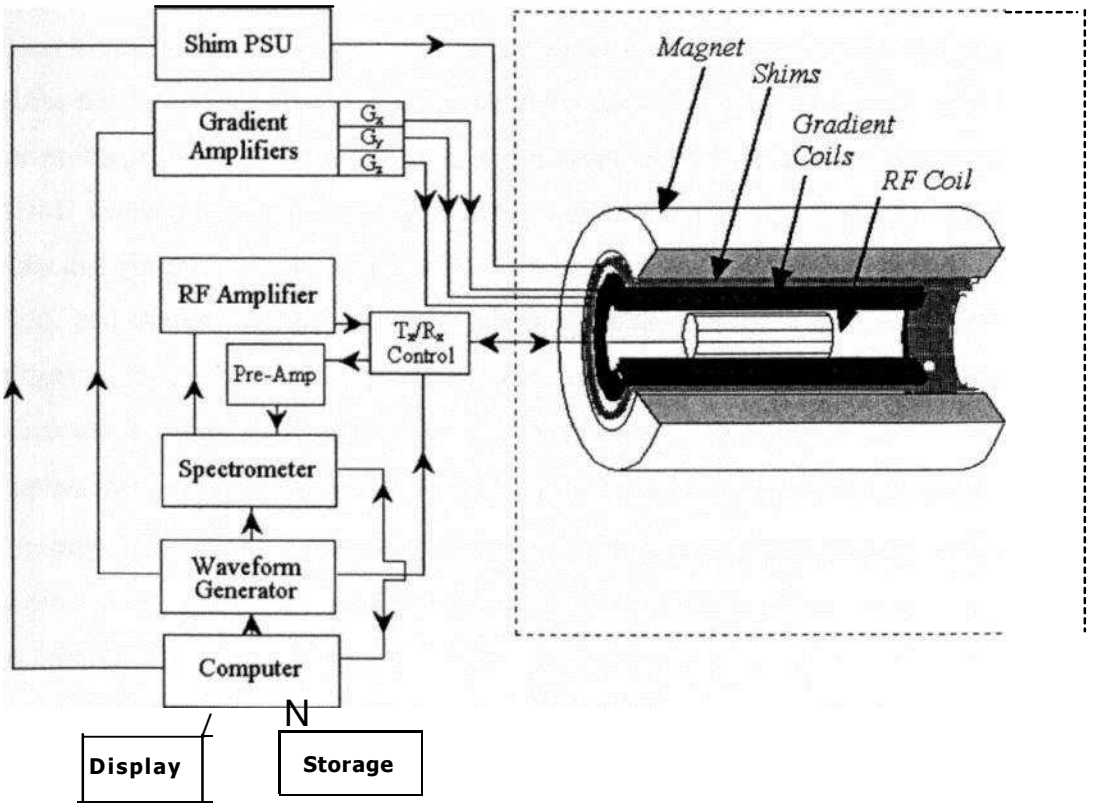

Figure 3.5: Schematic Diagram of an **MRI** scanner

The magnet

As stated in section 3.1, in **MRI** it is highly advantageous to use a large homogeneous static magnetic field and for this reason superconducting magnets are commonly employed. The magnet used is a 3 T horizontal bore superconducting magnet made by Oxford Magnet Technology. The resonant frequency for ^{1}H is 127.868 MHz. The superconducting wire is made from a Nb/Ti alloy and is immersed in liquid helium at 4.3° K to maintain it below its transition temperature and hence in the superconducting state. A nitrogen jacket surrounds the helium vessel in order to reduce the helium boil off

rate. The field homogeneity of the magnet was measured to be approximately 0.5 ppm over a 35 cm diameter spherical volume at the magnet isocentre.

Shim Coils

In order to make it more homogeneous, the static magnetic field can be adjusted by a process known as shimming. Two types of shimming are used, active and passive.

Passive shimming is achieved by placing small pieces of iron within the magnet bore. These ferromagnetic objects concentrate field lines, and can therefore be used to correct for problems such as spot defects in the magnet coil winding or local metal structures. Active shimming is achieved by passing current through appropriately designed shim coils that generate small magnetic fields that either add to or subtract from the main static field, and thereby correct for field inhomogeneities. When a sample is placed in the magnetic field, susceptibility effects can cause field inhomogeneity, which can be corrected by the shim coils. On the Nottingham 3T system, active shimming is implemented by optimisation of T_2* measured from a region of interest in the sample. In commercial systems a variety of different algorithms are used to perform auto-shimming, a process by which the field homogeneity is optimised, often using phase mapping techniques.

Gradient coils

Optimal design of field gradient coils is a topic of much research in MR systems. Here, a `home made' head insert gradient coil was used which comprises three orthogonal gradients that can be switched on and off rapidly to allow for spatial encoding in **EFL** The z-axis gradient is made from 28 hoops spread evenly over a cylinder of internal diameter 38 cm. The x and y gradient coils are both made from co-planar arc units. The challenge in gradient coil design is making large linear gradient fields that can be switched quickly. In order for rapid switching to be possible, the gradients must have a low self-inductance, however low self-inductance coils are inefficient and therefore large currents are required to produce appropriate fields. In order to achieve this on the Nottingham 3 T system a capacitor is placed in series with the gradient amplifier and coils in order to produce a resonant circuit that is used specifically for the switched

readout gradient used in EPI. Maximum power transfer is achieved using a sinusoidal switched **LC** ere **L** is the self-inductance of the gradient coils and C is the capacitance of the resonant capacitor. A digital gradient waveform is output by the waveform controller, which is subsequently converted to an analogue signal. Signal amplification is achieved using Techron 7700 3-phase 415 V linear power amplifiers, which are each capable of producing approximately 20 $\mathbf{AV^{I}}$ **.** These amplified current waveforms are then sent to the gradient coils.

Pre-emphasis eddy current correction

The Nottingham 3 T imaging system employs a pre-emphasis unit in order to correct for gradient induced eddy currents. As previously noted, eddy currents pose a problem in MR since their associated magnetic fields add linearly to the static and gradient fields and can therefore cause image artefacts. The pre-emphasis correction unit effectively provides real time eddy current field correction by altering the waveform controller output such that when superimposed, the field from the adjusted gradient waveform output, and the eddy current field, add linearly to give the original required field.

RF coils and transmission

RF coil design and RF pulse design are also major areas of research in MRI. RF coils are required to both transmit the RF pulse, and receive the resulting transverse signal. Separate coils can be used for transmission and reception however since the properties required that make an RF coil a good transmitter also make it a good receiver, in practice it makes sense to use a single coil for both tasks. Exceptions to this rule occur if one is interested in a particular part of the anatomy, in which case a surface coil is often employed as a receive coil, since this can (in general) be positioned closer to the sample allowing for a higher signal to noise ratio. Recent literature has also focused on the use of multiple RF receive coils. In these 'parallel-imaging' techniques, a number of surface coils are used to receive the induced MR signal. These signals are combined with information on the sensitivity profiles of each receive coil allowing the reconstruction of a final image. Parallel imaging techniques such as SENSE [14] or SMASH [15] not only

allow for a higher signal to noise ratio in the final images, but can also speed up the imaging process since spatial information on coil sensitivity is known a priori.

For all experiments presented here, a single RF coil is used which forms part of a resonant circuit, tuned specifically to the resonant frequency of the proton (i.e. approximately 128 MHz at 3T). The resonant circuit is connected to the RF electronics via a coaxial cable (resistance 50 S1). In order to avoid reflections at the interface between the coil and the cable, the impedance of the coil must be matched to the impedance of the cable and this is done by the addition of an extra capacitor in the coil electronics.

For obvious reasons, the coil is at its most efficient when the current induced in the coil from the precessing sample magnetisation is a maximum. This is equivalent to attaining maximum RF field magnitude for some given input power. The sensitivity of the coil is affected by two different parameters known as the filling factor and quality (or 'Q') factor. The filling factor is defined as the ratio of the sample volume to coil volume and if we ignore the effects of RF field inhomogeneity across the coil volume, then the sensitivity of the coil is maximised when the filling factor is equal to unity. This follows from the fact that the coil is at its most efficient when placed as close as possible to the sample. The Q-factor of the coil is a measure of the quality of the resonant circuit. Q is usually defined by the equation:

$$_{Q} = v_{A} \qquad [3.22]$$

Where v_o is the proton resonant frequency and A v is the 3 dB bandwidth of the resonant peak. From a hardware point of view, Q factor is defined by the ratio of reactance to resistance of the coil. In practice resistance should be kept as low as possible since a high coil resistance will increase the level of thermal noise in the signal and therefore lead to a poor signal to noise ratio and reduction in image quality. This means that in MR applications, the Q-factor of the RF coil should be kept as high as reasonably possible.

RF field homogeneity is an important part of RF coil design. This is because B_1 inhomogeneities will cause different sample regions to experience a different flip angle,

causing spatial variation in the signal amplitude. Further, if an RF coil exhibits an inhomogeneous transmit profile then it will exhibit an inhomogeneous receive profile. For these reasons, coils designed for imaging over large volumes are generally optimised such that the fields produced are homogeneous over a realistic volume.

3.2.2 Safety in MR systems

In general magnetic resonance imaging is thought to be free from harmful effects to the subject. This is largely because the RF radiation used in MRI is at a relatively low frequency, and therefore low energy when compared to the ionising radiation used in X-ray CT for instance. Having said this, hazards associated with static magnetic fields, gradient switching fields and RF radiation have to be recognised and suitable measures must be put in place in order to ensure subject safety.

Large magnetic fields

Arguably the biggest safety risk in MRI is posed by the large magnetic fields that are required for imaging. If ferromagnetic objects are brought into close proximity of the magnet bore then the resulting force will attract them towards the magnet, where they would arrive with high velocity. With a subject in the magnet this projectile effect poses a major danger. More subtle effects of the large magnetic field have also been highlighted and of particular concern are subjects with heart pacemakers, and ferromagnetic aneurysm clips. The large static magnetic field can cause a heart pacemaker to malfunction, whilst the force on a ferromagnetic aneurysm clip may act to dislodge it resulting in internal bleeding. If appropriate measures are taken to screen subjects prior to scanning, and to ensure that no ferromagnetic objects pass into the scan room then the risks posed by large magnetic fields are minimal. However, whilst there are no reported long-term effects of exposure to large magnetic fields, some short-term effects have been reported including vertigo, nausea and a metallic taste in the mouth [16].

Gradient fields

The rapidly changing gradient fields pose another significant safety risk in MR. The rapidly changing fields can induce currents along the conductive nerve fibres in the

human body [17], in some cases causing stimulation of those cells if the change in field exceeds — $60Ts^{-1}$. This effect is known as peripheral nerve stimulation or PNS, and is easily prevented by ensuring that the gradient fields are kept well below this critical threshold.

RF field

Further risks in MRI come from the RF field [18], and concern the RF power transmitted to the body. The absorption of RF radiation can cause tissue heating, which may pose a problem particularly in tissues that are not well perfused with blood. In the normal case, local increase in tissue temperature would induce a local increase in blood flow where the blood itself acts as a coolant, dissipating the heat and lowering the temperature. However, some tissues (the lens of the eye is a good example) are not well perfused with blood, meaning that they are less efficient at regulating temperature and so a small amount of RF heating can potentially cause tissue damage.

In MRI RF heating is measured by the specific absorption rate or SAR. For some given tissue SAR is a calculable property and depends on induced electric field, RF pulse sequence duty cycle **(D),** the tissue density, tisse conductivity (a**)** and the patients size. It is calculated from the average power passing into the RF transmitting coil, and the body mass immersed in the RF transmitting field. For a sphere of tissue of radius **r, SAR «** $or^2B_0^2a^2D$, where a is the flip angle. SAR is expressed per kilogram of body weight and if we neglect cooling effects, a SAR of 1 Wkg^{-1} applied for an hour would result in a temperature rise of approximately 1 °C. Generally, the SAR value is kept below a threshold such that RF heating is maintained below 1° C.

Another risk of RF radiation is heating of metallic objects. The application of RF radiation to metal causes a significant rise in temperature. This means that if metallic objects are in contact with the skin during scanning then burns can result. Tatoos have also been reported to cause burns when subjected to RF radiation due to metalic particles in the dyes used.

3.3 REFERENCES

1. Mansfield, P., Morris, P.G., Nuclear Magnetic Resonance in Biomedicine. 1982, New York: Academic Press.

2. Morris, P.G., Nuclear magnetic resonance imaging in medicine and biology. 1986, New York: Acedemic Press.

3. Callaghan, P.T., Principles of Nuclear Magnetic Resonance Spectroscopy. Oxford Science Publications. 1993, Oxford: Clarendon Press.

4. Mansfield, P., Grannell, P.K., NMR Diffraction' in Solids. Journal of Physics C, 1973. 6: p. L422.

5. Garroway, A.N., Grannell, P.K., Mansfied, P., Image Formation in NMR by a Selective Irradiative Process. Journal of Physics C, 1974. 7: p. L457-I462.

6. Bailes, D.R., Byrant, D.J., Contemporary Physics, 1984. 25: p. 441.

7. Edelstein, W.A., Glover, G.H., Hardy, C.J., Redington, R.W., Spin-Warp NMR Imaging and Applications to Human Whole-Body Imaging. Physics in Medicine and Biology, 1980. 25: p. 751-756.

8. Blockley, N.P., Francis, S.T., Gowland, P.A., Investigating the change in Cerebral Blood Volume to an event Related Stimulus using an Infusion of Gd-(HP-DO3A). In Proceedings of the International Society for Magnetic Resonance in Medicine, Miami, 2005(Abs #1494).

9. Mansfield, P., Multi Planar Image Formation using NMR Spin Echoes. Journal of Physics C, 1977. 10: p. p L55-L58.

10. Francis, S.T., MRI Perfusion Techniques (PhD Thesis). 1998, University of Nottingham.

11. Gibson, A.M., High-Speed Functional Magnetic Resonance Imaging (PhD Thesis). 2002, University of Nottingham.

12. Buonocore, M.H., Gao, L., Ghost Artefact Reduction for Echo Planar Imaging Using Image Phase Correction. Magnetic Resonance in Medicine, 1997. 38: p. 89-100.

13. Glover, P., High Field Magnetic Resonance Imaging (PhD Thesis). 1993, University of Nottingham.

14. Pruessmann, K.P., Weiger, M., Scheidegger, M.B., Boesiger, P., SENSE: Sensitivity Encoding for Fast MRL Magnetic Resonance in Medicine, 1999. 42: p. 952-962.

15. Sodickson, D.K., Manning, W.J., Simultaneous Acquisition of Spatial Harmonics (SMASH): Fast Imaging with Radiofrequency Coil Arrays. Magnetic Resonance in Medicine, 1997. 38: p. 591-603.

16. Redington, R.W., Dumoulin, C.L., Schenck, J.F., Roemer, P.B., Souza, S.P., Mueller, 0.M., Eisner, D.R., Piel, J.E., Edelstein, W.A., MR Imaging and Bioeffects in a Whole Body 4.0 Tesla Imaging System. Society for Magnetic Resonance Imaging, 1988. 20.

17. Cohen, M.S., Weisskoff, R.M., Rzedian. R.R., Kantor, H.L., Sensory Stimulation by Time-Varying Magnetic Fields. Magnetic Resonance in Medicine, 1990. **14:** p. 409.

18. Budinger, T.F., Thresholds for physiological effects due to RF and Magnetic Fields used in NMR imaging. IEEE Transactions on Nuclear Science, 1979. NS-26: p. 2821-2825.

CHAPTER FOUR

MAGNETOENCEPHALOGRAPHY: THEORY AND INSTRUMENTATION

OVERVIEW

This final theory chapter is intended to provide an overview of magnetoencephalography. The chapter is split into three sections: Section 4.1 concentrates on the neural basis of MEG. Initially the gross structure of the human brain is examined and the functional specialisation of particular brain regions is discussed. Following this we look at the types of cell found within the human brain, their electromagnetic properties, and their contribution to the MEG signal. In section 4.2, the instrumentation used in MEG is discussed. The fundamental "concepts underlying the Superconducting Quantum Interference Device (SQUID) are explained, and noise reduction strategies introduced, with particular emphasis placed on the CTF 151 Channel 'Omega' system used in later experiments. Finally, section 4.3 discusses briefly the neuromagnetic effects commonly observed in MEG.

4.1 THE GENERATION OF NEUROMAGNETIC FIELDS

The human brain is without doubt the most complex organised structure that is known to exist. It contains in excess of 10^{10} cells in the outermost layer (the cerebral cortex) alone, and these cells transmit electrical signals between one another via approximately 10^{14} connections [1]. It is this passage of information between cells that is of interest to us in MEG. In short, the electrical signals used by the brain to convey information comprise tiny electrical currents that pass down conductive nerve fibres. As with all electrical currents, these produce tiny magnetic fields outside of the head. The goal of MEG is to detect these magnetic fields above the scalp surface, and reconstruct the resulting field map into some useful measure of brain functionality.

4.1.1 Brain structure and function

Macroscopically, the human brain may be thought of as being split into several constituent parts. However it is the cerebral cortex that we shall be primarily concerned

with. The cerebral cortex is a 2 — 4 mm thick sheet of grey tissue that is thought to have a total surface area of approximately 2500 cm^2. In order that it fits into the cranial cavity formed by the skull, this sheet is folded in a complex way, giving rise to its uneven look. Figure 4.1 shows a simplified drawing of the human brain with some of the anatomical features highlighted.

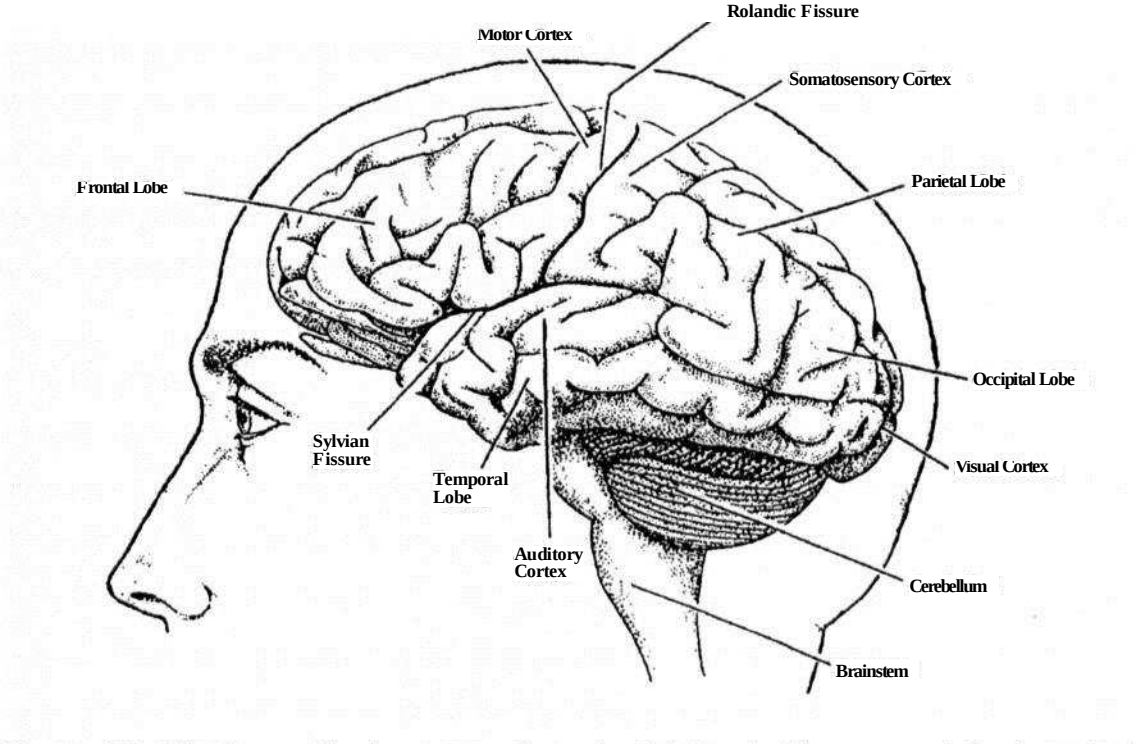

Figure 4.1: The human brain as seen from the left hand side. Some of the important anatomical and functional structures are highlighted. Figure reproduced from [2].

The cortex is divided into two separate hemispheres, left and right, separated by the longitudinal fissure. These left and right hemispheres are further separated by a deep grove known as the Rolandic fissure or central sulcus, which runs vertically down each hemisphere cutting it in two, and a third deep groove, known as the Sylvian fissure, which runs horizontally and laterally around the cortex. As shown in Figure 4.1, each hemisphere comprises four lobes, known as the frontal lobe, the temporal lobe, the parietal lobe and the occipital lobe.

The brain is not simply divided anatomically; functional divisions between different brain regions also exist. For example, the primary processing of visual stimuli takes place in the visual cortex (V1), located at the back of the brain in the occipital lobe, auditory processing takes place in primary auditory cortex (Al) buried deep within the Sylvian fissure and sensory-motor functions are controlled by primary somatosensory (Si) and motor (M1) cortices located posterior and anterior to the Rolandic fissure respectively. These areas are also shown in Figure 4.1. The remaining regions are taken up by association cortices, which are thought to respond to stimulation in a more complex way. (For example V5, located lateral to V1 in the occipital cortex is thought to respond to motion in the visual field.) The invention of high-resolution functional imaging techniques have led to a good understanding of functional divisions and most areas of the human cortex have now been explored (see for example [3]).

4.1.2 Neurons

Despite differences in both appearance and functionality between different cortical regions, all areas are essentially made from two types of cell, neurons, and glial cells. Neurons are responsible for actual information processing within the brain and the periphery, and can be thought of as the primary building blocks of the brain and nervous system. They are characterised by their excitable membrane and when stimulated by some neuro-chemical interaction, an electrical pulse is allowed to flow along their length. A single neuron consists of a cell body, (the soma), the dendrites, which are thread like extensions of the soma, the axon, a single fibre responsible for carrying the electrical pulse or action potential, and the nerve ending, which exists at the end of the axon. The basic structure of a single neuron is shown in Figure 4.2.

The cell bodies and dendrites of neurons comprise what is known as grey matter. Grey matter forms the cerebral cortex and also exists in deeper sub-cortical nuclei. The axonal connections between neurons form the brain's white matter, so called because of the bright appearance of axons. Axonal connections exist between different cortical areas and brain nuclei as well as between the brain and periphery. Connections also exist between the two brain hemispheres, the most prominent being the Corpus Callosum.

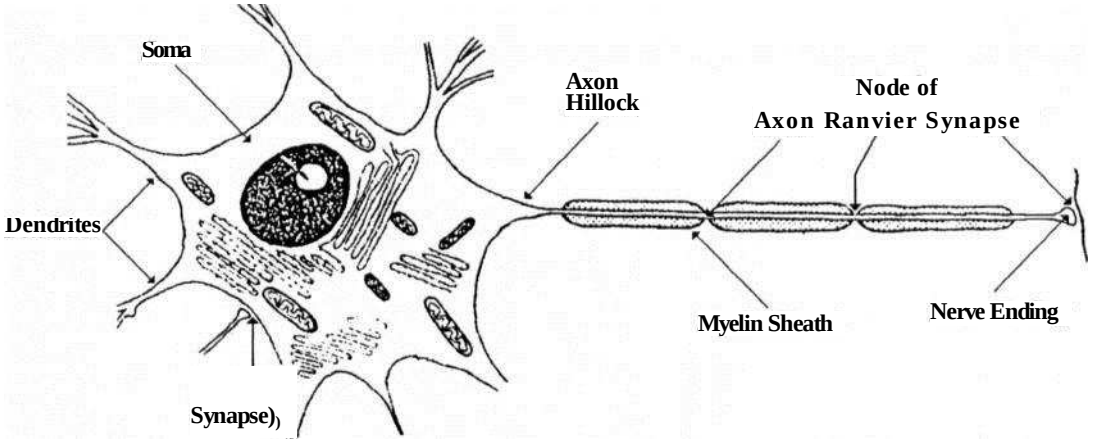

Figure 4.2: The basic structure of an individual neuron showing the soma, the dendrites, the axon, and the nerve ending. Upon receipt of appropriate neuro-chemical stimulation, the cell body depolarises allowing an electrical pulse, or action potential to flow down the axon, terminating at the nerve ending where it induces secretion of a second neurotransmitter.

The neuronal cell wall is made from a fluid filled tubular membrane, which restricts the passage of ions in to and out of the cell. Outside the cell, concentrations of Na^+ and Cl are high whilst the concentration of K^+ is low. Conversely, inside the cell the concentration of le is high and the concentrations of Na^+ and Cl^- are low. This ionic restriction results in a charge imbalance of approximately 70mV between the inside (-) and outside (+) of the cell. This is the so-called 'resting' or 'Nernst' potential and it remains unperturbed until the cell is stimulated by some neuro-chemical event. In order to explain the mechanics of this disturbance, consider first the simplest situation in which there are only two neurons, the first, pre-synaptic cell connected to the second post-synaptic cell via what is known as an excitatory synapse. When an Action potential arrives at the nerve ending of the pre-synaptic cell it stimulates release of a neurotransmitter from the synaptic vesicles (chemical pockets contained within the nerve ending of the pre-synaptic neuron). This neurotransmitter is secreted at the nerve ending and travels into a 50 nm wide gap known as the synaptic cleft. The chemical travels across the synaptic cleft and binds to receptor molecules on the dendrite or soma of the postsynaptic cell. As a result, these receptor molecules change their shape becoming

more (or less) permeable to ions. The ensuing flow of charged particles (usually Na^+ or IC^+ ions) changes the membrane potential of the postsynaptic cell. This process is shown diagrammatically in Figure 4.3.

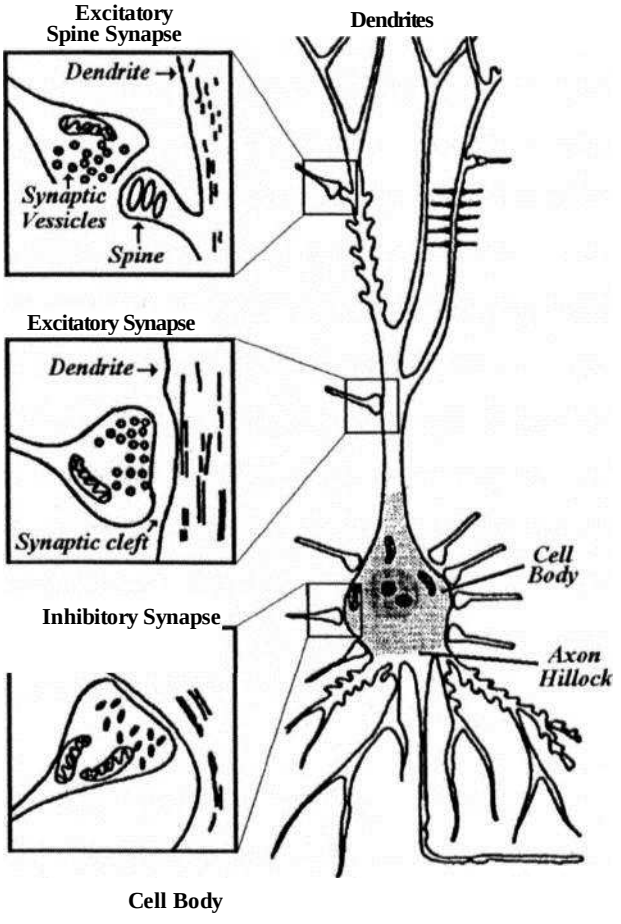

Figure 4.3: A schematic representation of the pyramidal cell with three types of synapse highlighted. (Modified from [2].)

Synapses come in two forms, inhibitory, and excitatory. Intracellular potential is increased by stimulation at an excitatory synapse whilst it is decreased by stimulation at an inhibitory synapse. Upon stimulation by an excitatory neurotransmitter, ion currents flow into the cell and (due to the electric field set up by the inflowing ions) along the dendrites towards the soma. These dendritic currents are known as post-synaptic currents. In

reality, the dendrites and soma of a single neuron will typically have many thousands of connections from other neurons. If enough excitatory synapses are stimulated the resulting influx of ions will depolarise the cell. If the voltage reaches some critical value

then the cell will 'fire' meaning that an action potential will begin at the soma and pass down the axon of the post-synaptic cell. Conversely, stimulation of enough inhibitory synapses will cause the cell to become hyperpolarized and the cell will remain unperturbed (i.e. no action potential will be induced).

Neurons themselves can be divided into two classes pyramidal cells and stellate cells, each made distinct by its geometry. Pyramidal cells are relatively large and their dendrites reach out parallel with one another in a direction that tends to be perpendicular to the cortical surface. Since dendrites guide the flow of ionic currents this means that for **a** network of pyramidal cells, the direction of current flow also tends to be perpendicular to the cortical surface. The dendrites of stellate cells spread out symmetrically, meaning that the cortical current distribution from a stellate cell is also symmetrical. This cell geometry is an important factor in MEG since a symmetrical current distribution will induce no measurable magnetic field due to field cancellation. This argument would suggest that it is pyramidal cells that are of primary interest to us in MEG since the summed parallel current flow across many thousands of cells might produce a magnetic field that is detectable outside the head.

4.1.3 Glial Cells

Glial cells are generally smaller than neurons and their job is to provide metabolic support. There are three types of glial cell, Astrocytes, oligodendrocytes and Schwann cells.

Astrocytes occur close to blood vessels and their processes terminate in 'end feet,' which make contact with both the capillary wall and the neurons. They provide metabolic support to the active neurons by mediating the passage of nutrients from the blood supply to the excitable cells. In doing this they also form part of the blood:brain barrier by preventing any toxins that may be in the blood reaching the neuronal network. Astrocytes also provide protection by removing any potentially toxic substances from the vicinity of neurons that they surround. This includes the removal of neurotransmitters from the

synaptic cleft following receptor stimulation. Figure 4.4 shows schematically the relative positioning of the astrocyte, neuron and blood vessel.

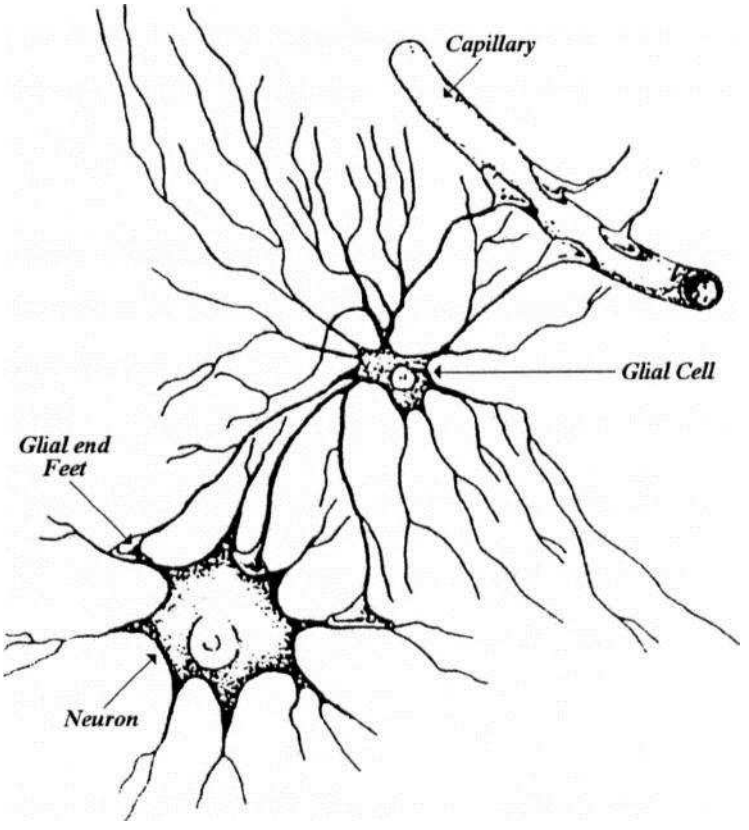

Figure 4.4: The relative positioning of the Astrocyte, neuron and blood vessel.

Oligodendrocytes provide structural support for the neurons by forming a myelin sheath, which surrounds the axon (see Figure 4.2). The myelination process involves an oligodendrocyte wrapping itself around the axon, such that its plasma membrane forms a spiral around the axon. The myelin sheath forms a resistive layer that aids conduction along the nerve axon. At the points where one glial cell ends and another begins there is a small gap known as a node of Ranvier. It is due to these resistive sheaths and the nodes of Ranvier that action potentials appear to 'jump' from one node to the next as they traverse the axon length, (i.e. the action potential flows much quicker in the myelinated regions than the unsheathed regions.) Schwann cells also perform this same role of myelination, however these act in the peripheral nervous system and not in the cortex itself.

4.1.4 Postsynaptic potentials and generation of neuromagnetic fields

At the level of individual neurons, two different types of neuronal current exist, namely action potentials, which flow along the myelinated axon of a neuron following depolarisation of the soma, and post-synaptic potentials, which comprise ion flow within the dendrites following synaptic stimulation. These two distinct current types result in different magnetic field patterns.

Post-synaptic currents comprise the influx of ions to the dendrite or soma of a post-synaptic cell. The strength of these current sources (i) decreases with distance from the point of initial influx (x), such that:

$$i(x). \; expE\text{-}4 \qquad [4.1]$$

Where A is the characteristic length scale of the exponential decay and is given by $[C^{\cdot}$ $membrane\ P\ intl12$ where $cr_{,,,,,,,,,one}$ is the conductance of the cell membrane and $p_{i,,,}$ is the resistance per unit length of the intracellular fluid [4]. For a cortical neuron, **A** is typically of the order **0.1 — 0.2** mm.

Post-synaptic current can be modelled as a current dipole, a line element of current **I,** pumped from source at position rj to sink at **r2** where r1 and **r2 are** in very close proximity. The current dipole moment is given by

$$\mathbf{Q} = \quad \mathbf{—1._2)} \qquad [4.2]$$

In the case of the post-synaptic current dipole, its magnitude may be approximated by:

$$Q\ PSP = {}^{I}\ PSP^{2} \quad [43]$$

Where the average post-synaptic current **(lp$_s$p)** can be estimated using the change of voltage AV associated with the post-synaptic potential thus:

$$I\ p_s p = \frac{\mathrm{AV}_{rA}}{pint} \quad \text{V+.91}$$

If **d** represents the dendritic diameter and cru_u the intracellular conductivity then:

$$pant = \mathbf{rd}^{2}{}_{\mathrm{aim}}^{4} \qquad \mathbf{[4.5]}$$

Thus, we find that:

$$Q_{sp} \approx \frac{2D1^2 \cdot}{asn'AV\ 4} \quad [4.6]$$

Inserting typical values (d = 1 pm o,,, = 1 1 fr^{l}in^{-}' and AV = 25 mV) we find that for a single post-synaptic potential, Q 25 fAm . Further, the Biot Savart law implies that the magnetic field from this intracellular dipolar current falls off as $(\text{Dis tan ce})^2$

Following the passage of postsynaptic currents, there must me some mechanism by which to restore the resting potential of the cell. This is accomplished by metabolically driven ion pumps, which are located within the cell membrane and are able to expel ions by transporting them from the intra cellular space to the extracellular space, a process that requires a relatively large amount of energy since they must work against both the potential difference and concentration difference between the cell and its surroundings. The expulsion of ions from the dendrites of neurons causes the generation of an electrical field between the point at which the ions are expelled, and the initial point of influx. This field then sets up an extracellular current known as a secondary, or volume current flowing in the opposite sense to the intracellular current. This is shown in Figure 4.5. We will see in the next chapter that (with the use of certain approximations) the effect of these volume currents on the measurable magnetic field is minimal.

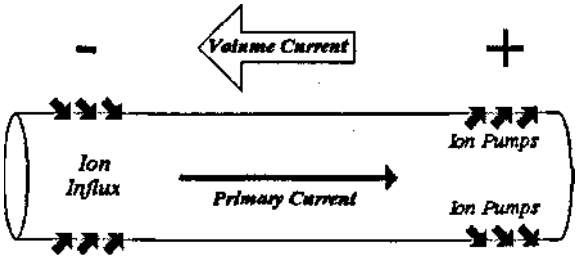

<hune Current!

Figure 4.5: Post synaptic current: The primary current is caused by an in influx of ions to the cell following neuro-chemical stimulation of receptor molecules. Extra-cellular volume currents are a result the electric field set up by ion expulsion from the cell.

4.1.5 Action potentials and generation of neuromagnetic fields

Action potentials comprise a progressive transient disturbance in the cell resting potential that travels down the nerve axon from the soma to the nerve ending. An action potential will occur when the voltage at the axon hillock reaches the critical threshold voltage of approximately —40 mV. At this point, voltage sensitive ion channels change their permeability to $\mathbf{Na^+}$ and $\mathbf{K^+}$ and briefly, the cell becomes positively charged with respect to the extracellular space. This change of potential causes ion channels in the neighbouring region of the axon to change their permeability, and hence the action potential travels further down the axon. Ion pumps expel $\mathbf{Na^+}$ and K+ ions from the axon following depolarisation. This transport mechanism means that the action potential can be characterised by a leading edge of depolarisation followed quickly by a trailing edge of repolarisation. The membrane potential provides energy such that the action potential remains unattenuated as it travels along the axon length. Furthermore, should the soma become depolarised beyond the critical threshold voltage required (i.e. V > **-40 mV)** the amplitude of the action potential does not increase, the rate of firing however does.

In a long, straight length of axon, the action potential can be described accurately as two opposing current dipoles, the separation of which depends on current velocity. This current distribution and the resulting field pattern are shown schematically in Figure 4.6.

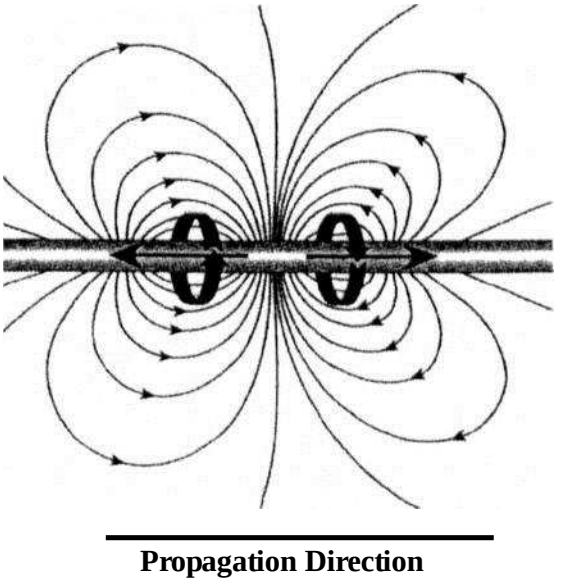

Figure 4.6: The two opposing current dipoles that characterise an action potential.

The two back to back current dipoles forms current quadrupole, the magnetic field from which falls off as / $(\text{Distance})^3$

The dipole moment of each dipole is approximately 100 fAm, four times larger than the single dipole caused by the post-synaptic current. However, because the field induced by the action potential falls off as $\frac{1}{(\text{Distance})^3}$, and not $\frac{1}{(\text{Distance})^2}$ as is the case with the post-synaptic current, it is thought that it will contribute less to any detectable external magnetic field. Further, in order for a magnetic field to be detected, the initial current distribution must comprise the sum of many individual cells (of the order of 10^6). The duration of a single action potential is of the order 1 ms whereas a single post-synaptic current might last up to 10ms, giving a ten fold greater probability of simultaneous activation and hence summation of magnetic fields. Finally, a single neuron might have many dendrites, but only a single axon, again making the contribution from post-synaptic currents greater than that from action potentials. For these reasons, it is postulated that the largest component of detectable magnetic field from ion flow in the brain will come from post-synaptic currents found in the dendrites of pyramidal cells. If approximately 10^6 individual pyramidal neurons contain parallel dendritic current of dipole moment —25 nAm, then a measurable magnetic field of order Pico-Tesla will be produced outside the head.

4.2 DETECTION OF NEUROMAGNETIC FIELDS

The neuromagnetic fields resulting from neuronal current flow are typically of order — 100 fT. This is approximately one part in 10^8 of the Earths magnetic field and also small when compared to magnetic fields produced by laboratory equipment and geomagnetic noise. This makes detection of neuromagnetic fields problematic and the only detector that offers sufficient sensitivity is the Superconducting Quantum Interference Device (SQUID) [5, 6]. Here, the fundamental concepts behind SQUID technology and noise reduction strategies are introduced, with particular emphasis on the CTF 151-channel 'Omega' system at the Wellcome trust laboratory for MEG studies, Aston University, Birmingham UK.

4.2.1 Superconductivity

Superconductivity was discovered by H. Kamerlingh Onnes in 1911 following speculation that the resistance of pure metals might fall to zero at T = 0 K. In fact, the effect was far more dramatic. Onnes showed that an abrupt transition to a state of zero resistance occurred at a well-defined transition temperature, T_c, and that this was unaffected by impurity concentration. Since then, many elements have been shown to exhibit superconducting properties, and these, in general, can be split into two distinct types.

All pure superconducting samples (except Nb) exhibit type I behaviour, meaning that their superconductivity is destroyed when an external magnetic field is applied whose strength is equal to or greater than some critical value **B, .** Logically, it therefore follows that for a long straight superconducting wire, there exists some critical current beyond which the associated magnetic field will exceed **B,** and superconductivity will subside. However, in 1933, Meissner and Ochsenfeld showed that due to surface screening currents, the magnetic field inside a superconductor is zero. This is known as the Meissner effect and can be used to distinguish between the two superconductor types. With increasing magnetic field **B,** all type I superconductors show a complete Meissner effect up to some critical field B,, beyond which they become resistive. Conversely, type

II superconductors exhibit a complete Meissner effect up to a lower critical field Ba, beyond which a partial Meissner effect exists up to a second critical field Ba, where generally B_{c2} » **B.** Typical SQUID's used in MEG are made either from Pb alloy, or Nb, both type II superconductors. This is because they maintain their superconductivity to higher fields.

A successful microscopic theory of superconductivity was proposed in 1957 by Bardeen, Cooper and Schrieffer and is known as the BCS theory [7-10]. They suggested that an energy gap, d, exists between electrons exhibiting superconducting properties, and the so-called 'normal' (non superconducting) electrons. This energy gap exists because superconducting electrons are bound together in pairs (known as 'Cooper' pairs), the binding energy of which is 26,. The idea that two electrons can bind together is somewhat counter intuitive, since one expects the Coulomb interaction to push them apart. However, this is not the case since firstly, the repulsive force is partially screened out by the other electrons, and secondly, the electrons also interact with the positive ions of the lattice. As an electron passes between positive ions it causes a spatial disturbance, each ion being 'dragged' towards the electron. The large positive ions move slowly relative to the electrons and the passage of the first, single electron leave's behind a `wake' of positive charge. This positive wake attracts and binds the second electron. (Formally, the two electrons are attracted by exchange of a virtual phonon, in much the same way as exchange of virtual bosons mediate the nuclear strong interaction.)

Electrons are fermions, and as such the Fermi exclusion principle states that no two electrons can exist in the same state. However, when two electrons combine to form a Cooper pair, they transform from two fermions into a single boson, and any number of bosons may exist in the same state at any one time. BCS theory shows that the binding energy of Cooper pairs is maximised when all of the Cooper pairs exist in the same state, and hence all have the same wavefunction (given by Equation 4.7).

$$0 = 0 \exp(tq.r) \qquad [4.7]$$

Where **r = (r_1 + r_2)** represents the centre of mass co-ordinate of the Cooper pair, **q** is the pair momentum and 0_0 is the ground state wavefunction for a Cooper pair at rest.

Superconductivity is therefore a co-operative phenomenon, the more pairs acquiring the equivalent wavefunction, the stronger the binding energy between them. However, if the wavefunction of a single pair changes, then that pair looses its binding energy. The equivalent wavefunctions of all of the Cooper pairs explains the superconductor's infinite conductivity: since the pairs must exist in the same state, their centre of mass motion must be equivalent, meaning that they all travel in the same direction with equivalent momentum. This motion of cooper pairs forms the supercurrent, which is not affected by phonon or impurity scattering since if one electron is affected, the second compensates to maintain centre of mass momentum and hence superconductivity. The Cooper pair current can therefore only be affected by something influencing all pairs equally, i.e. an electric or magnetic field.

4.2.2 The order parameter and flux quantisation

The fact that all cooper pairs share a common wavefunction means that, conveniently, they can be specified completely by a single function. (This yields the rather attractive result that just two position variables can be used to describe — 10^{29} electrons per cubic metre!) By ignoring the relative motion of the two electrons in a Cooper pair and regarding it as a point particle, only the dependence of the wavefunction on the centre of mass co-ordinate is required, this can be taken into account by the order parameter, which for a uniform current density mirrors the wavefunction thus:

$$kr) = W \exp(iqx) \qquad [4.8]$$

The current density associated with such a wavefunction can be shown to be [10]:

$$Ar). \; 2m \; ihe \; {}_{(iv^* \; v \; wv \; w^*)} 2e \; {}^{*}{}^{2}_{yfA} \qquad [4.9]$$

Letting **q.r = 0,** and inserting this into Equation 4.9 gives:

$$\mathbf{j\,(r)} = — \; -_{\mathbf{T}}{}^{\mathbf{e}}{}_{\mathbf{r}}{}_{\mathbf{-i}}\mathbf{lyf(r} \; \text{rove+} \; 2eA) \qquad [4.10]$$

For a superconducting sample in the Meissner state, far from the sample surface we must have j = 0, meaning (from Equation 4.10) that:

$$h\nabla\Theta = -2eA \qquad [4.11]$$

Integrating this equation around a closed loop within the superconductor gives:

$$\oint_C h\nabla\Theta.dl = \Theta = -2eciAdl \qquad [4.12]$$

Since the order parameter has been modelled on a wavefunction, the properties and boundary conditions of the wavefunction must also hold true. Therefore, the order parameter must be single valued, and the phase change around a closed loop, AB, must equal ± 21in where n is a positive integer or zero. Using Stokes' theorem it is possible to transform the closed loop integral on the right hand side of Equation 4.12 into a surface integral thus:

$$\oint_C 244.d1 = -2e \int_S \nabla \times A.dS \qquad [4.13]$$

Where the surface integral is over the surface of circle C. It follows that

$$\Theta = 27ath = -2e \int_S B.dS = -2e0 \qquad [4.14]$$

And we therefore see that the magnetic flux 0 through our closed loop is quantised in units of $\frac{nh}{e}$. This same result can be applied to a superconducting loop of wire with a persistent current flowing.

4.2.3 Josephson junctions

A Josephson junction is formed when two macroscopic superconductors are weakly coupled. To qualify this, consider two superconductors with order parameters $v_i = |y_i|\exp(i0_1)$ and $v_2 = 1w_2|\exp(i0_2)$ separated by a small gap. If the two samples are at the same temperature then $|M|^2 = |V21|^2 =$ but in the absence of interaction across the gap, the phases 0, and 0_2 will, in general, be different. If the two samples are brought into contact then a strong interaction would be induced between them, the phases of each region will equalise and all the cooper pairs are forced into the same state. In the case of a weak interaction the two samples interact such that the lowest energy state is one in

which $0_1 = 0_2$, however a phase difference between the two regions can be generated if either a small tunnelling current flows across the gap, or a voltage is applied across it.

There are many ways of achieving weak coupling between samples but the most common is to separate the two by an oxide layer of a few atoms thickness. When $T < T_i$, Cooper pairs can tunnel through the gap in the absence of an applied voltage. This tunnelling current is a result of the extension of order parameter for each superconductor into the gap. Figure 4.7 shows the exponential decay of the order parameter with distance into the gap for two superconductors separated by an oxide layer of width d.

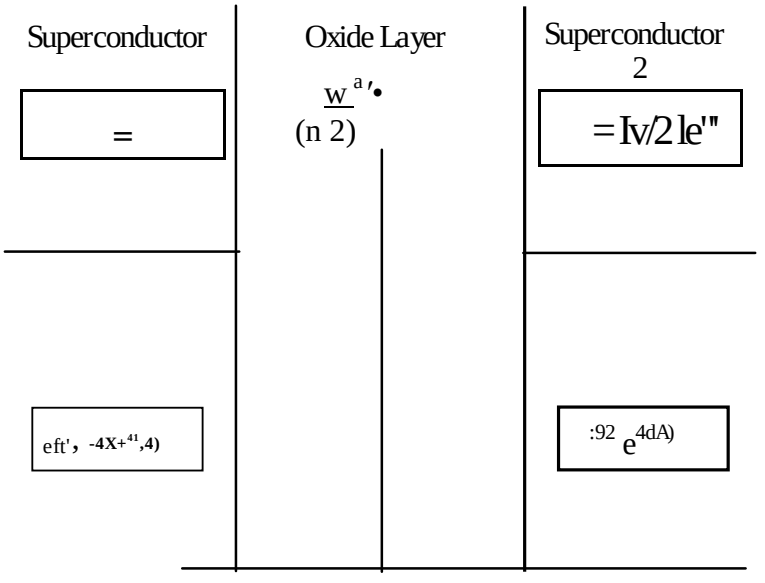

Figure 4.7: The order parameters for two superconductors weakly coupled at a Josephson junction.

Within the gap itself, the order parameters add such that:

$$v = (\text{—}^{n}d^{i} \quad \text{exp}[0_2 + IC(x \text{—} dAb \qquad [4.15]$$

The current across the junction is given by Equation 4.9 and if A = 0 it can be shown that:

$$= \frac{e\,hn}{2m} K\,exp(— Kd)[— exp(i[0,— 0_2\,1) + ex\,p(40_2 — 0,1)1 = j_o\,sin(8) \qquad [4.16]$$

Where $j_o = {}^{ehn}s\_\ K\,exp(— Kd)$ and $8 = 0_1 — 0_2$, meaning that the current across the gap is dependent on the phase difference between the two order parameters. If a current is caused to flow through the junction, then the phase difference adjusts itself so that Equation 4.16, known as the *Josephson equation,* is satisfied. The existence of Cooper pair flow across the junction is known as the *DC Josephson effect.*

4.2.4 Quantum Interference

The superconducting quantum interference device (SQUID) comprises a superconducting ring interrupted by two identical Josephson junctions as shown in Figure 4.8.

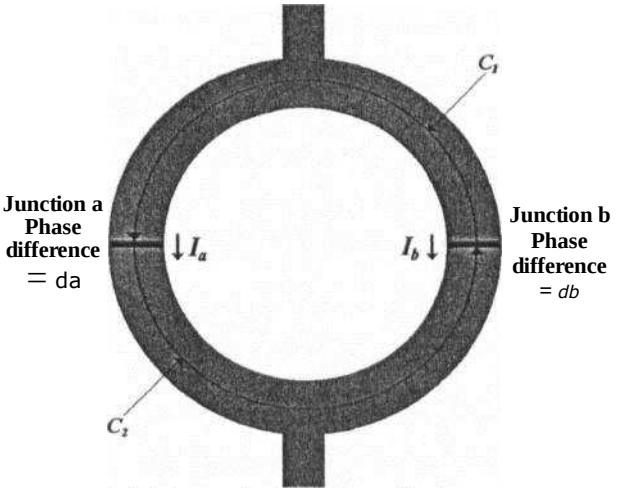

Figure 4.8: A superconducting ring separated by two Josephson junctions forming a DC SQUID.

Equation 4.16 implies that the current, **I,** flowing through the two junctions in parallel is:

$$I = AJ_{o}[sin(8_a) + Sin(g_b)1 \qquad [4.17]$$

Using trigonometric identities this can be rearranged to give:

$$I = 2AJ_o\ cos[8o\ \underline{28b}\ sin\ [8a\ 2^{8h}] \qquad [4.18]$$

Now consider the curves C, and ***C2*** shown in Figure 4.8. These curves exist at the centre of the bulk superconductor and since current density vanishes far from the sample surface, Equation 4.11, (specifically, **hV 0 = –2eA)** must hold. Integrating around these curves (see also Equation 4.12) we find that:

$$= —^{2e} \text{fAill} \qquad \text{And} \qquad {}^{\circ}b,2 - {}^{o}a.2 = \text{e}\ \mathbf{I}\ \text{riA411.} \qquad [4.19]$$

Summing these two equations gives:

$$Oa.I - 0,_{1,2} + 0_{b,2} - O_{bi} = o_a - 5_b = \text{e} — \frac{\text{friats.} = \text{sr-}}{\mathbf{c}} \qquad [4.20]$$

That is to say, the quantity $5. - 8_{b,}$ and hence the current I, is dependent on the magnetic flux through the ring. (Notice that in order to compute the integral around the full loop the contributions from the two oxide layers in the Josephson junctions have been ignored. Since A varies smoothly across the narrow junction gap, this error is negligible). Rewriting Equation 4.20 we now find that

$$/ = 2AJ_0\ \text{COS}\left[\mathbf{1}_{\mathbf{h}}\mathbf{0}\ \mathbf{sin}\ \frac{\mathbf{ab}}{J} + 2\right] \qquad [4.21]$$

and therefore the maximum current allowed through the junctions is:

$$\underset{\mathbf{h}}{1} = /_0 \text{COil}\ 01 \qquad [4.22]$$

The current will therefore vary periodically with magnetic flux. This effect is known as quantum interference. Because the flux quantum is so small, a device similar to that shown in Figure 4.8 with total area of 1 cm^2 would run from a minimum to a maximum current for a change in magnetic field of just 10^{-11} T. It is for this reason that the SQUID can be used as a sensitive device for measurement of small magnetic fields.

4.2.5 The DC SQUID operating principle and the MEG System

As described above, tunnelling of Cooper pairs allows the passage of small currents through a SQUID ring, however it can be shown that if this current becomes greater than some critical value, 1_c, then the junctions become resistive, and a voltage drop across the weak links is induced. Equation 4.22 shows that if a magnetic field is allowed to impinge

on the ring, it will induce a change in the magnitude of current flowing through the ring, however, if a bias current l_c has also been applied, then a change in magnetic field will no longer induce a change in current, but rather a change in the voltage across the weak links. This voltage drop, also a periodic function of flux, is used in detection of small magnetic fields.

A basic schematic diagram of SQUID circuitry is shown in Figure 4.9 A. The external neuromagnetic field is connected to the SQUID via a superconducting flux transformer. The flux is then coupled to the SQUID through the mutual inductance **M**

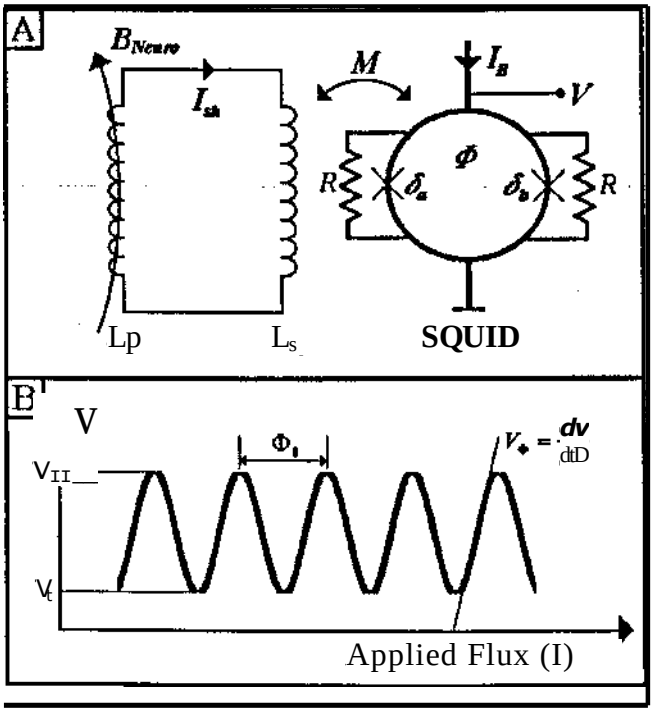

Figure 4.9: A) Schematic diagram of the DC SQUID. B) The flux to voltage transfer function for the DC SQUID.

A bias current $\mathbf{I_b ?\_ l_c}$ is allowed to flow through the SQUID and as the magnetic flux threading the ring is modulated, the voltage drop across the SQUID becomes a multi-valued periodic function (see Figure 4.9B) and the SQUID is generally operated on its

steepest part, where the so-called transfer coefficient $\frac{d}{d\Phi} = \frac{}{}$ is a maximum. In short, (4.1)

the operation of the DC SQUID is as follows.

1. Time varying neuromagnetic fields cause current variation in the pickup coil. These in turn cause current flow in the signal coil.
2. The signal coil is coupled to the SQUID ring via a mutual inductance M. This means that the current in the signal coil alters the flux threading the ring.
3. The ring responds with additional currents to compensate for the field (in agreement with the principle of flux quantisation). However, the applied bias current means that the critical current has already been reached; therefore the extra current flow causes a measurable voltage drop across the weak links.
4. The voltage drop is detected by the SQUID electronics, which in turn apply a feedback current to the ring to counterbalance the induced current
5. The output of the required feedback current is measured as a voltage produced across a resistor in the feedback circuit. This serves as the output of the magnetometer system.

SQUID electronics and feedback circuitry forms a large area of research and it is beyond the scope of this chapter to describe it in detail. For a good review, the reader is referred to [2].

The MEG system to be used in later experiments is the CTF 151 channel `Omega' system at the Wellcome trust laboratory for MEG studies, Aston University, Birmingham, UK. This system employs 151 Nb DC SQUID' s to detect fields at different locations and orientations around the head. These detected magnetic fields are combined in such a way to form 151 usable measurements of neuromagnetic field.

4.2.6 Noise reduction strategies

The problem often encountered in MEG is that recordings of neuromagnetic fields are contaminated by environmental and instrumental magnetic noise sources. In the

laboratory environment where computers, monitors, amplifiers and the like are commonplace, the magnetic noise is several orders of magnitude higher than the neuromagnetic signals in which we are interested (see table 4.1). Low frequency artefacts are a particular problem because they are difficult to shield and they act to contaminate the frequency range of the neuromagnetic signals themselves. For these reasons effective shielding against magnetic noise is a vital part of MEG.

Flux Density (fT)	**Source**
10^{19}	Earths steady magnetic field
10^{9}	Laboratory noise
10^{8}	Urban Noise (traffic etc.)
10^{7}	Geomagnetic noise
10^{6}	Magnetised lung contaminants
10^{5}	Abdominal Currents
10^{4}	Cardiogram, oculogram
10^{3}	Epileptic and spontaneous brain activity
10^{2}	Cortical evoked activity
10	SQUID noise
1	Brainstem evoked activity

Table 4.1: Sources of magnetic noise and their amplitude (adapted from [3])

Shielded Rooms

The simplest and most effective method of reducing the effect of external magnetic noise is to place the detector system in a magnetically shielded room. At the Wellcome trust laboratory for MEG studies, this is achieved by the use of layers of μ-metal and Aluminium. μ-Metal typically has permeability —80,000 [2], and works to shield the detector system from external magnetic fields whilst the Aluminium layers, which are sandwiched between the layers of μ-metal, serve as an eddy-current and RF shield. When an external magnetic field impinges on the room it follows a path of greatest permeability, namely through the walls, around, and away from the detector system. This

shielding is most effective at high frequency and at 100 Hz, signals can be attenuated by as much as 50 — 60 dB. However, at low frequency <0.1 Hz, this is reduced to —20 — 30 **dB.**

Gradiometers

The levels of attenuation provided by the shielded room are still not sufficient for making measurements with a simple SQUID magnetometer system, since the magnetic noise penetrating the shielded room is still several orders of magnitude larger than the neuromagnetic signals required. Further isolation of the neuromagnetic signals can be achieved by a simple modification to the magnetometer system. The strength of neuromagnetic fields follows approximately the inverse square law, meaning close to the field source, the field gradient is large whereas far from the source, the field gradient is much less. This fact can be exploited in MEG by measurement of the field gradient, rather than magnetic field itself. Traditionally, a small modification to the coil geometry would be made such that an additional compensation coil is introduced in series with L_p, (see Figure 4.10) making the recorded signal effectively **dB / dr .** Gradiometers of this kind are physically wound coils where a single detector consists of two loops of wire wound in opposition. A time varying magnetic field passing through the detector induces oppositely directed currents, which partially cancel out. The net current measured is therefore representative of the field gradient. Physical gradiometers come in two forms: Axial gradiometers comprise two oppositely wound coils displaced from one another in the radial direction, meaning that the field gradient is also measured in the radial direction. Planar gradiometers have their coils shifted tangentially, meaning that the field gradient is measured perpendicular to the radial direction. Gradiometers allow for effective noise reduction in recorded MEG signals, however, in practice they cause the system to become less sensitive to deeper sources than to shallow sources.

In the CTF system, the idea of field gradients is taken further by the use of a novel synthetic gradiometer system. Here radial field gradients measured using physical axial gradiometers, however this information is combined with information taken from several distal reference measurements in order to allow a high order synthetic gradiometer

measurement. In order to illustrate the principle of the synthetic gradiometer system, let us first consider the simple example of the first order gradiometer synthesized from a primary magnetometer sensor at position **r,** and a three-component vector reference magnetometer at position **r'.** This is shown in Figure 4.10.

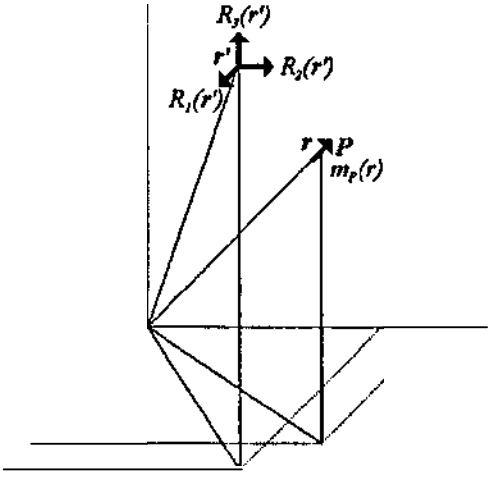

X i

Figure 4.10: Experimental set up in a first order synthetic gradiometer system.

The primary magnetometer will measure magnetic field perpendicular to the plane of the coil. Therefore, if the coil normal vector is **P,** the gain of that sensor a_p, and the external magnetic field **B(r),** then the measured field would be given by m_p (r) = a_p[P.B(r)]. If the three components of the vector magnetometer are orthogonal, and have the same gain, a_R, then its output will be given by $\mathbf{R}_k$ **(r')= a**$_R$**k(e)** where k = 1,2,3 , $\mathbf{B}_k$ **(r')** are the three orthogonal components of magnetic field at position **r'** and $\mathbf{R}_k$ **(r')** form the magnetometer output vector **RH.** The first order gradiometer output is given by:

$$g^{(1)} = m_p(r) - \frac{cr}{a_R} (P.R(r9) \qquad [4.23]$$

Expansion of the magnetic field using the first two terms of a Taylor series about the origin gives:

$$B(r') = B(r) + \sum_{k=1}^{3} \frac{\partial}{\partial x_k} (x_{k'} - x_k) \qquad [4.24]$$

Where x_k represents the three orthogonal components of r and likewise x_k' represent the three orthogonal components of r'. This can be rewritten in terms of the first gradient tensor, i.e.

$$\begin{bmatrix} B_{x1} \\ B_{x2} \\ B_{x3} \end{bmatrix} = \begin{bmatrix} \frac{\partial B_x}{\partial x} & \frac{\partial B_x}{\partial y} & \frac{\partial B_x}{\partial z} \\ \frac{\partial B_y}{\partial x} & \frac{\partial B_y}{\partial y} & \frac{\partial B_y}{\partial z} \\ \frac{\partial B_z}{\partial x} & \frac{\partial B_z}{\partial y} & \frac{\partial B_z}{\partial z} \end{bmatrix} \begin{bmatrix} x_1 - x_1 \\ x_2 - x_2 \\ x_3 - x_3 \end{bmatrix} \qquad [4.25]$$

Defining a gradiometer baseline vector, $b = r' - r$, then Equation 4.25 reduces to simply $AB = Gb$, where G is the first gradient tensor. The first order gradiometer can then be re-expressed as:

$$g^{(1)} = a_p P.G.b \qquad [4.26]$$

Equation 4.26 shows that the synthetic first order gradiometer is a projection of the first gradient tensor onto the primary magnetometer orientation, P, and the baseline b.

Second order synthetic gradiometers are formulated in a similar fashion. In this case, we consider first two first order gradiometers with outputs $g^{(1)}$ and $g^{(1)'}$, parallel baselines (b and b'), and coil orientation vectors (P and P'). The second order gradiometer baseline, q, connects the two gradiometer sensors. Using similar arguments it can be shown that:

$$g^{(2)} = g^{(1)} a_g \qquad g^{(1)'} = a_{p'} G^{(2)} q b \qquad [4.27]$$

Where a_g is the first order gradiometer gain, and $G^{(2)}$ is the second order gradient tensor at the co-ordinate origin. The above procedure can be generalized and it can be shown that second or third order gradiometer outputs can be synthesized from magnetometers, first order gradiometers or their combinations. The synthetic higher order gradiometer significantly reduces environmental noise [11, 12]. They also behave in a

similar way to the primary magnetometers on which they are based. For a review of the advantages of the synthetic third order gradiometer see **[1 1].**

4.3 DETECTABLE NEUROMAGNETIC EFFECTS

Even after magnetic noise attenuation due to both the shielded room and gradiometer systems, noise remains a problem in MEG and for this reason novel filtering and averaging techniques are commonly employed. However, these techniques must depend largely on the effect of interest sought in the MEG recording and so these should be considered prior to MEG data analysis.

4.3.1 The Evoked response and sustained field effects

Many studies have used MEG in order to focus on the brain's 'evoked response.' The evoked response is generally time-locked and phase-locked to some externally or internally applied stimulation, and comprises a transient spike at or near the onset and offset of the applied stimulation period. The evoked response is commonly detected by repetition of a stimulus paradigm. If a number of trials of the same paradigm are recorded and subsequently averaged together, the phase locked nature of the evoked response means that it remains prominent in the final average dataset, whereas non-phase-locked (random) noise will be attenuated. Typical studies have involved the detection of evoked responses in visual [13], somatosensory **[14]** or auditory [15] cortices.

In addition to the traditional MEG evoked response, a significant sustained component of magnetic field has also been reported. Sustained fields comprise what appears to be a baseline shift throughout the period of stimulation (i.e. between transient spikes at stimulus onset and offset). Such fields are not generally observed in MEG because it is normal practice to apply a high pass filter prior to data processing (in order to suppress low frequency noise). Sustained fields have also remained largely undetected in EEG since in addition to 1/f amplifier noise (similar to that observed in MEG) EEG is also

subject to 1/f electrode noise (due to electro-chemical instabilities at the electrode skin interface [16]). This leads to MEG being an improved technique with which to detect sustained fields when compared to EEG. (In particular, use of the synthetic gradiometer should make it relatively easy to record sustained effects.) Sustained fields have been documented in primary auditory cortex using both EEG [17, 18] and MEG [19, 20] and in primary somatosensory cortex using MEG [21].

4.3.2 Oscillatory effects

In addition to the stimulus evoked, phase-locked responses described above, aspects of spontaneous brain activity can also be detected using MEG. The existence of spontaneous oscillatory brain activity has been well documented and the first non-invasive measurement of the 8 — 13 Hz 'alpha' wave was made by Hans Berger in 1924. Since then a series of different brain activities have been characterised and are tabulated below.

Name	Frequency range	Description
Delta	< 4 Hz	Slowest of all spontaneous brain activity, the delta rhythm is most prominent in deep sleep.
Theta	4 — 8 Hz	As with the delta rhythm, spontaneous activity in the theta band is also associated with sleep.
Alpha	8 — 13 Hz	Most prominent in awake and relaxed subjects, alpha waves are blocked by visual or somatosensory stimulation.
Beta	13 — 30 Hz	Beta activity is often associated with the motor cortex and is thought to reflect active cortical processing.
Gamma	30 —100 Hz	Gamma activity is often associated with the visual cortex and is thought to represent active cortical processing.

Table 4.2: Brief descriptions of some characteristic brain oscillatory activity.

Berger also showed that these spontaneous cortical rhythms could be modulated by external stimuli, for example it was shown that alpha waves are blocked by visual stimulation. More recently, it has been shown that external stimulation can cause more subtle modulation of oscillatory activity. Effects comprising time-locked but non-

phase-

locked changes in oscillatory amplitude have been reported [22]. These subtle effects have often been overlooked in EEG and MEG since, due to their non-phase-locked nature, they are suppressed by trial averaging. A stimulus induced increase in oscillatory power in some frequency band of interest is known as Event Related Synchronisation (ERS), whilst a decrease in oscillatory power is known as Event Related Desynchronisation (ERD). The importance of these effects is somewhat unclear, however recent literature [23] has suggested that localised alpha and beta desynchronisation is intimately linked to brain activation in that area. Further to this, a paper by Singh **et al** (2002) [24] has demonstrated a striking co-localisation between ERD and (positive) BOLD effects in language and visual tasks.

The work to be described in later chapters furthers these previously made measurements by the localisation of neuromagnetic effects and spatiotemporal assessment of their correlation with the BOLD effect. A number of heterogeneous neuromagnetic effects will be shown to be detectable in response to simple stimulation of primary cortices. These effects comprise both time and phase locked transient responses, sustained fields and high frequency oscillatory effects including event related synchronisation and desynchronisation.

4.4 REFERENCES

1. Bear, M.F., Connors, B.W., Paridiso, M.A., Neuroscience: Exploring the brain Second Edition. 2001, Philadelphia: Lippincott, Williams and Wilkins.

2. Hamalainen, M., Hari, R., Ilmoniemi, R.J., Knuutila, J., Lounasmaa, 0.V., Magnetoencephalography - Theory, Instrumentation and applications to non-invasive studies of the working human brain. Reviews of Modern Physics, 1993. 21(2): p. 413 460.

3. Orrison, W.W., Functional Brain Imaging. 1995, St. Louis: Mosby.

4. Scott, A.C., Neurophysics. 1977, New York: Wiley.

5. Zimmerman, J.E., Thiene, **0.,** Harding, IT., Design and operation of stable :I-biased superconducting point-contact quantum devices and a note on the properties of perfectly clean metal contacts. Journal of Applied Physics, 1970. 41: p. 1572 - 1580.

6. Cohen, **D.,** Magnetoencephalography: Detection of the brains electrical activity with a superconducting magnetometer. Science, 1972. **5:** p. 664 - 666.

7. Bardeen, J., Cooper, L.N., Schrieffer, J.R., Physics Review, 1957. 106: p. 162.

8. Bardeen, J., Cooper, L.N., Schrieffer, J.R., Physics Review, 1957. 108: p. 1175.

9. Kittel, C., Introducton to solid state physics. 1971, New York: John Wiley and Sons.

10. Hook, J.R., Hall, H.R., Solid State Physics 2nd Ed. 1991, New York: Wiley.

11. Vrba, J., Robinson, S.E., Signal processing in Magnetoencephalography. Methods, 2001.**25:** p. 249 - 271.

12. Vrba, J., Haid, G., Lee, S., Taylor, B., Fife, A.A., Kubik, P., McCubbin, J., and Burbank, M.B., Biomagnetomers for unshielded and well shielded environments. Clinical Physics and Pysiological Measurements, 1991. **12 Suppl. B:** p. 81 - 86.

13. Ahlfors, S.P., Ilmoniemi, R.J. Hamalainen, M.S., Estimates of visually evoked cortical curents. Electroenceph. Clin. Neurophys., 1992. 82: p. 225 - 236.

14. Hari, R., Hamalainen, H., Hamalainen, M., kekoni, M., Sams, M., tiihonen, J., Separate finger representations at the human second somatosensory cortex. Neuroscience, 1990. **37:** p. 245 - 249.

15. Hari, R., The neuromagnetic method in the study of human auditory cortex. Auditory Evoked magnetic fields and electric potentials in volume 6 of Advances in audiology, 1990. edited by F.Grandori, M.Hoke and G.L.Romani: p. 222 - 282.

16. Mackert, B.M., Wubbeler, G., Burghoff, M., Marx, P., Trahms, L., Curio, G., Non-invasive long term recordings of cortical 'direct current' (DC-) activity in humans using magntoencephalography. Neuroscience Letters, 1999. 273: p. 159-162.

17. Picton, T., Woods, D., Proulx, G., Human auditory sustained potentials. I. The nature of the response. Electroenceph. Clin. Neurophys., 1978a. 45: p. 186-197.

18. Picton, T., Woods, D., Proulx, G., Human auditory sustained potentials. II. Stimulus relationships. Electroenceph. Clin. Neurophys., 1980b. 45: p. 198-210.

19. Hari, R., Aittoniemi, K., Jarvinen, M., Katila, T.,Varpula, T., Auditory evoked transient and sustained magntic fields of the human brain. Experimental Brain Research, 1980. 40: p. 237-240.

20. Lammertmann, C., Lutkenhoner, B., Near-DC magnetic fields following a periodic presentation of long-duration tonebursts. Clin. Neurophysiol., 2001. 112(3): p. 499-513.

21. Forss, N., Narici, L., Hari, R., Sustained activation of the human SII cortices by stimulus trains. Neuroimage, 2001. 13(3): p. 497-501.

22. Pfurtscheller, G., Lopes da Silva, F.H., Event-realted EEG/MEG synchronization and desynchronization: basic principles. Clinical Neurophysiology, 1999. **110:** p. 18421857.

23. Lopes da Silva, F.H.P., G., Basic concepts on EEG synchronisation and desynchronisation. Handbook of electroencephalography and clinical neurophysiology. Vol. 6. 1999, Amsterdam: Elsevier.

24. Singh, K.D., Barnes, G.R., Hillebrand, A., Forde, E.M., Williams, A.L., Task related changes in cortical synchrony are spatially coincident with the haemodynamic response. Neuroimage, 2002. **16:** p. 103-114.

CHAPTER FIVE

A NOVEL DETECTION METHOD FOR NEUROMAGNETIC SIGNALS

OVERVIEW

This, the first of four experimental chapters presents a technique for solution of the inverse problem and detection of neuromagnetic signals in MEG. The chapter begins with a discussion of the neuromagnetic forward problem and solutions to this are derived for a simple current dipole model. Following this, the neuromagnetic inverse problem is introduced and a recently developed solution (the non-linear beamformer) is derived from first principles' and its advantages and limitations discussed. This non-linear beamformer is then combined mathematically with the Hilbert transform and the General Linear Model thus introducing a novel method of source localisation that is statistically equivalent to that used in fMRL This new method is tested on a two-source simulation showing its ability to localise accurately both phase-locked and non-phase-locked sources. Finally the method is tested on real MEG data taken from a patient suffering a scintillating scotoma (a visual disturbance associated with migraine) and is shown to
locate accurately both frontal and temporal lobe sources. This novel combination of beamformer mathematics, the Hilbert transform and general linear model provides a useful mathematical framework for comparison between MEG and fMRI and is to be used again in the experiments described in later chapters. (This work has previously been published, see [1.1 and appendix)

5.1 THE FORWARD PROBLEM

The forward problem is defined as follows [2]; given a known cortical current distribution inside the head, can we calculate the resulting magnetic field distribution outside the head? This is a well-defined problem and as such has an analytical solution. In this first section a solution is derived using a set of simplifying assumptions in which we approximate cortical current distribution to a current dipole placed within a spherical head model.

5.1.1 Maxwell's Equations and the Quasi-static Approximation

We begin our discussion of the forward problem by considering the frequency band in which we shall be working. It will be shown that it is possible to significantly simplify the forward solution if we assume a 'quasi-static regime.' To qualify this, consider first the well known Maxwell equations of electromagnetism which state:

$$\nabla \times E = -\frac{\partial B}{\partial t} \qquad [5.1]$$

$$\nabla \times H = J + \frac{\partial D}{\partial t} \qquad [5.2]$$

$$\nabla \cdot D = \rho \qquad [5.3]$$

$$\nabla \cdot B = 0 \qquad [5.4]$$

Where **pH =B, D=tE, pis** the density of free charges, **J** is the density of free currents, **e** represents the permittivity and **p** the permeability of the material in question [3].

These four equations form the cornerstone of electromagnetic theory and along with the Lorentz force equation, **F =q(E+vxB),** and the continuity equation, $\nabla \cdot J = -\frac{\partial \rho}{\partial t}$ they can be used to predict all macroscopic electromagnetic phenomena.

In a passive, non-magnetic medium, current density may be written as the sum of a simple Ohmic current and a polarization current given by a time varying electric field such that:

$$J = \sigma E + \varepsilon \frac{\partial E}{\partial t} \qquad [5.5]$$

In a quasi-static regime, it is necessary that the contribution of the time derivative of electric field to total current is small when compared to the Ohmic term. Expressed mathematically this means that:

$$\sigma E \gg \varepsilon \frac{\partial E}{\partial t} \qquad [5.6]$$

For a uniform conductivity and permittivity, and considering an oscillating electric field with frequency **f we** can write:

$$E = E_0(r')e^{v*} \qquad [5.7]$$

Differentiating this time varying field gives:

$$\frac{\partial E}{\partial t} = 2\pi i f E_o \varepsilon_r' \varepsilon_o \mu_o = 274 t E \qquad [5.8]$$

meaning that Equation 5.6 reduces to:

$$2\pi f \varepsilon_r \varepsilon_o << 1 \qquad [5.9]$$

in general, MEG studies deal with time varying electromagnetic fields that oscillate at frequencies not greater than 100 Hz. Furthermore, if $\sigma = 0.3 S^{-1} m^{-1}$ and $\varepsilon = 10^5 \varepsilon_0$ (typical values for the human brain [2]) then $\frac{2\pi f \varepsilon_r \varepsilon_o}{\sigma} \pm .10^{-3} << 1$ and therefore the contribution of the time varying electrical field to total current (and hence magnetic field B) can be considered negligible. Similarly, it can be shown that the contribution of time varying magnetic field, $\frac{\partial B}{\partial t}$, to the electric field, E, is also negligible [2] meaning that in the frequency range 0 5. f 5 100 Hz, the quasi-static approximation holds.

In order to show how the quasi-static approximation simplifies the Maxwell equations, consider again Equation 5.1, specifically $\nabla \times E = -\frac{\partial B}{\partial t}$. Under the quasi-static approximation this becomes $\nabla \times E = 0$ since the time varying component of the magnetic field is ignored. Generally it can be shown that the curl of the gradient of any scalar field is zero (Mathematically $\nabla \times (\nabla X) = 0$), and therefore under the quasi-static approximation, the electric field may be written as the gradient of some scalar potential thus:

$$E = -\nabla V \qquad [5.10]$$

The use of the electric scalar potential, V, will considerably simplify all subsequent calculations

5.1.2 The solution to the MEG forward problem

We saw in chapter 4 that two types of current contribute to the MEG signal (see Figure 4.5). Primary currents, **.1^{P}(r'),** flow through the dendrites of active neurons and comprise ion currents caused by the opening and closing of cellular channels in response to some neurochemical stimulation. Volume currents, **J^{v}(e),** represent the return path of these ions within the extra cellular space and are caused by the static electric field between the current source and current sink (the source being the point at which all charges are expelled from the cell). For this reason, when considering the cortical current distribution, one should consider the sum of **J^{P} (r') and J^{v}**

$$\mathbf{J(r')=J^{P}(rs)+J^{v}(r')} \qquad \mathbf{[5.11a]}$$

Since volume currents result from an electric field, this can be re-expressed as:

$$\mathbf{J(r')=J^{P}(r')+cr(r')E(r')} \qquad \mathbf{[511b]}$$

Further, from Equation 5.10 this becomes:

$$\mathbf{J(r')=J^{P}(r')—o^{-}(r')VV(r^{1})} \qquad \mathbf{[5.11c]}$$

The forward problem involves the calculation of the magnetic field distribution, **B(r),** outside the source space (i.e. the head), given a known primary current distribution, **J^{P}(r'),** inside the source space. The solution itself depends on the shape of the source space, the conductivity profile, and the form of the primary current **J^{P}(rs).** For the moment, let us assume that the source space is an arbitrarily shaped volume conductor G with piecewise constant conductivity cY$_{G}$ inside, and **a=** 0 outside. The volume **G** is bounded by some surface **S** representing the edge of the scalp. A solution to the forward problem can be derived based on the Ampere-Laplace law (the continuous counterpart of the Biot Savart Law), which in the quasi-static regime states:

$$\mathbf{B(r)}— \text{'a°} \frac{\mathbf{f.1(r^{1})xR}}{4\text{n-}61 \quad 11R113} \qquad \mathbf{[5.12]}$$

Where **r'** refers to any location within the source space, **G,r** is any point outside G at which the field is calculated, and **R =r —r' .**

From Equation 5.11c we know that the current distribution $J(r')$ is made up of both the primary current $J^P(r')$, and its associated volume current $J^V(r') = -\sigma_G \nabla V(r')$, therefore:

$$B(r) = \frac{\mu_0}{4\pi} \int_{V_G} \left(J^P(r') - \sigma_G \nabla V(r') \right) \times \frac{(r - r')}{|r - r'|^3} dv \qquad [5.13]$$

Which may also be written:

$$B(r) = B^P(r) - \frac{\mu_0}{4\pi} \sigma_G \int_{V_G} \nabla V(r') \times \frac{(r - r')}{|r - r'|^3} dv \qquad [5.14]$$

where

$$B^P(r) = \frac{\mu_0}{4\pi} \int_{V'} J^P(r') \times \frac{(r - r')}{|r - r'|^3} dv' \qquad [5.15]$$

The first term in Equation 5.15 is related only to primary current, and the second only to volume currents. Taking the identity $\nabla \times (V\nabla g) = \nabla V \times \nabla g$ where $\nabla g = \frac{(r - r')}{|r - r'|^3}$, Equation 5.15 becomes:

$$B(r) = B^P(r) - \frac{\mu_0 \sigma_G}{4\pi} \int \nabla V \times \frac{(r - r')}{|r - r'|^3} dv' \qquad [5.16]$$

Using the general expression $\int_V \nabla \times X dv = \int dS \times X$, we find that:

$$B(r) = B^P(r) - \frac{\mu_0 \sigma_G}{4\pi} \int_S V(r') \frac{(r - r')}{|r - r'|^3} \times n(r') dS \qquad [5.17]$$

Where $n(r')$ is the outer unit normal of the surface element dS. Equation 5.17 is known as the Geselowitz formula [2, 4, 5] and is the general solution to the forward problem for a bounded conductor model of arbitrary shape containing some general current distribution. Physically this formula implies that the volume current produces a measurable component of magnetic field equal to that produced by a surface current distribution $-\sigma_G \nabla V(r')$, where r' falls on surface S. Such surface currents are, of course, fictitious, however they do provide an excellent means by which to represent mathematically the volume currents, and is some instances calculate their contribution to the final magnetic field produced.

Now suppose that the bounding surface S is made spherically symmetric with respect to some origin. Using the Geselowitz formula, and taking only the radial component of magnetic field produced we find that:

$$/3,.(r)= B^{P}(r).e_r -^{/11(}L_{4ir}{}^{G} I\ n(e)c/SxV(r^{1})— {}^{R}{}_{3\ r}[5.18]$$

Where **e,** is the unit vector in the radial direction. Since **n(r9=r X,l** and e_r = follows that the integrand tends to zero. Therefore, if a spherically symmetric volume conductor is used as a head model, the radial component of the magnetic field becomes:

$$\mathbf{13,(r)=B^{P}(r).e_r=^{1}\text{-}^{11}5j^{P}(e)x—^{R}.e_r\ dv'}\ [5.19]$$

Meaning that, although other components of **B(r)** contain contribution from the volume currents, the radial component doesn't and since it is the radial component that we detect using the gradiometer set up described in chapter 4 (see also [6]), this use of a spherical conductor model can significantly simplify the forward solution. Of course in reality, the head is not a perfectly spherically symmetric conductor, and realistic head models can be applied using and numerical solutions for **B,.(r)** derived and include the contribution from volume currents. However it can be shown that in most cases, a multi-sphere head model (i.e. a model consisting of a single best fitting sphere for each MEG sensor) is easier to implement, and in most cases just as good [7].

Having eliminated volume currents from our forward solution only one problem remains, namely that of defining a realistic primary current distribution and in both EEG and MEG, primary current is often approximated to a current dipole, a unidirectional current at a point source, equivalent to a primary current that may extend over a few square mm of the cortex (see also chapter 4). Mathematically we represent a current dipole as:

$$\mathbf{J^{P}(E)=Qa(rs–r_Q)} \qquad [5.20]$$

Where **Q** represents the dipole moment (both strength and direction) and **5(e–r_Q)** represents a unit response at position $\mathbf{r_Q}$ i.e. the delta function. It may be convenient to think of **Q** as aline element of current pumped from source at $\mathbf{r_i}$ to sink at **r2** where **ri** and

r2 are in very close proximity. Using the dipole approximation we first note that outside the volume G, the total current $J = 0$, and therefore according to the Maxwell equations (see Equation 5.2) V x B = 0 and the magnetic field outside G can' be represented as the divergence of a scalar magnetic potential U thus:

$$B(r)\_ -p_0 VU(r) \qquad [5.21]$$

In order to find an expression for U, we fix r outside G and consider a line integral along the radius $r + te$, for 0 5 t co [5]. Because U vanishes at infinity we obtain:

$$\begin{aligned} U(r) &= -1VU(r + te_r)e, dt \\ &= \frac{1}{Po}\int_0 IB,,(r+te_r)dt \\ &= \frac{1}{0}\text{-}1B^{(p)}(r+te_r).e_r dt\, Po \\ &= \frac{1}{zt} z\, Qx(r \qquad \frac{dt}{olr+te,-r_e 1^3} \end{aligned} \qquad [5.22]$$

Where we have used Equations 5.15, 5.19 and 5.20 in order to derive the final line of Equation 5.22. The final integral can be calculated to show that [5]:

$$U(r) - \frac{1\, Qxr.r_e}{4ff\ F} \qquad [5.23]$$

Where:

$$F = \text{Ir} - r_Q\text{I} \qquad - r_e\,\text{I} + \text{Ir1}^2 - r_e r) \qquad [5.24]$$

Now, applying Equation 5.21 to Equations 5.23 and 5.24 it can be shown that:

$$B(r) = {}_4F_2\ (FQxr_n - Qxr_n.rVF) \qquad [5.25]$$

Where [5]:

$$VF - \frac{\text{Ir} - \text{ral2} +}{\text{Id}} \frac{(r - r_e)r}{\text{Ir} - r_g\,\text{I}} + 21\text{r}\ r_o\,\text{I} + 214\,[\text{Ir}\ r_o 1 + 21\text{r1} + \frac{(r - re)r}{\text{Ir} - r_a\,\text{I}}, \overline{\qquad} i_{re} \qquad [5.26]$$

The above solution to the forward problem is equivalent to that originally published by Sarvas et al (1987) [5]. Other, equivalent derivations have been made by Grynszpan and Geselowitz (1973) [8] and Ilmoniemi [9], however it is the Sarvas equation (5.26) that is

used as a forward problem solution for work presented here. Equations 5.24, 5.25, and 5.26 were implemented in MATLAB and are used in subsequent forward solution calculations for both simulation and lead fields.

5.2 THE INVERSE PROBLEM

The neuromagnetic inverse problem states [2, 5]: Given a known distribution of magnetic field outside the head, can we calculate the current density distribution inside the head? This is an ill-defined problem in physics because due to field cancellation effects, any single measured magnetic field distribution could be caused by an infinite number of current distributions in the brain. Despite the difficulties, several methods have been proposed to solve the neuromagnetic inverse problem, all of which make assumptions on the type of current distribution observed. The most common assumption is that an area of active cortex can be modelled by an equivalent current dipole (as described above). Generally this assumption is reasonable given that the active area is small when compared to the distance from which it is observed. Beyond this, each of the inverse problem solutions has its own unique assumption set, which must be understood if that solution is to be applied successfully. It is beyond the scope of this chapter to mention explicitly all of the inverse problem solutions, and for an excellent review, the reader is referred to Baillet **et al.,** (2001) [10]. Here, three of the most successful inverse solutions are briefly discussed.

The oldest, and simplest inverse problem solution in MEG is known as dipole fitting [11]. Here, a dipole is placed in the source space and an iterative algorithm allows that dipole to shift in position, orientation and magnitude. On each iteration, the resulting magnetic field is calculated using the forward solution and compared to the actual field measured. Optimal solutions are derived based on a minimisation of the difference between the measured and modelled fields. The major assumption is that the number of active neuronal sources is small, and known a-priori, meaning that this model becomes more realistic when dipole fitting is applied over small time windows. (Typically one attempts to explain activity in small —10 ms blocks during which only one or two dipoles are assumed to be active.)

In minimum norm estimation [2, 12], the assumption is that the source configuration with the least energy that also minimises the differences between the measured and estimated fields accounts for the recorded data. Such algorithms suffer because these source configurations must always exist in the most superficial layer of cortex, meaning that an arbitrary depth weighting must be factored in (weighted minimum norm estimation). A number of techniques by which to do this have been proposed, [2] including one in which a depth bias is introduced based on active locations derived from fMRI data. The problem with this approach is that it necessarily assumes a linear relationship between the effects measured in MEG and those measured in fMRI, which may not be the case in general.

A third inverse problem solution is known as the MEG beamformer [13]. The beamformer effectively represents a special case of the weighted minimum norm approach, where the weighting is applied based on the assumption that timecourses of neuronal sources remain uncorrelated for the duration over which the fit occurs. Unlike dipole fitting and minimum norm, which have been used mainly to explain field patterns measured during a short time window in averaged responses, beamformers have been most successful in identifying induced changes in cortical oscillatory power. Since these induced changes occur on a longer time scale, this means that beamformers perform better in blocked experimental designs, making them ideal for use in stimulus paradigms similar to those used in fMRI. In the next section, the mathematical principles behind the beamformer approach are put forward and its solution is derived.

5.2.1 Lead Fields

The lead field is derived from the solution to the forward problem (see Equation 5.26), and describes the sensitivity of the i^{th} MEG sensor to a current distribution at position **r'** in the brain. If **b**, is the output of the i^{th} MEG sensor then the lead field /$_i$(r') must satisfy the equation:

$$b_i = 11_i(\mathbf{r}').\mathbf{J}(\mathbf{r}')\mathbf{dv} \qquad [5.27]$$

For a simple dipolar current distribution in a spherical head model this simplifies to give:

$$\mathbf{Q},\mathbf{r}_0)=\mathbf{1}_;(\mathbf{r}_o).\mathbf{Q} \qquad [5.28]$$

Thus under these assumptions, the lead field is readily obtained from Equation 5.26 and a knowledge of the geometry of he MEG system.

5.2.2 The Linearly Constrained Minimum Variance Beamformer Problem

The dipolar source strength (or dipole moment) at any position in the brain can be written as a three-component vector $\mathbf{Q(r_{i2})}$ In the MEG beamformer approach [13], the idea is to approximate that dipolar source strength to $\mathbf{6(r_{(2)})}$ using a weighted sum of the magnetic field measurements at each of the **N** MEG sensors i.e.

$$\mathbf{Q(r')=W^T(r')x(t)} \qquad [5.29]$$

Where W is the **N x** 3 weights matrix and x(t) is the **N** — dimensional vector of field measurements at each of the MEG sensors taken at time t.

Ideally, it would be possible to define the matrix W such that:

$$\mathbf{W^T(r_o)L(r')=} \begin{cases} \mathbf{I \ if \ ' = _o} \\ \mathbf{0 \ if \ r' \ r \ ro} \end{cases} \mathbf{r} \qquad [5.30]$$

Where the matrix **L(r')** is the **(N x 3)** matrix of lead fields formulated using Equations 5.26 and 5.28. The first column of LW) represents the detectable magnetic field strength b_i at each of the MEG sensors due to a current dipole at position **(r')** having unit moment in the z direction, and zero moment in the 9 and i directions. Similarly, the second and third columns represent the fields created by unit dipoles in the 9' and directions respectively. For a situation in which the columns of **W(r'),** and $\mathbf{W(r_o)}$ are

linearly independent, it is possible to solve Equation 5.30 mathematically. However for an experimental situation, this will not be the case, and one must derive a solution for 1V(r') that is in some way optimal. Using the Linearly Constrained Minimum Variance (LCMV) beamformer [13], this optimisation is achieved by the minimisation of the variance of **6(r')** subject to the linear constraint that:

$$\mathbf{W(r_o)L(r_o)=I} \qquad [5.31]$$

This linear constraint ensures that the energy originating from the source position remains in the estimate whilst the minimisation suppresses energy from all other locations in the brain. Furthermore, the LCMV technique forces the suppression of energy from position r' only if there is significant energy originating there. The unity passband ensures the estimate $afr_0)$ is the optimal estimate of dipole moment magnitude.

Mathematically, the LCMV beamformer problem can be posed as:

$$\min_{WOO} tr[C(Q(r_0))] \text{ subject to } W^T (1._0)1-(r_o) = I \quad [5.32]$$

Where $C(Q())$ represents the $3 x 3$ covariance matrix of the dipolar source.

Substituting for $C(Q(r_o))$ in Equation 5.32 we obtain:

$$\min_{WOO} triw^T (r_0)C(x)W(r_o subject \text{ to } W^T (r_0)1,(r_0) = I \quad [5.33]$$

Which represents the final mathematical formulation of the LCMV beamformer problem and can be solved using the method of Lagrange multipliers. The quantity $W^T(r_o)C(x)W(r_o) = {}^T(r_{t2})xr$ and can be thought to represent source power at any given time. Hence physically, the LCMV technique can be thought of as an energy minimisation.

5.2.3 Solution to the L.C.M.V. Beamformer Problem

As stated above, the LCMV beamformer problem is solved using the method of Lagrange multipliers, the derivation of the solution is given below but for clarity, both the location subscripts and the matrix notation are omitted. A Lagrangian, $F(W,M)$, is obtained by multiplication of the linear constraint by the Lagrange multiplier M thus:

$$F = t \quad CW AW^T L\text{-}112M1 = trtW^T CW + \text{IV } L — IJM + [W^T L\text{-}1]1111 \quad [5.34]$$

Since $(AB)^T = B^T A^T$ we can write that:

$$\text{alV}^T L\text{-}414 = M^T [\text{wr L- If} = \text{mr}[\text{ew-I}] \quad \textbf{[5.35]}$$

and since $tr(A) = tr(A^T)$, the matrix Equation 5.34 can be rewritten:

$$F = trIW^T CW + [W^T L\text{-}1141 + M^r [LW^T \quad [5.36]$$

It is then simple to show that Equation 5.36 is equivalent to the perfect square in W :

$$F\ tr\,i_W r_{m\,c} - Iy(W + c - i_{im})_{m\ m} T_{mTLT\ c\text{-}I\ Lm} \quad [5.37]$$

In Equation 5.37, the only term dependent on W is the first, and therefore we can minimise the Lagrangian by setting this term to zero, thus:

$$W + C^{-1}LM = 0 \text{ or } W = -C^{A}LM \quad [5.38]$$

We can now solve for the Lagrange multiplier matrix by substituting for W in the linear constraint:

$$wT1 = 1 \quad [5.39]$$

Where $W = -C^{A}LM$ and therefore $W^{T} = -'LIVT$ c-i).

It therefore follows that:

$$-M^{T}L^{T}(C^{A})L = / \quad [5.40]$$

Thus solving for the Lagrangian

$$MT = \_[LT\ (cr - 1)Lr \quad [5.41]$$

and since $W^{T} = -M^{T}L^{T}G^{A}$:

$$_{w}r_{(r,\ )} = [e_{(r,} \quad {}^{1}(x).1.(e)re(r')C^{1}(x) \quad [5.42]$$

Giving us our final solution for the weights vector [13]. The power of the beamformer technique now becomes clear. Under the quasi-static approximation, using a spherical head model of uniform conductivity and approximating cortical current flow to a dipole, it is possible to reconstruct an estimate of the three-dimensional dipolar source strength for any position within the brain using Equation 5.29. The accuracy of these estimates depends largely on the signal to noise ratio of the MEG data, since the beamformer weights matrix depends wholly on the data covariance (see Equation 5.42).

Equation 5.42 and the above derivation represent the general solution to the 'Linear' Beamformer. That is to say, the approximation takes into account a three component dipole moment $Q(r_Q)$ having components in the 1, ji and z directions. However, the beamformer solution simplifies when we take into account the fact that MEG is insensitive to radial dipoles and so it would be equally possible to derive an accurate

solution using only a two-component dipole moment $\mathbf{Q(r_Q)}$ where both components have directions in a plane tangential to the radial direction. This simplifies even further if we consider a single dipole moment direction. The dipole is centred on position $\mathbf{r_o}$, and its orientation rotated in the tangential plane to find some optimum direction (defined by the maximum in the projected power estimate). This is known as the `non-linear beamformer' or (since the idea of a 'non-linear linearly constrained minimum variance beamformer' sounds a little counter intuitive!) Synthetic Aperture Magnetometry (SAM) [14] and has been applied uniquely to MEG data (although a 3-dimensional non-linear optimisation could be applied in EEG). The equation for the beamformer solution becomes:

$$\mathbf{W^T(r')=[12(r')C\text{-}1(x)L(r')1^1 L^T(r')}\,)C^{-1}(\,x\,) \quad [5.43]$$

Where the weights matrix has now become a weights vector, as has the lead fields since only one source orientation is considered. Further, the source strength estimate may now be written:

$$\boldsymbol{y_e(t)=W_e^r(r')x(t)} \quad [5.44]$$

Giving a scalar estimate of source strength at time t for location $\mathbf{r'}$ **.** The location index within the source space is now written as the subscript **8** and must comprise both the three-component position vector $\mathbf{r_o}$, and an angle giving orientation of the dipole in the plane tangential to the radial direction. By applying Equation 5.44 sequentially to each instantaneous magnetic field measurement, a timecourse of source strength (known as a virtual electrode (VE) [14]) can be formulated. Equation 5.44 is summarised schematically in Figure 5.1:

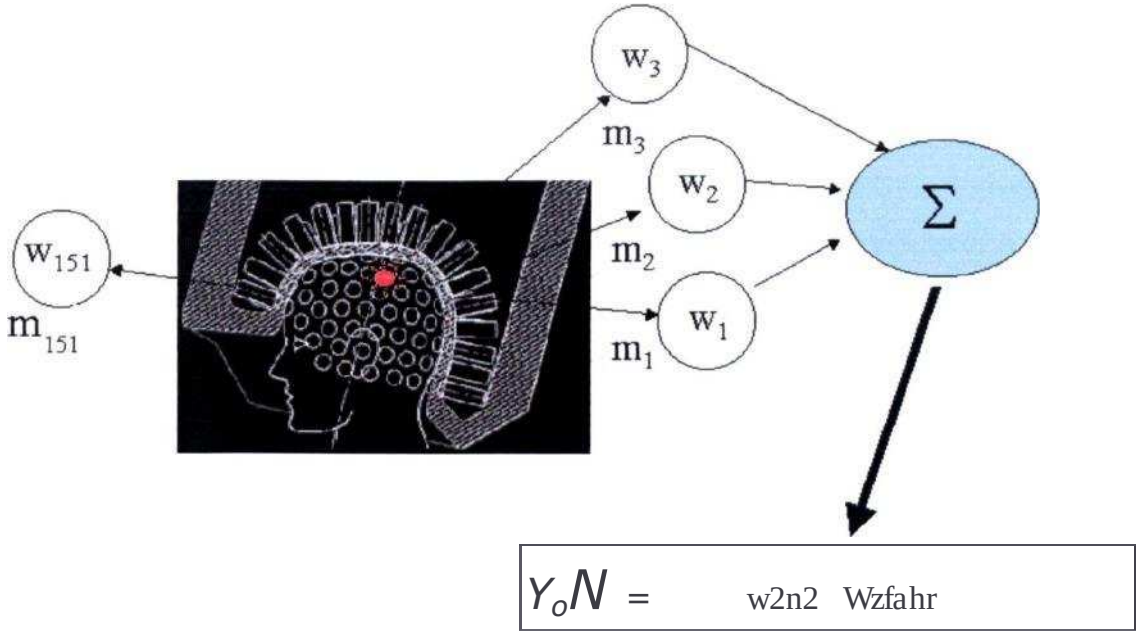

Figure 5.1: A schematic representation of the non-linear beamformer. The magnetic field measurement at each MEG sensor is multiplied by a weighting parameter in order to derive an estimate of source strength for some chosen location in the brain.

It should be noted from Equation 5.44 that the only factors allowed to bias the beamformer solution are i) the data (manifested as the data covariance matrix C(x)) and ii) the lead field, itself based on the forward solution and hence the volume conductor model, current dipole and quasi-static approximations. Only if all of these approximations hold will the beamformer yield a correct solution. Further, the beamformer suffers one other major limitation: namely that separate, yet temporally covariant sources will be suppressed. The reason for this is that if two separate sources are correlated in time, the lead fields vectors corresponding to the 2 sources will add. The vector sum will be different from each constituent lead field and in fact, may not even correspond to the lead field for any single source within the brain. Power minimisation subject to the unity passband (i.e. Equation 5.33) for any selected position in source space will then cause this vector sum to be rejected, because it does not match the lead field vector expected from that position. This may go on to cause source suppression if (and only if) the two sources are correlated temporally. However, perfect correlation between

sources is unlikely because both source noise and sensor (SQUID) noise will tend to eliminate it. Further it has been shown [13] that a correlation of 0.7 is required to cause complete source suppression, which is unlikely given the SNR of MEG, and given the fact that in beamformer approaches long time windows are generally employed. A great deal of evidence now exists suggesting that the beamformer approach to the MEG inverse problem can lead to accurate reconstruction of neuronal current sources [15-41].

5.2.4 The Hilbert Transform

As described in chapter 4, a number of heterogeneous neuromagnetic effects are detectable in MEG and these effects are found to differ temporally. The beamformer allows us to project this temporal information back into the source space, such that neuromagnetic effects are observable in virtual electrode traces. Further, the source strength can be expressed in terms of an accurate dipole strength, not the magnetic field measured. However, some method by which to identify the time-frequency signatures of various neuromagnetic effects, and characterise their spatial distribution is still required.

A similar problem has been previously identified and solved in functional magnetic resonance **imaging** and the most generally applicable method is the General Linear Model (GLM) [42]. The GLM allows its user to model temporal effects of interest that may occur in raw data. By doing this at each virtual electrode within the source space, the spatial distribution of such effects may be obtained. So, for example, if a sustained field effect was expected, one could model this as a Top-Hat function defined mathematically as:

$$f(t)=\begin{cases} 0 & \text{if} \quad t-A<-/2 \\ 1 & \text{if} \quad -{}^{1}/_{2}\,.t-A5{}^{1}/_{2} \\ 0 & \text{if} \quad t\_A>y\,2 \end{cases} \qquad [5.45]$$

where /represents the width of the Top-Hat in time and A represents its temporal offset. The GLM allows the calculation of some statistical parameter to be defined showing the presence or absence of the top hat at each virtual electrode placed in source space. By plotting this parameter as a function of position, a statistical parametric map (SPM) can be obtained. The application of the GLM to model sustained neuromagnetic effects is

therefore clear, however, the application of the GLM to model effects at higher frequency (i.e. ERD and/or ERS) is somewhat less obvious. Since change in oscillatory power is generally time locked but not phase locked to an applied stimulus [43], it is difficult to model measured oscillatory behaviour in a virtual electrode using the GLM. Such non-phase locked effects are far more suited to short term Fourier and wavelet analyses (see Nikouline et al. 2000 [44] or Furlong et al 2004 [40] for examples). However, it is possible to use the GLM to model temporal modulation in oscillatory power in a frequency band of interest, the problem then being to ascertain an envelope of this modulation from the virtual electrode trace. For simple cases, this could be achieved by percentage synchronization and desynchronisation calculations (See Pfurtschellar and Lopes Da Silva, 1999 [43]), however a more temporally resolved method of detecting such changes involves the use of the continuous Hilbert transform. The continuous Hilbert transform [45, 46] and associated analytic signal have previously been used to describe cortical synchronization and desynchronisation in EEG [47] and in other related areas [48]. Computation of the analytic signal for any given oscillatory signal will yield the envelope of the oscillatory activity. Such an envelope can then be modelled using the GLM.

We represent the timecourse of a single virtual electrode by $_{ye}$ (t). The corresponding analytic signal $z_0(t)$ is given by [46]:

$$z_e(t) = y_a + iH(y_a(t)) \qquad [5.46]$$

where $H(y_e(t))$ represents the Hilbert transform of $_{y9}$ (t) and is given by:

$$H[y_a(t)] = {}^{1} \text{ f } Y'^{2}L^{i)}\text{- du}] \qquad [5.47]$$

$$t—u$$

P denotes the Cauchy principal value of the integral and is used to take account of the singularity at t = u. This integral effectively represents a convolution of $y_e(t)$ with X_n, .

If $F(y_e(t))$ denotes the Fourier transform of $y_e(t)$, and $F(z_0(0)$ denotes the Fourier transform of z_a (t), then

$$F(z_a(t)) = F(y_e(t)) + iF(H(y_e(t))) \qquad [5.48]$$

Expressing $H(y_o(t))$ as a convolution:

$$F(z_o(t)) = F(y_{o(t)}) + iF(y_o(t)0) \qquad [5.49]$$

The Fourier transform of y is $-i\,\mathrm{sgn}(w)$, where $\mathrm{sgn}(w) = \begin{cases} 1 & \text{if } co > 0 \\ 0 & \text{if } (0 = 0, \text{ thus:} \\ -1 & \text{if } w < 0 \end{cases}$

$$F(z_o(t)) = F(ye^{(t))\{1} + \mathrm{sgn}(^0))\} \qquad [5.50]$$

and so

$$F(z_o(0) = \begin{cases} 2F(y_o(t)) & \text{if } co > 0 \\ F(y_e(t)) & \text{if } co = 0 \\ 0 & \text{of } co < 0 \end{cases} \qquad [5.51]$$

The analytic signal may be obtained by inverse Fourier transformation of Equation 5.51. The magnitude of the analytic signal is defined in Equation 5.52, and gives the envelope of the measured activity in $y_e(t)$:

$$E(Y = 11(Y\,0(0)^2 + (Y(0))^2 \qquad [5.52]$$

In general, a single virtual electrode trace y_e (now written as a vector time course) may contain any number of independent oscillatory signals in various frequency bands (alpha, beta, etc.), each modulated in a different way. The application of a band pass filter, followed by envelope detection using the Hilbert transform will yield an envelope showing this modulation of oscillatory power in the frequency band selected by the band pass filter. This low frequency envelope can then be mapped spatially using the GLM. Thus, in this context, the Hilbert transform can be thought of as a mathematical tool to convert oscillatory activity into a simple sustained effect such that it can be modelled using the GLM.

5.2.5 The General Linear Model

The GLM itself is to be based on that described by Worsley and Friston (1995) [42] which has been commonly used in fMRI analysis. When applied to the envelope of any one virtual electrode trace $E(y_0)$ it states:

$$\mathbf{E}(\mathbf{y_e}) = \mathbf{G}\mathbf{1}\mathbf{1}_0 + \mathbf{e_0} \qquad [5.53]$$

Where **G** is the design matrix, which contains a single column for each temporal effect modelled. These effects can include expected temporal modulation of a frequency band of interest as well as any predictable confounding effects. The vector $/3_8$ comprises a single parameter representing the magnitude of each of the modelled effects. The vector $\mathbf{e_e}$ represents deviations from the model caused by scanner and/or physiological noise that cannot be incorporated into the model (i.e. random noise). In the special case of the effect of interest being a sustained field and not an oscillatory response, the application of the Hilbert transform is irrelevant and $\mathbf{E}(\mathbf{y_e})$ in Equation 5.53 and all subsequent equations should be replaced with y_o.

In using the GLM it is assumed that elements of $\mathbf{e_e}$ are unbiased, have constant variance, are uncorrelated and follow a Gaussian distribution (Seber 1977). However, confounding effects may exist in MEG data that do not meet with these assumptions. These confounding effects comprise aspects of spontaneous brain activity that can cause noise autocorrelation after projection through the beamformer. Common MEG artefacts such as eye blinks, cardiovascular, respiration and muscular effects from the body as well as noise from the local environment, should be suppressed by the beamformer, since they do not originate from the source space. However, some of these effects may leak through the spatial filter, again causing autocorrelation in virtual electrode data. Such effects cause the elements of the vector $\mathbf{e_e}$ to become correlated such that application of the GLM becomes impractical. This problem has again been identified and solved in fMRI, the simplest solution involving application of a temporal smoothing kernel [42]. In general, temporal autocorrelation is not thought to be as great a problem in MEG as in fMRI, as MEG provides a direct measure of neural activity. However, application of a temporal filter to MEG data produces a known autocorrelation and hence allows for the accurate prediction of the degrees of freedom in the smoothed $\mathbf{E}(\mathbf{y_e})$. This is a great advantage, particularly in the spatial characterization of low frequency effects, as it enables calculation of the statistical quantities associated with the GLM.

In order to perform temporal smoothing, a Gaussian smoothing kernel was designed of the form:

$$F(t) = \frac{1}{\sigma\sqrt{2\pi}} e^{-\frac{t^2}{2\sigma^2}}$$

Where a represents the width of the smoothing kernel and is chosen based on the temporal scale of the modelled effects. It can be thought of as a low pass filter but in the GLM is applied as a convolution in time using a convolution matrix $\boldsymbol{K}$, whose rows represent temporally shifted versions of the smoothing kernel (Equation 5.54). After filtering, Equation 5.53 becomes:

$$\boldsymbol{KE(y_e) = G^* \beta_e + e_e} \qquad [5.55]$$

Where $\boldsymbol{G^* = KG}$ and represents the smoothed design matrix. $\boldsymbol{e_e = Ke_e}$ and represents the residual error between the model and the smoothed data. The GLM can now be applied as described in [42], in order to compute $\boldsymbol{b_e}$, an estimator of β_e where:

$$\boldsymbol{b_e = (G^{*T} G^{*})^{-1} G^{*T} KE(y_e)} \qquad [5.56]$$

The appropriate parameter in vector $\boldsymbol{b_e}$ is used, together with its associated variance [49], to produce a single T-statistic for each voxel. So for example, if we wish to spatially map the effect modelled by the i^{th} column of the design matrix then

$$\boldsymbol{T = \frac{b_e(i)}{\sqrt{var(b_e(i))}}} \qquad [5.57]$$

where

$$\boldsymbol{var b_e = c \cdot \sigma_e^2 (G^{*T} G^{*})^{-1} G^{*T} V G^{*} (G^{*T} G^{*})^{-1}} \qquad [5.58]$$

if $V = \boldsymbol{KIC^T}$ and

$$\boldsymbol{\hat{a}_e = \frac{r_e^T}{\sqrt{trace(RV)\, RV}}} \qquad [5.59]$$

where $r_e = \boldsymbol{RKE(y_e)}$ is a vector of residuals derived using the residual forming matrix $\boldsymbol{R = I - G^{*} (G^{*T} G^{*})^{-1} G^{*T}}$ and I is the identity matrix. (For a complete description of this method see [42]). T-scores, calculated using Equation 5.57 can indicate the presence or absence of any effect encompassed within the design matrix. By applying this

technique to all virtual electrodes in the volume of interest, a statistical parametric map can be made showing the spatial distribution of the effect modelled. Furthermore, these maps can be thresholded based on a p-value calculated using the degrees of freedom, which in turn is derived from the smoothing filter [42].

5.2.6 Summary

In short, the GLM-beamformer technique combines the non-linear MEG beamformer with the mathematics of the Hilbert transform and the general linear model to develop a novel method with which to derive statistical parametric maps showing the spatial localisation of neuromagnetic effects. The above theory suggests that this technique should locate accurately both low and high frequency neuromagnetic effects detectable in MEG. In addition, it provides a useful mathematical framework for the analysis of MEG data and its comparison with BOLD fMRI, since the implementation of the GLM for MEG is statistically equivalent to that used in fMRI

5.3 GLM-BEAMFORMER APPLIED TO SIMULATIONS

Having developed the theory of the GLM-beamformer technique, what follows is the first proof of principle study.

5.3.1 Simulation of data

Initially, simulated data were used to examine the accuracy of the GLM-beamformer technique. For all simulations, the third order gradiometer configuration of a 151 channel Omega system (CTF Systems Inc., Port Coquitlam, Canada) was used. The source space was based on a subject's head shape measured from a high resolution anatomical MRI scan (MPRAGE sequence at 1.5 T with a 256x256x180 matrix size and a 1 mm isotropic resolution). Two separate sources were positioned on the cortical surface, which had also been extracted from a subject's anatomical MRI. The orientation of each source was defined to be perpendicular to the local cortical surface; positions were chosen pseudo-randomly and independently and are shown in Figure 5.3A. The sources were dipolar, of **strength 2 nAm, with additive uncorrelated noise** of amplitude 1 nAm. For the solution to the forward problem, the best fitting sphere to the subject's head shape was used as a

volume conductor model. The forward solution itself was based on the derivation by Sarvas (see section 5.1 or [5]). Ten epochs of data were created for both sources, each epoch being 2 s long, and comprising 0.5 s baseline followed by 1.1 s activation and a further 0.4 s baseline. The first source was a Top-Hat function (see Equation 5.45 where for a single epoch r =1.1s and A =1.05s). The second source was a sinusoid of 20 Hz, modulated by a Top-Hat function (where again for a single epoch r =1.1s and A =1.05s). White noise was added to the simulated data at each MEG sensor with a r.m.s. amplitude of 90 fT (10fT / 41^{7}1i with a 81Hz bandwidth). The first source (the Top-Hat function) was intended to represent a time and phase locked sustained field response, similar to those reported previously [50, 51]. The second (sinusoidal) source represented a time locked but non-phase-locked event related synchronisation at 20 Hz, and was intended to be similar to those effects previously observed by Singh et al (for example) [32].

5.3.2 The Covariance Window and Band Pass Filtering

The application of the GLM-beamformer method requires the choice of a time-frequency covariance window C(**x)** over which the weight vectors are calculated (see Equation

- 5.43). The use of a large covariance window is advantageous since it minimizes the problem of suppression of correlated sources commonly associated with beamformer techniques [13, 52] (because the sources are less likely to remain correlated over a larger temporal window). For this reason weight vectors should ideally be calculated over a covariance window encompassing all time samples and as large a frequency window as possible. The choice of covariance window should not be confused with the choice of frequency band over which the Hilbert transform and GLM are applied. Choice of this second window can be made based on the expected activation (i.e. for experimental data one may choose the alpha band, beta band and so on). In practice the choice of frequency band used in the covariance window and the band pass filter should be matched. This is so that the r.m.s. noise levels are consistent for both the calculation of the weights vector, and application of the GLM. This has the unfortunate effect of narrowing the covariance window (in frequency) and increasing the risk of suppression of correlated sources, thus effectively introducing a trade off between frequency sensitivity and source suppression.

However, since the covariance window still encompasses all time samples, source correlation is minimized and is thus not thought to represent a major limitation to the method. The choice of pass band is trivial for simulated data since both sources lie at known frequencies. Two frequency bands were used for both the covariance window and band pass filter (0-2 Hz and 18-22 Hz), each encompassing a single source. The detection algorithm is described below and shown schematically in Figure 5.2.

5.3.3 Source Detection

The source space was divided into a regular 3D cubic grid of 0.5 cm side length (see Figure 5.2A). A non-linear beamformer using optimal source orientation (in the tangential plane) was used to create the lead field for each position in the source space. These lead fields were then used together with the MEG data, filtered using the covariance window, in the calculation of the weight vectors W_e . The best fitting sphere to the subject's head shape (defined using the anatomical MRI) was used as a volume conductor model in the forward solution in order to be consistent with the data simulation.

After calculation of the weight vectors, the raw MEG data were band pass filtered using a second order Butterworth filter to retain only the frequency band of interest (Figure 5.2B). Note that, to save computational time, this can be done prior to the construction of virtual electrodes since it is a linear operation, as is the projection of data through the weight vectors. The choice of the filter itself is not critical; a simple band pass filter can be used although ringing may be a problem for narrow pass bands. The calculated weight vectors were used to construct a set of virtual electrodes (Figure 5.2C), one for each voxel in the source space. For the oscillatory (20Hz) signal, the magnitude of the analytic signal, defined using the Hilbert transform, was taken for each virtual electrode and used to give the envelope of observed oscillatory activity in the frequency band of interest (Figure 5.2D). For the case of our sustained field (Top-Hat function) the application of the Hilbert transform was not necessary and so was omitted. The convolution matrix was then applied **(a** = 0.3 s) as per Equation 5.54 in order to smooth temporally the Hilbert transformed data in the case of the 20Hz source, and the virtual electrode data in the case

of the sustained field (Figure 5.2E). A design matrix was constructed with the effect of interest modelled by a simple Top-Hat function (identical to that used for simulation of the Top-Hat source) and smoothed as per the filter in Equation 5.45. The design matrix was fitted to the Hilbert transformed data (in the case of the 20Hz source) and the raw virtual electrode data (in the case of the sustained field) (Figure 5.2F) Volumetric images of T-scores were determined as per Equation 5.57, and thresholded for display at an uncorrected p-value of 0.001.

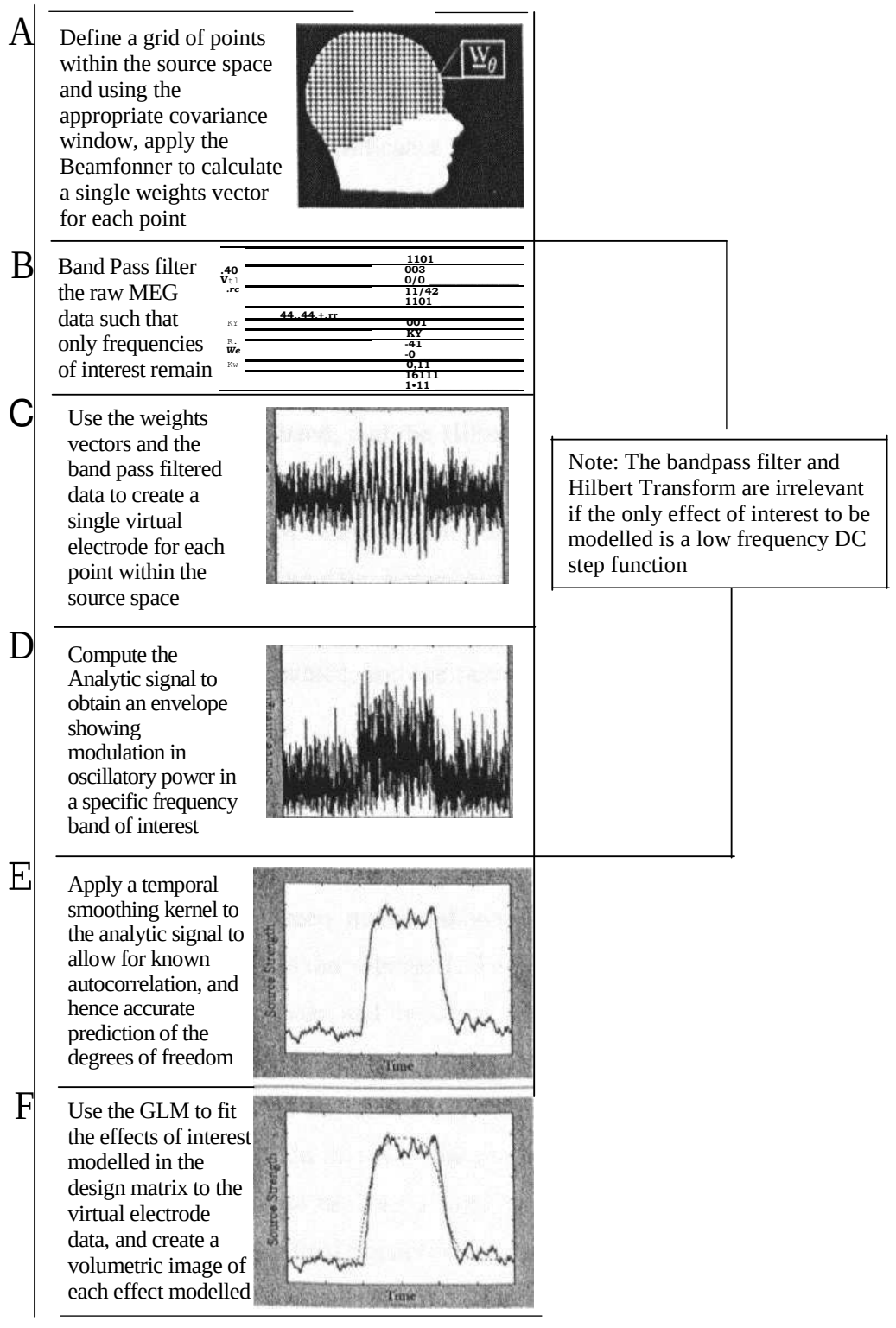

Fig 5.2: Schematic showing the steps involved in the GLM-beamformer methodology.

5.3.4 Statistical Testing of the GLM-Beamformer Method

To demonstrate that the GLM-beamformer technique results in a statistically valid test (i.e. given the case where no signal is present at a virtual electrode, the false positive rate is equal to or below the chosen significance level over many realizations) a Monte-Carlo simulation was used. For 10 different p-values (0.01 through **0.1** in steps of 0.01) 1000 virtual electrodes consisting of Gaussian random data were modelled. Since the projection of raw MEG data through the weights vector is linear, this is equivalent to creating 1000 sets of raw MEG data and projecting through the same weights vector. Each modelled virtual electrode was band pass filtered using a 2" order Butterworth filter with an 18-22Hz pass band, and the Hilbert transform was then taken in order to obtain the analytic signal, which was smoothed using a Gaussian temporal smoothing kernel **(Q = 0.3). The GLM** was used to fit a Top-Hat function to the filtered, transformed, smoothed, random data. For each of the 1000 iterations of this process, the total number of resulting T-statistics that corresponded to a p-value equal to or less than the selected threshold was counted, and the percentage of false positives plotted against the p-threshold.

5.3.5 Results **of the simulations — Source localisation**

Figure 5.3B shows the localization of the simulated DC source using the GLM-beamformer method. The green marker shows the original position of the Top-Hat source. The red overlay shows the volumetric T-statistic image. The discrepancy between the peak of the volumetric image and the actual source position was found to be 9.7 ± 5 mm. Figure 5.3C shows the localization of the 20 Hz source. Again the green marker shows the position of the 20 Hz source and the red overlay shows the corresponding volumetric T-statistic image. In this case, the discrepancy between the peak position and the actual source was found to be 3.4 ± 5 mm. To determine the size of the localization errors with respect to the maximal possible resolution of the beamformer (for this dataset) the intrinsic smoothness of the beamformer due to the correlations between neighbouring weight vectors was assessed [52]. We found the FWHM of the DC and 20 Hz peaks to be **27.0** mm and 13.8 mm respectively. These values are determined purely by the weights (and hence data covariance) and are independent of any subsequent GLM statistical

manipulation. This implies that the discrepancies observed between simulated and reconstructed source locations are of the same order as the intrinsic image smoothness in these regions. Judicious selection of the width of both covariance and band pass filter windows would enable these errors in peak location to be reduced.

Figure 5.4 compares the simulated sources and the time courses of the virtual electrodes corresponding to the maxima of the volumetric T-statistic images. Figure 5.4A shows the simulated Top-Hat source timecourse averaged across all 10 trials; Figure 5.4B shows the associated virtual electrode timecourse, again averaged across trials. Figure 5.4C gives the average timecourse of the envelope of the simulated 20 Hz source and Figure 5.4D shows the associated envelope of the 15-25 Hz virtual electrode signal. The envelopes for both the simulated source (Figure 5.4C) and virtual electrode (Figure 5.4D) were obtained by band pass filtering the associated timecourse (15-25Hz using a second order Butterworth filter) and computing the trial averaged analytic signal. Note that the raw 20Hz signal cannot be shown as it is non-phase locked, and thus cannot be averaged across trials. (The noise added to the simulated data is such that the 20Hz carrier is not visible in a single trial.) These plots show the strong temporal agreement between the simulated dipole timecourses and the virtual electrode trace obtained using the GLM-beamformer.

Figure 5.5 shows the result of the Monte-Carlo simulations. The data points show the relationship between the percentage of false positives and p-threshold, derived from the Monte-Carlo simulations. The solid line shows the theoretically expected relationship. There is good agreement between the theoretical and experimental results (given the limitations of the Monte-Carlo test) implying that the GLM-beamformer method can provide accurate and valid statistical results.

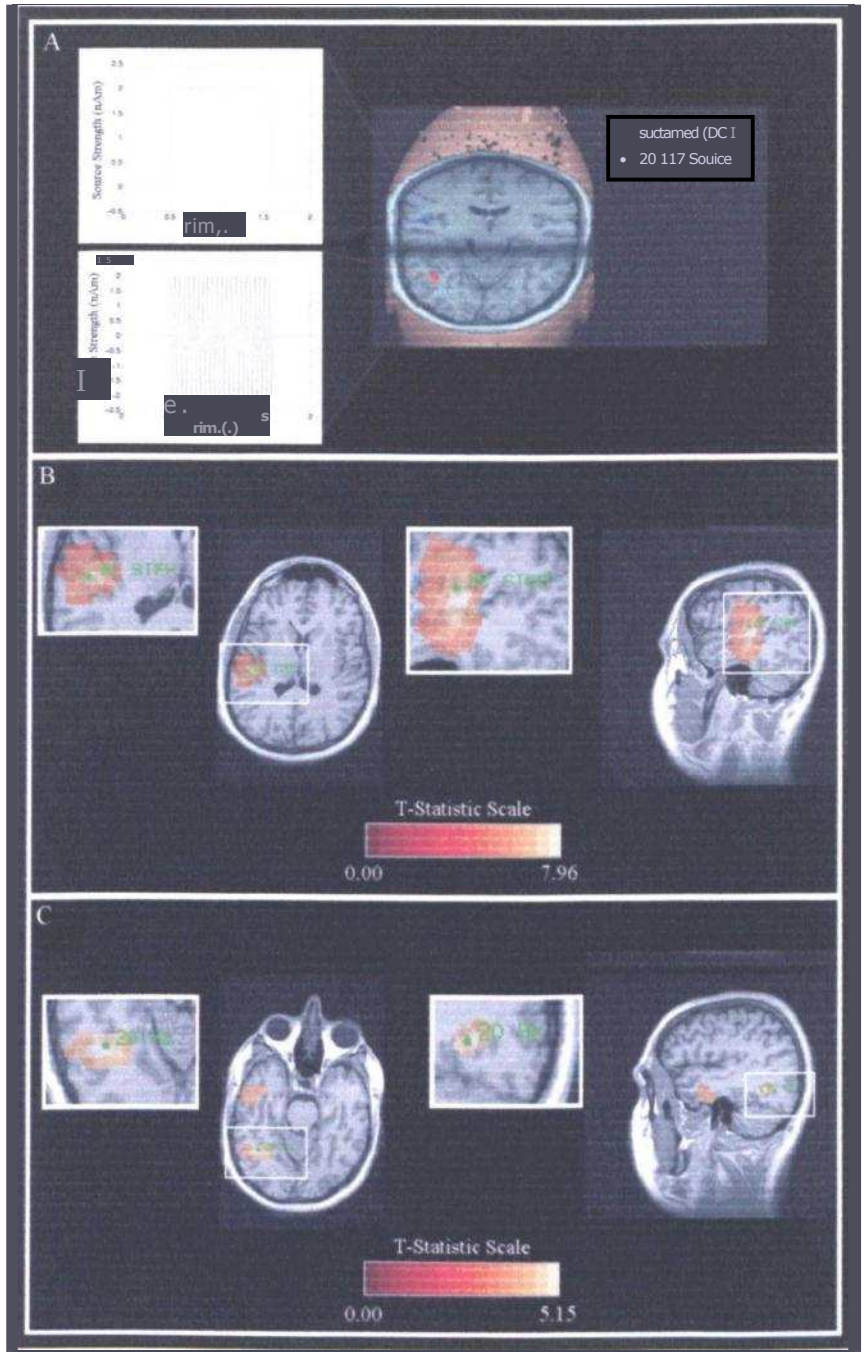

Fig 5.3: Localization of simulated sources: A) Shows the relative position of the Top-Hat and 20Hz sources within the cortex, together with their associated time courses (inset). B) Localisation of the Top-Hat source using the GLM-beamformer methodology. C) Localization of the 20 Hz source. In Both B and C the green marker shows the position of the simulated source and the red overlay shows the T-statistic image. All probability maps are thresholded at an uncorrected p-value of 0.001 (25 degrees offreedom).

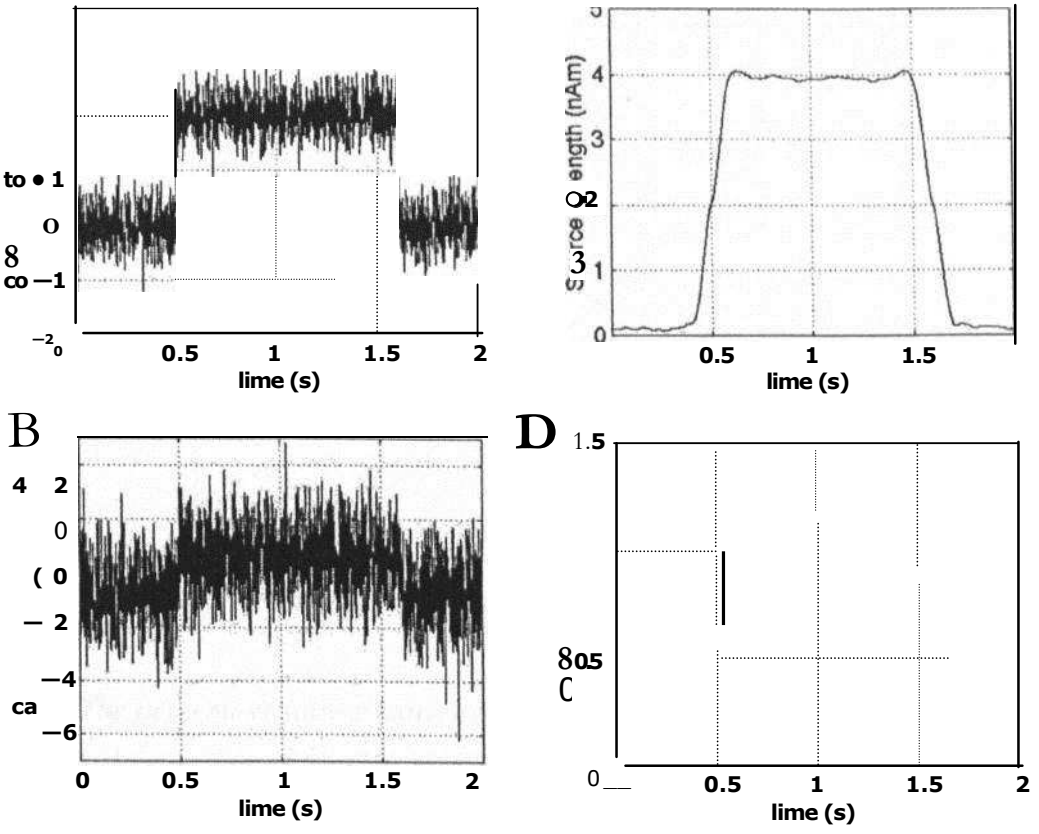

Fig 5.4: The temporal correspondence of the simulated sources and the virtual electrode timecourses for an averaged epoch. A) The simulated Top-Hat source timecourse averaged over 10 trials. B) The associated virtual electrode timecourse taken from the maximum in the volumetric T-statistic image and averaged over 10 trials. C) The timecourse of the envelope of the simulated 20Hz source averaged over 10 trials. The envelope was taken by band pass filtering the source timecourse (15-25Hz using a second order Butterworth filter) and computing the trial averaged analytic signal D) The associated envelope of the 15-25Hz signal measured in a virtual electrode placed at the maximum in the volumetric T-statistic image. Again the envelope was taken by band pass filtering the source timecourse (15-25Hz using a second order Butterworth filter) and computing the trial averaged analytic signal.

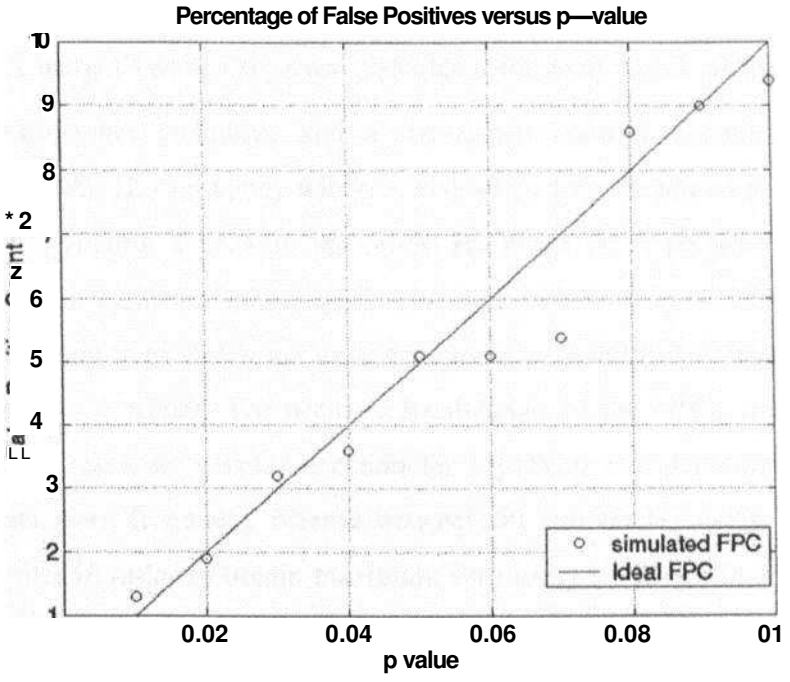

Fig 5.5. The percentage false positive count plotted against p-threshold. Results from the Monte-Carlo simulation (circular data points) compared to the theory (solid line).

5.4 EXPERIMENTAL EXAMPLE — THE SCINTILLATING SCOTOMA

5.4.1 Collection and analysis of experimental data

The experimental data were recorded using a 151-channel Omega system (CTF Systems Inc., Port Coquitlam, Canada), with a third order gradiometer configuration and a sample rate of 625 Hz. The recording was taken continuously over a 20-minute period from a patient experiencing a scintillating scotoma, a visual disturbance associated with migraine first described by Hubert Airy in 1854. These data were acquired previously[t] and have been presented as a MEG case study [39]. They are used again here to illustrate the application of the GLM-beamformer technique. For this purpose, only the final 400 s of the data were used, during which a strong increase in gamma band activity was noted in the temporal lobe that was coupled to decreasing gamma activity in the frontal lobe [39].

[t] Data were originally acquired by S.Hall, Wellcome trust laboratory for MEG studies, Aston University, Birmingham, UK. For details see reference 37

As with the simulated data, the source space was divided into a regular 3D cubic grid of 0.5 cm side. A weight vector (W_9) was calculated for each vertex of the grid using the non-linear beamformer technique and a covariance window encompassing the full duration and a 50-60 Hz-frequency window. Hall **et al.** [39] examined gamma band (30-200Hz) activity, finding a peak in the 50-60 Hz range. This frequency window was therefore chosen to gain maximum signal sensitivity to the effect of interest, whilst still keeping the duration over which the weight vector was calculated as wide as possible to minimize correlation effects. For accurate localization of the effect, a multiple sphere head model was taken as a volume conductor [7]. Prior to calculation of the weight vector, all data were frequency filtered between 50 and 60 Hz using a second order Butterworth filter in order to obtain maximum sensitivity to the gamma frequency band and to be consistent with the selected covariance window. The frequency-filtered data were projected through the spatial filter and the envelope of activity in this band determined using the Hilbert transform. In order to remove high frequency noise, the envelope was smoothed using a Gaussian smoothing kernel (**a = 4 s).**

Hall **et al.** showed that both the increase in gamma activity in the temporal lobe and the decrease in gamma activity in the frontal lobe are, to a first approximation, linear. For this reason the envelope of these gamma band effects was modelled using a simple straight line in the design matrix. This is represented by Equation 5.60, which refers to a single virtual electrode and is a specific case of Equation 5.55. (In Equation 5.60 the location subscript 0 has been omitted for clarity).

$$\begin{bmatrix} y_1 \\ \vdots \\ y_N \end{bmatrix} = \begin{bmatrix} t_1 & 1 \\ \vdots & \vdots \\ t_N & 1 \end{bmatrix} \begin{bmatrix} \gamma \\ e \end{bmatrix} + \begin{bmatrix} \varepsilon_1 \\ \vdots \\ \varepsilon_N \end{bmatrix} \qquad [5.60]$$

Here, y, represent the data and t, represent time. The gradient of the straight line, representing a linear increase in gamma band activity is given by the unknown

parameter fl_i and the 'steady state' activity by A . Using Equation 5.56 estimates of the unknown

parameters were obtained (b, and b_2), a T-statistic was defined based on the gradient of

the straight line for each voxel in the source space using Equation 5.57 and a T-statistical volumetric image was constructed and thresholded using an uncorrected p-value of 0.001 to show focal areas of maximal effect. In order to confirm the accuracy of the GLM-beamformer technique, this volumetric image may be compared to the original image produced by Hall **et al.** [39] using the standard non-linear beamformer implementation [14]. Virtual electrodes were also constructed for areas of interest to show the temporal effect located by the GLM-beamformer method.

5.4.2 Results — The scintillating Scotoma study

Figure 5.6 shows the volumetric T-statistic image for the experimental data, and highlights the spatial location of changes in gamma band activity. Increasing gamma activity is shown in red and occurs in the temporal lobe. Decreasing gamma activity is shown in blue and occurs in the frontal lobe. Both effects are associated with the scintillating scotoma. In order to confirm the success of the technique, virtual electrodes were placed at the peak of the activation foci and the non-normalized time courses of these electrodes are plotted in the figure, together with the 3D rendered image. The locations of the maxima of the increase and decrease of gamma band activity as defined here agree closely with those published in the original study.

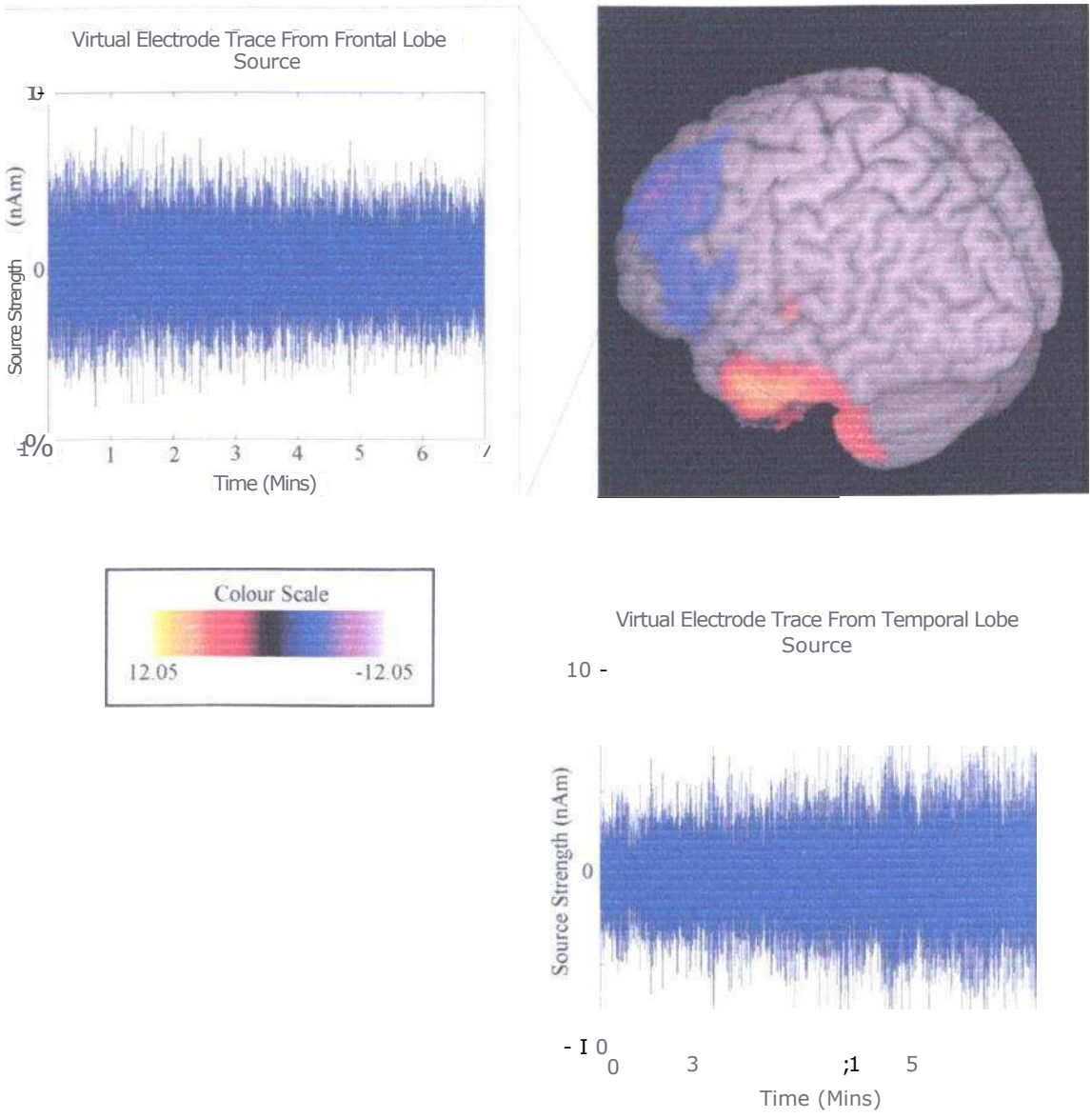

Fig 5.6: Spatial localization of the temporal effects associated with a scintillating scotoma. A linear increase in gamma band activity in the temporal lobe identified using the GLM-beamformer method is shown in red. A linear decrease in gamma band activity in the frontal lobe is shown in blue. The image has been thresholded at an uncorrected p-value of 0.001 (78 degrees of freedom). Virtual electrode traces from the foci of maximum linear increase and decrease in gamma band activity are also shown.

5.5 DISCUSSION — THE GLM-BEAMFORMER METHOD

The GLM-beamformer method described has been shown to be accurate in a variety of applications, however because the method rests heavily on the beamformer methodology, the problems intrinsic to that technique are still present here. In particular, it has been shown [13] that use of the beamformer technique causes spatially separate but covariant sources to be suppressed. However using a larger time window means that there is less chance of covariance between source time courses, and so this effect can be minimized by calculating the covariance matrix over a large temporal window [52]. Also using the beamformer approach, uncorrelated sensor noise is projected non-uniformly throughout the source space such that noise increases with increasing depth into the brain [52]. In the original implementation of the Linearly Constrained Minimum Variance (LCMV) beamformer technique [13], these non-uniform noise distributions were corrected by dividing projected source power by an estimate of projected noise power to give a 'neural activity index' [13] or `pseudo-z-statistic' [14]. In the GLM-beamformer method, no such noise correction is required. This is because due to the unity pass band constraint employed by the beamformer, source amplitude in any given virtual electrode will be correct, despite the noise scaling with virtual electrode position. The T-statistical maps presented are derived using Equation 5.59, where the numerator is representative of the amplitude of the modelled effect and the denominator is representative of the residuals left over after subtracting the model from the data.jor these reasons, the numerator will only be non-zero when the effect of interest is present at a given virtual electrode site, and hence noise correction is not a requirement for accurate localisation (in practice it can be shown that noise correction has no effect on T-statistical probability maps). The residuals in the denominator will scale with noise amplitude, and therefore position within the source space. As a consequence, given a series of uniformly distributed sources, the GLM-beamformer technique would be less sensitive to deep sources than to shallow sources. This is an intrinsic problem associated with MEG itself, not the beamformer methodology and reflects the increased detectability, and hence statistical significance of shallow sources [53].

The GLM-Beamformer method generates a T-statistic image that enables statistical quantities associated with the GLM to be calculated (for example a p-value may be derived for each image voxel). The derivation of these statistical quantities involves consideration of the temporal smoothing applied to the data via the convolution matrix **K.** As stated above, the number of degrees of freedom in a vector time series is dependent on the degree of autocorrelation in that time series. The application of a band pass filter, coupled with the use of the Hilbert transform and analytic signal increases the degree of autocorrelation in the data and therefore reduces the degrees of freedom. If the value of a (the width of the Gaussian smoothing kernel) is not sufficiently large, the application of the temporal filter may have a negligible effect on the degree of autocorrelation when compared to the effects of temporal smoothing and Hilbert transformation. If this were the case, then the degrees of freedom, predicted using only the temporal smoothing kernel, would be overestimated leading to artificially small p-values and an increase in the false positive rate above that expected from the p-threshold. For this reason, the degree of temporal smoothing should always be monitored and kept suitably high.

T-statistics calculated using the GLM-beamformer method refer only to the voxel (or virtual electrode) in question and in the current study uncorrected p-values are quoted. (For a useful description of the difference between corrected and uncorrected p-values see [54])The problems inherent to the uncorrected p-value are apparent in Figure 5.3C where a single false peak is observed forward of the genuine 20Hz peak. The maximum T-score in the false peak is less than that in the genuine peak and thus could be eliminated simply by decreasing the p-threshold of the image. In order to avoid such problems, the ideal solution would be to calculate a corrected p-value. However, the inherent smoothness in the beamformer image rules out a simple Bonferroni correction (i.e. dividing the p-threshold by the number of virtual electrodes) since the number of spatial degrees of freedom is unknown. For these reasons, other methods are required if a corrected p-value is to be applied and false positives eliminated. For single subjects, Barnes and Hillebrand [52] have outlined a method based on the assessment of spatial

smoothness that can be used to correct for multiple comparisons across a volume. This method could be readily applied to the GLM-beamformer technique.

Alternatively Singh **et al.** [55] have outlined non-parametric statistical methods [56] with which to develop robust, multiple comparison corrected, group statistics. Again this method could also be readily applied to the GLM—beamformer technique to look at statistical significance of modelled effects across a group. It is anticipated that the GLM-beamformer method, when used in conjunction with such techniques to obtain corrected p-values, will enable the design of more complex experiments in MEG, allowing for the detection of multiple effects of interest, paralleling studies already undertaken using PET and fMRI. A simple method for achieving this is by construction of contrast of parameter estimates [42]. Such contrasts may be used to test differential effects or interactions between any number of experimental conditions or independent components described in the GLM design matrix.

5.6 CONCLUSION

The GLM-beamformer method introduced shows how the Hilbert transform and General Linear Model can be applied to MEG beamformer data to identify the spatial distribution of known temporal effects. Simulations demonstrate the accuracy of the technique in locating low frequency effects that are time and phase locked to external stimuli and therefore potentially the GLM-beamformer method could be used to locate sustained field effects. (i.e. those described by Lammertmann and Lutkenhoner [51] and Forss **et al.** [50]). The 20 Hz source simulation shows that time locked but non-phase locked event related synchronization (ERS) or desynchronisation (ERD) [43] can also be localized using the GLM-beamformer method. This may be put to use in the identification of areas of ERD/ERS if specific modulation of the oscillatory effects is present.

Having said this the GLM beamformer technique is far from ideal. The problems inherent to the beamformer technique introduce limitations. Particularly the problem of suppression of correlated sources since it may be the case that a single, extended source may look like two or more temporally correlated sources that could possibly be

suppressed by the beamformer methodology. Further, since the beamformer solution is based on the approximations surrounding the forward problem, its ultimate success is dependent on these assumptions.

Despite the limitations, the success of the GLM-beamformer method in finding both the temporal and frontal lobe sources in the scintillating scotoma study is encouraging, and suggests that it will prove a useful method for the localisation of changing patterns of both sustained activity (DC effects) and oscillatory phenomena. Furthermore, the GLM used here for MEG is equivalent to that used in fMRI, meaning that the use of the GLM-beamformer technique allows for MEG and fMRI analyses within the same statistical framework. For these reasons, this technique is to be used again in subsequent chapters where it is involved in the detection and spatial localisation of neuromagnetic effects that may be related to the fMRI BOLD response.

5.6 REFERENCES

1. Brookes, M.J., Gibson,A.M., Ha11,S.D., Furlong,P.L., Barnes,G.R., Hillebrand,A., Singh,K.D., Holliday,I.E., Francis,S.T., Morris,P.G., *A General Linear Model for MEG Beamformer Imaging.* Neuroimage, 2004. In Press.

2. Hamalainen, M., Hari, R., Ilmoniemi, R.J., Knuutila, J., Lounasmaa, 0.V., *Magnetoencephalography - Theory, Instrumentation and applications to noninvasive studies of the working human brain.* Reviews of Modern Physics, 1993. 21(2): p. 413 - 460.

3. Cheng, D.K., *Field and Wave Electromagnetics.* 1989, New York: Addison Wesley.

4. Geselowitz, D.B., *On the magnetic field generated outside an inhomogeneous volume conductor by internal current sources.* IEEE Transactions on Magnetism, 1970. MAG-6: p. 346 - 347.

5. Sarvas, J., *Basic mathematical and electromagnetic concepts of the biomagnetic inverse problem.* Physics in Medicine and Biology, 1987. 32(1): p. 11 - 22.

6. Vrba, J., Robinson, S.E., *Signal processing in Magnetoencephalography.* Methods, 2001.25: p. 249 - 271.

7. Huang, M.X., Mosher, J.C., Leahy, R.M., *A sensor-weighted overlapping-sphere head model and exhaustive head model comparison for MEG.* Physics in Medicine and Biology, 1999.44: p. 423-440.

8. Grynszoan, F., Geselowitz, D.B., *Model studies of the magnetocardiogram.* Journal of Biophysics, 1973. 13: p. 911 - 925.

9. Ilmoniemi, R.J., Hamalainen, M.S., Knuutila, J., *The forward and inverse problems in the spherical model, in In Biomagnetism - Applications and Theory,* H. Weinberg, Stroink, G., Katila, T., Editor. 1985, Pergamon: New York. p. 278 282.

10. Baillet, M., Leahy,, *Electromagnetic Brain Mapping.* IEEE Signal Processing Magazine, 2001. November.

11. Tuomisto, T., Hari, R., Katila, T., Poutanen, T., Varpula, T., *Studies of auditory evoked magnetic and electric responses: Modality specificity and modelling.* Nuovo Cimento D, 1983. 2: p. 471 - 483.

12. Hamalainen, M.S., Ilmoniemi, R.J., Interpreting measured magnetic fields of the brain: Estimates of current distributions. (Helsinki University of Technology, Finland) Technical Report, 1984. TKKK-F-A599.

13. Van Veen, B.D., Van Drongelen, W., Yuchtman, M., Suzuki, A., Localisation of brain electrical activity via linearly constrained minimum variance spatial filtering. IEEE Transactions on biomedical engineering, 1997. 44(9).

14. Robinson, S., Vrba,J., Functional Neuroimaging by synthetic Aperture Magnetometry. In Recent Advances in Biomagnetism, ed. Yoshimoto T, Kotani M, Kuriki S, Karibe H, Nakasato N, Tohoku Univ. Press, Sendai, Japan., 1998: p. 302-305.

15. Dziewas, R., Sorbs, P., Ishii, R., Chau, W., Henningsen, H., Richelstein, E.B., Knecht, S., Pantev, C., Neuroimaging evidence for cortical involvement in the preparation and in the act of swallowing. Neurolmage, 2003. 20: p. 135 - 144.

16. Gaetz, W.C., Cheyne, D.O., Localization of human somatosensory cortex using spatially filtered magnetoencephalography. Neuroscience Letters, 2003.340: p. 161 - 164.

17. Hashimoto, I., Kimura, T., Iguchi, Y., Takino, R., Sekihara, K., Dynamic activation of distinct cytoarchitectonic areas of the human SI cortex after median nerve stimulation.. NeuroReport, 2001. 12(9): p. 1891 - 1897.

18. Hashimoto, I., Sakuma, K., Kimura, T., Iguchi, Y., Sekihara, K., Serial activation of distinct cytoarchitectonic areas of the human SI cortex after posterior tibial nerve stimulation. NeuroReport, 2001. 12(9): p. 1857 - 1862.

19. Herdman, A.T., Wollbrink, A., Chau, W., Ishii, R., Ross, B., Pantev C., Determination of activation areas in the human auditory cortex by means of synthetic aperture magnetometry. Neurolmage, 2003. 20: p. 995-1005.

20. Hillebrand, A., Singh, K.D., Holliday, I.E., Furlong, P.L., Barnes, G.R.,, A New Approach to Neuroimaging with Magnetencephalography. Human Brain Mapping, 2005.25: p. 199 - 211.

21. Hirata, M., Kato, A., Taniguchi, M., Ninomiya, H., Cheyne, D., Robinson, S.E., Maruno, M., Kumura, E., Ishii, R., Hirabuki, N., Nakamura, H., Yoshimine, T., Frequency-dependent spatial distribution of human somatosensory evoked neuromagnetic fields. Neuroscience Letters, 2002. 318: p. 73 - 76.

22. Ihara, A., Hirata, M., Yanagihara, K., Ninomiya, H., Imai, K., Ishii, R., Osaki, Y., Sakihara, K., H.I., Imaoka, H., Kato, A., Yoshimine, T., Yorifuji, S., Neuromagnetic gamma-band activity in the primary and secondary somatosensory areas. NeuroReport, 2003. 14(12): p. 273 - 277.

23. Ishii, R., Shinosaki, K., Ukai, S., Inouye, T., Ishihara, T., Yoshimine, T., Hirabuki, N., Asada, H., Kihara, T., Robinson, S.E., Takeda, M., Medial prefrontal cortex generates frontal midline theta rhythm. NeuroReport, 1999. 10(4): p. 675 - 679.

24. Ishii, R., Schulz, M., Xiang, J., Takeda, M., Shinosaki, K., Stuss, D.T., Pantev, C., MEG study of long-term cortical reorganization of sensorimotor areas with respect to using chopsticks. Cognitive Neuroscience and Neuropsychology, 2002. 13(16): p. 2155 - 2159.

25. Ishii, R., Dziewas, R., Chau, W., Soros, P., Okamoto, H., Gunji, A., Pantev, C., Current source density distribution of sleep spindles in humans as found by synthetic aperture magnetometry. Neuroscience Letters, 2003.340: p. 25 - 28.

26. Iwaki, S., Ueno, S., Imada, T., Tonoike, M., Dynamical cortical activation in mental image processing revealed by biomagnetic measurement. NeuroReport, 1999. 10: p. 1793 - 1797.

27. Kamada, K., Kober, H., Saguer, M., Moller, M., Kaltenhguser, M., Vieth, J., Responses to silent Kanji reading of the native Japanese and German in task subtraction magnetoencephalography. Cognitive Brain Research, 1998.7: p. 89 - 98.

28. Ploner, M., Gross, J., Timmermann, L., Schnitzler, A., Cortical representation of first and second pain sensation in humans. Proceedings of the National Academy of Science USA, 2002.99(19): p. 12444 - 12448.

29. Robinson, S.E., Vrba, J., Otsubo, H., Ishii, R., Finding Epileptic Loci by Nonlinear Parameterization of Source Waveforms. In Proceedings of the 13th International Conference on Biomagnetism, ed. Nowak H, Haueisen J, GieBler F, Huonker R, Jena, Germany., 2002: p. 220-222.

30. Sekihara, K., Nagarajan, S.S., Peoppel, D., Marantz, A., Miyashita, Y., Reconstructing Spatio-Temporal Activities of Neural Sources Using an MEG Vector Beamformer Technique. IEEE Transactions on Biomedical Engineering, 2001. 48(7): p. 760-71.

31. Sekihara, K., Nagarajan, S., Poeppel, D., Marantz, A., Miyashitam Y., Application of an MEG Eigenspace Beamformer to Reconstructing Spatio-

Temporal Activities of Neural Sources. Human Brain Mapping, 2002. 15: p. 199215.

32. Singh, K.D., Barnes, G.R., Hillebrand, A., Forde, E.M., Williams, A.L., Task related changes in cortical synchrony are spatially coincident with the haemodynamic response. Neuroimage, 2002. 16: p. 103-114.

33. Taniguchi, M., Kato, A., Fujita, N., Hirata, M., Tanaka, H., Kihara, T., Ninomiya, H., Hirabuki, N., Nakamura, H., Robinson, S.E., Cheyne, D., Yoshimine, T., Movement-Related Desynchronization of the Cerebral Cortex Studied with Spatially Filtered Magnetoencephalography. Neurolmage, 2000. 12: p. 298-306.

34. Ukai, S., Shinosaki, K., Ishii, R., Ogawa, A., Mizuno-Matsumoto, Y., Inouye, T., Hirabuki, N., Yoshimine, T., Robinson, S.E., Takeda, M., Parallel distributed processing neuroimaging in the Stroop task using spatially filtered magnetoencephalography analysis. Neuroscience Letters, 2002. 334: p. 9-12.

35. Van Drongelen, W., Yuchtman, M., Van Veen, B.D., Van Huffelen, A.C., A Spatial Filtering Technique to Detect and Localize Multiple Sources in the Brain. Brain Topography, 1996.9(1): p. 39-49.

36. Xiang, J., Wilson, D., Otsubo, H., Ishii, R., Chuang, S., Neuromagnetic spectral distribution of implicit processing of words. NeuroReport, 2001. 12(18): p. 3923-3927.

37. Xiang, J., Holowka, S., Sharma, R., Hunjan, A., Otsubo, H., Chuang, S., Volumetric localization of somatosensory cortex in children using synthetic aperture magnetometry. Pediatr. Radiol., 2003. 33: p. 321-327.

38. Hall, S., et al., The Missing Link: concurrent human and primate cortical gamma oscillations. Submitted. Neurolmage. Submitted to Neuroimage, 2004.

39. Hall, S.D., Barnes, G.R., Hillebrand, A., Furlong, P.L., Singh, K.D., Holliday, I.E., Spatio-temporal imaging of cortical desynchronisation in migraine visual aura: an MEG case study. Headache, 2004.44(3): p. 204 - 208.

40. FUrlong, P.L., Hobson, A.R., Aziz, Q., Barnes, G.R., Singh, K.D., Hillebrand, A., Thompson, D.G., Hamdy, S., Dissociating the spatio-temporal characteristics of cortical neuronal activity associated with human volitional swallowing in the healthy adult brain. Neurolmage, 2004. 22: p. 1447 - 1455.

41. Fawcett, I.P., Barnes, G.R., Hillebrand, A., Singh, K.D., The temporal frequency tuning of human visual cortex investigated using Synthetic Aperture Magnetometry. NeuroImage, 2004.21: p. 1542 - 1553.

42. Worsley, K.J., Friston, K.J., Analysis of fMRI time series revisited - again. Neuroimage, 1995. 2: p. 173-181.

43. Pfurtscheller, G., Lopes da Silva, F.H., Event-realted EEG/MEG synchronization and desynchronization: basic principles. Clinical Neurophysiology, 1999. 110: p. 1842-1857.

44. Nikouline, V.V., Wikstrom, H., Linkenkaer-Hansen, K., Kesaniemi, M., Ilmoniemi, R.J., Huttunen, **J.,** Somatosensory Evoked Magnetic Fileds: Relation • to Pre-stimulus Mu Rhythm. Clinical Neurophysiology, 2000. **111:** p. 1227 - 1233.

45. Byron, F.W., Fuller, R.W., Mathematics of classical and quantum physics Vol.1. 1970: Addison-Wesley.

46. Blackledge, J.M., Digital Signal Processing. 2003, Chichester: Horwood Publishing.

47. Clochon, P., Fontbonne, J.M., Lebrun, N., Etevenon, P., A new method for quantifying EEG event related desynchronisation: Amplitude envelope analysis. Electroencephalography and Clinical Neurophysiology, 1996. 98: p. 126-129.

48. Liang, H., Lin, Z., McCallum, R.W., Artifact reduction in electrogastrogram based on empirical mode decomposition method. Medical & Biological Engineering and Computing, 2000. 38(1): p. 35 - 41.

49. Seber, G.A.F., Linear regression analysis. 1977: Wiley-Interscience.

50. Forss, N., Narici, L., Hari, R., Sustained activation of the human SI' cortices by stimulus trains. Neuroimage, 2001. 13(3): p. 497-501.

51. Lammertmann, C., Lutkenhoner, B., Near-DC magnetic fields following a periodic presentation of long-duration tonebursts. Clin. Neurophysiol., 2001. 112(3): p. 499-513.

52. Barnes, G.R., Hillebrand, A., Statistical Flatening of Beamformer Images. Human Brain Mapping, 2003. 18: p. 1-12.

53. Hillebrand, A., Barnes, G.R., A Quantitative Assessment of the Sensitivity Of Whole-Head MEG to Activity in the Adult Human Cortex. Neuroimage, 2002. 16: p. 638-650.

. Clare, S., Functional MRI - Methods and Applications, in School of Physics and Astronomy. 1997, University of Nottingham.

55. Singh, K., D, Barnes, G.,R, Hillebrand, A., Group imaging of task-related changes in cortical synchronisation using nonparametric permutation testing. Neuroimage, 2003. 19(4): p. 1589-1601.

56. Nichols, T.E., Holmes, A.P., Nonparametric permutation tests for functional neuroimaging: a primer with examples. Human Brain Mapping, 2002. 15: p. 1-25.

CHAPTER SIX

THE COMBINATION OF FUNCTIONAL MAGNETIC RESONANCE IMAGING AND MAGNETOENCEPHALOGRAPHY

OVERVIEW

This chapter describes the application of blood oxygenation level dependent functional magnetic resonance imaging (BOLD fMRI) and magnetoencephalography (MEG) to a simple visual brain activation experiment. Initially, the fundamental physical principles behind the BOLD response are explained. The limitations in current theories on the biophysical basis of the BOLD response are highlighted and possible connections between the haemodynamic changes measured in BOLD and the measurable neuromagnetic fields detected in MEG are introduced. The experiments themselves and the data analysis techniques employed are described in detail; MEG analysis involved the novel GLM-beamformer technique whilst BOLD analysis made use of standard techniques. The results are described quantitatively and the fMR1 BOLD response is shown to be spatially and temporally coincident with a number of heterogeneous neuromagnetic effects. A discussion of results is put forward which includes a detailed description of the limitations of this study including the paradigm and the experimental techniques employed. To conclude, areas of possible further research are suggested including extensions to the beamformer model and changes to the visual paradigm. (This work has previously been published, see (1) and appendix.)

6.1 INTRODUCTION

6.1.1 Introduction to the BOLD response

Since its inception in the early 1990's, functional magnetic resonance imaging (fMRI) [2] has revolutionised the field of cognitive neuroscience by providing a non-invasive means of mapping human brain function *in vivo.* The most widely applied method is known as Blood Oxygenation Level Dependent (BOLD) fMRI, and is thought to highlight those brain regions in which increased activity in local neuronal networks causes an

increase in metabolic demand. Note however that this explanation is not universally accepted.

Current theories state that the signal change associated with BOLD fMRI is due to a complex interplay between regional cerebral blood flow (rCBF), regional cerebral blood volume (rCBV), the cerebral metabolic rate of oxygen (CMRO2), and neuronal activity. Increased cellular activity in some localised neuronal network is thought to lead to dilation of local blood vessels, and therefore a regional increase in CBV and CBF. However, this is not met by a proportionate increase in CMRO2 and therefore results in an excess of oxygenated blood in the capillaries and venuoles close to the site of the neuronal network. As we shall see, oxygenated and deoxygenated blood have very different magnetic properties, and therefore these local oxygenation changes cause fluctuations in the MR signal, which result in a measurable effect in rapidly acquired MR images.

6.1.2 BOLD contrast mechanisms

The vast majority of blood oxygen is bound to haemoglobin. Attachment is via the **haem** group, a complex of **Fe** and protoporphyrin. Oxygen molecules bind to the iron using the four unpaired electrons in the **Fe** outer shell. The net amount of bound oxygen is dependent on the local partial pressure of oxygen, and this mechanism allows oxygen to be carried to metabolising tissues where it is used in energy production. In the absence of bound oxygen, the four unpaired electrons in the outer shell of the **Fe** make deoxyhaemoglobin strongly paramagnetic. However, on oxygenation, the four unpaired electrons are transferred to the bound 0_2 molecule and the haemoglobin changes to a diamagnetic state. It is this oxygenation dependent change in the magnetic properties of haemoglobin that results in an endogenous contrast agent for MR imaging. The paramagnetic deoxyhaemoglobin will cause local field perturbations that will differ from those caused by the diamagnetic oxyhaemoglobin. This difference causes a change in the MR signal that is dependent on the local concentration of deoxyhaemoglobin. In turn this depends on the regional haemodynamics (rCBF, rCBV) as well as regional oxygen concentration.

To understand further the mechanisms behind the BOLD effect a physiological model must be employed. Consider first Figure 6.1 where a blood vessel is modelled as an infinitely long cylinder placed at arbitrary angle (0) to the external magnetic field (B_o).

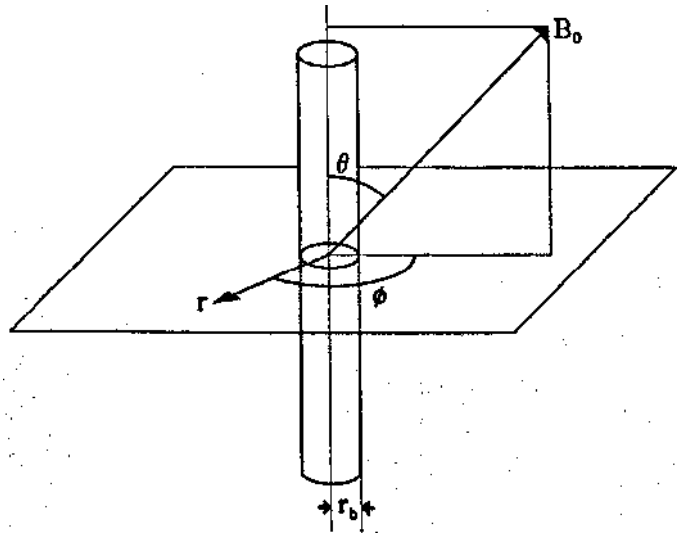

Figure 6.1: Physiological model of a blood vessel oriented at angle° with respect to the magnetic field

Using this simplified approach, it is possible to derive analytical expressions for the magnetic field perturbation caused by oxygen concentration both inside and outside the vessel [3]. If Ax_o is the maximum susceptibility difference between fully oxygenated, and fully deoxygenated blood (see also section 3.1.6), Y is the fraction of oxygenated blood present and r_b is the vessel radius then:

$$\text{"mar[RAVASCULAR)} \quad {}^{2}X4\,0^{-} \qquad {}_{r}^{2} \qquad [6.1]$$

$$_{0}(^{rb)}\sin^{2}(0)\text{COS}(20)$$

and

$$\text{coRAVASCULAR)} = 27440(1 - Y)co_0\,k\,OS^2(0) - Xi \qquad [6.2]$$

Where Aco_o represents the induced shift in precessional frequency from co_o = "B_o. If a blood vessel exists within an imaging voxel then the magnetic field within that voxel will be perturbed according to the above equations. Notice that in both the extravascular and the intravascular case, the field perturbations are dependent on vessel orientation with

respect to the static field. This introduces a directional dependence of the BOLD signal, meaning that some vessels may be rendered fMRI 'silent' simply due to their orientation. This is not thought to be a problem in capillaries since the BOLD effect will be averaged across voxels that are large when compared to capillary diameter. Therefore a number of vessels will exist within a single voxel and an average of all vessel orientations will be observed. However, the BOLD effect can also occur in larger vessels, distant to the actual site of neuronal activation and downstream in the vasculature. In these larger vessels, no averaging takes place and directional dependence may influence results.

Let us, for the moment, ignore the intravascular field effects and concentrate fully on the extravascular field component (see Equation 6.1). The net effect on the MR signal can be understood in terms of static and dynamic averaging. Consider an imaging experiment in which a slice selective RF pulse is applied followed by a delay (TE), (which represents the effective echo time,) and an echo planar readout. (i.e. TE represents the time delay between the RF pulse and the centre of an echo planar imaging module, and hence the point at which the centre of k-space is sampled.) The susceptibility difference between the vessel and its surrounding tissue causes a BOLD induced field inhomogeneity. This, in turn, will cause spins across a voxel to precess at slightly different angular frequencies, meaning that spins in different locations within a voxel will dephase as they evolve, leading to signal loss. This is an example of dephasing due to a static effect and modelling studies have shown that above some critical vessel size, the static dephasing effect will become independent of vessel size, and dominate the BOLD signal over dynamic effects [4]. However, static dephasing is a $\mathbf{T_2}$ * effect and can therefore be eliminated by the use of a spin echo (in place of gradient echo) imaging sequence.

In addition to static BOLD effects, signal loss can also be induced by dynamic averaging. If typical water diffusion distances during the delay TE are comparable to the distances spanned by the magnetic field gradients induced by the BOLD field inhomogeneity then the effect of those field inhomogeneities will be dynamically averaged, i.e. the magnetic field that the diffusing water molecule 'sees' will change along the diffusion path. This means that the phase accumulated by precessing spins in the water molecule will be given

by an average of all of the fields observed by the molecule. If the diffusion length is large compared to the extent of the inhomogeneity, then the diffusing water will, on average, pass through regions where the field is both increased and decreased, and therefore spins will not undergo a significant phase change. Similarly, if the diffusion length is small compared to the extent of the inhomogeneity, then the diffusing water will still not see a significant field change, and again spins will undergo no significant phase change. However, if the diffusion length is on the same scale as the inhomogeneity, then spin dephasing will be a maximum. This raises an important point as to the length scale of the field perturbation. The extravascular field change falls off as the inverse of squared distance from the vessel, however it is also proportional to the square of vessel radius meaning that the field from large vessels extends over larger distances. In general, if a TE between 30 ms and 80 ms is used, then the free water diffusion length is optimised such that it is comparable with the extent of field perturbations from capillaries. Therefore, not only are phase changes maximised, but also they are sensitised to the small diameter capillaries, rather than to larger diameter veins. Notice also that the size of the field inhomogeneity is proportional to co_o . We should observe increased diffusion effects from smaller vessel sizes at larger field strengths not only because of the increased susceptibility field but also because as field is increased, the $\mathbf{T_2}$ * relaxation time of brain tissue decreases. Optimal TE is set by $\mathbf{T_2}$ * since we can show that to maximise the MR signal difference between oxygenated and deoxygenated blood, the echo time TE should be set to $\mathbf{T_2}$ * . Therefore as $\mathbf{T_2}$ * is reduced, TE should also be reduced, giving free water molecules less time to diffuse and therefore sensitising the dynamic diffusion effects to inhomogeneity effects on a smaller length scale, hence smaller vessels.

Not included in the model depicted in Figure 6.1 are Intravascular effects, which will also effect the BOLD signal. Haemoglobin is contained within the red blood cells and the presence of deoxyhaemoglobin will cause magnetic susceptibility differences across the red blood cell boundaries, and hence field inhomogeneities around the cells themselves. Clearly, the dimensions of a red blood cell are small when compared to the free water diffusion length. The effect is therefore one of dephasing due to dynamic averaging, and

it affects both large and small vessels equally. A secondary intravascular effect comes as a result of CBV increase and depends on the difference between blood and tissue relaxation times. If blood $\mathbf{T_2}$ were longer than tissue $\mathbf{T_2}$ then an increase in blood volume would produce an increase in signal. Conversely if blood $\mathbf{T_2}$ was shorter than tissue **T2** then an increase in blood volume would produce a decrease in signal. At 3 T, the $\mathbf{T_2}$ for oxygenated blood is comparable to the $\mathbf{T_2}$ for grey matter, but the $\mathbf{T_2}$ for deoxygenated blood will be less than the $\mathbf{T_2}$ for grey matter. It can be argued that an increase in CBV will (at least initially) cause an increase in the blood oxygen fraction, and therefore is assumed to result in a signal increase. At higher fields (7 T), the $\mathbf{T_2}$ of blood is sufficiently short that the intravascular signal should be lost.

6.13 The haemodynamic response

As stated above, the measurable variation in signal intensity due to the BOLD response is a result of the interplay between changes in CBF, CBV, CMRO2 and neuronal activation. The main signal increase is thought to be a result of a large, localised increase in CBF in response to neuronal activation, which is not met by a proportionate increase in CMRO2. This leads to an excess of oxygenated blood in the capillaries and venuoles close to the site of neuronal activation. More oxygenated blood leads to less spin dephasing and hence to a larger signal. However, transient effects are also thought to exist in the temporal profile of the BOLD response, which is shown in Figure 6.2.

The **early negative response,** often termed the **initial dip** was first observed in optical haemodynamic measurements, but has since been reported in fMRI [5]. It is thought to represent a decoupling of the CBF and CMRO2, meaning that oxygen consumption begins before the increase in CBF leads to an increase in oxygenated blood volume. The post stimulus undershoot has been consistently observed in many fMRI experiments and this is thought to be representative of an increase in deoxygenated blood volume that remains for some seconds after CBF has returned to a baseline state (although this is still a matter for debate, see chapter 7). If, following the large positive response, vessels

remain dilated such that CBV remains elevated, then deoxygenated blood may collect

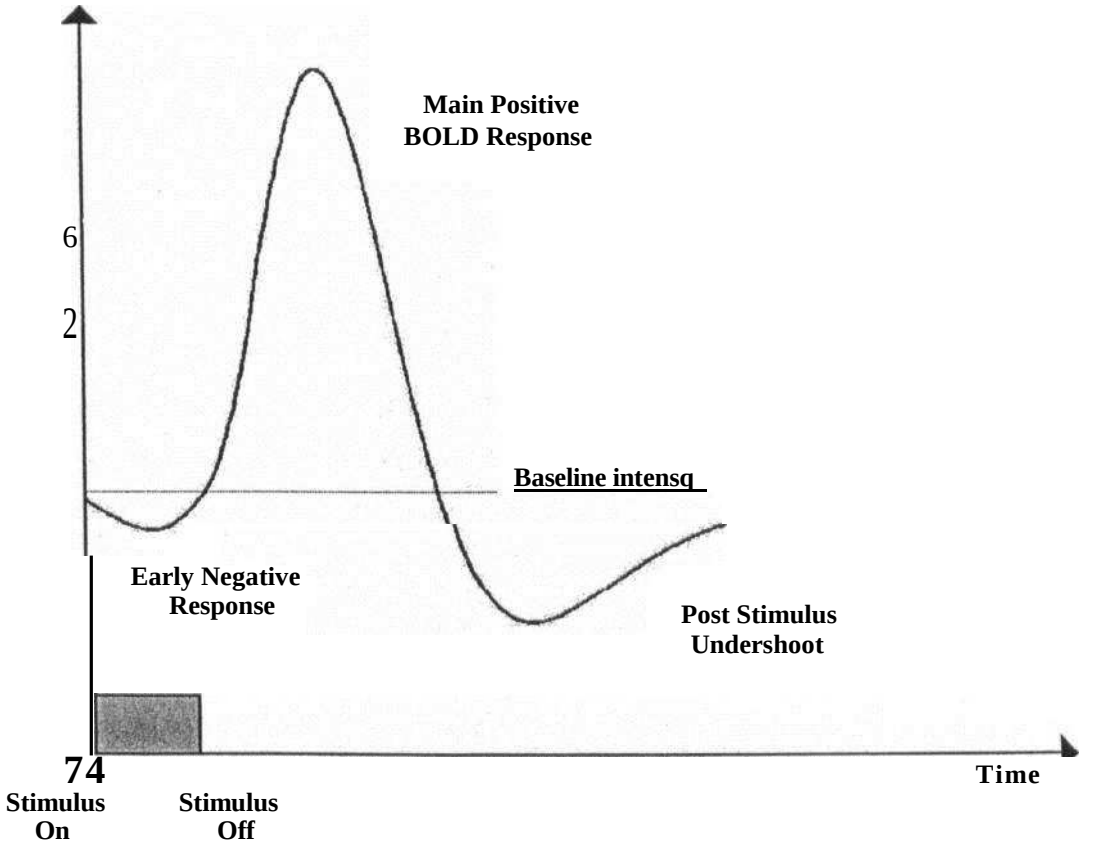

within the imaging voxel, leading to a reduction in the MR signal.

Figure 6.2: The temporal profile of the haemodynamic response.

6.1.4 BOLD fMRI and MEG

BOLD fMRI has enjoyed a great deal of success as a means to map non-invasively the functionality of brain areas. However, its ultimate success is arguably limited due to its current inability to provide a quantitative measure of brain activity. The absolute characterisation of the BOLD response has proved difficult and this is due to its convoluted nature. However, key to its characterisation is an understanding of the link between the measured BOLD response and its underlying neuronal basis. This problem has, in part, been addressed by comparing fMRI BOLD responses with simultaneous, microelectrode recordings [6, 7], but the invasive nature of this approach restricts its

use to animal studies. Assessment of a quantitative relationship between neuronal activity and

the BOLD response has also been attempted by Rees et al. [8], however assessment of this relationship remains difficult without direct invasive techniques to measure neuronal activity. We have seen in chapters four and five that magnetoencephalography provides a direct but non-invasive measure of neuronal activity. Comparison between fMRI and MEG data should therefore shed light on the neural basis of fMRI without the need for animal based approaches.

The relationship between MEG and the fMRI BOLD response has been investigated previously and existing literature [9] focuses on a comparison between the MEG transient evoked response and the fMRI BOLD response. However, previous work [10-13] has shown that a number of heterogeneous neuromagnetic effects can be detected using MEG, all of which may be relevant if a truly accurate model of the relationship between neuronal activity and the BOLD response is to be derived.

As previously described, sustained fields comprise phase-locked baseline shifts throughout the period of stimulation and have been previously documented [12-16] in the MEG literature. Such effects are likely to represent metabolically demanding neuronal activity that is sustained throughout the period of stimulation, and therefore should be included in any future model of energy usage. In addition, oscillatory effects comprising time-locked but non-phase-locked event related synchronisation and desynchronization have also been recorded [11, 17] and evidence suggests that they may be of some importance in a comparison between MEG and the BOLD response [10]. If these oscillatory effects represent a change in the overall level of activity, it would be expected that this would be reflected by an altered metabolic requirement and hence a BOLD response, whereas, if as their names imply, they represent primarily synchronisation/desynchronisation without a change in neuronal firing rate, it is possible that they could be largely fMRI silent. In either event, they are likely to be associated with neuronal responses that do alter metabolic state and thus give rise to BOLD effects.

In the experiments that follow, the GLM-beamformer technique introduced previously is used as a statistical framework for comparison of the range of neuromagnetic responses

with fMRI BOLD results. Neuromagnetic responses are compared both spatially and temporally to those recorded using BOLD fMRI for the case of a simple visual paradigm.

6.2 EXPERIMENTAL METHOD

Five healthy volunteers (3 male, 2 female, age 27 +/- 4 years) with no known neurological disorders, head trauma, contraindication to MR, or medication were recruited to the study, which was approved by the Ethical Committees of Aston and Nottingham Universities. Each subject participated in both MEG and fMRI studies.

6.2.1 The Visual Paradigm

A visual paradigm was employed consisting of a static checkerboard pattern during the ON period and a fixation cross during the baseline (OFF) period. The paradigm was adapted for optimal MEG and fMRI data acquisition. The MEG paradigm employed an inter-stimulus interval (ISI) of 15 s, consisting of a 2 s pre-stimulus baseline, followed by 5 s of stimulus presentation and an 8 s post-stimulus rest period. This was repeated for 40 trials and was presented to the subject through a window in the shielded room via a front-silvered mirror. For fMRI studies, the post stimulus rest period was extended to 18 s to allow the haemodynamic response to decay back to a baseline state. It was also possible to reduce the number of trials to 10 due to the increased signal to noise ratio available in fMRI. The stimulus was presented on a back projection screen placed across the bore of the magnet and viewed via a pair of prism glasses. Eye movement during visual stimulation would cause the receptive fields in primary visual cortex to vary, generating non-stationary MEG and fMRI signals in both primary visual cortex and in the parietal visual areas. In order to remove these possible confounds, in both MEG and fMRI experiments, the fixation cross remained on the screen both during the stimulus presentation and during the baseline period.

6.2.2 Functional MRI data collection

Functional MRI data were acquired on the 3T MRI scanner at the SPMMRC using an insert head gradient coil and whole head TEM RF volume coil (see chapter three). The sequence used was optimised for optimum BOLD contrast. Single shot MBEST gradient

echo (GE) EPI images were taken from a region of interest at the back of the head comprising 10 contiguous coronal slices. This region of interest covered the whole of the primary visual cortex and associated areas.

The use of rapid MR imaging to sample the haemodynamic response in both space and time requires careful selection of the imaging parameters in order to ensure an adequate temporal resolution, spatial resolution and signal to noise ratio. Optimisation of these three parameters introduces certain trade offs that must be considered prior to carrying out an fMRI experiment. In order to obtain good spatial resolution (i.e. a large matrix size and small voxels) long image acquisition times are required, which reduces the temporal resolution available. A reduction in voxel size will also lower the signal to noise ratio. Conversely, if a high temporal resolution is required, a small matrix and large voxels must be used in order to reduce the image acquisition time. However, whilst large voxels increase signal to noise ratio, a short volumar repetition time means that the longitudinal magnetisation does not have time to fully recover between images. This means that the initial longitudinal magnetisation available prior to each imaging pulse is reduced; hence the imaging signal is also reduced. Finally, if the voxel size is greater than the active region, then partial volume effects [3] will reduce the (BOLD) contrast to noise ratio. Given that the cerebral cortex is — 2 — 4 mm thick, this effect is highly likely.

For the visual BOLD experiment, the repetition time (T_R) was set to 100 ms per slice, giving an overall volumar repetition time, and hence temporal resolution, of 1 s. Using this $\mathbf{T_R}$, an imaging matrix size of 64 x 64 pixels per slice, with a slice thickness of 6 mm and in plane resolution of 4 x 4 mm was achievable without placing too much stress on the gradient coils. The echo time was set to 40 ms in order to achieve sufficient BOLD contrast, but also maintain sufficient signal to noise ratio in the final images. The short repetition time also meant that the intensity recorded in the first volumar image was greater than that recorded in subsequent images. This T_i saturation effect is well documented in fMRI literature and after a small number of volumes have been acquired, the system will reach a steady state. Those initial images were simply ignored. Following

steady state onset, the flip angle was optimised to give maximum intensity in the MR images.

6.2.3 Functional MRI data analysis

The recorded FMRI data were analysed using standard techniques. Analysis comprised pre-processing, motion correction, spatial smoothing, and statistical estimation. Full descriptions of each of these steps are given elsewhere [18], however for completeness, a brief description of each step is given below.

- Data pre-processing comprised three simple steps. Initially the image data were corrected for Nyquist ghost artefacts by manually changing the phase in alternate lines of k-space. The extent of ghost correction was gauged by eye and the phase angle was adjusted until the ghost was minimised. Following this, the experimental pre-scans (saturation scans) were extracted to ensure that the effects of T_1 recovery had reached a steady state. Finally, images were reduced in size (segmented) eliminating the extra-cranial space. This step simply serves as a data reduction technique in order to speed up computational time.
- One of the major detrimental effects to final functional image quality in fMRI is subject motion. This can cause two types of artefact in fMRI time series: i) Suppose following the $\mathbf{n^{th}}$ image, the subject's head either moves or rotates within the magnet. All subsequent images will be spatially displaced such that the time course of some voxel will result from two different brain regions. This effect can be corrected by motion correction algorithms (see for example [19]). ii) Perhaps less obvious is the fact that subject motion will destroy the steady state magnetisation that has built up over the duration prior to the n^{th} image. This secondary effect is much harder to correct for using post-processing techniques.
  In order to minimise motion artefacts, motion plots from all five subjects were analysed. These plots, derived from the SPM99 motion correction algorithm, show 3 dimensional translation and rotation about the subjects' original position. Any dataset in which motion was larger than the smallest voxel dimension (i.e. 4 mm) was discarded in order to minimise steady state effects. The SPM99 motion

correction algorithm was then applied to the images (http://www.fil.ion.ucl.ac.uk/spm/).

- A key conflict in the analysis of fMRI time series is that of efficiency against bias [20]. Ideally one would like to maximise the efficiency in detecting genuine areas of activation, whilst preventing any bias in the final results that may arise due to data processing. This raises an important point since in general, the functional response is on a similar amplitude scale to the noise. In most cases, both spatial and temporal smoothing are applied to fMRI data in order to reduce the white noise level. However, whilst this will improve detection efficiency, if inappropriate filters are used they may bias the final results. (For example the use of a very large spatial filter may lead to an artificially large spatial extent of the final detected activation.) For the visual experiment, data were spatially smoothed using a 4 mm FWHM Gaussian smoothing kernel. This was thought to be sufficient to improve detection efficiency without biasing source extent. A low pass (Gaussian) temporal filter (FWHM = 4 s) was also applied to the time course data in order to remove high frequency (thermal) noise. In order to prevent low frequency drift, a high pass temporal filter was applied with a $^{1}_{50}1/z$ cut off frequency.

  Finally, statistical parametric maps of significant BOLD contrast were constructed using the General Linear Model. This is applied in a directly analogous way to that described in chapter four in relation to MEG data. The effect of interest in the GLM design matrix comprised a simple boxcar waveform defining the visual stimulus delivery. In order to account for the delayed haemodynamic response, this waveform was convolved with a standard haemodynamic response function in SPM99. In order to take into account any time latency in the BOLD response, the simple HRF model was supplemented with its temporal derivative. To test the significance of the final functional images, all BOLD statistical parametric maps were thresholded using a corrected p-value of 0.05. Co-registration of activation maps onto anatomical images was achieved using the AIR (Automated Image Registration) algorithm [19] in MEDx® (Sensor Systems) software.

6.2.4 MEG data collection

MEG data were acquired using the 151-channel Omega system at Aston University (see chapter four for details). Data were collected at a sampling rate of 625 Hz, in forty 15 s epochs. The previously described, third order, synthetic gradiometer system was employed and this allows the system a large dynamic range. It is therefore possible to record data without the need for a high pass frequency filter. Such filters are available on the omega system and are commonly used to filter out 1/f noise. However, they remained switched off for the duration of the visual experiment in order that any sustained (DC) changes could be detected. A 200 Hz low pass anti-aliasing filter and a 50 Hz powerline filter were applied to the MEG data that had also been DC corrected. (Note that by deriving the baseline offset from the control period, DC correction had no effect on any measured sustained response.) Trials in which eye blinks were thought to interfere with the stimulus response were removed.

In order to perform spatial reconstruction on the MEG data, the MEG sensor positions must be recorded with respect to the subject's brain anatomy. This was achieved by placing three electrodes on the subject's head prior to data collection. The three electrodes were positioned above the nose and ears, and their positions with respect to the MEG sensors were recorded by the MEG system. Following data acquisition, a 3D digitiser (Poihemus Isotrack) was used both to digitise the shape of the subject's head, and to record the positions of the three electrodes with respect to the subject's headshape. During digitisation, the head position was maintained by the use of a bite bar [21]. This digitised head shape was mapped onto the head surface extracted from an anatomical MR image (taken using an MP-RAGE sequence at 1.5 T with 1 mm^3 resolution). This allows a known relative positioning of the electrodes with respect to the anatomical MR image and hence brain anatomy. Finally, since the original position of the electrodes relative to the MEG sensors is known, the MEG sensor positions can be determined with respect to the anatomical image. This process had previously been automated (www.ece.drexel edu/ICVC/Ali gn).

Recording of the electrode positions by the MEG scanner both before and after data collection also served as a (somewhat crude) method for assessing subject motion. For the present study, if the sum total of subject motion in any direction recorded in this way was found to be greater than 5 mm over the course of the recording, then that dataset was rejected.

6.2.5 MEG data analysis

MEG data analysis comprised two separate stages: initially, a comparison between the GLM-beamformer technique, and some other established technique was required. For this reason the first level of analysis comprised use of a simple Synthetic Aperture Magnetometry (SAM) metric [22, 23]. Having defined frequency bands of interest using this technique, the GLM-beamformer method was used both to confirm the results of the SAM metric, and to probe for the existence of a sustained field, which SAM is unable to do.

Using the simple SAM metric, data were initially band pass filtered (using a Hanning window) to obtain signals at a given frequency band of interest. Source reconstruction was then achieved using a non-linear beamformer and a multiple sphere head model [24] to obtain source strength estimates at a number of positions in the cortex. Pseudo-T-statistic images were then derived for each point in source space by measurement of the relation between integrated oscillatory power in the active time window and that in the passive time window [22]. Such measurements reveal the change in oscillatory power between active and passive time windows as a function of position in source space. The active contrast window was selected to span the five seconds of stimulus presentation and the passive contrast window was selected to span the final five seconds of the post stimulus rest period in each trial. Eight separate frequency bands were selected for analysis (5 — 10 Hz, 10 — 15 Hz, 15 — 20 Hz, 20 — 30 Hz, 30 — 40 Hz, 40 — 45 Hz, 55 — 70 Hz and 70 — 100 Hz), the 45 — 55 Hz band being omitted in order to avoid mains frequency artefacts, and the 0 — 5 Hz band being omitted since this particular SAM metric is unsuitable for localisation of sustained field effects. A single pseudo-T-statistical volumetric image was constructed for each subject and frequency band. Using this initial

SAM analysis, specific frequency bands of interest (8 — 13 Hz, typically defined as the alpha band and 55 — 70 Hz, a frequency range of interest within the 30 — 200 Hz gamma band) were selected for further analysis using the GLM-beamformer technique.

Following the definition of frequency bands of interest using SAM, the GLM-beamformer technique was used to create images showing the distribution of cortical oscillatory power within these frequency bands. The algorithm used was identical to that described in chapter five: data were initially band pass filtered and projected through a non-linear beamformer (again using a multiple sphere head model to be consistent with the SAM metric). Following this spatial filtering, the resulting data were Hilbert transformed [25] and the analytic signal calculated in order to obtain the envelope of synchronisation/desynchronisation in the 8 — 13 Hz and 55 — 70 Hz frequency bands. The GLM was then used to create volumetric T-statistical parametric maps showing the spatial distribution of synchronisation and desynchronisation across the head. Synchronisation and desynchronisation were modelled as a simple boxcar function in the GLM design matrix. However rather than convolution with an HRF as was the case with the fMRI BOLD analysis, a Gaussian smoothing filter (a = 0.6 s) was used both to force a Gaussian statistical distribution, and to define accurately the number of temporal degrees of freedom in the filtered, transformed data. The MEG statistical parametric maps were thresholded at an uncorrected $p < 0.001$.

The existence of a phase-locked sustained response was also probed using the GLM-beamformer technique. Here, since the expected signal is simply a boxcar, no Hilbert transform was required and so this step was omitted (see also chapter five). The same boxcar function was selected as the effect of interest in the GLM design matrix and again a Gaussian smoothing filter **(a =** 0.6 s) was used. Statistical parametric maps were constructed for each subject showing the spatial distribution of the sustained response. All such images were thresholded at an uncorrected p-value of 0.001, for consistency with the oscillatory power maps.

6.2.6 Quantitative assessment of spatial localisation and temporal analysis

A quantitative assessment of the location of the BOLD effect in comparison to gamma band synchronisation, alpha band desynchronisation, and the sustained field was undertaken in Talairach space. Anatomical images for individual subjects were normalised to the standard Talairach brain using SPM99. These transforms were then applied to all of the functional maps yielding the position of BOLD response and the three neuromagnetic effects in Talairach space. The centres of intensity (location of maximum T-score) for these activation foci were found using MRI3DX (www.aston.ac.uk/lhs/staff/singhkd/mri3dx), and their positions in Talairach co-ordinates recorded.

Temporal analysis of the MEG data was carried out using Virtual Electrodes placed at locations defined by the GLM-beamformer functional maps. To allow quantitative assessment of the temporal relationship between the three detectable neuromagnetic effects, virtual electrode traces were derived using the non-linear beamformer. In the case of the sustained field, raw signals were averaged across all 40 trials in order increase the signal to noise ratio. In order to study alpha band ERD and gamma band ERS, the data were band pass filtered from 8 to 13Hz and 55 to 70Hz respectively, using a 2^{nd} order Butterworth filter. The average of the absolute value of the analytic signal was then taken, giving the envelope of synchronisation/desynchronisation. Time course plots were obtained for each subject and filtered using a median filter of width 0.5 s. Time courses were also averaged across subjects. Correlation coefficients were calculated on an individual subject basis (using normalised neuromagnetic signals) in order to obtain a quantitative estimate of the correlation between the temporal profiles of the three neuromagnetic effects. These correlation coefficients were subsequently averaged across subjects.

6.3 RESULTS

Table 6.1 summarises the results of the MEG time frequency analysis using the traditional SAM methodology. It is clear that consistent effects across subjects are observed in the 5 — 15 Hz band and the 55 — 70 Hz band. Although other effects are apparent, they are not consistent across subjects and for this reason, the frequency bands for GLM-Beamformer analysis were selected to be the alpha band (8 — 13 Hz) and gamma band (55 — 70 Hz).

Frequency band	Subject SP	Subject MB	Subject AG	Subject KH	Subject AP
5 —10 Hz	ERD (Visual)	ERD (Visual)	ERD (Visual)	ERD (Visual)	ERD (Visual)
10 — 15 Hz	ERD (Visual)	ERD (Visual)	ERD (Parietal)	ERD (Visual)	ERD (Visual)
15 — 20 Hz	ERD (Visual)	ERD (Parietal)	ERD (Visual)	ERS (Visual)	ERS (Visual)
20 — 30 Hz	Not Significant	ERD (Parietal)	Not Significant	ERS (Visual)	Not Significant
30 —40Hz	Not Significant	ERS (Visual)	Not Significant	ERS (Visual)	ERS (Visual)
40 — 45 Hz	Not Significant	ERS (Visual)	Not Significant	ERS (Visual)	ERS (Visual)
55 — 70 Hz	ERS (Visual)	ERS (Visual)	ERS (Visual)	ERS (Visual)	ERS (Visual)
70 — 100 Hz	Not Significant	Not Significant	Not Significant	ERS (Visual)	Not Significant

Table 1: Summary of the results of MEG time frequency analysis using a traditional SAM methodology. The table lists the type of effect observed (ERD or ERS), and the area of cortex where it is most prominent.

Figure 6.3 shows the spatial distribution of the sustained field, alpha band ERD, gamma band ERS and BOLD signals for a single representative subject (SP), obtained using the GLM-beamformer methodology. Images show probability maps overlaid onto axial and sagittal slices of the corresponding anatomical MRI. In the alpha and gamma band oscillatory power maps, the red overlay represents an increase in oscillatory power during visual stimulation, whereas the blue overlay represents a decrease. The sustained field image represents the spatial distribution of a significant sustained response. The probability map relating to the BOLD signal shows areas of significant BOLD contrast. For the representative subject shown, the haemodynamic BOLD change and all three neuromagnetic effects (sustained field, alpha and gamma power changes) occur predominantly within the visual cortex and appear co-localised. Comparison of these images with Table 6.1 shows the consistency between the traditional SAM metric and the GLM beamformer technique for this single subject.

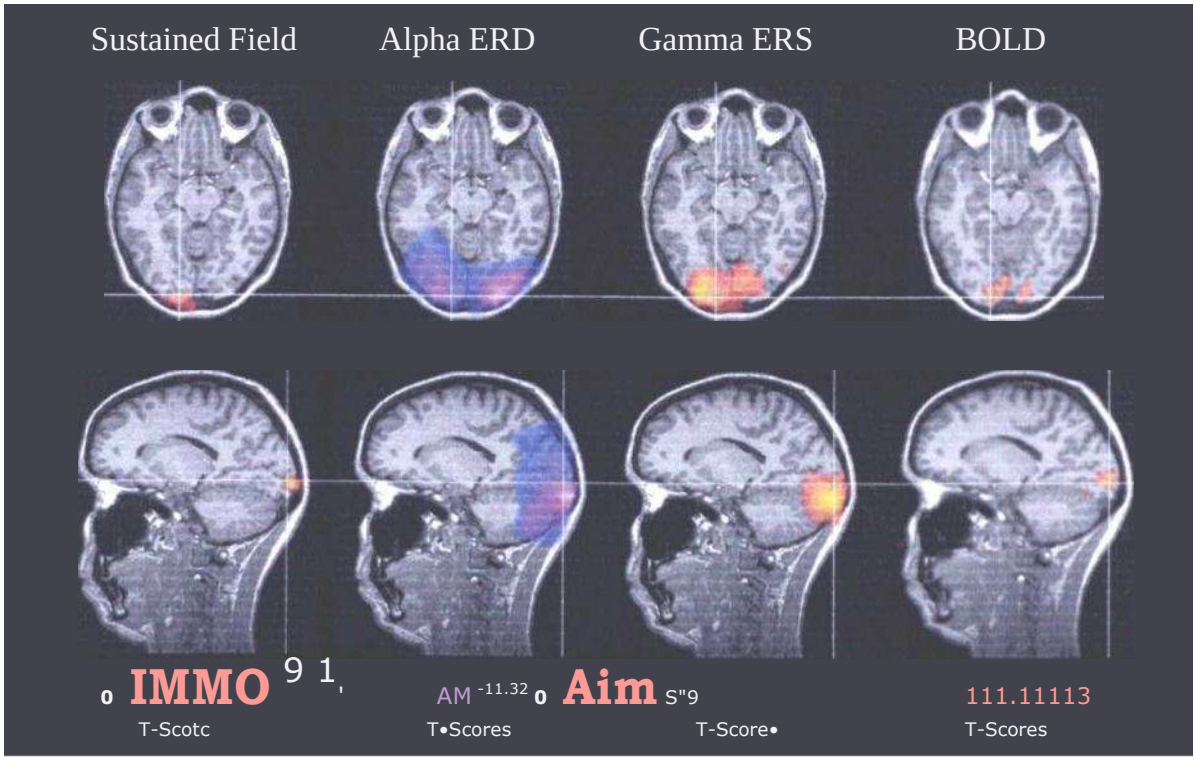

Figure 6.3: The spatial distribution of the sustained field, alpha band power change, gamma band power change and BOLD signals for a single subject (SP).

Table 2 summarises quantitatively the occurrence and spatial location of observed BOLD and neuromagnetic effects across the subject group. For all four effects studied, the Talairach co-ordinates of the centre of intensity of activation foci are given (averaged across subjects and quoted along with standard error).

Effect	Occurrence of bilateral response	Occurrence of unilateral response	Average Talairach co-ordinate (LHS) (mm)	Average Talairach co-ordinate (RHS) (mm)	Average 3D separation from BOLD (mm)
BOLD Effect	5	0	[-12±11 - 94 ±4	[10±3 -93±4	N/A
Sustained Field	4	1	[7 ± 5 15±6 - 97 ±1	1±5 23 ± 7 -91±6	8 ±12
Gamma-Band ERS	3	2	8 ± 7 -15 ± 4 -94 ±1	3 ± 8 [24±12] -93±6	9±15
Alpha-Band ERD	4	1	[3±6 [-- 21± 21	2±14 [18 ± 3	11±9

Table 6.2: The spatial location of the centre of intensity of activation across the subject group (N = 5). Talairach co-ordinates quoted as [Medial - Lateral / Anterior - Posterior / Superior - Inferior].

Table 6.2 also shows the laterality of the various effects, giving the number of subjects in which a particular response was bilateral and the number of subjects in which that response was unilateral. Also, for the three-neuromagnetic effects observed, the average 3D spatial separation from the centre of intensity of the BOLD effect has been calculated (averaged across both hemispheres). These results show that to within the error bounds calculated, the sustained field, gamma band ERS, and alpha band ERD all overlap with

the BOLD response. The calculated error in position of the various effects can be explained either by the intrinsic smoothness of the beamformer, errors in co-registration, or the fact that the BOLD response may exhibit draining vein effects shifting the foci of activation to the venous compartment.

In order to investigate further the neuromagnetic effects across the group, for each of the five subjects, virtual electrodes were placed at the centres of intensity as defined in Table 6.2. The temporal characteristics of the electrical phenomena for all subjects are shown in Figure 6.4a; the average across subjects and the associated standard error is shown in Figure 6.4b. The upper panel shows the average time course of the raw virtual electrode signal, and therefore represents the sustained field effect. The central panel shows the envelope of gamma band ERS derived from the analytic signal. The lower panel shows the envelope of alpha band ERD again derived from the analytic signal. It can be seen that the alpha response shows a larger standard error and hence a larger inter subject variability than the other two neuromagnetic effects. Correlation coefficients were calculated representing the temporal correlation between the sustained field and gamma ERS ($r_{sF.47}$), the sustained field and alpha ERD ($_{SF}$and gamma ERS and alpha ERD ($r_{p,a}$). When averaged across subjects these were found to be $r_{sp....7}$, = 0.7 ± 0.1, = 0.65 ± 0.1 and $r_{a,\_,7}$ = 0.54 ± 0.1.

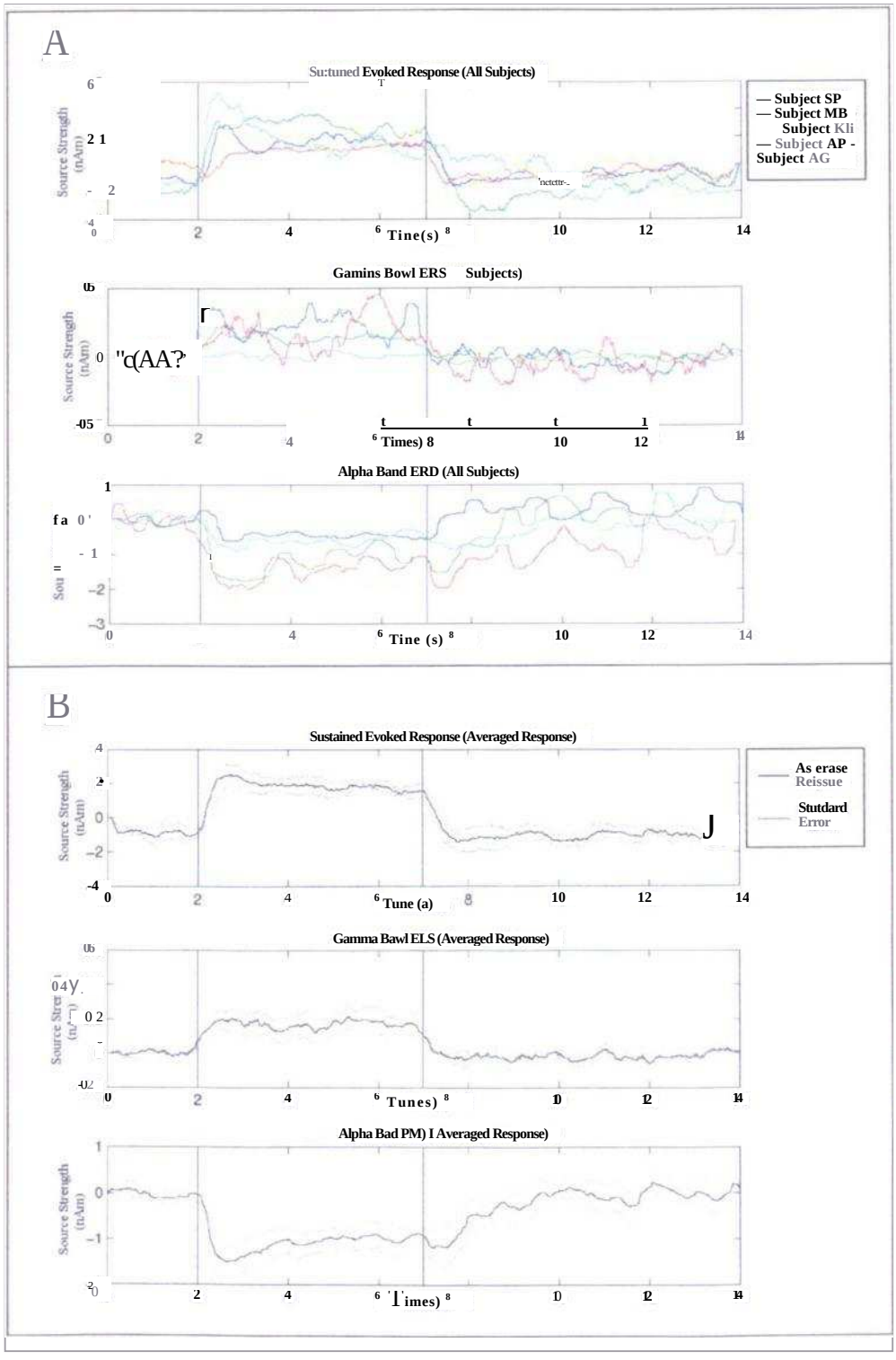

Figure 6.4: The temporal characteristics of the neuromagnetic phenomena. Virtual electrodes were placed at the foci of the neuromagnetic effects as defined by the relevant probability maps. A shows the results for each of the five subjects. B shows the average across subjects. Vertical solid lines at 2 and 7 s indicate the onset and offset of the visual stimulus, respectively.

In addition to the above temporal analysis, in which virtual electrodes were placed at centres of intensity defined independently for each neuromagnetic effect by the GLM-beamformer, a similar analysis was undertaken with a single virtual electrode placed at the peak of the BOLD response. This second temporal analysis was undertaken in order to support further the evidence from Table 6.2 that the observable neuromagnetic effects do indeed overlap spatially with the BOLD response. The result, averaged across all five subjects is shown together with standard errors in Figure 6.5.

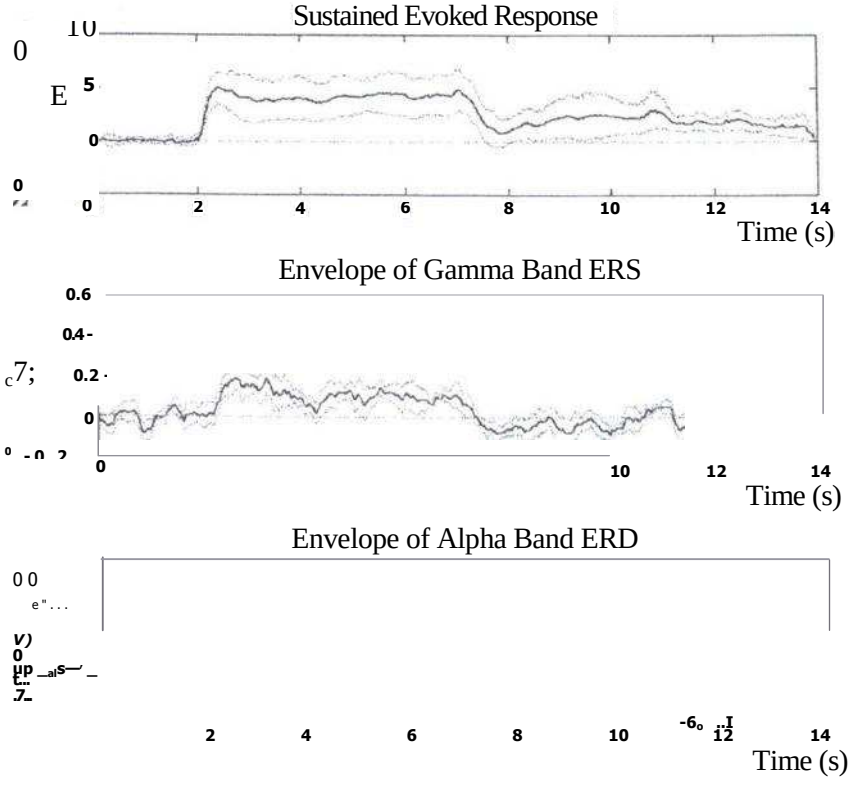

Figure 6.5: Temporal profiles of the three neuromagnetic effects from virtual electrodes placed at the foci of the BOLD response

Figure 6.5 shows conclusively that to within the spatial resolution limits of the beamformer model, these three neuromagnetic effects do spatially overlap both with each other, and with the BOLD response.

6.4 DISCUSSION — NEUROMAGNETIC EFFECTS AND BOLD FMRI

6.4.1 The neuromagnetic effects

Alpha band ERD is thought to originate from the involvement of a large neural network of cell assemblies in information processing, and is a suspected prerequisite to gamma band ERS which reflects the co-operative or synchronised behaviour of a large number of neurons within a network [26-28]. Recent findings suggest that the alpha band ERD is both larger and spatially more widespread in tasks of increased complexity or attention [29]. This may explain the large inter subject variability in the alpha band response in this study, apparent in Figures 6.4 and 6.5.

Gamma oscillations are thought to reflect active information processing, with the high frequency gamma band response allowing rapid coupling or synchronisation between spatially separate cell assemblies [30]. The amplitude of the gamma band response is modulated by stimulus contrast [31], again suggesting that gamma responses play an integral part in information processing. The sustained response has previously been observed in both the somatosensory [16] and auditory [12, 13] cortices. It is thought to reflect either successive excitation in the upper layers of the cortex summing to give a sustained response, or the activity of sustained cells. Neither explanation however, is universally accepted.

Despite recent advances, the origin of the neuromagnetic effects observed remains unclear. It is however apparent that the sustained response, alpha band ERD and gamma band ERS all represent significant deviations from the natural resting state of the cortex. This in turn means that each neuromagnetic effect is a potential contributor to the BOLD effect, and should not be ignored when comparing MEG and fMRI datasets. The link between oscillatory change and the BOLD response has been reported previously [10] for relatively complex cognitive paradigms where the majority of MEG changes were ERD's in the 5 — 10 and 15 — 25 Hz bands. The present study extends this work by demonstrating in a simple visual paradigm, co-localisation and temporal co-variation with the BOLD response of the stationary field and gamma ERS in addition to alpha ERD.

6.4.2 Spatial Localisation and Brain Metabolism

The GLM-beamformer technique for the generation of MEG statistical parametric maps is equivalent to that used by SPM in BOLD fMRI. This methodology therefore provides a useful statistical framework with which to combine the two imaging modalities. Its accuracy has now been shown in simulation (see section 5.3), on experimental data (the scintillating scotoma presented in section 5.4), and is further supported here by the fact that results are consistent with the more traditional SAM methodology (although this should not be over interpreted since both techniques are based on the same non-linear beamformer, and so to some extent this is to be expected). Perhaps the most interesting application however is the implication that to within the resolution limits of the techniques used, the BOLD effect, alpha band ERD, gamma band ERS, and the sustained field are co-localised.

Arguably, the fact that neuromagnetic effects are co-localised to the BOLD response should come as no surprise. It is thought that the major determinant of cortical oxygen and glucose consumption is the re-establishment of ionic concentrations associated with postsynaptic activity rather than spiking activity [32-36]. Empirical evidence suggests that spiking activity contributes no more than 3 % to the resting cortical energy consumption [37], and an increase in mean spiking rate on activation will have little effect on the local metabolism. However, both excitatory and inhibitory post-synaptic potentials (EPSP's and IPSP's) will have a significant effect on local metabolic demand. (IPSP's will cause hyperpolarisation thus reducing the probability of spiking and therefore the mean spiking rate.) Extending this, Logothetis et al. [7] report a strong correlation between the magnitude of Local field potentials (LFP's), representing synchronised synaptic activity, and the BOLD response, supported by the work of Waldvogel et al. [38]. Attwell and Lauglin [39] have estimated that in the grey matter of the human brain, approximately 74% of ATP consumption is associated with repolarisation following the passage of synaptic currents. All of the above evidence leads to the conclusion that it is post-synaptic events, rather than neuronal spiking, that is the major cause of metabolic demand in the human brain. In chapter four, it was shown that neuromagnetic effects recorded in MEG also originate from postsynaptic events.

Therefore, given the evidence, one might speculate that if the BOLD response is a genuine representation of a localised increase in metabolic demand caused by heightened cell activity, then it, and any neuromagnetic effects detectable in MEG, must be fundamentally linked. The results presented here suggest that this is indeed the case, however the relative contributions of each of the detectable neuromagnetic effects on metabolic demand is the subject for further study.

6.4.3 Limitations to the present study

The first major limitation to the present study arises from the fact that full field visual stimulation leads to bilateral activation across the primary visual cortex. This may result in two possible confounds. Firstly, cancellation of magnetic fields from opposing neuronal sources acting across the banks of the calcarine fissure may cause suppression of bilateral activity. This may account for why some subjects appeared to show unilateral neuromagnetic activation maps. Secondly, the beamformer technique will cause suppression of two sources if those two sources are temporally correlated [40]. Given that we expect bilateral activation in primary visual cortex and that the signal from these two sources is expected to be to some extent temporally correlated, this may also be a possible cause of the unilateral nature of the neuromagnetic responses. However for complete suppression of the two sources they must correlate such that their correlation coefficient is 0.7 . Given the magnitude of both source noise and SQUID noise, the likelihood of this effect causing signal suppression is questionable.

Another limitation to the present study is that we currently have no way of ascertaining which of the three detectable neuromagnetic effects is most closely linked to the BOLD response. The gamma band oscillatory changes have a similar temporal profile to the sustained response, and both are spatially correlated with the BOLD response. This might indicate that ERS effects are not due simply to reorganization of phase synchrony that is fMRI 'silent', but rather are metabolically demanding activations. Alpha band ERD is also well correlated in time but given the inter subject variability observed one could argue that it may be less of a contributor to the BOLD effect than gamma ERS and sustained field. These arguments are however speculative, and the precise relative contribution to

the BOLD response of gamma ERS, alpha ERD and the sustained response cannot be ascertained from these experiments.

6.6 CONCLUSION

The solution of the MEG inverse problem and the relationship of electrical activity to the BOLD response are tightly coupled problems. That is, near perfect correspondence would be possible if we were to change the beamformer assumption set to include the measured BOLD response as a statistical prior. This said, the correspondence between MEG and fMRI images using a simple beamformer assumption set (i.e. with no statistical priors based on BOLD measurements) is compelling, especially when one takes into account the intrinsic spatial smoothness of the MEG images [23]. Modification of the beamformer assumption set is a clear area for further work. However, biasing the beamformer output based on the fMRI BOLD response will not help in ascertaining any useful information about the relative contribution of the neuromagnetic effects to the BOLD response. Ideally, some way of separating the neuromagnetic effects spatially would be required; this might involve looking either for variations in their centre of intensity, or variations in their spatial extent. In either case, the current spatial resolution of the beamformer technique is not sufficient, and therefore further work is required (see also chapter 8).

Deriving useful information on the neural origins of BOLD by combination with MEG is difficult because, in effect, they represent measurable quantities at opposite ends of a series of biophysical processes. The change in neuronal activity detected using MEG is coupled to increases in CBF, and CBV, which along with changes in blood oxygenation, ultimately result in the BOLD effect. This system is complicated by non-linearities making its complete characterisation difficult, particularly when only using MEG and BOLD measurements. This separation may however be bridged by the use of further measurements in MRI. Arterial spin labelling can be used to measure both CBV and CBF, which could potentially provide important information on the metabolic demands of the neuromagnetic effects. In short, these quantitative measurements may provide a means to further investigate the link between MEG and the BOLD response.

6.7 REFERENCES

1. Brookes, M.J., Gibson,A.M., Ha11,S.D., Furlong,P.L., Barnes,G.R., Hillebrand,A., Singh,K.D., Holliday,I.E., Francis,S.T., Morris,P.G., GLM-beamformer method demonstrates stationary field, alpha ERD and gamma ERS co-localisation with fMRI BOLD response in visual cortex. Neuroimage, 2005. 26: p. 302-308.

2. Ogawa, S., Menon, R.S., Tank, D.W., Kim, S-G., Merkle, H., Ellermann, J.M., Ugurbil, K., Functional brain mapping by blood oxygenation level dependent contrast magnetic resonance imaging. Journal of Biophysics, 1993. 64: p. 803-812.

3. Jezzard, P., Matthews, P.M., Smith, S.M., Functional MRI : an introduction to methods. 2001, Oxford: Oxford University Press.

4. Gibson, A.M., High-Speed Functional Magnetic Resonance Imaging (PhD Thesis). 2002, University of Nottingham.

Hu, X., Le, T.H., and Ugurbil, K., Evaluation of the early response in fMRI in individual subjects using short stimulus duration. Magnetic Resonance in Medicine, 1997.37: p. 877 - 884.

6. Heeger, D.J. and D. Ress, What Does fMRI Tell Us About Neuronal Activity. Nature, 2002.3: p. 142-151.

7. Logothetis, N.K., et al., Neurophysiological investigation of the basis of the fMRI signal. Nature, 2001.412(6843): p. 150-7.

8. Rees, G., Friston, K.J., Koch, C., A direct quantitative relationship between the human and macaque VS. Nature Neuroscience, 2000.3: p. 716 - 723.

9. Dale, A., et al., Related Articles, Links Dynamic statistical parametric mapping: combining fMRI and MEG for high-resolution imaging of cortical activity. Neuron, 2000. 26(1): p. 55-67.

10. Singh, K.D., Barnes, G.R., Hillebrand, A., Forde, E.M., Williams, A.L., Task related changes in cortical synchrony are spatially coincident with the haemodynamic response. Neuroimage, 2002. 16: p. 103-114.

11. Pfurtscheller, G., Lopes da Silva, F.H., Event-realted EEG/MEG synchronization and desynchronization: basic principles. Clinical Neurophysiology, 1999. 110: p. 1842-1857.

12. Lammertmann, C., Lutkenhoner, B., Near-DC magnetic fields following a periodic presentation of long-duration tonebursts. Clin. Neurophysiol., 2001. 112(3): p. 499-513.

13. Hari, R., Aittoniemi, K., Jarvinen, M., Katila, T.,Varpula, T., Auditory evoked transient and sustained magntic fields of the human brain. Experimental Brain Research, 1980. 40: p. 237-240.

14. Picton, T., Woods, D., Proulx, G., Human auditory sustained potentials. I. The nature of the response. Electroenceph. Clin. Neurophys., 1978a. 45: p. 186-197.

15. Picton, T., Woods, D., Proulx, G., Human auditory sustained potentials. II. Stimulus relationships. Electroenceph. Clin. Neurophys., 1980b. 45: p. 198-210.

16. Forss, N., Narici, L., Hari, R., Sustained activation of the human SII cortices by stimulus trains. Neuroimage, 2001. 13(3): p. 497-501.

17. Lopes da Silva, F.H.P., G., Basic concepts on EEG synchronisation and desynchronisation. Handbook of electroencephalography and clinical neurophysiology. Vol. 6. 1999, Amsterdam: Elsevier.

18. Clare, S., Functional MRI - Methods and Applications, in School of Physics and Astronomy. 1997, University of Nottingham.

19. Woods, R., S. Cherry, and J. Mazziotta, Rapid automated algorithm for aligning and reslicing PET images. JCAT, 1992. 16: p. 620-633.

20. Friston, K.J., Josephs, 0., Zrahn, E., Holmes, A.P., Rouquette, S., and Polinr, J.P.,, To Smooth or not to Smooth, Bias and Efficiency in fMRI time-series analysis. Neuroimage, 2000. 12(2): p. 196-208.

21. Singh, K.D., Holliday, I.E., Furlong, P.L., Harding, G.F.A., Evaluation of MRI-MEG/EEG co-registration strategies using Monte Carlo Simulation. Electroenceph. Clin. Neurophys., 1997. 102: p. 81 - 85.

22. Robinson, S., Vrba,J., Functional Neuroimaging by synthetic Aperture Magnetometry. In Recent Advances in Biomagnetism, ed. Yoshimoto T, Kotani M, Kuriki S, Karibe H, Nakasato N, Tohoku Univ. Press, Sendai, Japan., 1998: p. 302-305.

23. Barnes, G.R., Hillebrand, A., Statistical Flatening of Beamformer Images. Human Brain Mapping, 2003. 18: p. 1-12.

24. Huang, M.X., Mosher, J.C., Leahy, R.M., A sensor-weighted overlapping-sphere head model and exhaustive head model comparison for MEG. Physics in Medicine and Biology, 1999.44: p. 423-440.

25. Blackledge, J.M., Digital Signal Processing. 2003, Chichester: Horwood Publishing.

26. Pfurtscheller, G., Event-related synchronization (ERS): an electrophysiological correlate of cortical areas at rest. Electroenceph din Neurophysiol., 1992. 83: p. 62-69.

27. Pfurtscheller, G., C. Neuper, and J. Kalcher, 40-Hz oscillations during motor behaviour in man. Neurosci. Lett., 1993. 164: p. 179-182.

28. Pfurtscheller, G. and F.H. Lopes da Silva, Event-realted EEG/MEG synchronization and desynchronization: basic principles. Clin Neurophysiol., 1999. **110:** p. 1842-1857.

29. Fries, P., et al., Modulation of oscillatory neuronal synchronisation by selective visual attention. Science, 2001. 291: p. 1560-1563.

. Gray, C.M., et al., Oscillatory responses in cat visual cortex exhibit inter-columnar synchronisation which reflects global stimulus properties. Nature, 1988.338: p. 334-337.

31. Hall, S.D., Holliday, I.E., Hillebrand, A., Furlong, P.L., Singh, K.D., Barnes, G.R., Distinct contrast response functions in striate and extra-striate regions of visual cortex revealed using Magnetoencephalography (MEG). Clinical Neurophysiology. 116(7): p. 1716-1722.

32. Yarowsky, P.J. and D.H. Ingvar, Neuronal activity and energy metabolism. Fed Proc, 1981. **40:** p. 2353-2363.

33. Kadekaro, M., A.M. Crane, and L. Sokoloff, Differential effects of electrical stimulation of the sciatic nerve on metabolic activity in spinal cord and the dorsal root ganglion in the rat. Proc. Natl. Acad. Sci. USA, 1985.82: p. 6010-6013.

34. Nudo, R.J. and R.B. Masterton, Stimulation induced I* 14C32-deoxyglucose labeling of synaptic activity in the central auditory system. J. Comp. Neurol., 1986. 245: p. 553-565.

35. Jueptner, M. and C. Weiller, Review: does measurement of regional cerebral blood flow reflect synaptic activity? Implications for PET and fMRL NeurolmageJ 1995. 2: p. 148-156.

36. Arthurs, O.J. and S.J. Boniface, What aspect of ;MIR' BOLD signals best reflects the underlying electrophysiology in human somatosensory cortex? Clin. Neurophysiol., 2003. **114:** p. 1203-1209.

37. Cruetzfeldt, 0.D., Neurophysiological correlates of different functional states of the brain, in Brain Work: The coupling of function, metabolsim, and blood flow in the brain, D.H. Ingvar and N.A. Lassen, Editors. 1975: Munskgaard.

38. Waldvogel, D., et al., The relative metabolic demand of inhibition and excitation . Nature, 2000.406: p. 995-998.

39. Attwell and Laughlin, An Energy Budget for Signaling in the Grey matter of the Brain. Journal of Cerebral Blood flow and Metabolism, 2001.21: p. 1133-1145.

40. Van Veen, B.D., Van Drongelen, W., Yuchtman, M., Suzuki, A., Localisation of brain electrical activity via linearly constrained minimum variance spatial filtering. IEEE Transactions on biomedical engineering, 1997. 44(9).

CHAPTER SEVEN

QUANTITATIVE MEASUREMENTS USING FMRI

OVERVIEW

This final experimental chapter presents a novel technique involving the use of magnetic resonance imaging for the non-invasive measurement of arterial cerebral blood volume (aCBV). The in vivo measurement of aCBV can provide important information about brain physiology and function under both normal and pathological conditions. In addition, the spatial selectivity and quantitative nature of such measurements makes them highly relevant for comparison with other imaging modalities (e.g. MEG). Initially, the motivation behind aCBV measurements and their relevance in multi-modality imaging is put forward. Subsequently, arterial spin labeling (ASL) is introduced and mathematical models of the induced magnetization show that in addition to measurement of flow (its usual role in MM) ASL can be combined with the 'Look Locher' sampling strategy to make quantitative measurements of blood volume. The experimental set up is described in detail and includes simulations showing how the pulse sequence developed can be optimized to give aCBV measurements. Results show that the sequence can be used for both fast Tt measurements, and the quantification of resting state aCBV. The aCBV values calculated using this technique are shown to be in agreement with those obtained in previous studies using invasive techniques. Further, a proof of principle pilot study shows how the technique may be used to measure activation-induced changes in aCBV.

7.1 INTRODUCTION

Since its inception in the early 1990's **[1],** Blood Oxygenation Level Dependent (BOLD) fMRI has been used extensively in functional brain imaging studies. However, as alluded to in the previous chapter, despite the successes, the fundamental biophysical mechanisms underlying the BOLD response remain poorly understood. The basic picture of the BOLD response is simple: an increase in electrical neuronal activity leads to an increased consumption of ATP (the brains primary energy source). Oxidative metabolism of glucose then increases to restore the ATP levels and this requires an increase in blood

flow in order to supply the required glucose and oxygen. The local vasculature responds to this increased demand by vascular expansion, which in turn allows a blood flow increase. The combination of enlarged blood volume, increased blood flow and the rise in blood oxygenation results in a measurable BOLD response.

BOLD imaging is undoubtedly limited by its inability to provide a quantitative measure of neuronal activity. In general, we assume that the greater the amount of neuronal activity, the larger the energy demands on the local tissue become, and therefore, the larger the BOLD response. This is likely to be true, at an elementary level, however accurate quantification of the BOLD response would require an in depth knowledge of the intervening steps. Attwell and ladecola [2] have argued convincingly that whilst the energetic requirements of active neurons are likely to be the major reason for the BOLD effect, they cannot be the active driving force behind it. They argue that: "The haemodynamic response to neural activity is not initiated by signals arising from an energy deficit of the tissue, but, rather, it is driven locally by fast glutamate mediated signaling processes, and more globally by amine and acetylcholine mediated neural systems." [2] In other words, it is neurotransmitter signaling that drives the increase in blood volume and blood flow, and it should be assumed that metabolic demand is intimately linked to neurotransmitter release.

There is some evidence in the literature to support this opinion. The importance of glutamate in blood flow regulation is highlighted by the fact that glutamate receptor antagonists block activation-induced changes in cortical blood flow. filial cells are also implicated in control of the BOLD response since gene knockout of the glial glutamate transporter can induce attenuated blood flow responses to somatosensory activation. Whilst the exact biochemical mechanisms are not yet fully understood, we know that activation of NMDA-receptors by glutamate induces the production of nitric oxide (NO) and adenosine (Adn.), both well-known vasodilators. Further, activation of astrocytic glutamate receptors stimulates the release of arachidonic acid (AA) and other related compounds (epoxyeicosatrienoic acid (EET)) that are also powerful vasodilators. It is possible that release of these chemicals could induce the changes in local vessel volume

that are required to induce the increases in blood flow and volume required for the BOLD effect. A much-simplified schematic representation of this process is shown in Figure 7.1. For further detail, and the primary sources, the reader is referred to Attwell and Iadecola (2002), Fillez et al (1999) and Williams (2004) [2-4].

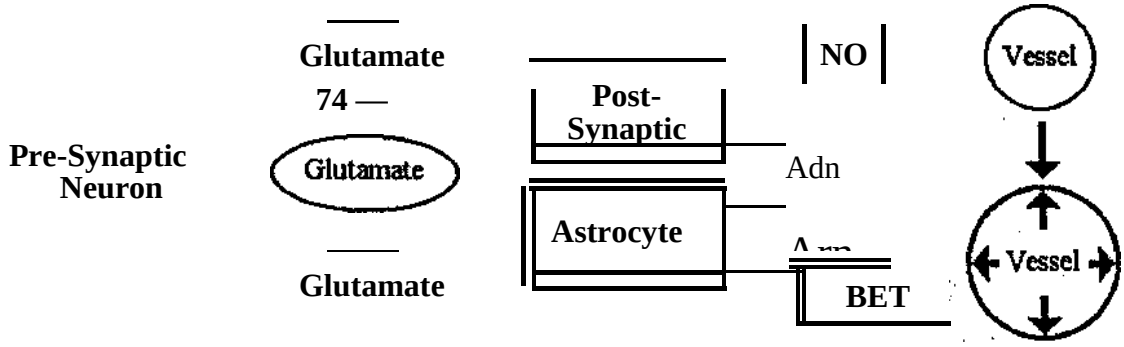

Figure 7.1: Simplified schematic representation of neurotransmitter induced vasodilation. Activation of NMDA-receptors by glutamate induces the production of Nitric Oxide (NO) and Adenosine (Adn). Activation of astrocytic glutamate receptors stimulates the release of arachidonic acid (AA) and other related compounds (epoxyeicosatrienoic acid (EET)). NO, Adn, AA, and EET are all vasodilators and may lead to an increase in blood volume, commensurate increase in blood flow, and ultimately a measurable BOLD eff*ect. (Adapted from [4].)* •

If the above theory holds true, then it follows that the closest measurable correlate (in MR imaging) to neuronal activity, and hence neuromagnetic effects measured using MEG, is (arguably) the change in arterial cerebral blood volume (aCBV) induced by the neurotransmitter related vasodilators. This change in aCBV should not be confused with the change in venous CBV described by Buxton et al. [5] whose seminal work shows how the elastic properties of venous vessels leads to a pooling of deoxygenated blood in the venous compartment. Buxton's original model ignored any blood volume change on the arterial side, but showed that the elastic properties of the venous compartment may explain the origin of the post stimulus undershoot commonly observed in BOLD fMRI studies. In order to make clear the distinction between venous and arterial blood volume, one can consider a three-compartment vascular model, comprising an arterial and

capillary non-exchange compartment, a capillary exchange compartment and a venous compartment. This is shown schematically in Figure 7.2. In this model, we assume that neurotransmitter coupled vasodilators induce an increase in blood volume in the arteriole and capillary sections. This change in arterial and capillary blood volume mediates an increase in blood flow local to the site of neurotransmitter release. Blood flows from this first, non-exchanging compartment into a second compartment where exchange of blood oxygen, blood water and metabolites takes place between the vessel and brain tissue. Finally the blood passes into the venous compartment where the increased volume causes a ballooning of the elastic vessel wall (as described by Buxton et al. [5]).

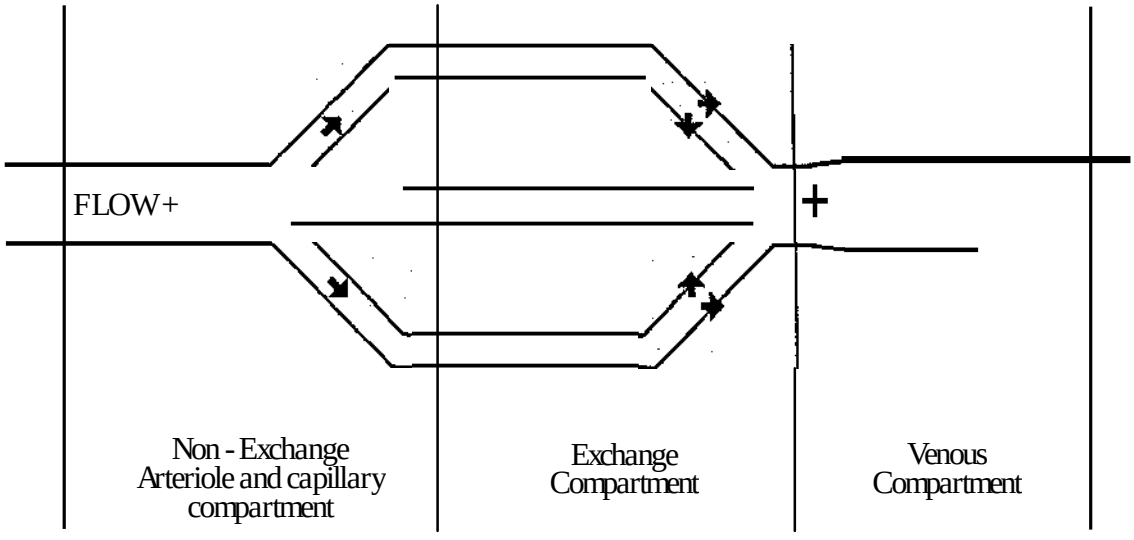

Figure 7.2: Schematic representation of a three compartment vascular model including the non-exchange compartment, an exchange compartment and a venous compartment.

The objective of the experiments to be described is to introduce a new methodology for the non-invasive measurement of arterial blood volume in the non-exchange compartment. The in vivo measurement of aCBV can provide important information about brain physiology and function. The previous arguments also suggest that when taken together with measurements of cerebral blood flow (CBF) and the BOLD response, aCBV may provide useful information on BOLD fMRI, as well as being a closely related correlate of the neuromagnetic response measured using MEG.

Typically, in vivo measurements of total CBV have been obtained using contrast agents, whilst arterial CBV (aCBV) has been measured using intravascular perfluorocarbon and ^{19}F NMR [6, 7]. However, these are invasive techniques and hence restrictive relative to a non-invasive imaging methodology. More recently, non-invasive aCBV measures have been achieved using arterial spin labeling (ASL) techniques [8], however to sample sufficiently the arterial inflow curve, several TI values are required, making experiments time consuming (-60min). In the experiments that follow, ASL techniques [9, 10] are used in combination with a Look-Locher sampling strategy [11] and Echo Planar Imaging [12] (see also chapter 3) in order to derive non-invasively aCBV measures in under 15 minutes.

Initially, the Look-Locher Echo Planar Imaging (LL-EPI) technique [13-15] is used to make fast T_1 measurements and hence show that our LL-EPI sequence, implemented on the 3T MRI scanner at the SPMMRC, (see chapter 3) works correctly. Once implemented, the LL-EPI sequence is combined with arterial spin labeling in order to derive MR signals that are sensitive to aCBV. Using ASL, magnetization is labeled in a slice other than that to be imaged (usually using a 180° inversion pulse). The appearance of labeled blood is then monitored in the imaging slice such that the spatial distribution of blood flowing from the labeling slice to the imaging slice can be monitored. A number of techniques by which to do this are available and commonly used to measure either blood flow or blood perfusion between the vasculature and brain tissue. Here, Flow sensitive Alternating Inversion Recovery (FAIR) [16] and Signal Targeting using Alternating Radio-frequency (STAR) [17] are combined with the Look-Locher sampling strategy to obtain a signal from arterial blood that is related to arterial blood volume, which is quantified using the three compartment model and both the FAIR and STAR ASL techniques. Whilst this work is largely based on resting state aCBV measurements, it is clear that if useful information is to be gained with regard to neuronal activity and the BOLD response, then we require dynamic measures of changes in aCBV on brain activation. The limitations of the LL-EPI sequence and its effectiveness in measuring aCBV change are highlighted both in the discussion, and the following chapter.

7.2 THEORY

7.2.1 The LL-EPI Pulse sequence

The Look Locher sampling scheme [11] was originally devised as a fast method of measuring T1 relaxation times in both Nuclear Magnetic Resonance (NMR) and Electron Spin Resonance (ESR). The sequence comprises a single 180-degree inversion pulse followed by a train of low flip angle readout pulses and, in the case of Look-Locher Echo Planar Imaging (LL-EPI) [13], appropriately timed MBEST Echo Planar Imaging modules. This technique allows for repeated sampling of the longitudinal magnetization in real time as it recovers following the inversion pulse. A pulse sequence diagram of the LL-EPI sequence is shown in Figure 7.3.

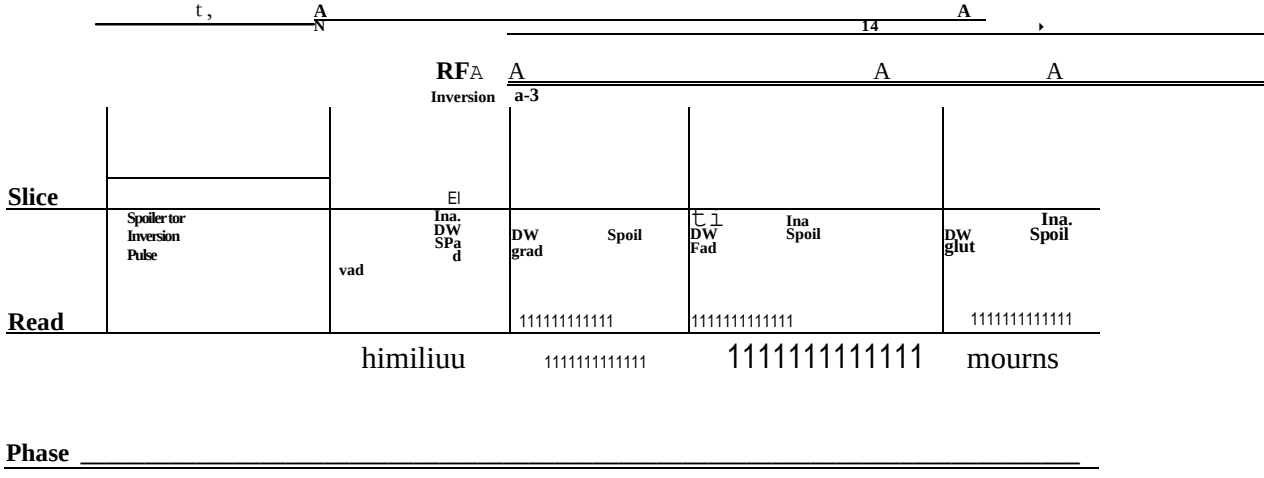

Figure 7.3: The Look Locher Echo Planar Imaging sequence. The sequence comprises a single 180° inversion pulse followed by a train of low flip angle readout pulses. Following each readout pulse an echo planar imaging module samples spatially the transverse magnetization. The sequence diagram also shows the relative timings of spoiler gradients. Incremental spoiler gradient pulses are used to prevent stimulated echoes following the readout pulses. A single large spoiler gradient is used to destroy any unwanted phase coherence brought about by the inversion pulse.

In using the LL-EPI sequence to measure T1 relaxation times, the small perturbations made on the magnetization by the readout pulses must be taken into account, since rather than following a 'standard' T1 recovery curve, the spin system is driven into a steady state by readout pulses as it recovers.

7.2.2 LL-EPI sequence **to** measure Ti relaxation

For a single spin isochromat, in order to model the longitudinal magnetization in the LL-EPI sequence, two separate effects must be considered; spin-lattice relaxation, and the effect of the RF readout pulses. In the case of a simple, homogeneous sample with no flow effects, the spin lattice relaxation is given by the solution to the Bloch equation:

$$\frac{dM(t)}{dt} = \frac{M - M(t)}{T} \qquad [7.1]$$

where M_0 is the resting state magnetization. If $M = 0)$ is the initial longitudinal magnetization, which is then allowed to relax for duration r, the final longitudinal magnetization, M(t = r) is given by:

$$M(t = r) = M_0 1 - exi - 1 + M(t = 0)exp(-\frac{r}{T}) \qquad [7.2]$$

The LL-EPI readout pulses used here were chosen to have a constant flip angle a, therefore following any single readout pulse, the longitudinal magnetization is perturbed such that:

$$M_{AFTER} = M_{BEFOR} E^{cos[a]} \qquad [7.3]$$

Using Equations 7.2 and 7.3, we find that if $A\ 1_{114}$ is the longitudinal magnetization of our single spin isochromat immediately following the $(n-1)^{th}$ pulse, and similarly M_n, is the longitudinal magnetization immediately following the n^{th} pulse then:

$$\begin{cases} M_o[1 - 2\ exp(-dcos[a] & for\ n=1 \\ 1M_0[1 - exp(-M\ exp(ilcos[a] & for\ n>1 \end{cases} \qquad [7.4]$$

Iterative application of Equation 7.4 allows us to monitor the state of the longitudinal magnetization as it recovers from the inversion pulse to the steady state imposed by the LL-EPI readout pulses.

In order to model the signal received during the LL-EPI sequence we must note that the LL-EPI readout pulses are slice selective in the z-direction, meaning that the flip angle a

the magnetization, $M_{,,}$, and the total signal received, $S_{,,}$, following the n^{th} readout pulse will all be a function of z. $S_{,,}$ is therefore given by the integral of magnetization across the slice width (i.e. along z), viz:

$$S_{,,} = \int_{-\infty}^{\infty} \text{isinkr(z)}\} 1/_{,,}(z)dz$$

$$S_n = \begin{cases} \text{isin}[a(z)1\, M_0[1 - 2\exp(\text{il z} & \text{for n=1} \\ \text{Isinkr(z)}\, M_0[1 - \exp^{i} - {}^{2}1 + M\exp & \text{z for n>1} \end{cases} \quad [7.5]$$

This simple description of the LL-EPI sequence shows how the signal received immediately following the **n^{th}** readout pulse is dependent on the longitudinal magnetization immediately following the $(n-1)^{h}$ pulse. Thus, in order to model mathematically the evolution of longitudinal magnetization throughout the sequence, an iterative process is required. This makes the LL-EPI sequence ideal for computational simulation and Equation 7.5 can be incorporated into algorithms to model the spin system and estimate T1. Modeling the LL-EPI sequence in this way is valid only if no flow is present in the sample. Any spins that may be flowing into the imaging slice will not have experienced perturbations due to previous LL-EPI readout pulses, and will therefore cause flow dependent signal fluctuations.

7.2.3 LL-EPI and Arterial Spin Labeling

The fundamental principle of ASL is to magnetically label nuclear spins (usually) using a 180° inversion pulse outside the imaging slice, and then to sample the magnetization in the imaging slice as labeled spins flow through it. The time taken for spins to pass through the imaging slice depends on the local blood velocity and the width of the labeled slab, and is generally on the order of a few seconds. During this period, the inflowing magnetization must be sampled at a number of different time points (TI values) and the resulting curve (showing in-slice magnetization as a function of time) can be used to quantify flow related effects. Traditionally, ASL has been used for measurement of both blood flow rate, and blood perfusion, however using standard techniques, only a single TI can be used per inversion pulse, making experiments time consuming.

The quantification of arterial cerebral blood volume using standard ASL techniques is difficult. This is because the measured signal is representative of both arterial flow in the non-exchange compartment, and perfusing blood in the exchange compartment. For accurate quantification, these two effects must be separated, meaning that two image sets must be acquired with and without blood flow suppression. This doubles the total experimental time making aCBV measures even more time consuming than flow and perfusion measurements. Furthermore, the convoluted nature of the measured signal can make the final results unreliable.

The LL-EPI sequence represents a mechanism for rapid sampling of the evolution of magnetization following some perturbation. This makes the LL-EPI sampling strategy ideal for combination with ASL, since it allows the measurement of inflowing magnetization at a number of time points (TI values) following just a single inversion. Furthermore, as we shall see, the LL-EPI readout pulses act to progressively suppress blood as it flows through the non-exchange compartment such that when it reaches the exchange and venous compartments, it's contribution to the measured signal can be assumed to be negligible. This suppression makes the signal from a LL-EPI-ASL sequence potentially more sensitive to aCBV than that from traditional ASL methodologies.

The combination of LL-EPI with the Flow sensitive Alternating Inversion Recovery (FAIR) ASL technique involves a simple modification to the original LL-EPI pulse sequence. In LL-EPI-FAIR, the inversion pulse is made to alternate between selective and non-selective excitations, both centered over the imaging slice (see Figure 7.4A). A selective inversion slab covers just the imaging slice (overlapping by a small amount to account for imperfections in the slice profile and ensure that all of the spins in the imaging slice are properly inverted). A non-selective inversion slab perturbs spins covering a wider area, modifying the inflowing blood to the imaging slice. The LL-EPI readout images acquired following a selective inversion are then subtracted from those acquired following a non-selective inversion. The contrast mechanism in the resulting

images is mediated by the difference between non-inverted, and inverted spins flowing into the imaging slice. This results in a set of flow sensitive images.

A combination of the LL-EPI sampling strategy with Signal Targeting with Alternate Radio-frequency pulses (STAR) follows a similar principle, the major difference being the offset of the inversion slabs from the imaging slice (see Figure 7.4B). In the STAR technique, magnetization is labeled (inverted) outside the imaging slice by a wide selective inversion pulse. This magnetization then flows into the imaging slice where it is sampled. As with FAIR, a subtraction is used, primarily to account for off resonance (Magnetization Transfer) effects [18]. In general, arterial flow in the head is assumed to be in an upward direction from the neck. The 'tag' inversion slab is positioned below the imaging slice and inflowing blood is monitored as it flows from the tagging slab into the slice. A control inversion slab of equal slab width is placed above the imaging slice. Both the tag and control inversion slabs are equidistant from the centre of the imaging slice. Subtraction of images taken following a tagging inversion, from those taken following a control inversion results in a flow sensitive image set.

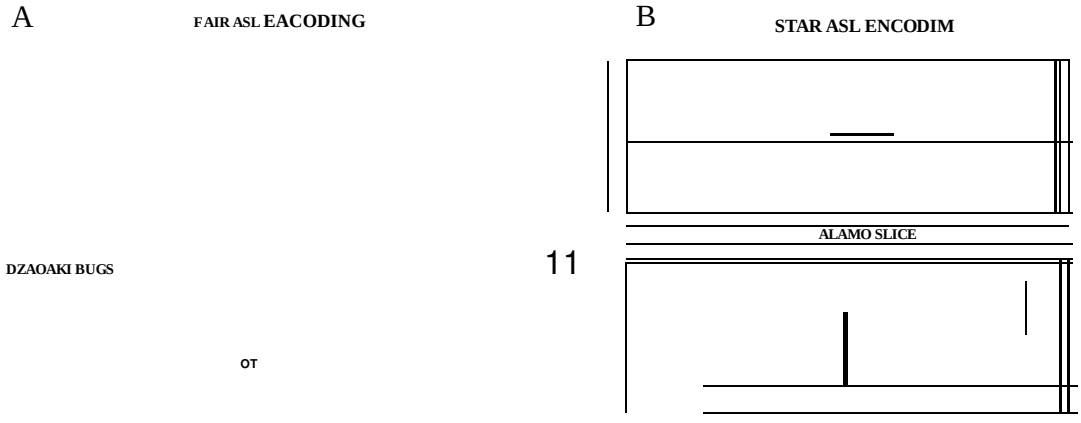

Figure 7.4: A summary of the FAIR and STAR ASL techniques

The advantage of the STAR technique is that it is inherently sensitive to direction. In general, one assumes that arterial flow is upwards in the head, and venous flow downwards. (This assumption may not hold true in some cases but as a general rule it

works!) This means that whereas in the FAIR images, flow into the imaging slice from above or below will cause a signal perturbation in the same direction, in the case of STAR, inflow from above the imaging slice will cause a perturbation in the opposite sense to inflow from below the imaging slice, (i.e. flow from above will appear dark whilst flow from below will appear bright).

7.2.4 Mathematical modeling of the aCBV signal

As described in the introduction, three separate compartments are required in order to describe aCBV and activation induced aCBV change (see again figure 7.2). Initially, we assume that following an initial transit time, 8,, magnetically labelled blood flows into the non-exchange compartment of the imaging plane where it gives rise to a difference signal. Blood remains in this non-exchange compartment for a time $_r$ before entering the exchange compartment, and then ultimately the venous compartment. As described above, we assume that the progressive suppression of the magnetization in these two latter compartments leads to them having little or no effect on the overall measured aCBV-sensitive signal. The exchange and venous compartments are therefore omitted from the model. In practice, this means that all blood in the imaging slice contributing to the aCBV signal is assumed to reside in the non-exchange compartment. This is a major advantage of LL-EPI-ASL over the more traditional ASL methodologies and is a requirement for accurate quantification of aCBV.

The mathematical model of the flow signal measured using LL-EPI is complicated by magnetization perturbations brought about by the readout pulses. In order to gain a physical interpretation of this signal, consider Figure 7.5, which shows a simplified model of blood flow through the non-exchange compartment, taken at a specific time point of interest, **tints** immediately prior to the fourth readout pulse. For the purposes of this example, we assume that $r_{e.} > S_a + t_i + 30$ meaning that labeled blood has not reached the exchange compartment by time $t = ti_{n,}$. (Note that this is not generally the case since for larger blood flow rates, tagged blood may have flowed through the non-exchange compartment during this interval. The final implementation of the mathematical model will allow for all possibilities, this single example is used only to illustrate the

principle.) The flow rate F is defined as the volume of blood passing some stationary point, per unit time. Meaning that absolute volume measurements are given by the flow rate multiplied by a time interval. With this in mind, it follows that total aCBV in the non-exchange compartment is given by:

$$aCBV = Fr_u, \qquad [7.6]$$

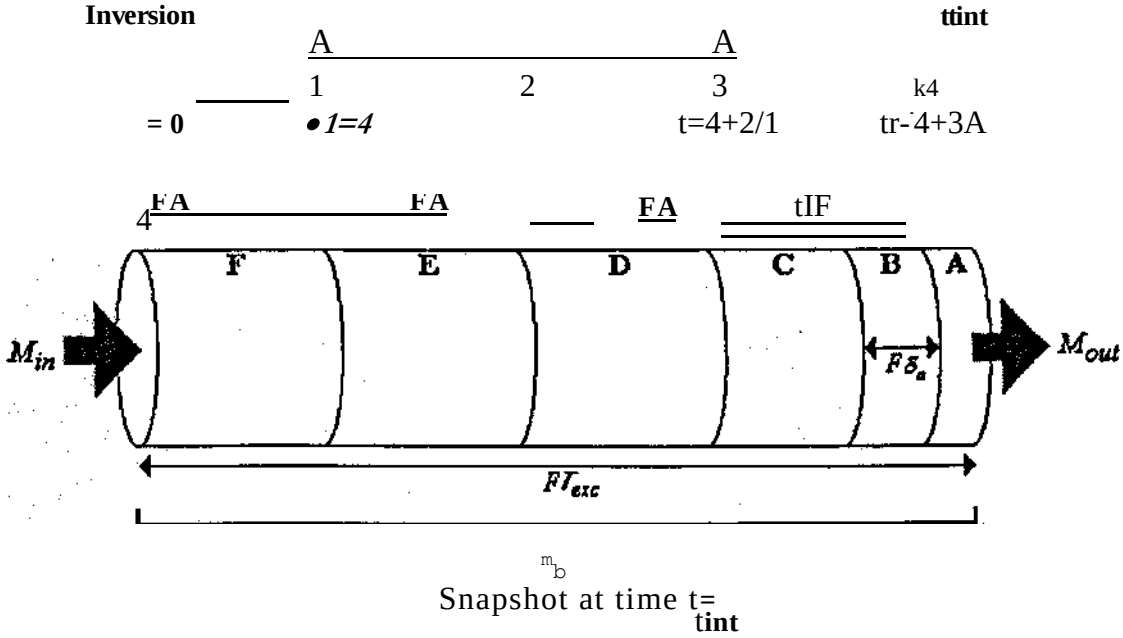

Figure 7.5: A simplified view of the non-exchange compartment showing how the temporal dynamics of the LL-EPI sequence lead to sectioning of the non-exchange blood volume.

As shown in Figure 7.5, the LL-EPI sequence has caused the non-exchange compartment to be divided into 6 sections, each having its own characteristic spin history, and hence magnetisation. The magnetisation in each of these sections can be explained in terms of the pulse sequence, which, for ease of explanation, we will assume to be LL-EPI-STAR (see Figure 7.4B). The blood in section 'A' was within the non-exchange compartment of the imaging slice at time t = 0 and therefore will have experienced each of the three LL-EPI readout pulses that have passed (but will not have experienced the initial inversion pulse). The blood in section 'B' was initially outside the imaging slice, however it too will not have experienced the inversion pulse since it's initial position was between the

imaging slice and the tagging slab. (See also Figure 7.4. Due to slice selection gradient and RF imperfections, a small gap is left between the tagging slab and the imaging slice. Magnetisation in section B originally resided in this gap.) It will have flowed into the imaging slice between t = 0 and t = t_i (since for this example we assume 15. < t;) and so will have experienced LL-EPI readout pulses 1, 2 and 3, meaning that although its origin is different, at t = , it's magnetisation will be equivalent to that of blood in section 'A.'

Blood in section 'C' was within the inversion slab at t = 0 and so spins in this section will have initially been inverted. This blood then flowed into the imaging slice between t = 0 and t = t_i and so will also have experienced the three LL-EPI readout pulses. This means that the magnetisation in section C can be calculated as having seen a single 180° pulse and three readout pulses. Blood in section **'D'** will also have experienced the inversion pulse, however because it flowed into the imaging slice between t = t_i and t = t_i + A , it will have 'missed' the first readout pulse and only have experienced pulses 2 and 3. A similar argument suggests that blood in section `E' will have experienced the inversion pulse and readout pulse 3. Finally, Blood in section 'F' will have experienced the inversion pulse, but as yet has not experienced any LL-EPI readout pulses since it arrived in the time interval between t = t_e + 2A and t = t_i + 30 . Between each of the pulses, blood in all compartments relaxes as per Equation 7.2.

This sectioning of the non-exchange compartment highlights the complications brought about by the LL-EPI sequence. A range of blood magnetisation exists within the non-exchange compartment (e.g. sections A — F) and the aCBV sensitive signal must be modelled mathematically based on all elements within this range. The model is complicated further by the fact that many arterial vessels will exist within a single image voxel. This means that in reality, for any given voxel, both S. and $r_{«}$ will not be single valued, but rather represent a continuous range of values corresponding to the passage of blood along different paths within the vasculature. For this reason, the model is implemented using average values of both 8_a and r_{ex},, and an average value of magnetization calculated across all sections within the non-exchange compartment.

The mathematical model of the flow signal is based on three variables, —in, M Mout and Mb. Min represents the magnetisation of blood flowing into the non-exchange compartment. Mout represents the magnetisation of blood flowing out of the non-exchange compartment, and mb represents the average blood magnetisation per unit volume inside the non-exchange compartment. Total magnetisation is therefore given by $M_b(t) = aCBVm_b(t)$. **Given that** $m_b(t)$ **is the mean magnetisation per unit volume of blood inside the non-exchange compartment at time t, and** m_{bo} **is the unperturbed value of blood magnetisation per unit volume then, assuming a LL-EPI-STAR sequence, we can write:**

$$(M_b(t)) = 0 \text{ for } t < \qquad [7.7]$$

and

$$aCBV\frac{d}{dt}(m_b OD - \frac{aCBV(M_b^{\circ} M_b OD + FA\,1\,kW - FM_{...}(t)\,for\ t_{8,}}{T1b} \qquad \textbf{[7.8]}$$

where F indicates blood flow, TH, is the spin lattice relaxation time for arterial blood, $Mi_n(t)$ **is the bulk magnetisation of blood flowing into the non-exchange compartment at time t, and** $M_{out}(t)$ **is the bulk magnetisation of blood flowing out of the non-exchange compartment at time t. Notice that the magnetisation per unit volume has been multiplied by aCBV in order to give bulk magnetisation.**

Now consider a short interval between readout pulses in the LL-EPI sequence. (Note the interval A is chosen such that a number of readout pulses occur within the time interval T_{om}**) An example is highlighted in Figure 7.6:**

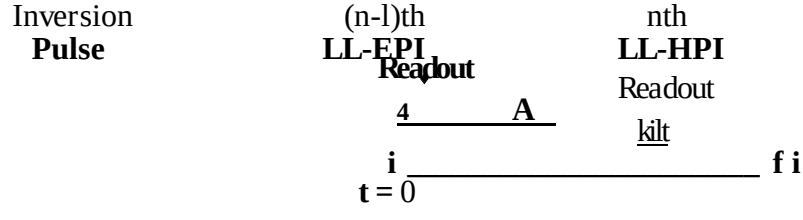

Figure 7.6: Interval of interest in the LL-EPI sequence, t represents the time elapsed since the $(n-1)^{th}$ LL-EPI readout pulse. **.e1** is the spacing between readout pulses.

The magnetisation of the inverted blood flowing into the imaging slice at time t is given by:

$$M_{,,} = S_{,;}\ exp-\text{—}$$

$$\left(\right.$$

$$\text{Tlb} \quad \text{+MbO} \quad - \qquad [7.9]$$

$$1-eXp\ t\text{—}$$

$$\text{k , T l b}$$

where $S_{,;}$ is the magnetisation of the inflowing blood at the time of the $(n\text{-}1)^{h}$ readout pulse.

Similarly, the magnetisation flowing out of the imaging slice at time t is given by:

$$Mow = S_{ro}\ ex\ -T + M_{bo}\ 1\text{–}eXP \qquad [7.10]$$

$$T_{lb} \qquad T_{lb}$$

where $S_{,0}$ is the magnetisation of blood flowing out of the non-exchange compartment at the time of the $(n\text{-}1)^{h}$ readout pulse. Inserting Equations 7.9 and 7.10 into Equation 7.8 we find that: **[7.11]**

$$aCBV \pm(m_b(0^1)=\frac{aCBV(m_{bo}\text{-}mbOD\ \mathbf{r}_{6\,ro}\ \mathbf{1}}{T_{lb}} + FLS - S_{jexp}{}^{f} \qquad T_{lb}$$

[7.12]

which can also be written:

$$\frac{1}{dt}(m_b(t))+\frac{1}{Tib}m_b(t)=\frac{71}{7;_1,\ aCBV}\text{--}\,^{\circ}+\,^{F}\,[S\bullet - S\,jexp$$

This linear, first order ODE is of the form

$$y'(t)\text{-}t\text{-}\ Py(t)= Vt) \qquad [7.13]$$

where

$$^{P} = \mathbf{Xrb} \qquad [7.14]$$

$$Q_{=}\ T_{i,,}\ + aCBV\ (S"\ -\ S\ )exp\ -\ ^{t} \qquad \textbf{[7.15]}$$

$$\backslash\ rib$$

The general solution to this equation is given by:

$$y(t)= exp(-\ 1)p\ exp(1)dt + C\ exp(-\ 1) \qquad [7.16]$$

where

$$I = \int P\,dt = \qquad [7.17]$$

and C is the constant of integration. Substituting Equations 7.14 — 7.16 into Equation 7.13 and integrating we find that:

$$?NOW = ?no + \frac{Ft}{a}\,(S_{,,} - S_{ao})\exp_{j}t \cdot Tie + C\exp\backslash\frac{T_{in}}{v} \qquad [7.18]$$

The constant of integration is determined by the boundary condition that at t = 0, $m_b(t) = m_{bi}$. Inserting this condition into Equation 7.18 it can be shown that:

$$c = -M_b^{\circ}$$

and therefore:

$$aCBVm_b(t) = aCBVm_{bo} + (s_4 - S_{,,,})Fte^{71'} + (m_{b/} - m_{bo})aCBVe^{716} \qquad [7.19]$$

Equation 7.19 represents the general solution to Equation 7.11. Of key importance is the physical interpretation of the three terms Sri, $S_{,0}$, and mbi, which represent the value of magnetisation flowing into the non-exchange compartment, the value of magnetisation flowing out of the non-exchange compartment, and the average value of magnetisation per unit volume in the non exchange compartment respectively at a time point immediately following the previous readout pulse (i.e. t = 0 in figure 7.6).

Simulation and data fitting algorithms modeling the LL-EPI-STAR/LL-EPI-FAIR signals were implemented using C [1]. The algorithm initially calculates the number of pulses that have occurred in the previous r . So for example, if the readout pulse of interest is at 850 ms, and $r_{,vrc}$ = 500 ms , then the algorithm works out how many pulses occurred in the previous 500 ms (for example 5 if A =100 ms). Then, starting from the signal at time (850.— 500 =) 350 ms, the algorithm loops around each pulse and calculates progressively the flipped blood signal using Equation 7.2. This iterative process allows calculation of the mean blood magnetization exiting the non-exchange compartment at

the time point of interest (i.e. M_{out}). Magnetization entering the non-exchange compartment (Mi_n) is given simply using Equation 7.1 since it will not have experienced any LL-EPI readout pulses, and therefore no iterative calculation is required. Given $\mathbf{Mi_n}$ and $_{Mout,}$ the average magnetization, mb, within the non-exchange compartment is given by Equation 7.19.

After a time **4 (-4 +** r_ad tagged blood passes from the non-exchange compartment, to the exchange compartment and water (along with oxygen and other metabolites) exchanges between the blood and tissue. The difference signal for the exchange compartment is given by

$$\frac{\quad}{\mathbf{dt}} = 0 \ \mathbf{for\ t <} \qquad [7.20]$$

$$\frac{dMsu\ .Ald,,,e(t)^{-111}0,,i.\ \mathbf{.fM_kW}}{\mathbf{dt}} \qquad \mathbf{fA\ I_d.(1)\ for\ t\ z\ 8_c} \qquad [7.21]$$

Where **f** is the perfusion rate, and **A** the blood:brain partition coefficient. Notice that the main differences between Equation 7.20 and Equation 7.7 are the inclusion of the blood perfusion term, **1,** and the blood:brain partition coefficient **A.** Equation 7.21 can be solved a similar way to Equation 7.7 in order to describe relaxation of spins in the exchange compartment. The aim of the experiments that follow is to calculate aCBV in the non-exchange compartment and therefore whilst Equation 7.21 proves instructive to highlight the differences between the non-exchange aCBV model, and a more classical perfusion model, the solution to this equation is not to be used in detailed mathematical modelling of the experiments to be described. The exchange compartment model is however used in simulations in order to show that the readout pulses enable full suppression of the exchange signal.

The C algorithm was implemented by Dr S.T.Francis, Sir Peter Mansfield Magnetic Resonance Centre, School of Physics and Astronomy, University of Nottingham, UK.

7.3 EXPERIMENTAL METHOD

7.3.1 Sequence optimization

As alluded to in the previous section, blood flowing through the non-exchange compartment, destined for the exchange site is progressively suppressed by the LL-EPI readout pulses if the readout pulses are separated by a time less than *rexc*. This suppression means that if short spacing between readout pulses and high flip angles are employed, the longitudinal magnetisation of blood reaching the exchange site is greatly reduced. This, in turn, leads to a reduced sensitivity of the LL-EPI sequence to the exchange component and represents a major advantage of LL-EPI over the more traditional ASL methodologies in measurement of aCBV. This is illustrated in Figure 7.7, where the compartmental signals are compared for standard FAIR, and LLEPI-FAIR sequences with different flip angles.

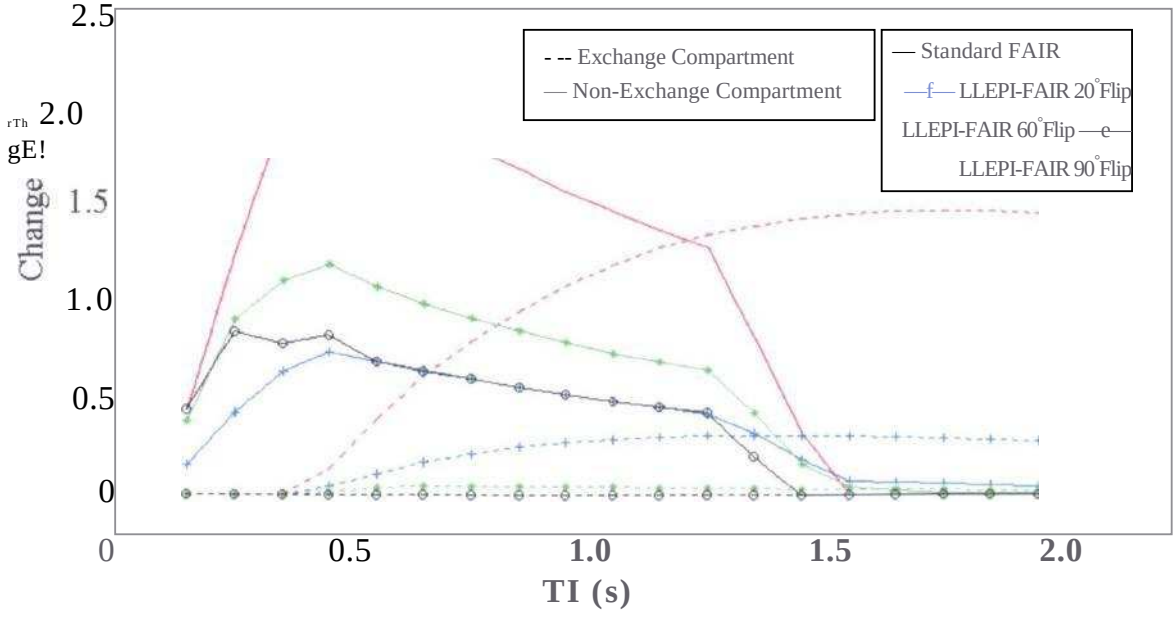

Figure 7.7: Simulation of the non-exchange/exchange compartment difference curves for the FAIR and LLEPI-FAIR sequences. LLEPI-FAIR curves are shown as a function of readout pulse flip angle.(Simulated assuming LI = 100 ms, CBV =1.5 %, CBF =110 m1/100g/min, d_a =0./s, r_{ex}= 0.3s, Ac = 0.4s, and time taken for the non-selective bolus to pass through the arterial compartment = 1.3s)

In measuring the standard FAIR blood magnetization inflow curve, two distinct maxima are observed, the first due to the non-exchange component (solid line) and the second due to the exchange component (broken line). As shown in the figure, these two peaks overlap substantially and their separation is possible only by undertaking two experiments, one of which incorporates the use of a diffusion weighted pulse in order to suppress the signal from flowing spins (see also section 7.5.2). In LLEPI-FAIR with large flip angle and small readout spacing, the above simulation shows that the exchange compartment is progressively suppressed as the flip angle is increased, leaving the difference signal weighted to the non-exchange compartment. Conversely, at low flip angle and long readout spacing, the sensitivity of LLEPI-FAIR to perfusion can be increased. In this application, the signal of interest is that in the non-exchange compartment. For this reason readout pulses with a flip angle of —50° were chosen to optimize both signal to noise of the non-exchange compartment, and suppression of the exchange compartment. Other sequence parameters were also extracted from this initial simulation and 20 LL-EPI readout pulses were used in order to sample adequately the signal of interest. The initial delay t_i was set to 150 ms. (Initially 100 ms was used but at this low value, eddy currents persisting after the inversion spoiler gradient pulse caused artifacts in the first LL-EPI image.) The delay between readout pulses, A, was set to 100 ms as per the simulation.

7.3.2 Spoiler gradients

One of the main difficulties with the LL-EPI sequence is the appearance of image artifacts caused by the persistence of phase synchronization from one readout pulse to the next. The mathematical model of the LLEPI sequence, summarized by Equation 7.19, requires that no transverse magnetization persists between RF pulses, however this may not be the case if: i) $\mathbf{T_2}$ * is long compared to the sampling interval A, or ii) the induced transverse magnetization is refocused by stimulated echoes. Unwanted transverse magnetization can be dephased by the inclusion of a spoiler gradient placed immediately after the MBEST imaging module. Following image acquisition, these spoiler gradients comprise a single positive gradient pulse that dephases spins and crushes any remaining transverse magnetization. Whilst a spoiler of fixed magnitude will destroy persisting

transverse magnetization induced by a previous RF pulse, unfortunately it would have no effect on the reduction of echo coherence caused by stimulated echoes. This is because, magnetization that is dephased by a spoiler gradient following the first readout pulse may be refocused by a spoiler gradient, equal in magnitude, in a later readout pulse, thus leading to its appearance as an artifact in later images. This means that in order to ensure suppression of stimulated echoes, one must incrementally increase the amplitude of the spoiler gradient pulses with the readout pulse number **(n).** Previous work by Wang et al [19] has shown that in an ideal sequence, spoiler amplitude should increase as a geometric series in n, and this ensures total suppression of stimulated echoes. However, they also show that an arithmetic series is very nearly as effective, far easier to implement, and is less demanding on the gradient coils and amplifiers. For this reason an arithmetic series was chosen here.

In addition to incremental spoiler gradients after each readout pulse, a single, large spoiler gradient was also applied after the 180-degree pulse in order to eliminate any unwanted phase coherence induced. Also, the sequence was run with a short (3 s) TR, so that magnetization could remain following each LL-EPI set. In order to ensure that this was not the case, a second large spoiler gradient pulse was included at the end of each LLEPI set.

7.4 PHANTOM T1 MEASUREMENTS

All LL-EPI data were obtained using the 3T MRI scanner described previously, with a custom-built head gradient coil and a whole head TEM RF coil. Transaxial images were acquired with the phase and readout gradient fields in the x and y directions respectively. Initially, the LL-EPI technique was used to measure T_i in a phantom. Values taken from these initial LL-EPI experiments were then compared to those obtained using a standard inversion recovery sequence in order to ensure that the LL-EPI imaging sequence and spoiler gradients were correctly set.

7.4.1 Experimental method and data processing

The sequence was set up and run with t_i =150 **ms ; A =100 ms , N =** 20, and a flip angle (FA) of approximately 50° (though this was shown to vary across the sample due to inhomogeneity in **B_1).** MBEST EPI images with an in plane resolution of 3 mm x **4 mm and a slice thickness of 6 mm were acquired using a matrix size of 64 x 64 and echo time of 35 ms. The inversion spoiler, the incremental spoilers, and the end spoiler were optimized by amplitude modulation in order to ensure minimal effect of persisting transverse magnetization and stimulated echoes. (Optimization was performed for each individual subject or phantom. In general, spoiler values were lower for in-vivo imaging than they were for the phantom.) 100 sets of 20 LL-EPI images were acquired in order to allow for signal averaging, and thus compensate for the lower signal to noise in LL-EPI when compared to the standard IR sequence. In order to account for T_i saturation effects in the LL-EPI images the first 10 LL-EPI sets were discarded and only the final 90 used to formulate an average.**

The inversion recovery sequence also employed MBEST EPI readout modules with identical image resolution and matrix size. The sequence parameters were TR = 18 s, TE = 35 ms; FA — 50° and TI values of 150; 250; 350; 450; 550; 650; 750; 850; 950; 1050; 1150; 1250; 1350; 1450; 1550; 1650; 1750; 1850; 1950; 2050; 3050 and 4050 ins.

The phantom itself had previously been constructed from agar gel, water and gadolinium in various concentrations. The phantom had four separate compartments with concentrations of 16µM Gd/25m1 — 1.8% w/w agar; 11µM Gd/25m1 — 1.8% w/w agar; 9.5µM Gd/25m1 — 1.6% w/w agar and 0µM Gd/25m1 — 0.25% w/w agar, which had been selected specifically to give T1 values of approximately 500ms 700 ms, 800 ms and 3000 ms respectively.

The recovery of longitudinal magnetization following an inversion pulse involves a change in signal polarity at the null point (as shown in Figure 2.10). However MR images are generally displayed in magnitude form in order to account for any phase variation caused by magnetic field inhomogeneity. It would be possible to fit a mathematical

model of the modulus signal derived from Equation 7.2 (in the case of inversion recovery) or 7.5 (in the case of LL-EPI) in order to obtain final **Ti** values, however this is less robust than fitting to correctly signed data. Further, a modulus fit becomes even more unreliable using the LL-EPI sequence due to its inherent low signal to noise. For these reasons, sign correction was applied to both the inversion recovery and the LL-EPI image sets.

In order to obtain correctly signed images the technique of Gowland and Leach [20] was employed. This algorithm is based on the premise that a relative phase shift of 180-degrees is observed when the spin signal changes from negative to positive (i.e. either side of the zero crossing during signal relaxation). The algorithm to correctly sign modulus images was implemented in MATLAB and compares the phase of the final image in a LL-EPI (or IR) image set to that in subsequent images. When a phase change of 180° or larger is observed then the sign of the image is changed. It should also be noted that due to the presence of various values of **Ti** in a single image, this must be done on a pixel-by-pixel basis.

In order to account for variation in flip angle across the phantom, 20 MBEST EPI images (64x64 matrix size and repetition time of 18 s) were acquired at 20 different RF field amplitudes. These data were fitted using a squared sinusoidal model in order to estimate flip angle variation. These fitted flip angle data were then used in signal modeling.

Modeling of the LL-EPI recovery signal was achieved as per section 7.2.2 and this iterative algorithm was implemented using MATLAB. Modeling of the inversion recovery data was achieved as per section 7.2.2. In both the inversion recovery and **LL-EPI** cases, fitting of the modeled signal to the measured signal was realized by minimization of the sum of squares of residuals between the modeled and experimental data. The fitting algorithm itself was an unconstrained non-linear optimization [21], which is an inbuilt function in the MATLAB programming environment. Parameters **Ti** and Mo were estimated based on this fitting procedure and the modeled data.

7.4.2 Results

Figure 7.8 shows the recovery curves taken from a single voxel for both the LL-EPI and IR sequences. The estimated value for T_i was 0.71± 0.01 s in the case of the IR sequence, and 0.70 ± 0.01 s in the case of the LL-EPI sequence showing equivalence between the two sequences for this particular case.

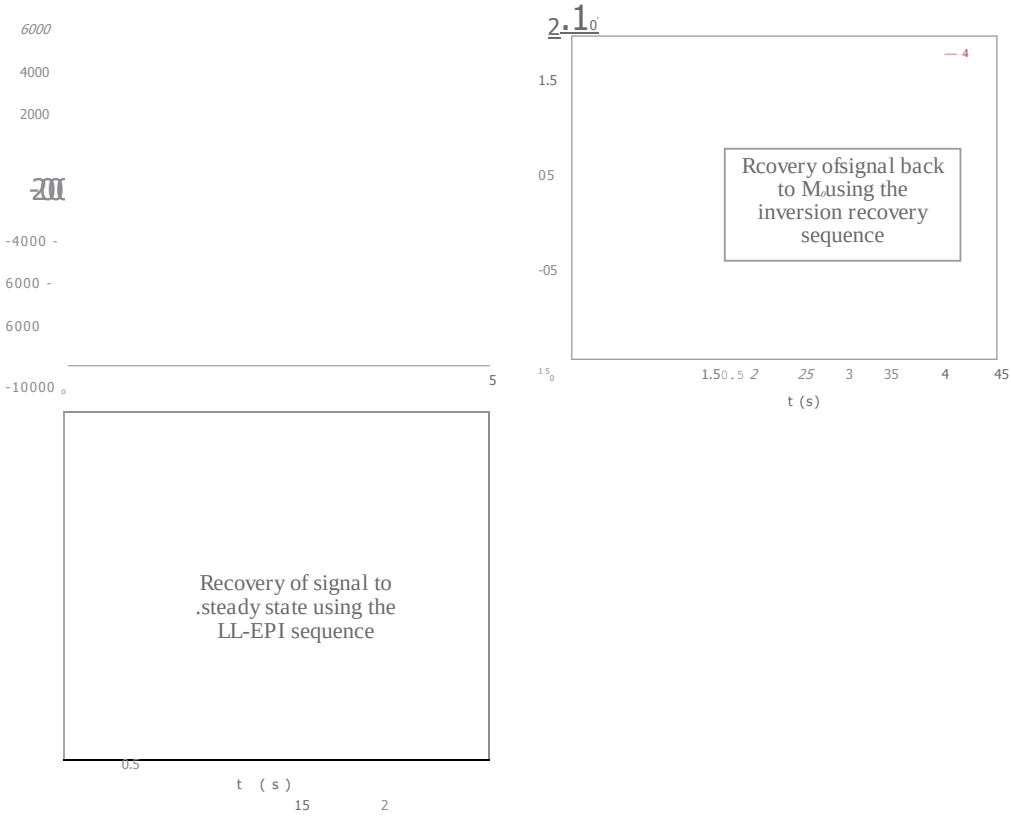

Figure 7.8: Recovery curves taken from a single voxel for both the LL-EPI and IR sequences. The red crosses show the experimental data and the blue line show the theoretical fits.

Ti maps derived from the phantom data are shown in Figure 7.9. Clear differences in the T_i values are observed for the 4 quadrants of the phantom. Furthermore, these appear to be in agreement across the two sequences.

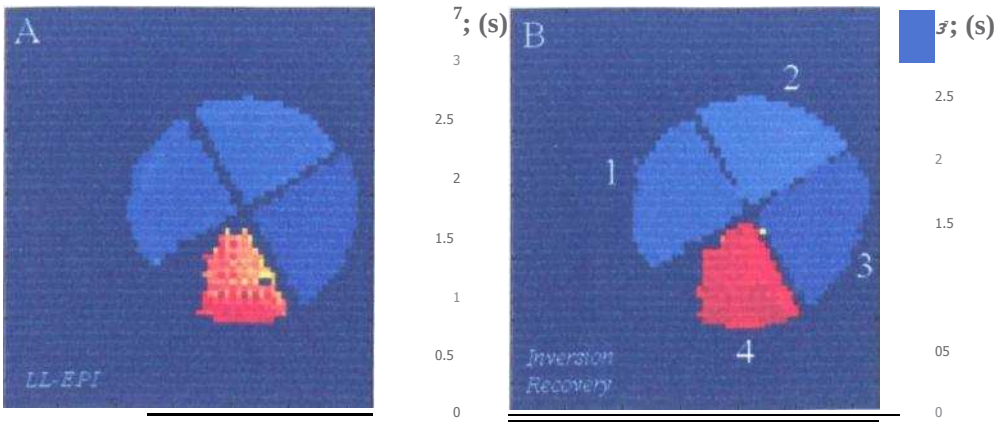

Figure 7.9: T1 maps derived from the phantom data. A shows the T_1 map derived from the LL-EPI sequence. B shows the T1 map derived from the inversion recovery sequence

In order to assess quantitatively the equivalence between the LL-EPI and inversion recovery sequences, regions of interest were defined over the four quadrants of the phantom and mean T_1 values measured across these regions for both the LL-EPI and IR sequences. The results of this quantitative analysis are given in Table **7.1.**

SEQUENCE	Quadrant 1	Quadrant 2	Quadrant 3	Quadrant 4
LL-EPI	0.81 ±0.01 s	0.70 ± 0.01 s	0.51 ± **0.01** s	2.90 ± 0.1 s
IR	0.83 ± 0.01 s	0.72 ± 0.01 s	0.51 ± 0.01 s	3.0 ± 0.01 s

Table 7.1: Quantitative assessment of the Ti values derived from the LL-EPI and 1R sequences. Quadrant numbers are given in Figure 7.9.

In fitting the data, the optimization algorithm estimates M A 1 = 0)= $_0e^{-1}$%* in addition to the Tt for each individual pixel. Measurement of the variation in M(t = 0) across the image is a useful parameter since it reflects the induced resting state magnetization (Mo) of (in this case) the four quadrants of the phantom. Table 7.2 shows the M(t = 0) values calculated for all four quadrants in both the LL-EPI and IR sequences

SEQUENCE	Quadrant 1	Quadrant 2	Quadrant 3	Quadrant 4
LL-EPI	19300 ± 100	17600 ± 200	20000 ± 100	28100 ± 300
IR	19100 ± 100	17200 ± 200	19600 ± 100	27700 ± 200

Table 7.2: Quantitative assessment of the M(t = 0) values derived from the LL-EPI and IR sequences for all four quadrants.

7.43 Discussion

The above experiments show both the validity of the LL-EPI sequence in making Ti measurements, and that the LL-EPI sequence has been appropriately optimized. The occurrence of stimulated echoes or other image artifacts in the LL-EPI data would cause spurious data points that would not match the mathematical model of magnetization.

This, in turn, would cause differences in Ti values estimated across the image. The agreement between the two sequences implies that optimal spoiler gradient amplitudes and sequence timing has been obtained, thus preventing such errors.

The errors in the fitted **Ti** and M(t = **0)** values have been calculated either from timing uncertainties in the sequence itself, or quoted as standard error across pixel measurements. Small errors in the measured value of t, and **A** can cause empirical errors in the model timing, and therefore problems with the final T1 values obtained. Equivalently, imperfections in the phantom, or magnetic field inhomogeneity could cause spatial variation in parameter estimation. Errors were estimated using both empirical error, and standard error measurements. In all cases the larger of these two values is displayed, however in most cases these values concur.

7.5 ARTERIAL CEREBRAL BLOOD VOLUME MEASUREMENTS

Having used the phantom measurements as a means of setting up and validating the LL -EPI sequence, that sequence was then adapted for LL -EPI-FAIR and LL-EPI-STAR.

7.5.1 ASL sequence geometry

The FAIR ASL routine was implemented as shown in Figure 7.10A. The imaging slice was centered at the origin (i.e. given zero frequency offset) in the z-direction and was 6mm wide (3mm either side of the origin). The selective inversion slab was defined to be 20mm wide, again centered at the origin. The selective inversion was made to overshoot the imaging slice (by 7mm on either side) to ensure full inversion across this volume. The non-selective inversion slab was 200mm wide, and again was centered at the origin, (thus overshooting the selective inversion slab by 90mm on each side and the imaging slice by 97mm on either side). As noted in the theory section, the contrast mechanism for this sequence is provided by the difference between the selective and non-selective inversion slabs. In taking the difference images, one effectively observes a 90mm wide bolus of unperturbed blood (i.e. blood that has not undergone a 180-degree flip) flowing into the imaging slice.

In the STAR ASL sequence (B), the imaging slice was again centered at the origin (i.e. given zero frequency offset) in the z-direction and was 6mm wide (3mm either side of the origin). The 'tag' inversion slab was offset by 55 mm inferior from the origin and was **defined to be 90 mm wide. The control inversion slab was offset by 55 mm superior from the origin and was also 90 mm wide. (Notice also that for LL-EPI-STAR a saturation pulse was applied to the imaging slice prior to the tag or control inversion.)**

In both FAIR and STAR a 90mm wide bolus of labeled arterial blood flows into the imaging slice. In the case of FAIR this labeled blood comprises the unperturbed spins that remain outside the selective inversion slab, but within the non-selective inversion slab. In the case of STAR, the labeled blood comprises the inverted blood from the tagging inversion slab. In both cases the sequence geometry is equivalent and this is shown in Figure 7.10.

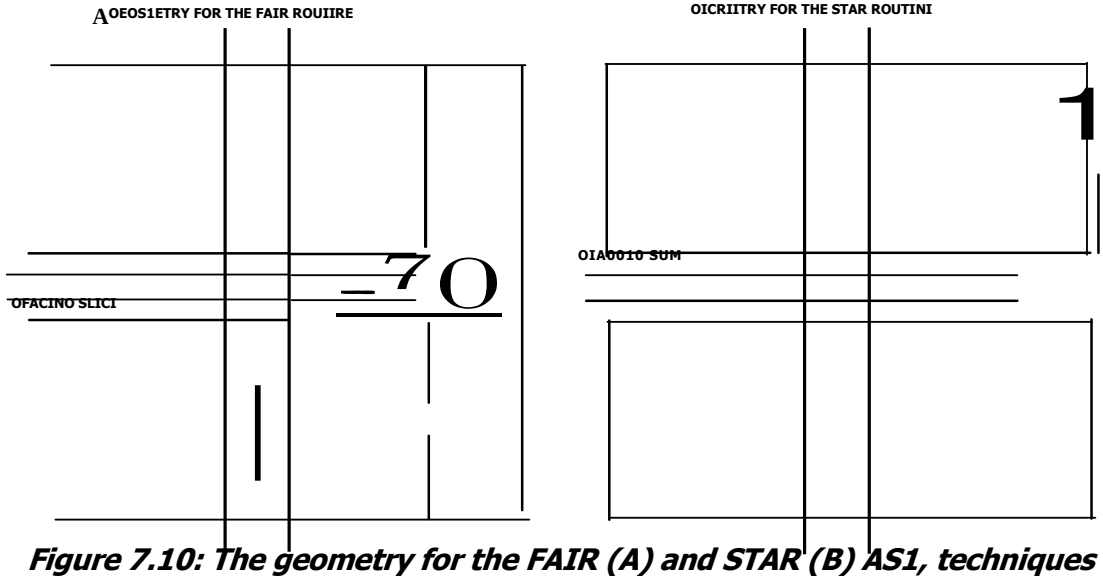

Figure 7.10: The geometry for the FAIR (A) and STAR (B) AS1, techniques

7.5.2 Diffusion weighting and b-values

Using the LL-EPI-ASL techniques, the effect of adding various levels of diffusion weighting were investigated. A bipolar gradient lobe (amplitude $G_{i,w}$ and duration g_m,) was added to the sequence following each LL-EPI readout pulse. This diffusion-weighted pulse dephases the magnetization from spins that arc moving with respect to the diffusion

gradient direction, which in this case was chosen to be the slice (or z) direction. The addition of diffusion weighted gradients in this way causes a suppression of moving spins such that:

$$S = S_0 exp(-bD) \qquad [7.22]$$

Where S is the measured signal in the presence of a diffusion-weighted gradient, So is the signal with no diffusion-weighted gradient, D is the diffusion coefficient and b represents the strength of the diffusion weighting and is given by:

$$b = 126 j^8 DW^{\frac{12}{3}} G_{DW}^2 \qquad [7.23]$$

where $y = 2.68 \times 10^8$ $rads^{-1}T^{-1}$ and G_{Dvi} is the diffusion weighting gradient strength.

Blood flow is not, in general, thought of as diffusion, or modeled using diffusion coefficients. However, diffusion weighting can still be applied in this way to suppress flow in large vessels. Application of the gradient field causes spins at any given position along the z-axis to dephase. If these spins were static, rephasing would be easily achieved by application of a second gradient of equal amplitude and duration but opposite polarity. However, if spins are in motion then dephasing and rephasing will take place at different locations with respect to the z-axis, therefore different field strengths, and so moving spins will remain dephased. For a given gradient duration and amplitude (and hence b-value) the effect of the diffusion weighting will be to dephase magnetization from spins flowing above some critical velocity v, with respect to the z-direction. This critical velocity is given by [22]:

$$v, — \frac{5}{(1)WGDv} \qquad [7.24]$$

In the experiments undertaken, five different b-values were employed, giving five different levels of velocity suppression summarized in Table 7.3. b-values were increased by modulation of the gradient amplitude (rather than the pulse duration). This was in order to maintain consistent pulse sequence timing for different diffusion weightings. Notice also that for a b-value of zero, i.e. no diffusion weighting, no critical velocity exists since flow at all rates can be measured by the ASL sequence. (In practice, a small

amount of diffusion weighting is inherent to the EPI pulse sequence, however this was assumed to be negligible.)

b-value (smm^4)	Critical velocity ti_c (mms^{-1})
0	N/A
0.2	76
0.9	38
2.6	22
4.4	17

Table 7.3: b-values and associated critical velocities.

7.5.3 The difference signal

As stated above, the flow signal is obtained by image subtraction, control — tag in the case of LL-EPI-STAR, or selective — non-selective in the case of LL-EPI-FAIR. This difference signal requires normalization prior to fitting and for this reason it proves instructive to examine the constituent components of the difference signal.

Consider the LL-EPI-FAIR signal recorded following a tagging inversion pulse. This can be written as:

$$S_{Tag} = S_c(aCBV\ldots 114_{Ob} \exp -\frac{t}{T_{2:}*} \quad [7.25]$$

Where S_c is the scanner factor and is used to account for amplifier gain etc. ***Mob*** is the resting state magnetization of blood, Mot is the resting state magnetization of tissue, $X1^{TAG}$ is the effect of the sequence on the inflowing tagged blood signal and X, is the effect of the sequence on the tissue signal. Similarly the signal recorded following a control inversion is given by:

$$S_{CO,,} = S, aCBV\,Al_{ob} \exp -- \quad [7.26]$$

Where $_x$ (**CONTROL**) is the effect of the sequence on the inflowing blood following a control inversion pulse. In subtracting the two signals, since X, (i.e. effect of the sequence on tissue) will be equivalent for both control and tag inversions we obtain:

$$S_{con,,.01} - S_{Td} = S_c .aCBV .M_{ob} \exp\frac{(}{T2b^*} \quad [7.27]$$

The appearance of a scanner factor in Equation 7.24 means that the recorded signal requires normalization. This was achieved by measurement of M(t = 0) using the LL-EPI sequence as described in section 7.4. This same LL-EPI sequence was applied to the head, ensuring that the inversion pulse was non-selective and therefore inflowing blood was not labeled. Assuming that the effect of flowing blood on the LL-EPI sequence is small we estimate that:

$$M(t = 0) = S_c M_{cv} \exp(* \quad [7.28]$$

Note that in making this measurement, a diffusion-weighting gradient (b = 4.4 smni[1]) was used in order ensure that any signal due to blood flow was minimized. Normalization of Equation 7.27 by 7.28 gives:

$$\frac{M}{M} \quad [7.29]$$

Which can also be written:

$$\text{Difference} = M\,0.EfFaCBV(X,'''TR°L - {}_{x}i:AG) \quad [7.30]$$

Noting that $\frac{Al c^4}{,} = $, the blood brain partition coefficient.

In modeling the LL-EPI-ASL signal, the signal following both the tag and control (or selective and non-selective inversion) are modeled separately and the difference signal obtained and fitted. $MO,EFF,$ was estimated using Equation 7.29 where 2 = 0.9 , $T2b^* = 50$ ms $T_{2t^*} = 45$ ms and the echo time was 35 ins.

It should be noted that another (more accurate) technique by which to normalize the LL-EPI-ASL signals is by direct estimation of the Me• of blood using LL-EPI-ASL responses taken from within the sagittal sinus. Such techniques do not require estimation of $2, T_{2b^*}$ and $T_{2, *}$ and so are thought to be more accurate. However, they are made difficult

to implement by the poor signal to noise ratio and resolution available in the required region.

7.5.4 Experimental details

All experiments were carried out on the 3T scanner at the SPMMRC on which both the LL-EPI-FAIR and LL-EPI-STAR sequences had been implemented. In all cases the sequence was run with t_i =150 **ms;** A =100 ms , **N =** 20, and a flip angle of approximately 50° (varying across the sample due to **B,** field inhomogeneity). MBEST EPI images of a single slice were acquired with an in plane resolution of 3 mm x 4 mm, a slice thickness of 6 mm, a matrix size of 64 x 64 and echo time of 35 ms. (The echo time was set specifically in order to allow sufficient time for diffusion weighted gradient pulses.) The inversion spoiler, the incremental spoilers, and the end spoiler were optimized by amplitude modulation for each individual subject. Three separate experiments were undertaken.

Initially, the LL-EPI-STAR sequence was used to confirm the validity of the technique. Two healthy volunteers with no known neurological disorders, head trauma, contraindication to MR, or medication were recruited for this initial study, which was approved by the local ethics committee. Three separate metrics were used for each subject. Firstly the LL-EPI-STAR sequence was run with a repetition time of 3 s and the inversion pulse alternating between tag and control every other LL-EPI set. In total 270 image sets were acquired, (i.e. 135 tag and 135 control) giving a total experimental time of under 14 **mins.** Secondly a LL-EPI experiment (TR = 3 s and 50 image sets) with diffusion weighting (b = 4.4smm') was undertaken in order to measure the normalizing factor. Finally an RF map was taken in order to measure variation in flip angle across the head. Following image acquisition, data were sign corrected (as described in section 7.4 using the Gowland and Leach method), motion corrected using Medx [23], and modeled as previously explained.

In the second set of experiments, the effect of various levels of diffusion weighting was investigated using the LL-EPI-FAIR technique. Data were acquired as above in four

healthy subjects. Five separate experiments were undertaken at five separate diffusion weightings (given in Table 7.3). In order to reduce total experimental time, the number of image sets acquired was reduced from 270 to 90 (45 selective and 45 non-selective) for each diffusion weighting. Images were processed as described above.

In the final set of experiments, the LL-EPI-FAIR and LL-EPI-STAR sequences were compared. Six healthy volunteers took part in the study and a total of 90 image sets (45 selective and 45 non-selective) were acquired using both sequences. Images were processed as described above in both the FAIR and STAR cases.

7.6 RESULTS

7.6.1 Quantitative aCBV Measurements

Figure 7.11 shows a set of difference images derived from the LL-EPI-STAR sequence for a single representative subject. No diffusion weighting was applied and therefore the flow signal remains both in large arterial vessels and the smaller arterioles and capillaries in grey matter. Notice that high signal intensity for large arteries occurs in earlier images, whereas the highest signal intensity in the smaller vessels occurs in later images. Notice also that the sagittal sinus appears dark, an example of the inherent sensitivity to flow direction in the LL-EPI-STAR sequence.

In order to highlight the differences in flow signal between vessel types two voxels of interest were selected. The first close to the large internal cerebral arteries and the second in the grey matter. Figure 7.12 shows the differences between the flow signal observed in these two regions. The upper two plots show the LL-EPI-STAR signal from the large internal cerebral arteries, the lower two plots show the LL-EPI-STAR signal in grey matter. In both cases the upper panel shows the raw signals whilst the bottom panel shows the difference signal. The positions of the two voxels are shown inset. Notice that in the case of the artery, the signal peaks earlier in time when compared to the grey matter. This is indicative of the faster flow in larger vessels. Notice also the higher signal intensity in the artery relative to the grey matter.

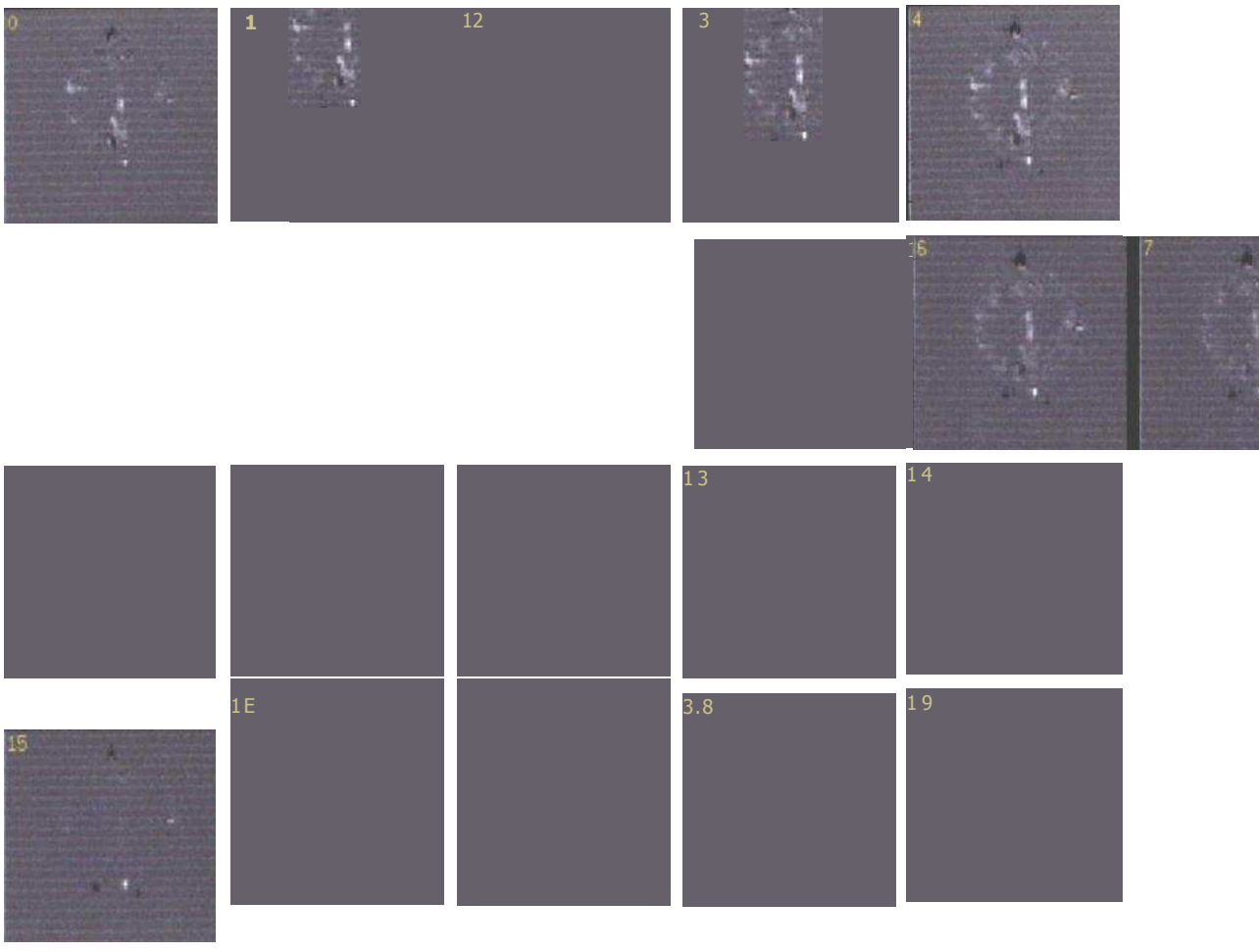

Figure 7.11: Difference images derived from the LL-EPI-STAR sequence for a single representative subject.

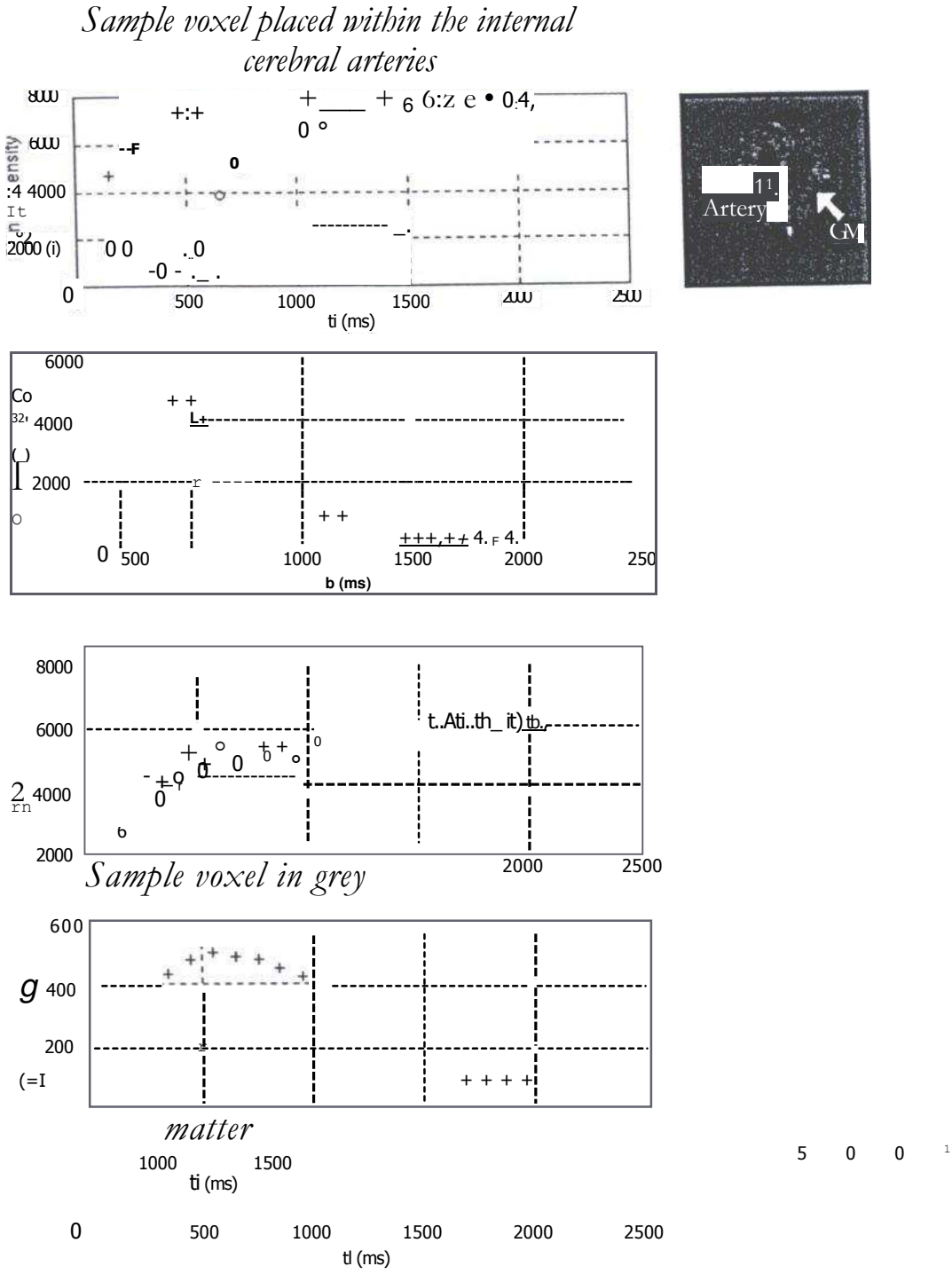

Figure 7.12: Flow sensitive signal. The upper two plots show the LL-EPI-STAR signal from a ROI positioned close to the large internal cerebral arteries. The lower to plots show the LL-EPI-STAR signal in grey matter. In both cases the upper panel shows the raw signal and the bottom panel shows the difference signal. For the raw data shown, the crosses represent the control data and the circles represent the tag. The positions of the two voxels are shown inset.

The difference signals from these two voxels were used, together with the least squares fitting algorithm and mathematical model to estimate aCBV values for the two pixels. Blood volume measurements were found to be 2.9 ± 0.4% and 17 ± 3% for the grey matter area and arterial area respectively.

Having successfully applied the fitting procedure to LL-EPI-STAR data from single voxels, the algorithm was then adapted to calculate aCBV values on a voxel by voxel basis. Such calculations resulted in an image showing the spatial variation of aCBV across the head. This is shown in Figure 7.13. Areas of highest aCBV are close to the major arteries. Areas of grey matter can also be seen, and the lowest aCBV measures are within the white matter regions as expected.

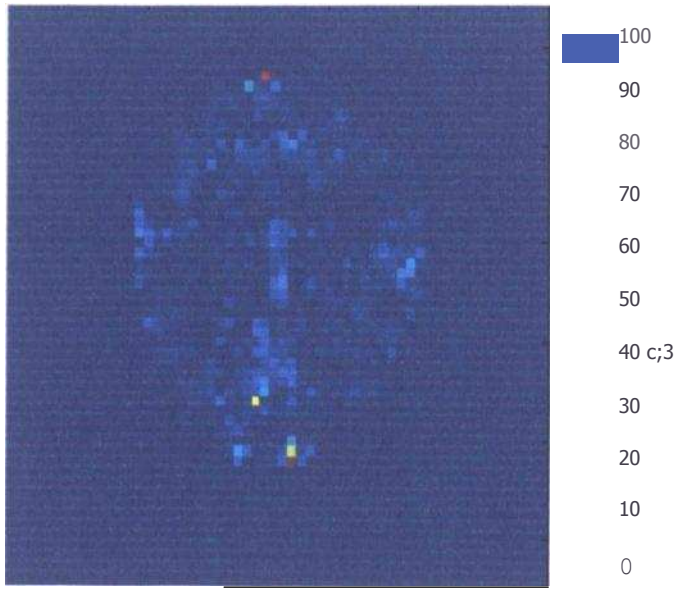

Figure 7.13: aCBV map derived from LL-EPI-STAR data.

7.6.2 **LL-EPI-FAIR with Diffusion weighting**

The LL-EPI-FAIR sequence was run with five different levels of diffusion weighting in order to assess its effect on the flow signal. The results from a single subject are shown in Figure 7.14. The data shown were taken from a large region of interest over the large internal arteries (shown inset) and averaged across pixels. Notice that, as expected, the flow signal is reduced with increased diffusion weighting. This is because the signal from blood in faster flowing vessels is attenuated by the bipolar gradient pulse. Note also that

at the highest level of diffusion weighting, the signal is completely eliminated. This shows the insensitivity of the LL-EPI sequence to the signal from the exchange compartment, a factor of the sequence design.

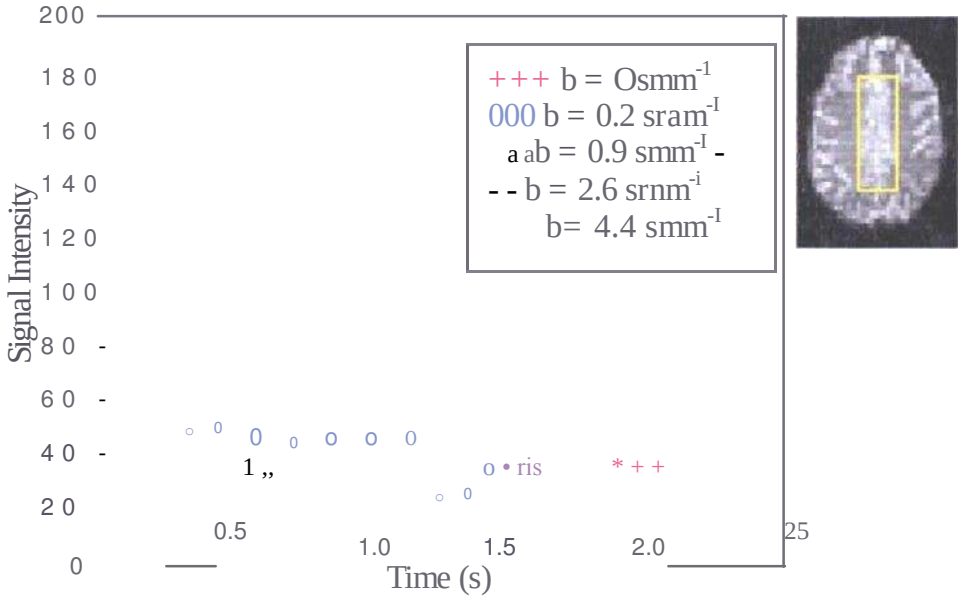

Figure 7.14: The effect of diffusion weighting on the flow signal measured using LL-EP1-FAIR.

In order to make a quantitative analysis of the effect of diffusion weighting on the flow signal and aCBV measurements, images were divided into 3 regions, the central region (region 2) containing the large arteries, and two lateral regions (regions 1 and 3) consisting mainly of grey and white matter. These regions are shown in Figure 7.15. Notice that the large veins at the front and back of the head have been omitted.

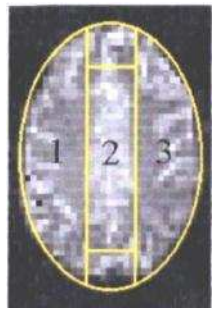

Figure 7.15: The three regions defined for quantitative analysis.

The mean (n = 4) percentage of blood in each of the three regions was derived as a function of b-value and critical velocity. These values are given in Table **7.4.** As expected, with no diffusion weighting, region 2 displays the greatest CBV as it contains the cerebral arteries; this is in agreement with the aCBV map in Figure **7.13.** Notice also that the percentage aCBV is reduced as b-value is increased.

b-value (smnf^{l})	Critical velocity (mnis"^{1})	aCBV Region 1 (%)	aCBV Region 2 (%)	aCBV Region 3 (%)
0	**N/A**	**0.7 ± 0.2**	**0.8 ± 0.2**	**0.5 ± 0.3**
0.2	**76**	**0.4 ± 0.2**	**0.2 ± 0.1**	**0.2 ± 0.1**
0.9	**38**	**0.4 ± 0.3**	**0.3 ± 0.3**	**0.3 ± 0.2**
2.6	**22**	**0.2 ± 0.2**	**0.2 ± 0.1**	**0.1 ± 0.1**
4.4	**17**	**0.05 ± 0.1**	**0.05 ± 0.1**	**0.03 ± 0.1**

Table 7.4: Quantitative analysis of the LL-EPI-FAIR data with diffusion weighting.

7.6.3 LL-EPI-FAIR vs. LL-EPI-STAR.

Finally, both the LL-EPI-STAR and LL-EPI-FAIR sequences were run on the same subject in order to assess the equivalence of the two ASL techniques. Figure 7.16 shows the LL-EPI-FAIR (left) and LL-EPI-STAR (right) timecourses taken from a voxel of interest derived from the difference images. In both cases, the upper panel shows the raw signals, averaged over all LL-EPI sets. Notice here that in the case of FAIR, data follow approximately an inversion recovery curve but are driven into steady state by the LL-EPI readout pulses. For the STAR case, data follow approximately a saturation recovery curve, but again are driven into a steady state by the readout pulses. The bottom panels in both cases show the difference signals. Selective — non-selective in the case of FAIR and control — tag in the case of STAR. Importantly, despite the differences in geometry of the two techniques, the difference curves look similar with approximately equivalent amplitudes.

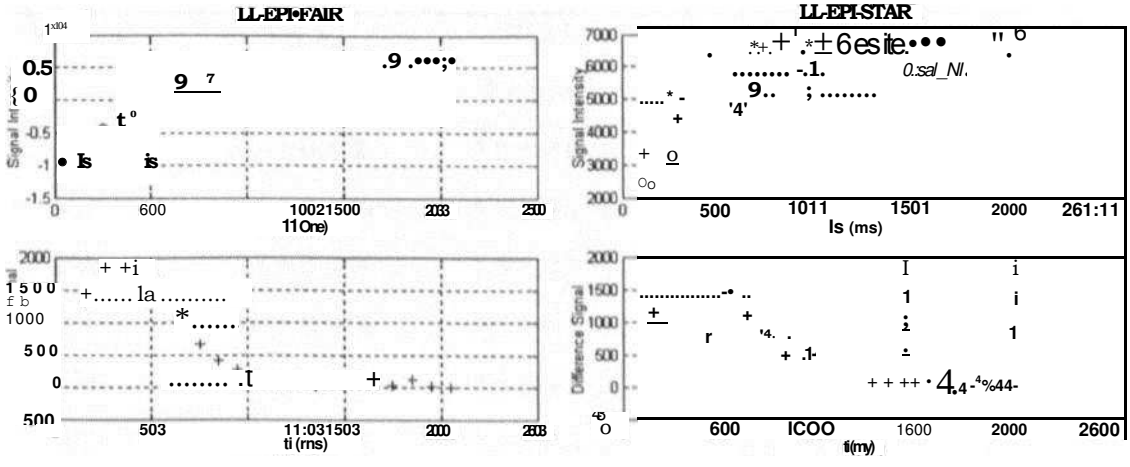

Figure 7.16: The aCBV signal taken from a single voxel of interest in using the FAIR and STAR sequences. Notice that whilst the recorded intensities look very different (i.e. inversion recovery for the FAIR saturation recovery for the STAR) the difference signals look very similar.

In order to compare quantitatively the LL-EPI-FAIR and LL-EPI-STAR techniques across the (n = 6) subject group, **two regions of interest were defined, the first over a** region containing mostly grey matter and **the second over a region containing mainly the**

internal cerebral arteries. Figure 7.17 shows the relative positioning of these two regions overlaid onto a T_i weighted single slice image. Table 7.5 shows the results of this quantitative analysis. Here, notice that good quantitative agreement is observed between the FAIR and STAR derived aCBV values. Also, as expected, the CBV values for the large internal arteries are on average higher than those calculated in grey matter.

Figure 7.17: Example areas of interest placed over the large internal arteries (1) and grey matter (2)

Subject	FAIR Region 1	STAR Region 1	FAIR Region 2	STAR Region 2
SL	3.2 ± 0.8 %	3.8 ± 0.6 %	0.9 ± 0.2 %	0.7 ± 0.1 %
AJ	5.6 ± 0.2 %	5.1 ± 0.1 %	1.2 ± 0.3 %	1.3 ±0.2 %
PW	1.4 ± 0.3 %	1.5 ±0.3 %	1.1 ± 0.2 %	1.2 ±0.2 %
LJ	4.0 ± 0.9 %	3.2 ± 0.8 %	1.0 ± 0.2 %	1.2 ±0.2 %
JM	3.5 ± 0.9 %	4.5 ± 0.6 %	0.9 ± 0.2 %	1.1 ±0.2%
IC	3.0 ± 0.6 %	3.2 ± 0.4 %	1.2 ± 0.2 %	1.2 ± 0.2 %

Table 7.5: Quantitative comparison of the LLEP1-FAIR and LL-EP!-STAR techniques across the n = 6 subject group.

7.7 ACTIVATION INDUCED ACBV CHANGE — A PILOT STUDY

The results presented above represent absolute quantification of aCBV in the resting state brain, however it is clear that if the LLEPI-ASL technique is to be used in investigation of the **BOLD** response and its links to neuronal activity, then dynamic measurement of aCBV change on brain activation is required. To this end, a simple pilot study was performed in order to assess the feasibility of the use of LL-EPI-STAR in brain activation studies.

The LL-EPI-STAR sequence was set up and run as described previously. The experiment was carried out as before ($t_{;}$ =150 ms ; A =100 **ms , N =** 20, and a flip angle of approximately 50°). MBEST EPI images of a single axial slice covering both the left and right primary motor cortices were acquired, using an in plane resolution of 3 mm **x 4** mm, a slice thickness of 6 mm, a matrix size of 64 x 64 and echo time of 35 ms. As before, the inversion spoiler, the incremental spoilers, and the end spoiler were optimized by amplitude modulation. The LL-EPI-STAR sequence was run with a repetition time of 3 s and the inversion pulse alternating between tag and control every other LL-EPI set. The paradigm involved a simple finger-tapping task performed by the subject who was asked to follow a visual cue. Initially 10 LL-EPI sets were acquired in order to allow for **Ti** saturation effects. Following this, the simple blocked paradigm was introduced in which each trial consisted of 30 s of bilateral finger tapping followed by 30 s of rest. This meant that a total of 20 LL-EPI sets were acquired during each trial allowing acquisition of 10 difference images per trial (temporal resolution of 6 s). A total of 27 trials were used in order to allow for signal averaging. Processing of the acquired images was - achieved using custom made software and motion correction was applied using Medx [23].

In order to look for areas of stimulus related change in aCBV, the data from each LL-EP1 set were taken and images 4 to 8 from each set averaged in order to obtain a single aCBV weighted image per LL-EPI set. (Images 4 - 8 were chosen as this is where the greatest change in blood signal was expected.) Pixel timecourses from this volume weighted image set were then correlated with the stimulus waveform using a simple correlation coefficient metric. Areas of high correlation were overlaid onto a single slice. This is

shown in Figure 8.4. N.B no spatial or temporal smoothing was applied to these data prior to correlation coefficient analysis. Pixels of interest were identified using the correlation coefficient map and the flow signals from each of these were extracted, averaged across trials and compared in the active and resting states. The two timecourses taken from a region of interest defined by the correlation coefficient map and covering both left and right primary motor cortex is shown in figure 7.18.

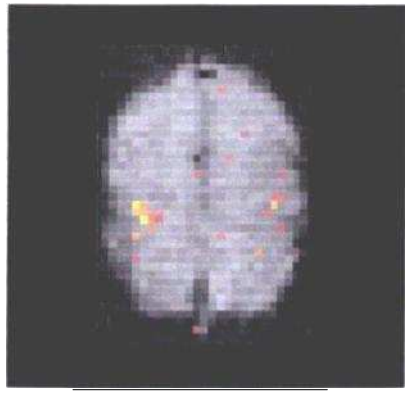

Figure 7.18: A correlation coefficient map showing areas of maximum aCBV change overlaid on an echo planar image of the slice selected.

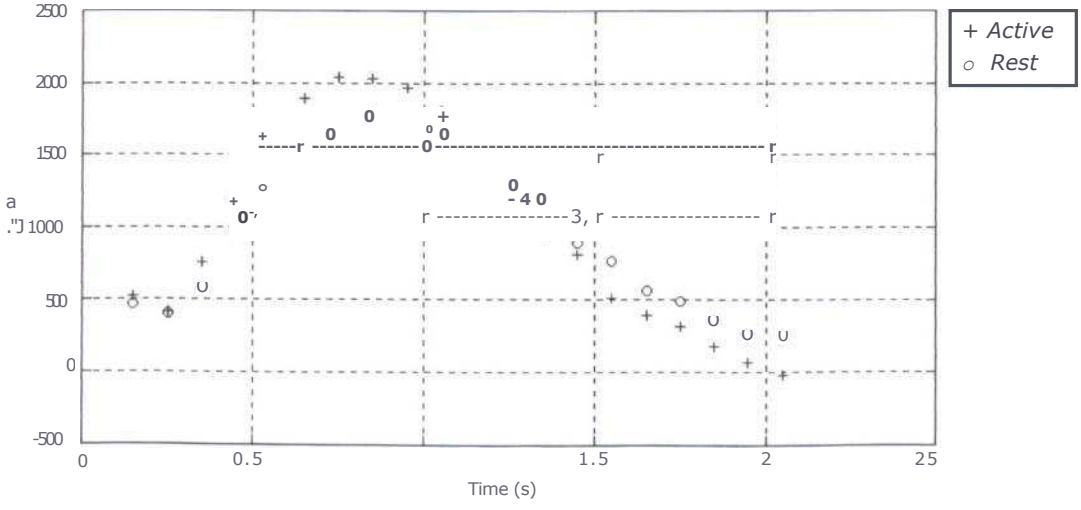

Figure 7.19: Active and resting state blood flow response curves taken from the region of interest defined by the correlation coefficient map. Crosses represent the active state (finger tapping) whereas circles represent the resting state.

Although the low resolution of the correlation coefficient map makes it difficult to locate anatomically the regions of highest aCBV change, they appear to be close to the sensorimotor strip as expected. The flow curves shown in figure 7.19 show that during activation, the blood flow response peaks earlier and exhibits higher overall amplitude than that measured in the resting state.

7.8 DISCUSSION — THE LL-EPI-ASL SEQUENCES

The results presented show that the combination of the LL-EPI sampling strategy with arterial spin labeling techniques allows collection of aCBV weighted images, and the non-invasive, quantitative measurement of arterial cerebral blood volume. Previous measurements of aCBV have been made using ^{19}F NMR in combination with arterial spin labeling and intravascular infusion of perfluorocarbons. These measurements suggest that Resting state aCBV values are approximately 1.3 % in the grey matter of rats [6-8]. The results given in Table 7.5 suggest that aCBV values in humans made using the LL-EPI technique are in agreement with these invasive techniques in animals. In addition, our results show that diffusion weighting gradient pulses can be incorporated into the LL-EP1 sequences in order to eliminate the flow signal from larger vessels, leaving only the capillary signal. We have further shown that to a first approximation, the LL-EPI-STAR and LL-EPI-FAIR sequences are equivalent, the only exception being the inherent sensitivity to flow direction in the STAR sequence. Figures 7.15 and 7.16 show that the blood volume measures are similar for both ASL techniques, and Table 7.5 shows that quantitative aCBV measures across an **n = 6** subject group are equivalent to within the experimental error.

aCBV measurements have been reported using a similar technique by Petersen **a al** [24]. These authors also use the LL-EPI sampling strategy in combination with arterial spin labeling to obtain quantitative measures of aCBV. The major difference between their technique and that described here is in the data analysis since they employ a model free deconvolution technique in order to derive aCBV values. Importantly however, the aCBV values quoted [24] using the deconvolution approach are in strong agreement with those

made here using our magnetization model. This shows that both analysis techniques are equally valid, and further confirms the validity of the results

The aCBV measurements made here are dependent entirely on the mathematical model of blood magnetization. The aCBV measurements derived appear reasonable, and are in good agreement with those previously published using invasive techniques. However, despite the success, there are limitations to the model used that may influence the final result, and so should not be ignored. The major limitation is the assumption that the arterial input function (AIF) (i.e. the magnetization profile of the inversion pulse measured in the z-direction) is a perfect boxcar. In reality, the AIF it is likely to be a smooth function, and could be affected both by the inversion pulse profile, and turbulent blood flow. As blood flows into the non-exchange compartment, the labeled and unlabeled blood water at the extremities of the tagged bolus will mix, causing smoothing of the AIF. In practice this could be included in the mathematical model of the non-exchange compartment by forcing a Gaussian distributed AIF as oppose to the boxcar used. Any imperfections in the inversion pulse profiles will also lead to a smoothing of the AIF, however these inversion profiles can be measured experimentally, and therefore these too could be included in the mathematical model of the non-exchange compartment. At this stage it is not clear what effect these apparent limitations will have on the final calculation of aCBV values. For this reason future work should see these improvements made to the model in order to derive more accurate measurements of aCBV.

In the LL-EPI sequence, flip angles were kept at approximately 50 degrees in order to achieve optimal suppression of the signal from the exchange compartment. However, this relatively low flip angle, combined with the short delay between LL-EPI readout pulses leads to a low signal to noise ratio in LL-EPI images when compared to those acquired using the traditional FAIR or EPI-STAR perfusion methodologies. Having said this, the large number of TI that can be sampled following a single inversion using LL-EPI means that although signal to noise ratio in individual images is lower, the signal to noise ratio per unit time is increased over the traditional ASL methods. It is for this reason that accurate measurements of blood volume can be obtained in under 15 minutes. In addition,

due to suppression of the exchange and venous compartments achieved by the readout pulses, the LL-EPI-ASL technique is more sensitive to aCBV change than the standard techniques and this leads to a more accurate quantification of aCBV.

Finally, the results presented in section 7.7 represent a simple pilot study, and so should not be over interpreted. However, they appear to show that a change in aCBV on neuronal activation is detectable using the LL-EPI-STAR technique. If this is indeed the case then the LL-EPI methodology looks like a highly promising technique for combination with MEG and should allow for a genuine quantitative comparison between dipolar source strength and arterial blood volume change in a LL-EPI-ASL / MEG comparison. Future work might also incorporate more traditional metrics of CBF made using ASL in order to characterize better a full range of MR measurable quantities. Such studies, whilst adequate on 3T scanners, would exploit the higher signal to noise and longer T1 relaxation times available at higher field strengths. For this reason it would be the suggestion of the author that any such study should be carried out at either 4.7 T or 7 T field strengths.

7.9 CONCLUSION

In conclusion, the results presented show that the combination of the LL-EPI sampling strategy with arterial spin labeling techniques allow collection of aCBV weighted images, and non-invasive, quantitative measurement of arterial cerebral blood volume. These measurements are in agreement with those made using a similar technique by Peterson et al [24], and those made invasive techniques in animals [6, 7]. Further, pilot study results show that this technique is applicable to measurement of activation induced aCBV change. Future work should include improvements to the mathematical model of magnetization in the non-exchange compartment, and the optimization of sequence parameters to investigate the use of LL-EPI to measure signals from the exchange compartment. The potential of the LL-EPI sequence to measure aCBV changes on neuronal activation should also be investigated, particularly on ultra high field strength MR scanners.

7.10 REFERENCES

1. Ogawa, S., Menon, R.S., Tank, D.W., Kim, S-G., Merkle, H., Ellermann, J.M., Ugurbil, K., Functional brain mapping by blood oxygenation level dependent contrast magnetic resonance imaging. Journal of Biophysics, 1993. 64: p. 803-812.

2. Attwell, D., Iadecola, C.,, The Neural Basis of Functional Brain Imaging Signals. Trends in Neuroscience, 2002. 25: p. 621-625.

3. Fillenz, M., Lowry, J.P., Boutelle, M.G., Fray, A.E.,, The Role of Astrocytes and Noradrenaline in Neronal Glucose metabolsm. Acta Physiol. Scand., 1999. 167: p. 275-284.

4. Williams, S.R., Neuronal Metabolism. 12th International Meeting of the International Society for Magnetic Resonance in Medicine, **2004. Educational weekend course on Functional MRI.**

5. Buxton, R.B., E.C. Wong, and **F. L.R.,** Dynamics of blood flow and oxygenation changes during brain activation: the balloon model. Magn Reson Med., 1998. 39(6): p. 855-864.

6. Duong, T.Q., Kim, S.,, In Vivo MR Measurements of Regional Arterial and Venous Blood Volume Fractions in Intact Rat Brain. Magnetic Resonance in Medicine, 2000. 43: p. 393-402.

7. Lee, S., Duong, T.Q., Yang, G., Iadecola, C., Kim, S.,, Relative Changes of Cerebral Arterial and Venous Blood Volumes During Increased Cerebral Blood Flow: Implications for BOLD fMRL Magnetic Resonance in Medicine, 2001. 45.

8. Hoad, C., Francis, S.T., Gowland, P.A.,, Arterial Blood Volume and Blood Volume Changes Measurd using ASL in Humans. In Proceedings of the International Society for Magnetic Resonance in Medicine, Kyoto, 2004: p. Abstract Number 1373.

9. Yang, Y., Perfusion MR Imaging woth Pulsed Arterial Spin Labelling: Basic Principles and Applications in Functional Brain Imaging. Concepts in Magnetic Resonance, 2002. 14: p. 347-357.

10. Detre, J.A., Leigh, J.S., Williams, D.S., Koretsky, A.P.,, Perfusion Imaging. Magnetic Resonance in Medicine, 1992. 23: p. 37-45.

11. Look, D.C., Locher, D.R.,, Time saving in measurement of NMR and EPR relaxation times. Review of Scientific Instruments, 1970.41(2): p. 250-251.

12. Mansfield, P., Multi Planar Image Formation using NMR Spin Echoes. Journal of Physics C, 1977. 10: p. p L55-L58.

13. Gowland, P.A., Mansfield, P.,, Accurate Measurement of T1 in Vivo in less than 3S using EPI. Magnetic Resonance in Medicine, 1993. 30: p. 351-354.

14. Francis, S.T., Pears, J.A., Butterworth, S., Bowtell, R.W., Gowland, P.A.,, Measuring the change in CBV upon cortical activation with high temporal resolution using Look-Locher EPI and Gd-DTPA. Magnetic Resonance in Medicine, 2003. 50: p. 483-492.

15. Gunther, M., Bock, M., Schad, R.,, Arterial Spin Lebelling in Combination with a Look-Locher Sampling strategy: Inflow Turbo Sampling EPI-FAIR (ITSFAIR). Magnetic Resonance-in-Medicine, 2001.46: p. 974-984.

16. Kim, S., Quantification of relative cerebral blood flow change by flow-sensitive alternating inversion recovery (FAIR) technique. Applications to functional mapping. Magnetic Resonance in Medicine, 1995. 34: p. 293-301.

17. Edelman, R.R., Chen, Q.,, EPISTAR MRI: Multislice Mapping of Cerebral Blood Flow. Magnetic Resonance in Medicine, 1998. 40: p. 800-805.

18. Francis, S.T., MRI Perfusion Techniques (PhD Thesis). 1998, University of Nottingham.

19. Wang, H.Z., Riederer, S.J.,, A Spoiling Sequence for Suppression of Residual Transverse Magnetisation. Magnetic Resonance in Medicine, 1990. 15: p. 175-191.

20. Gowland, P.A., Leach M.O.,, A Simple Method for the Restoration of Signal Polarity in Multi-image Inversion Recovery Sequences Measuring TI. Magnetic Resonance in Medicine, 1991. 18: p. 224-231.

21. Lagarias, J.C., Reeds, J.A., Wright, M.H., Wright, P.E.,, Convergence Properties of the Nelder-Mead Simplex Method in Low Dimensions. SIAM Journal of Optimization, 1998. 9(1): p. 112-147.

22. Wang, J., Alsop, D.C., Song, H.K., Maldjain, J.A., Tank, K., Salvucci, A.E., Detre, J.A., Arterial transit time imaging with flow encoding arterial spin tagging. Magnetic Resonance in Medicine, 2003. **50:** p. 599 - 607.

23. Woods, R., S. Cherry, and J. Mazziotta, Rapid automated algorithm for aligning and reslicing PET images. JCAT, 1992. 16: p. 620-633.

24. Petersen, E.T., Lim, T.C., Golay, X.,, *A Model Free Quantitative Arterial Spin Labelling Approach for Perfusion MRI.* In Proceedings of the ISMRM, Miami, 2005: p. Abstract Number 34.

CHAPTER EIGHT

CONCLUSIONS AND FUTURE DIRECTIONS

The work presented in the previous chapters represents an ongoing investigation into the relationship between functional magnetic resonance imaging and magnetoencephalography. Initially, the aim in combining the two techniques was centred on exploitation of the high temporal resolution available in MEG, and the high spatial resolution available in fMRI. However, results presented here show that both fMRI and MEG stand alone as useful tools for investigation of brain function, and it is their complementary nature that makes their amalgamation interesting. MEG measures neuronal activity directly, and in doing so enables quantitative measurement of electrical source strength. (Thus far, these measurements have not been possible using MRI, although recent studies have reported the detection of alpha waves using echo planar imaging with a very short TR [1].) In general, fMRI enables measurement of physiological parameters related to blood flow, blood volume and blood oxygenation, which are thought to be representative of neuronal metabolism. It is the link between brain electrical activity measured using MEG and metabolism measured using fMRI that makes the combination of MEG and fMRI an interesting and poignant topic, and not necessarily exploitation of the relative advantages of the two techniques.

8.1 THE MEG BEAMFORMER - LIMITATIONS AND EXTENSIONS

The MEG inverse problem has been described as the 'Achilles heel' of MEG due to the fact that it is an ill-defined problem, i.e. no unique solution exists. This is because field cancellation effects mean that an infinite number of different current distributions inside the head could result in the same magnetic field distribution outside the head. Despite the difficulties, a number of optimisation algorithms exist that use the available MEG data to estimate current distribution. Examples include dipole fitting [2], minimum norm estimation[2], weighted minimum norm estimation [2] and LORETA [3]. The MEG beam former is a representative member of this group and has enjoyed recent success as a technique for MEG data analysis.

In this work, the MEG beamformer was combined with the Hilbert transform and the general linear model in order to derive a useful and novel method for the detection and localisation of neuromagnetic effects. This technique allows for the accurate localisation of both high and low frequency effects and has been shown to work in a variety of applications. Simulations in chapter five showed its accuracy as a technique for localising sustained fields and high frequency synchronisation and desynchronisation effects in the case of a simple blocked paradigm. The scintillating scotoma study showed both its application as an analysis method for novel paradigms, and its validation in the analysis of experimental data. Further, the results in chapter six showed that the GLM-beamformer technique could be used to localise neuromagnetic effects detected in response to simple visual stimulation. In addition to results presented here, a large body of literature also reports the success of the beamformer technique (see [3] for a review), however, despite the successes, it is not without problems.

The beamformer technique can cause suppression of spatially separate yet covariant sources [4]. The use of large time-frequency windows over which to compute the covariance matrix, coupled with source noise are thought to minimise these effects (see chapter five), however they may still be apparent in the data shown. In some subjects, the neuromagnetic response to visual stimulation (shown in chapter six) appeared unilateral, whereas full field checkerboard stimulation is thought to evoke bilateral activation in primary visual cortex. This may be an example of the beamformer causing suppression of spatially separate but covariant sources, however an alternative explanation is that it represents cancellation of magnetic fields caused by opposing dipoles on opposite sides of the calcarine fissure. If the latter explanation holds, then such effects are representative of the limitations of MEG as an imaging modality, and not the beamformer model. However if the former holds then this represents an important limitation to the beamformer methodology. In order to investigate such effects, additional experiments or simulations are required and an investigation into the extent to which correlated sources are attenuated could provide an interesting area for future study. However, in terms of future study of the visual system, both field cancellation effects and suppression of correlated sources can be avoided by the use of quarter field stimulation. The optic nerve

undergoes a partial decussation in projection to the lateral geniculate nucleus [5], meaning that stimulation of the lower right visual field leads to activation in the lower left primary visual cortex. As proof of principle for this hypothesis, a single subject underwent quarter field visual stimulation in both MEG and fMRI. (The imaging parameters were equivalent to those listed in chapter six. The only difference between the two experiments was the use of a quarter field, rather than full field checkerboard stimulus.) The results of this pilot study are shown in Figure 8.1. Notice that all thee neuromagnetic effects and the BOLD response now exhibit a unilateral response, therefore eliminating the possibility of multiple source suppression.

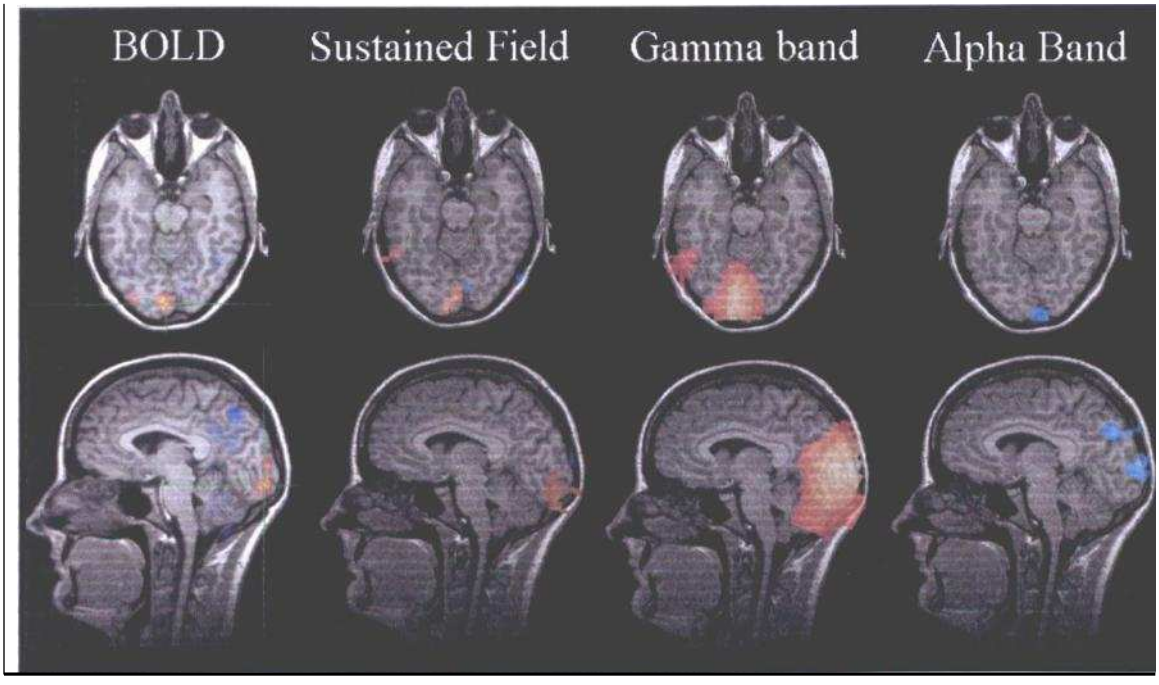

Figure 8.1.. Neuromagnetic and BOLD responses to quarter field visual stimulation.

Arguably the main problem with the current beamformer implementation is that it remains reliant on the dipolar model of neuronal sources. This approximation is inaccurate since real sources will have finite source extent and a range of source orientations, whereas the dipolar model incorporates a simple point source. The breakdown of the dipolar model has been shown by Hillebrand et al [6] who investigated beamformer source reconstruction in response to digit movement. In a simple finger movement task, subjects were asked to move a single digit, two digits or four digits.

Theory suggests that as the number of digits increases, the cortical area involved in that movement becomes larger. Results showed that as the cortical area grew, the beam former became less efficient at reconstructing the source, meaning that accurate localisation of extended sources is difficult using the beamformer model. This effect was thought to represent the breakdown of the dipolar lead field model used in the non-linear beamformer. As the extent of a source grows, the lead fields calculated using a dipolar model becomes a less accurate representation of the true field pattern produced. This breakdown of the dipolar model leads the beamformer reconstruction to become less accurate. For these reasons, extension to the dipolar model may prove an interesting area of future work.

A logical extension to the current model is a multi dipole expansion that makes use of the anatomical information that can be gained from high-resolution MR images. Figure 8.2 shows schematically both the simple dipole model, and a multi-dipole model. In the latter case, anatomical information could be input to the beamformer model in order to obtain a more accurate lead field pattern from a single distributed source.

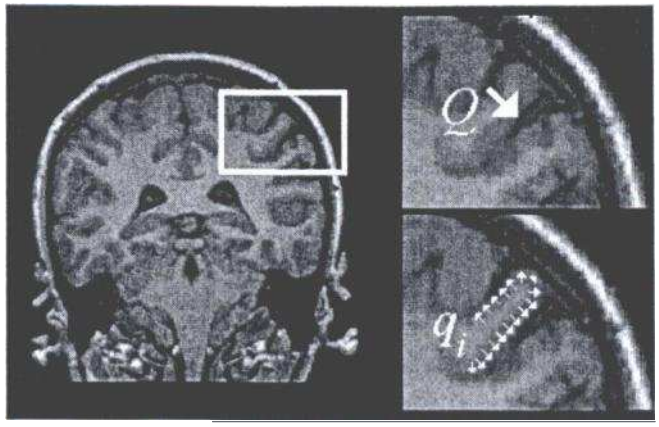

Figure 8.2: Contrasting beamformer models overlaid on a high resolution MR image. The upper right hand image shows the single dipole model used, the lower right hand plot shows a multi-dipolar estimation of a realistic extended source. Such multi-dipole models may prove useful in future extensions of the beamformer work

Lead field patterns taken from anatomically correct extended sources could, in theory, be used in the linearly constrained minimum variance beamformer. In this situation the beamformer, rather than minimising energy originating from sources at all spatial locations other than a single point, would minimise energy originating from sources external to the distributed source modelled. The orientation of distributed sources could be determined by cortical geometry, and beamformer projected power maximised as a function of both source position and source extent. This would allow investigation of not just source position, but also source extent using MEG. Such measures have thus far proved elusive.

8.2 NEUROMAGNETIC EFFECTS AND THE BOLD RESPONSE

Results given in chapter six show that, using MEG, it is possible to detect an 8 - 13 Hz (alpha) event related desynchronisation, a 55 - 70 Hz (gamma) event related synchronisation, and a sustained field effect in response to visual stimulation. Further, localisation of each of these three neuromagnetic effects using the GLM-beamformer technique suggests that they are spatially coincident with the BOLD response. The physiological significance of these three-neuromagnetic effects is unclear, however each represents a significant deviation from the resting state, and so may be related to metabolic demand, and therefore the BOLD response. An investigation into which of these thee neuromagnetic effects contributes most to the BOLD effect represents an attractive way forward, and is clearly poignant if one is to go on to use MEG measurements to characterise the BOLD response. However such calculations are beyond the scope of the simple experiments presented here. One might hypothesise that if the three-neuromagnetic effects represent three independent neuronal networks then they might be separable by their spatial extent. However as described above, the current beamformer implementation is unable to measure accurately the extent of a single source therefore rendering this type of distinction impossible without further advances in the lead field model. Relative contributions to the BOLD response may also be derived by further modification to the visual stimulus, however such modification is non-trivial.

Deriving useful information by combination of neuromagnetic responses and the BOLD response is difficult because, in effect, they represent measurable quantities at opposite ends of a series of biophysical processes [7]. We assume that it is synaptic activity between neurons that leads to an increase in post-synaptic currents, and therefore in neuromagnetic responses detectable in MEG. This synaptic activity also leads to release of vasodilators, which in turn causes an increase in aCBV. ACBV change causes an increase in blood flow, and the increased blood flow, volume and oxygenation leads to the measurable BOLD response. This is shown schematically in Figure 8.3 in which the assumed biophysical processes are shown in yellow.

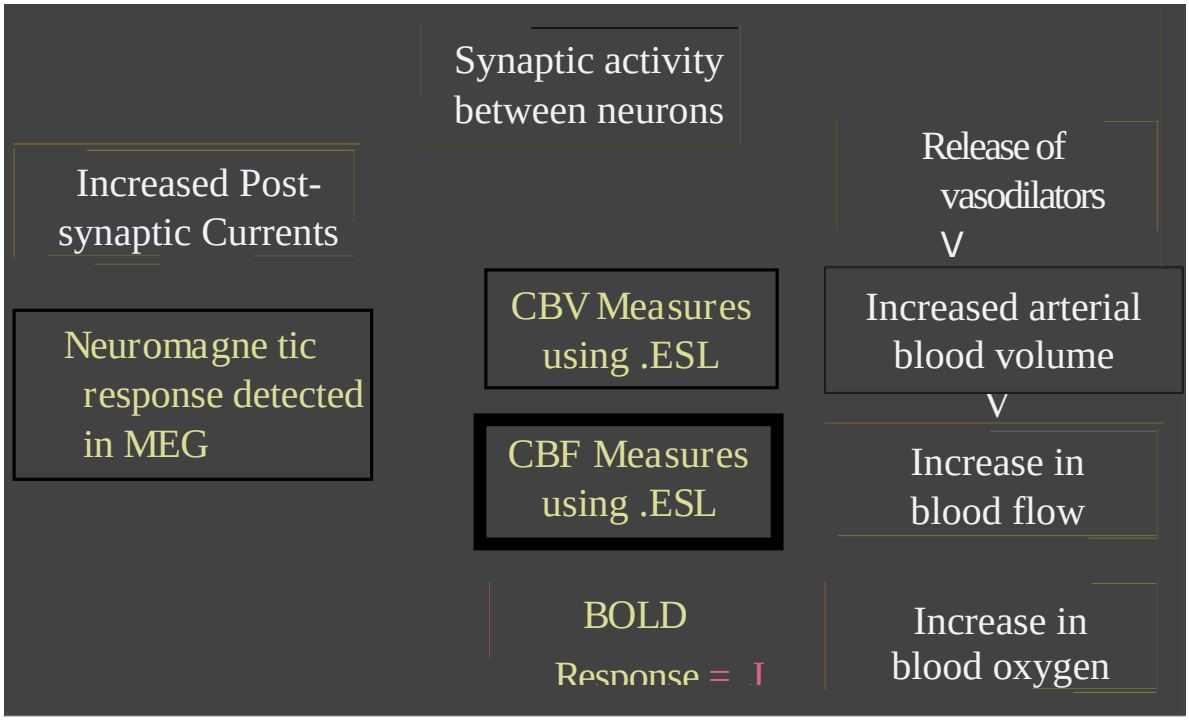

Figure 8.3: A simplified schematic of the BOLD response showing the biophysical steps (in the yellow boxes) and measurable quantities (in the red boxes).

The separation of neuromagnetic effects and the BOLD response may be bridged by the use of further measurements using MRI, and as explained in chapter seven, this was the motivation behind the LL-EPI measurements of cerebral blood volume. Arterial spin labelling measurements can be used to measure both aCBV and CBF, which may provide important information on the metabolic demands of the neuromagnetic effects.

Specifically, one might envisage the use of a graded stimulus in order to assess variation in electrical source strength, CBV, aCBV and BOLD amplitude as a function of stimulus intensity. Such experiments would allow measurement of the linearity between brain electrical activity and the metabolic measurements made using MRI.

In addition to measurements made possible using MRI, further insight may be gained by integration of magnetic resonance spectroscopy. Aspects of neurochemistry, specifically neurotransmitter release, are key to a complete understanding of both the MEG and BOLD signals. For this reason, methodologies involved with the measurement of characteristic neurochemistry in response to brain activation are clearly of some importance. MRS might provide an ideal framework with which to make such measurements and the combination of MEG and MRS adds an extra dimension to MEG-MR comparisons. Further, since neuronal activity and neurotransmitter release are tightly coupled events, this makes the synergistic application of MEG and MRS potentially more profitable than the combination of MEG and BOLD. Recent literature suggests that a relationship exists between release of GABA. and a 30 - 200 Hz (gamma band) synchronisation. Also, application of proton J-editing sequences now enables measurement of GABA concentration in vivo [8] (as does 13C MRS). It is currently unclear whether change in GABA concentration on neuronal activation is a measurable quantity in MRS, since it is likely that local GABA concentration remains the same on neuronal activation, and neurotransmitter cycling mediates synaptic events. However, such measurements are of fundamental interest and should not be overlooked in considering areas for future work.

8.3 QUANTITATIVE IMAGING AND ACBV

The results presented in chapter 7 show that the combination of the LL-EPI sampling strategy with arterial spin labelling techniques allows both the collection of aCBV weighted images, and quantitative measurement of arterial cerebral blood volume. Our measurements are in agreement with those made using a similar technique by Peterson et al, and those made using invasive techniques in animals. Furthermore, a simple pilot study showed that this technique is likely to prove useful in the assessment of activation-

induced changes in aCBV. This work represents the first step towards a quantitative comparison between the functional MRI and MEG. Future work could therefore exploit the LL-EPI-ASL techniques introduced here in order to measure quantitatively relative changes in dipolar source strength and aCBV for some graded stimulation (i.e. visual contrast or frequency of finger tapping). Further, the introduction of ultra high field systems (i.e. 7 T) will increase the available contrast to noise ratio in LL-EPI-ASL studies thus making measurements of this kind easier.

8.4 CONCLUDING REMARKS

The work undertaken has involved the use of MEG and fMRI as separate but complementary non-invasive functional brain imaging modalities. FMRI is now a well-established technique and represents a non-invasive means of making measurements of brain activation with unparalleled spatial resolution. The neuroimaging community has been slower in the uptake of MEG as an equivalent technique, and this has largely been due to the inability to solve the neuromagnetic inverse problem. However, recent use of inverse problem algorithms such as the MEG beamformer has allowed MEG to compete with fMRI, and it now offers reasonable spatial resolution as well as unparalleled temporal resolution.

It is the opinion of the author that both fMRI and MEG represent viable neuroimaging modalities and stand alone as techniques to make accurate non-invasive spatial and temporal measurements of physiological parameters in vivo. In combining the two techniques, it becomes possible to exploit the relative advantages of each modality. However, it is the complementary nature of fMRI and MEG that is of most interest, and this has provided a unique opportunity to investigate the underlying electrical and metabolic physiology of brain activation. Measurements made in this way can potentially bring about a new understanding of the human brain that has not previously been possible, ensuring that this area of research remains active and exciting for many years to come.

8.5 REFERENCES

1. Konn, D.R., Leach, S.A., Gowland, P.A., Bowtell, R.W., Initial attempts at directly detecting alpha wave activity in the brain using MRL Magn. Reson. Imaging, 2004. 22: p. 1413-1427.

2. Hamalainen, M., Hari, R., Ilmoniemi, R.J., Knuutila, J., Lounasmaa, 0.V., Magnetoencephalography - Theory, Instrumentation and applications to non-invasive studies of the working human brain. Reviews of Modern Physics, 1993. 21(2): p. 413 - 460.

3. Pascal-Marqui, R.D., Michel, C.M., Lehmann, D.,, Low Resolution Electromagnetic Tomography, A New Method for Localizing Electrical Activity in the Brain. International Journal of Psychophysiology, 1994. 18: p. 49-65.

4. Van Veen, B.D., Van Drongelen, W., Yuchtman, M., Suzuki, A., Localisation of brain electrical activity via linearly constrained minimum variance spatial filtering. IEEE Transactions on biomedical engineering, 1997. 44(9).

5. Bear, M.F., Connors, B.W., Paridiso, M.A., Neuroscience: Exploring the brain Second Edition. 2001, Philadelphia: Lippincott, Williams and Wilkins.

6. Hillebrand, A., Brookes, M.J., Singh, K.D., Furlong, P.L., Barnes, G.R.,, Spatial extent of neuronal activity measured with MEG beamformers. In Proceedings of the 11th Annual meeting of the Organisation for Human Brain Mapping, Toronto,, 2005.

7. Attwell, D., Iadecola, C.,, The Neural Basis of Functional Brain Imaging Signals. Trends in Neuroscience, 2002. 25: p. 621-625.

8. Rothman, D.L., Petroff, O.A.C., Behar, K.L., Mattson, R.H.,, Localised 1H NMR measurements of GABA in human brain in vivo. Proceedings of the National Academy of Science USA, 1993. 90: p. 5662-5666.